Development of a Cationic Mucic Acid Polymer-Based Nanoparticle siRNA Delivery System

Thesis by

Dorothy Weichi Pan

In Partial Fulfillment of the Requirements for the degree of

Doctor of Philosophy

CALIFORNIA INSTITUTE OF TECHNOLOGY

Pasadena, California

2016

(Defended May 5, 2016)

Dorothy Weichi Pan
ORCID: 0000-0003-4066-7750

ACKNOWLEDGEMENTS

There are numerous people to whom I am grateful who have made my thesis research possible and enriched my experience at Caltech.

First of all, I would like to thank my advisor, Professor Mark E. Davis, for his mentorship during my PhD. He makes himself available to his students, especially when they have puzzling data and questions. For an MD/PhD student aspiring to bridge the space between the laboratory and the clinic, his wealth of experience in translational medicine, business, and entrepreneurship after having brought two therapeutics to clinical trials was a valuable resource. I'd also like to thank Professor Jim Heath, the chair of my committee, for his leadership with Caltech's NanoSystems Biology Cancer Center, as well as my other committee members Professor Judy Campbell and Professor Dave Tirrell for their insights into proposing and planning projects.

Executing a project that starts with chemical synthesis takes testing to the *in vitro* and all the way to the *in vivo* stage requires many instruments and facilities, as well as the expertise for a broad range of subjects. Dr. Yen Yun at City of Hope kindly provided pharmaceutical antibodies that I used as targeting agents for my project. I'd like to thank Dave Vandervelde in the liquid NMR facility for suggesting useful methods and aiding me in the analysis of my polymers. Mona Shahgholi in the mass spectrometry facility trained on a couple instruments that allowed me to obtain the masses of crucial material. I also worked extensively with Alasdair McDowell doing cryo-transmission electron microscopy to confirm the size of my nanoparticles. Andres Collazo trained me and helped troubleshoot problems with confocal microscopy. Suresh Gupta, the computer guru in the chemical engineering department, was able to save me a lot of time trying to fix the many

computers operating instruments in our lab which crashed during my time performing experiments. The staff at the animal facility was also critical to performing mouse experiments, especially vet tech Gwen Williams for her thorough knowledge of procedures and intuition for mouse behavior, and veterinarian Dr. Karen Lencioni for her advice on caring for mice with tumors. Alyssa Maskell, Lorena Sandoval, and John Papsys provided animal husbandry for which I am appreciative.

I would also like to thank the members of my lab for being wonderful colleagues. Han Han, Leonard Medrano, Yashodan Bhawe, and especially Devin Wiley and Jonathan Zuckerman, provided a lot of mentorship when I was getting my project started. Ben Boal worked in the chemistry hood across from me and was a source of advice in synthetic procedures. My MD/PhD colleague Andrew Clark, as well as Emily Wyatt and Dana Levine, are always willing to discuss ideas and experiments. I had the privilege of mentoring undergraduate Kristin Anderson for two summers, as well as Jan Winkler from ETH and Merle Bischoff from Aachen for their master's theses, and I gained a lot of insight by helping them propose and guide them through their projects.

Agnes Tong in the chemistry graduate program office was a valuable resource with all things related to requirements, paperwork, and much more. Martha Hepworth was also helpful with a lot of secretarial tasks. Roland Rapanot is a rock star administrator for the USC-Caltech MD/PhD program and facilitates the organization of the MD/PhD journal club where I first met my advisor Mark Davis and learned about the types of projects worked on in his lab. I'd also like to thank the former and current program directors Drs. Robert Chow and Steve Mittelman for their dedication to training and mentoring physician-scientists.

Outside the lab, I was very involved in many activities at Caltech. The Catalina Community Associates and the Resident Associates have been an amazing team to work with in building and fostering a residential community. I'd like to thank Felicia Hunt and Larissa Charnsangavej for their support of residential life, and my RA and CCA colleagues Beau Pritchett, Swarnima Manohar, Corey Reeves, Christine Morrison, Emily Wyatt, Daniel Brooks, Camille McAvoy, and many other CCA's for their contributions, teamwork, and friendship. The Caltech Y is also a place that fosters a sense of adventure and service for the Caltech community. As a member of the outdoors committee, I'd like to thank the staff at the Y, Athena Castro, Portia Harris, Liz Jackman, and especially Greg Fletcher, for their support of all our student-led trips. Becky Schwantes, Jeremy Sandler, Casey Handmer, Howard Hui, William Frankland, Andrew Robbins, Joan Ballester, and Zoltan Tuza have been wonderful friends with whom I have led countless hikes and trips so that less experienced students could safely participate in adventures. Isaac Fees, Rebecca Rojansky, and I also led a Y hike where Rebecca (also an MD/PhD) and I had to deal with some altitude and medical issues that put our clinical reasoning to use in the wilderness!

Having been a musician for about 80% of my life, I was glad to be able to play the flute and piccolo with the Caltech-Occidental Symphony Orchestra and in chamber music groups. The orchestra conductor Allen Gross chose a variety of major symphonic repertoire with flute and piccolo parts that were both fun and challenging for us to play. It was amazing to make music with a fantastic flutist and friend, Megan Newcombe, and getting a review from Delores Bing after a concert that the flute section is the best section in the orchestra. Megan and I were joined by Jeffrey Thompson, Jill Craven, and Jeremy Yager in the trombone section for dinner before orchestra rehearsal every week, and had

conversations about music as well as careers – interviews, postdocs, and jobs – as they are all a step ahead of me in life after being a student. Concertmaster Sean Symon kept me company in another sound-proof practice room late at night in the music house. Zachary Erickson pestered me about the concerto competition until I finally decided to learn the Nielsen Flute Concerto and even got to play it with the orchestra. My flute teacher, Gary Woodward, is perhaps the most patient coach ever with an infinite number of ways to think about music and technical tricks up his sleeve. Hye-Sung Choe was a wonderful coach for my first chamber group at Caltech with Colin McKinney, Michael Zhang, and Jennifer Zhu playing Saint-Saens. Michael Kreiner has been a lot of fun to work with as bassoonist and coach for multiple of my chamber groups, including with Kelly Kim, Charles Cao, Jamie Rankin, and Aidan Chatwin-Davies. Aidan Chatwin-Davies was first a musical colleague, then a friend who also enjoyed hikes, but our relationship has become something more, and I appreciate him for supporting my hectic lifestyle.

Lastly, I'd like to thank my family for telling me I was crazy to do an MD/PhD but letting me do it and supporting me along the way anyways. My sister, Tiffany Pan, started medical school at USC during my PhD and is now ahead of me in medical school, holding true to her assertion that she would never do an MD/PhD even when she had a chance to apply into the program. However, her stories about her sick patients when she comes home from the hospital reaffirms to me the need for more research and discovery especially in the fields of neurology and oncology, and I have much to look forward to as I head back into the clinical portion of my training.

ABSTRACT

Cancer chemotherapy has advanced from highly toxic drugs to more targeted treatments in the last 70 years. Chapter 1 opens with an introduction to targeted therapy for cancer. The benefits of using a nanoparticle to deliver therapeutics are discussed. We move on to siRNA in particular, and why it would be advantageous as a therapy. Specific to siRNA delivery are some challenges, such as nuclease degradation, quick clearance from circulation, needing to enter cells, and getting to the cytosol. We propose the development of a nanoparticle delivery system to tackle these challenges so that siRNA can be effective.

Chapter 2 of this thesis discusses the synthesis and analysis of a cationic mucic acid polymer (cMAP) which condenses siRNA to form a nanoparticle. Various methods to add polyethylene glycol (PEG) for stabilizing the nanoparticle in physiologic solutions, including using a boronic acid binding to diols on mucic acid, forming a copolymer of cMAP with PEG, and creating a triblock with mPEG on both ends of cMAP. The goal of these various pegylation strategies was to increase the circulation time of the siRNA nanoparticle in the bloodstream to allow more of the nanoparticle to reach tumor tissue by the enhanced permeation and retention effect. We found that the triblock mPEG-cMAP-PEGm polymer condensed siRNA to form very stable 30-40 nm particles that circulated for the longest time – almost 10% of the formulation remained in the bloodstream of mice 1 h after intravenous injection.

Chapter 3 explores the use of an antibody as a targeting agent for nanoparticles. Some antibodies of the IgG1 subtype are able to recruit natural killer cells that effect antibody dependent cellular cytotoxicity (ADCC) to kill the targeted cell to which the antibody is bound. There is evidence that the ADCC effect remains in antibody-drug

conjugates, so we wanted to know whether the ADCC effect is preserved when the antibody is bound to a nanoparticle, which is a much larger and complex entity. We utilized antibodies against epidermal growth factor receptor with similar binding and pharmacokinetics, cetuximab and panitumumab, which differ in that cetuximab is an IgG1 and panitumumab is an IgG2 (which does not cause ADCC). Although a natural killer cell culture model showed that gold nanoparticles with a full antibody targeting agent can elicit target cell lysis, we found that this effect was not preserved *in vivo*. Whether this is due to the antibody not being accessible to immune cells or whether the natural killer cells are inactivated in a tumor xenograft remains unknown. It is possible that using a full antibody still has value if there are immune functions which are altered in a complex *in vivo* environment that are intact in an *in vitro* system, so the value of using a full antibody as a targeting agent versus using an antibody fragment or a protein such as transferrin is still open to further exploration.

In chapter 4, nanoparticle targeting and endosomal escape are further discussed with respect to the cMAP nanoparticle system. A diboronic acid entity, which gives an order of magnitude greater binding (than boronic acid) to cMAP due to the vicinal diols in mucic acid, was synthesized, attached to 5kD or 10kD PEG, and conjugated to either transferrin or cetuximab. A histidine was incorporated into the triblock polymer between cMAP and the PEG blocks to allow for siRNA endosomal escape. Nanoparticle size remained 30-40 nm with a slightly negative ca. -3 mV zeta potential with the triblock polymer containing histidine and when targeting agents were added. Greater mRNA knockdown was seen with the endosomal escape mechanism than without. The

nanoparticle formulations were able to knock down the targeted mRNA *in vitro*. Mixed effects suggesting function were seen *in vivo*.

Chapter 5 summarizes the project and provides an outlook on siRNA delivery as well as targeted combination therapies for the future of personalized medicine in cancer treatment.

PUBLISHED CONTENT AND CONTRIBUTIONS

Pan, D.W. and Davis, M.E. Cationic mucic acid polymer-based siRNA delivery systems. *Bioconjugate Chem.* **2015**, *26*, 1791-1803. doi : 10.1021/acs.bioconjchem.5b00324

D.W.P participated in the conception of the project, performed synthesis and experiments, prepared the data, and participated in the writing of the manuscript.

Ahmed, M., Pan, D.W., and Davis, M.E. Lack of *in vivo* antibody dependent cellular cytotoxicity with antibody containing gold nanoparticles. *Bioconjugate Chem.* **2015**, *26*, 812-816. doi : 10.1021/acs.bioconjchem.5b00139

D.W.P participated in the conception of the project, performed experiments, prepared the data, and participated in the writing of the manuscript.

TABLE OF CONTENTS

LIST OF FIGURES

Number *Page*

LIST OF SCHEMES

Number *Page*

LIST OF STRUCTURES

Number *Page*

LIST OF TABLES

Number *Page*

Chapter 1

Introduction

Targeted therapeutics for cancer

Cancer is currently the second leading cause of death in the United States.[1] With 8 million cancer-related deaths in 2012, malignancies are also one of the major causes of death and disability worldwide.[2] The most common types of cancer diagnosed as well as leading to death are those arising from sites in the lung, breast, prostate, and colon, as shown in Figure I.1.[1] In addition to the human burden caused by cancer, the financial costs are considerable. In 2009, an estimated $286 billion in medical costs and in lost productivity was caused by new cancer diagnoses, with 94% of that amount being incurred in developed countries such as the United States.[3] This price tag may be due to the use of newer therapies for cancer, which are more specific against the cancer and enable the patient to have a better quality of life that allows them to carry on most of their usual activities.

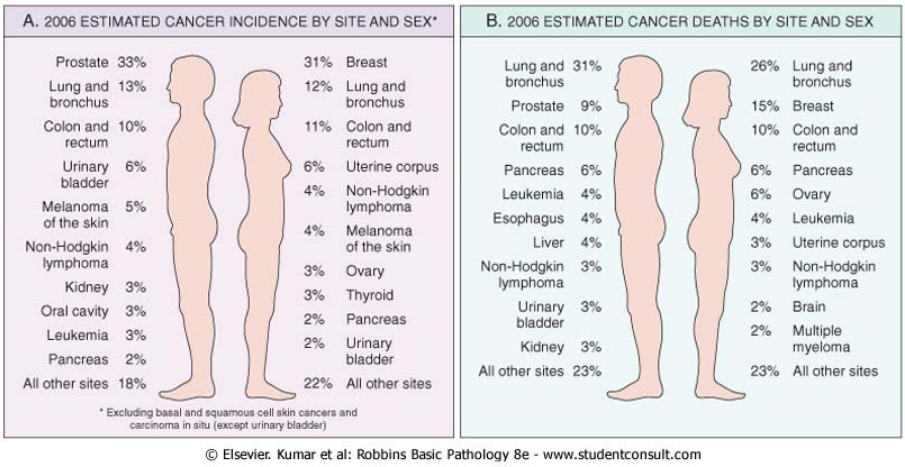

Figure I.1: Cancer incidence and death by site. From Stricker and Kumar in *Robbins Basic Pathology*, 8th Edition.

Although many toxic chemotherapeutics such as methotrexate and cisplatin are still part of many chemotherapy regimens, cancer treatment has advanced in the last 70 years from highly toxic drugs with many adverse effects to more specific therapies that cause fewer side effects. Some of the first toxic compounds used against leukemia were derivatives of nitrogen mustard and anti-folates.[4,5] Many of these chemotherapeutics used for cancer treatment target cell replication. Because cancer cells generally proliferate more rapidly than other cell types in the body, these types of chemotherapeutics have a larger impact on the malignant cells. However, because some cells in the body, such as blood cells, epithelial cells lining the gastrointestinal (GI) tract and skin or hair, need to be replenished fairly frequently, there can be severe adverse effects resulting from chemotherapeutics, such as anemia, nausea, vomiting, diarrhea, sores, and hair loss.

The first targeted therapy developed was Gleevec, or imatinib, which inhibits the tyrosine kinase domain fused by *bcr-abl* resulting from the Philadelphia chromosome 9;22 translocation.[6] Since then, numerous targeted therapies have been developed, many of which target tyrosine kinases – tyrosine kinase inhibitors (TKIs). For example, erlotinib and gefitinib are inhibitors of the intracellular tyrosine kinase domain in the epidermal growth factor receptor (EGFR) often overexpressed or mutated in non-small cell lung cancer (NSCLC), colorectal cancer, and head and neck cancers.[7-10]

In addition to TKIs, antibodies against the extracellular domain of EGFR, such as Erbitux (cetuximab) and Vectibix (panitumumab) have been developed to inhibit EGFR signaling in NSCLC, colorectal, and head and neck cancer, though cetuximab is currently only FDA approved for colorectal and head and neck cancer and panitumumab for colorectal cancer.[11-12] Genentech's blockbuster drug, Herceptin (trastuzumab), is also an

antibody which is directed against human epidermal growth factor receptor 2 (Her2).[13] Her2 is often overexpressed in up to 30% of breast cancers and some types of gastric cancer.[14,15] In all cases, eventually the malignant cells mutate and become resistant to the targeted therapy.[12,16-18] Therefore, newer targeted therapies are developed in an effort to overcome therapy resistance, and many of these targeted therapies are used in combination with other targeted therapies or chemotherapy, such as cetuximab with irinotecan, fluorouracil, and leucovorin (FOLFIRI) in metastatic colorectal cancer.[9,19-21]

The idea to combine a targeted antibody therapeutic with a chemotherapeutic as a single drug resulted in antibody-drug conjugates (ADCs). ADCs link a cytotoxic drug to an antibody to better target the chemotherapeutic agent to the appropriate cells. They were developed to enhance the potency of the antibody after resistance to trastuzumab developed, as well as create a sort of combination therapy with multiple modes of action in a single formulation.[22] Trastuzumab conjugated to the cytotoxic microtubule disruptor emtansine (DM1) shown in Figure I.2, Kadcyla (T-DM1) is an example of an FDA approved ADC, with many more in development at Genentech and other pharmaceutical companies.[23-24] Although T-DM1 initially is effective against transtuzumab-resistant cancers, resistance to the ADC eventually develops and combinations with other therapeutics are used in an attempt to rescue its function.[22-27]

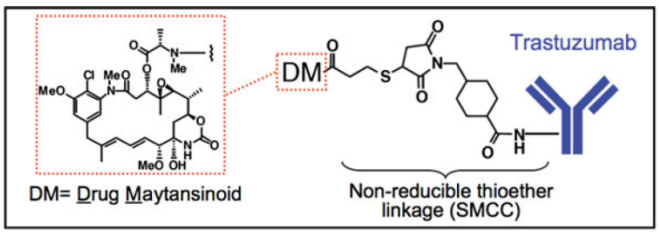

Figure I.2: Trastuzumab conjugated to a DM (T-DM1) is an example of an antibody drug conjugate that is FDA approved. From Junttila, et al. *Breast Cancer Res. Treat.* **2011,** *128,* 347-356.

Perhaps it is cancer's ability to outsmart each new therapy and the myriad side effects that these therapies cause that cancer has been dubbed "the emperor of all maladies."[28] TKIs, antibodies, and ADCs have been shown to be effective and less toxic than the cytotoxic chemotherapeutic agents, but some adverse effects remain. For example, TKIs and antibodies against EGFR can cause skin rashes and GI toxicity because EGFR is highly expressed in epithelial tissues. ADCs such as T-DM1 is also able to cause many of the side effects associated with cytotoxic chemotherapy, though it is obviously less toxic than emtansine alone, which is not tolerated by patients at all.[22] In an effort to develop a therapeutic that is more potent against malignant cells but less toxic to the patient, nanoparticles with more design complexity and flexibility show promise to enable multiple therapeutic modes of action with high drug-loading capacity while having minimal penetration to normal tissue.

Nanoparticle Therapies

The earliest nanoparticle therapeutics sought to reduce the toxicity of cytotoxic chemotherapeutics by encapsulating the drug in a liposome (doxorubicin, Doxil) or coating it with albumin (paclitaxel, Abraxane).[29,30] Although the development of nanoparticles (shown in Figure I.3) has a history of more than forty years, only a few of these early nanoparticle formulations have been FDA approved and are on the market as shown in Table I.1. A much larger number of nanoparticles therapies are in various stages of clinical trials.[30-32]

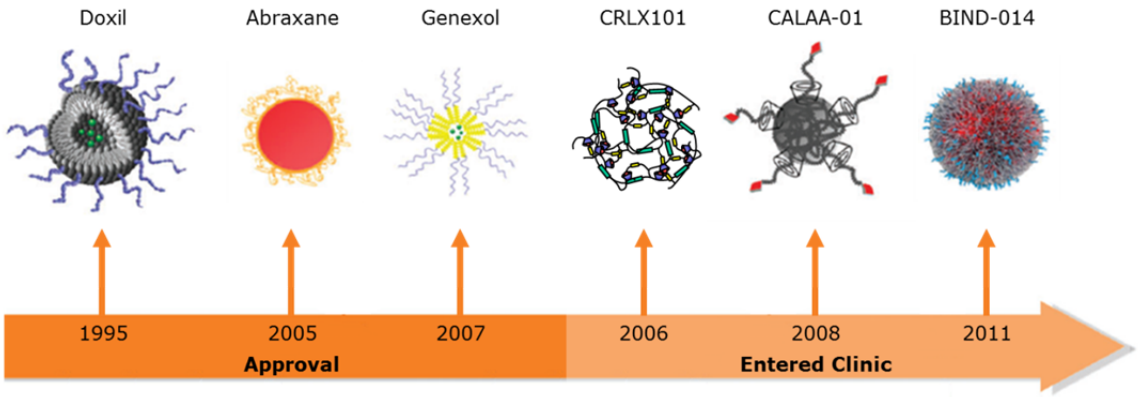

Figure I.3: Timeline of nanoparticle development. Doxil, Abraxane, and Genexol-PM (in Korea) are approved for cancer therapy. CRLX101, CALAA-01, and BIND-014 are in clinical trials for cancer therapy. Adapted from Kamaly, et al. *Chem. Soc. Rev.* **2012,** *41,* 2971-3010.

Despite the few nanoparticles that have been FDA approved, nanoparticles show efficacy and substantially decrease the toxicity of the chemotherapeutic agents that they have been formulated to deliver. For example, CRLX101, a cyclodextrin-PEG polymer containing camptothecin that forms a 30 nm diameter nanoparticle, has been shown to have few adverse effects compared to other camptothecin-containing drugs not in nanoparticle form (shown in Figure I.4). Adverse effects are seen in less than 40% of patients, with very few of the serious grade 3-4 adverse effects seen. It has been shown to preferentially localize in tumor tissue in gastric cancer without being present in adjacent normal gastric tissue.[33]

This passive targeting of nanoparticles to tumor tissue is due to what is named the enhanced permeation and retention (EPR) effect illustrated in Figure I.5. This phenomenon has origins in both blood vessel and lymphatic differences between tumor tissue and normal tissue. Blood vessels in tumor tissue are leaky and allow nanoparticles less than around 200 nm to pass through, unlike in normal tissue where they have tight junctions that prevent nanoparticle passage. Additionally, poor lymphatic drainage in tumor tissue

contributes to the accumulation of nanoparticles.[34] Passive targeting of nanoparticles by the EPR effect contributes to the enhanced safety profile of nanoparticle therapeutics, and enables the use of drug combinations with the nanoparticle-encapsulated drug that would otherwise be too toxic for the patient.

In addition to the improved safety profile of nanoparticle therapeutics, nanoparticles are able to encapsulate hydrophobic drugs that are not normally soluble in aqueous solution and protect a sensitive drug from being degraded before reaching the tumor.[34] Polymers can have high loading capacity of drug onto the polymer which forms the nanoparticle. The nanoparticles also can be targeted to particular cells within a tumor or to enhance cellular uptake of the therapeutic. If the targeting agent for the nanoparticle is also an effective therapeutic such as an antibody, then a nanoparticle with multiple mechanisms of action is created.

Nanocarrier	Name	Formulation	Drug	Indication	Status
Liposomes	Doxil® (Caelyx® in EU)	PEGylated liposome	Doxorubicin	Breast cancer, ovarian cancer, multiple myeloma, Kaposi's sarcoma	Market
	Myocet®	Non-PEGylated liposome	Doxorubicin	Breast cancer	Market
	DaunoXome®	Non-PEGylated liposome	Daunorubicin	Kaposi's sarcoma	Market
	DepoCyt®	Non-PEGylated liposome	Cytarabine	Lymphomatus meningitis, leukaemia, glioblastoma	Market
	Lipoplatin	PEGylated liposome	Cisplatin	Various malignancies	Phase III
	S-CKD602	PEGylated liposome	CKD-602	Various malignancies	Phase I/II
	NL CPT-11	PEGylated liposome	Irinotecan (CPT-11)	Glioma	Phase I
	CPX-1	Liposome	Irinotecan	Colorectal cancer	Phase II
	LE-SN38	Liposome	SN-38	Colorectal cancer	Phase II
	MBP-426	Tf-NGPE-liposome	Oxaliplatin	Various malignancies	Phase II
	MCC-465	Human antibody fragment (GAH)-PEG-liposome	Doxorubicin	Gastric cancer	Phase I
	Thermodox™	Heat-activated PEGylated liposome	Doxorubicin	Liver cancer, breast cancer	Phase III
	CPX-351	Liposome	Cytarabine+daunorubicin	Acute myeloid leukaemia	Phase II
	SGT-53	Transferrin-targeted DNA plasmid liposome	P53 gene	Various solid malignancies	Phase I
Polymeric nanoparticles	Abraxane® (ABI-007)	Albumin-bound nanoparticle (nab)	Paclitaxel	Breast cancer	Market
	BIND-014	PEG-PLGA nanoparticle	Docetaxel	Various solid malignancies	Phase I
	Docetaxel-PNP	Polymeric nanoparticle	Docetaxel	Various solid malignancies	Phase I
	CRLX101	Cyclodextrin-PEG nanoparticle	Camptothecin	Various malignancies	Phase II
	CALAA-01	Cyclodextrin-PEG-transferrin-nanoparticle	Anti-RRM2 siRNA	Various solid malignancies	Phase I
Polymeric micelles	Genexol-PM®	PEG-PLA micelle	Paclitaxel	Breast cancer, lung cancer, ovarian cancer	Market/Phase II
	NK911	PEG-PAA micelle	Doxorubicin	Various solid malignancies	Phase III
	NK105	PEG-PAA micelle	Paclitaxel	Gastric cancer	Phase II
	NC-6004 (Nanoplain™)	PEG-polyglutamic acid micelle	Cisplatin	Pancreatic cancer	Phase I/II
	NK012	PEG-PGA micelle	SN-38	Various solid malignancies	Phase II
	SP1049C	P-glycoprotein micelle	Doxorubicin	Various malignancies	Phase II
	Paclical®	Polymeric micelle	Paclitaxel	Ovarian cancer	Phase III
	NC-4016	Polymeric micelle	Oxaliplatin	Various solid malignancies	Phase I
Polymer-drug conjugate nanoparticles	Oncaspar®	PEG-drug	L-asparaginase	Leukaemia	Market
	PK1 (FCE28068)	HPMA-drug	Doxorubicin	Breast cancer, lung cancer, colorectal cancer	Phase II
	AP5280	HPMA-drug	Platinum	Various malignancies	Phase II
	ProLindac™ (AP5346)	HPMA-DACH-drug	Oxaliplatin	Ovarian cancer	Phase II
	Xyotax™, Opaxio™, CT-2103	Polyglutamic acid-drug	Paclitaxel	Lung cancer, ovarian cancer	Phase III
	CT-2106	Polyglutamic acid-drug	Camptothecin	Colon cancer, ovarian cancer	Phase I/II
	Delimotecan (Men 4901/T-0128)	Carboxymethyl dextran	T-2513	Various malignancies	Phase I
	DOX-OXD (AD-70)	Dextran	Doxorubicin	Various malignancies	Phase I
	MTX-HSA	HSA-drug	Methotrexate	Kidney cancer	Phase II
	XMT-1001	Fleximer®-drug	Camptothecin	Gastric cancer, lung cancer	Phase I
	Pegamotecan	PEG-drug	Camptothecin	Gastric cancer	Phase II
	PegAsys/PegIntron	PEG-drug	IFNα2a/-IFNα2b	Melanoma, leukaemia	Phase II
	NKTR-102	PEG-drug	Irinotecan	Breast cancer, ovarian cancer, colorectal cancer	Phase III
	DE-310	Carboxymethyldextran polyalcohol polymer	DX-8951	Various malignancies	Phase I/II
Lipid-drug	C-VISA BikDD	Lipid-conjugated-plasmid C-VISA-BiKDD	Pro-apoptotic Bik gene (BikDD)	Pancreatic cancer	Phase I
	ALN-VSP	Lipid-conjugated-antiKSP and antiVEGF	antiKSP and antiVEGF siRNA	Liver cancer	Phase I
	Atu027	Lipid-conjugated-antiPKN3	antiPKN3 siRNA	Various solid malignancies	Phase I
Other drug-conjugated based nanoparticles	Rexin-G	Retroviral-vector-dnG1 plasmid DNA (pathotropic NP)	G1 gene	Various solid malignancies	Phase I/II

GAH, human monoclonal antibody; PLA, polylactic acid; PAA, polyaspartate; KSP, kinesin spindle protein; siRNA, small interference RNA; PKN3, protein kinase N3; PEG, poly (ethyleneglycol); NGPE, N-glutaryl phosphatidylethanolamine; PLGA, poly (D,L-lactic-co-glycolic acid); HPMA, -N-(2-hydroxypropyl)-methacrylamide copolymer; DACH, di-aminocyclohexane; HSA, human serum albumin; VEGF, vascular endothelial growth factor

Table I.1: Nanoparticle delivery systems for cancer therapy on the market and in clinical development. From Egusquiaguirre, et al. *Clin. Transl. Oncol.* **2012,** *14*, 83-93.

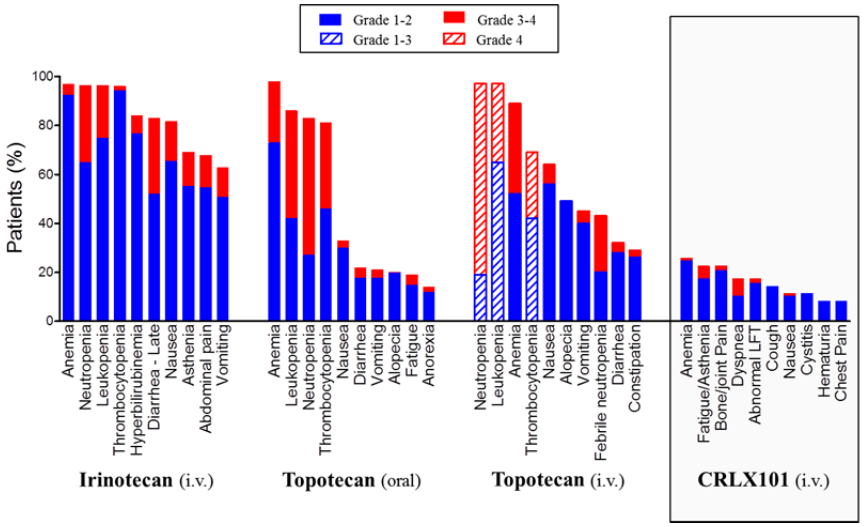

Figure I.4: Adverse effects of camptothecin-containing drugs and CRLX101, a nanoparticle which contains camptothecin. From Cerulean Pharma Inc., United States Securities and Exchange Commission Annual Report (http://www.sec.gov/Archives/edgar/data/1401914/000156459016014403/ceru-10k_20151231.htm)

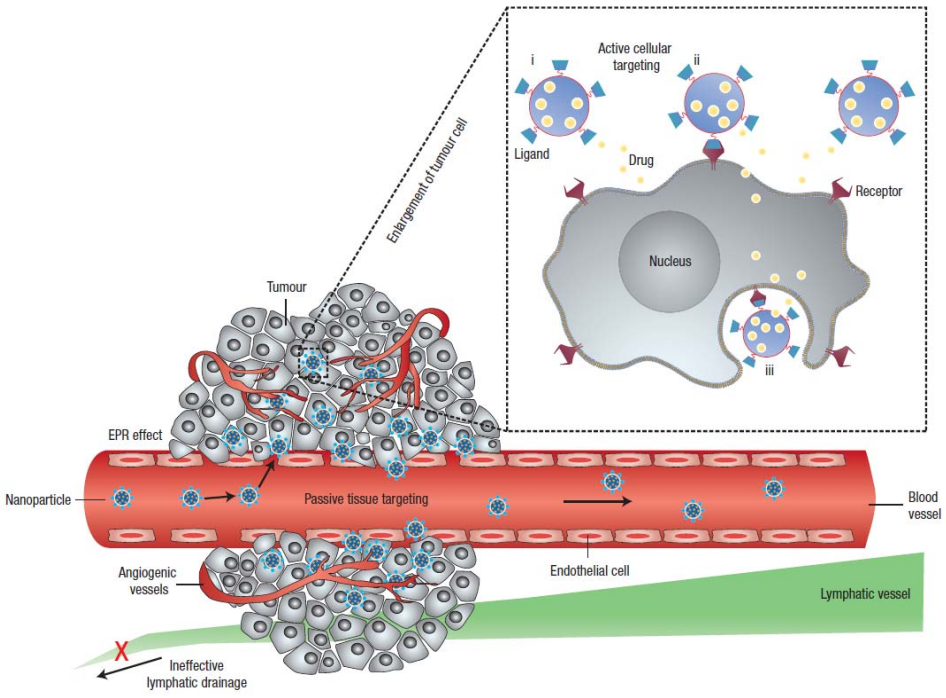

Figure I.5: The enhanced permeation and retention (EPR) effect of nanoparticles accumulating in tumor tissues due to leaky blood vessels and poor lymphatic drainage. From Peer, et al. *Nature Nanotechnology* **2007,** *2*, 751-760.

siRNA Delivery: Advantages and Challenges

Nanoparticle-based delivery of macromolecular agents as a therapeutic commenced with the discovery of RNA interference (RNAi) by Fire and Mello in 1998.[35] Small interfering RNA (siRNA) is a short double stranded RNA ca. 21 base pairs. It is able to very specifically cleave the messenger RNA (mRNA) complementary to it using the RNAi induced silencing complex (RISC) in the cytosol to silence an overexpressed or mutated gene, as shown in Figure I.6. siRNA sequences are now being developed with very high potency, so that the concentration required for silencing 50% of the mRNA is in the single digit picomolar scale. Because siRNA is catalytic, once it has reached the cell cytosol it will remain for a prolonged period of time subject to cell division rate.[36] RNAi has the promise of being able to silence any gene, including for intracellular proteins, such as KRAS, which have been considered "undruggable."[37] Once a nanoparticle siRNA delivery system is developed, it is able to deliver any siRNA sequence, including multiple siRNA sequences in the same particle for combined silencing of multiple genes fueling the cancer cell's growth. Silencing of multiple genes using multiple siRNA sequences in the same delivery system has been shown both in preclinical studies and clinical trials.[38,39]

Delivering siRNA can be challenging. siRNA needs to be protected from being degraded by nucleases present in the bloodstream as well from recognition by toll-like receptors (TLR's) which would activate the immune system.[40] This can be achieved by using a delivery system that protects the siRNA from being accessed by nucleases and immune components. siRNA also has a very short circulation time in the bloodstream, with rapid renal clearance.[41-46] Even with polycationic siRNA delivery systems, such as CALAA-01, circulation time is short and the nanoparticles are disassembled at the

glomerular basement membrane in the kidney.[42-46] Furthermore, the siRNA needs to be internalized into cells, where it is endocytosed into an endosome. Then the siRNA needs escape from the endosome and reach the cytosol to bind to RISC and perform its functions, as shown in Figure I.7.

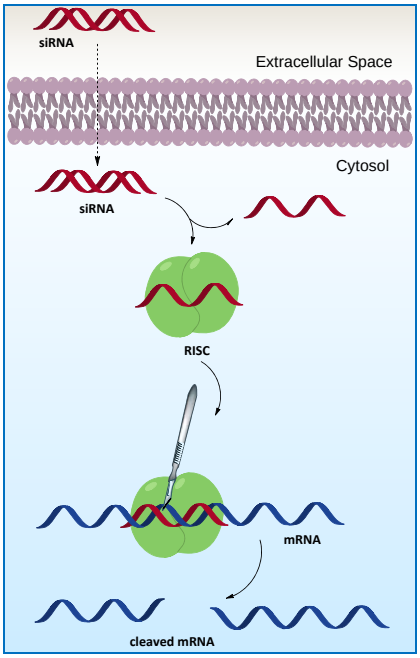

Figure I.6: siRNA mechanism of action

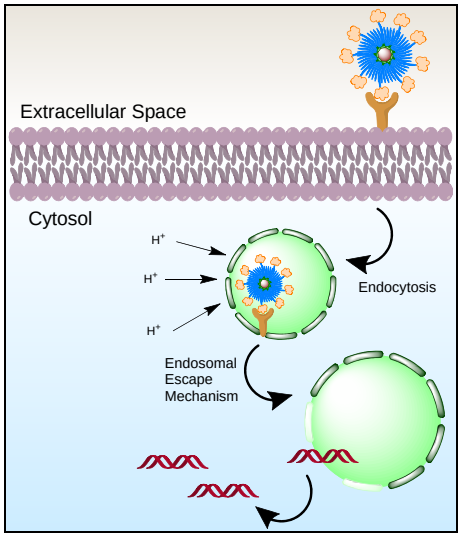

Figure I.7: siRNA nanoparticle endocytosis into an endosome necessitates an endosomal escape mechanism for siRNA to reach the cytosol where it can bind to RISC and perform its functions.

Despite the challenges that siRNA delivery faces, a number of nanoparticles containing siRNA for cancer therapy (Table I.2), as well as several other applications (Table I.3), have reached the clinic and shown to be effective, though there has yet one to be approved to date.[47-51] Furthermore, these siRNA-containing nanoparticles show fairly good safety profile.[41,48,52]

Company	Investigational therapeutic	siRNA target	Delivery vehicle	Infusion time	Dosing schedule	ClinicalTrials.gov identifier (start date; current status)
Calando Pharmaceuticals	CALAA-01	*RRM2*	Polymer (targeted)	30 min	Two 21-day cycles, two doses per week for the first two weeks	• NCT00689065 (Spring 2008; Phase I terminated)
Alnylam Pharmaceuticals	ALN-VSP (also known as ALN-VSP02)	*VEGFA* and *KSP*	Lipid (non-targeted)	15 min	Dosing every 14 days	• NCT00882180 (Spring 2009; Phase I completed) • NCT01158079 (Summer 2010; Phase I completed)
Silence Therapeutics	Atu027	*PKN3*	Lipid (non-targeted)	4 h	Daily dosing for three weeks, then twice-weekly dosing for four weeks	• NCT00938574 (Summer 2009; Phase I completed) • NCT01808638 (Spring 2013; Phase I/II active, not recruiting)
Tekmira Pharmaceuticals	TKM-PLK1 (also known as TKM-080301)	*PLK1*	Lipid (non-targeted)	30 min	Once-weekly dosing for three weeks	• NCT01262235 (Winter 2010; Phase I/II completed) • NCT01437007 (Summer 2011; Phase I completed) • NCT02191878 (Summer 2014; Phase I/II recruiting)
ProNAi Therapeutics	PNT2258 (single-stranded DNA)*	*BCL2*	Lipid (non-targeted)	2 h	21-day cycles, daily dosing for days 1–5 of each cycle	• NCT01191775 (Summer 2010; Phase I completed) • NCT01733238 (Winter 2012; Phase II active, not recruiting) • NCT02226965 (Winter 2014; Phase II recruiting)
Silenseed	siG12D LODER	*KRAS*	Biodegradable polymer matrix (local administration)	NA	NA	• NCT01188785 (Winter 2011; Phase I completed) • NCT01676259 (Winter 2015; Phase II not yet recruiting)
Senesco Technologies	SNS01-T	eIF5A^{K50R} plasmid eIF5A siRNA	Polyethylenimine (non-targeted)	Not reported	Twice-weekly dosing for six weeks	• NCT01435720 (Autumn 2011; Phase II active, not recruiting)
Mirna Therapeutics	MRX34 (microRNA mimic)*	miR-34	Lipid (non-targeted)	Not reported	21 day cycle, daily dosing for five days followed by a two-week break	• NCT01829971 (Spring 2013; Phase I recruiting)
Dicerna Pharmaceuticals	DCR-MYC	*MYC*	Lipid (non-targeted)	1 h	Once-weekly dosing for two weeks followed by a one-week break	• NCT02110563 (Spring 2014; Phase I recruiting) • NCT02314052 (Winter 2014; Phase Ib/II recruiting)
M.D. Anderson Cancer Center	siRNA-EPHA2-DOPC	*EPHA2*	Lipid (non-targeted)	Not reported	Twice-weekly dosing for three weeks	• NCT01591356 (Summer 2015; Phase I recruiting)

DOPC, 1,2-dioleoyl-sn-glycero-3-phosphatidylcholine; eIF5A, eukaryotic translation initiation factor 5A; *EPHA2*, ephrin type-A receptor 2; *KSP*, kinesin spindle protein; NA, not applicable; *PKN3*, protein kinase N3; *PLK1*, polo-like kinas 1; *RRM2*, ribonucleotide reductase subunit M2; siRNA, small interfering RNA; *VEGFA*, vascular endothelial growth factor A. *PNT2258 and MRX34 do not contain siRNA.

Table I.2: Nanoparticles containing siRNA for cancer treatment in clinical trials. From Zuckerman and Davis, *Nature Review Drug Discovery* **2015,** *14,* 843-856.

Virus infections					
RSV	RSV nucleocapsid	Naked siRNA	ALN-RSV01	Alnylam Pharmaceuticals	Completed, Phase II
HBV	Pre gen./Pre-C, Pre-S1, Pre-S2/S, X	Plasmid DNA	NUC B1000	Nucleonics	Completed, Phase I
	HBV conserved sequences	DPC	ARC-520	Arrowhead Research Corporation	Recruiting, Phase II
HIV	HIV Tat protein, HIV TAR RNA, human CCR5	Lentivirus	pHIV7-shI-TARCCR5RZ	City of Hope Medical Center/Benitec	Terminated, Phase 0
HCV	miR-122	Naked LNA	SPC3649 (LNA)	Santaris Pharm	Completed, Phase II
EBOV	EBOV polymerase L, VP24, and VP35 regions	SNALP	TKM-100201	Tekmira Pharmaceuticals Corporation	Terminated, Phase I
Other diseases					
Hypercholesterolemia	APOB	SNALP	PRO-040201	Tekmira Pharmaceuticals Corporation	Terminated, Phase I
Pachyonychia Congenita	keratin K6a	Naked siRNA	TD101	TransDerm, Inc	Completed, Phase I
Delayed graft function kidney transplant	P53	Naked siRNA	I5NP	Quark Pharmaceuticals	Active, Phase I/II
Acute renal failure	P53	Naked siRNA	I5NP	Quark Pharmaceuticals	Terminated, Phase I
Glaucoma; ocular hypertension	ADRB2	Naked siRNA	SYL040012	Sylentis, S.A.	Completed, Phase I/II
Dry eye syndrome	TRPV1	Naked siRNA	SYL1001	Sylentis, S.A.	Recruiting, Phase II
Wet AMD	VEGF	Naked siRNA	Bevasiranib	Opko Health, Inc.	Terminated, Phase III
Diabetic AMD	VEGF	Naked siRNA	Bevasiranib	Opko Health, Inc.	Completed, Phase II
Chronic optic nerve atrophy	Caspase-2	Naked siRNA	QPI-1007	Quark Pharmaceuticals	Completed, Phase I
AMD; CNV	VEGFR	Naked siRNA	Sirna-027/AGN211745	Allergan & Sirna Therapeutics Inc.	Completed, Phase II
AMD/DME	RTP801	Naked siRNA	PF-655	Quark Pharmaceuticals & Pfizer	Completed, Phase II

Resource: http://clinicaltrials.gov.

CNS, central nervous system; RSV, respiratory syncytial virus; HBV, hepatitis B virus; HIV, human immunodeficiency virus; HCV, hepatitis C virus; EBOV, Ebola virus; AMD, Age-Related Macular Degeneration; CNV, choroidal neovascularization; RRM2, Ribonucleotide reductase subunit 2; PKN3, protein kinase n3; KRAS oncogene, Kirsten rat sarcoma viral oncogene; LMP2, large multifunctional peptidase 2; LMP7, large multifunctional peptidase 7; MECL1, multicatalytic endopeptidase complex-like-1; HIV Tat protein, HIV-1-trans-activating protein; HIV TAR, HIV trans-activation response; CCR5, human CC chemokine receptor 5; VP24, virus protein 24; VP35, virus protein 35; APOB, apolipoprotein B; ADRB2, beta-2 adrenergic receptor; TRPV1, transient receptor potential vanilloid 1; VEGF(R), Vascular endothelial growth factor (receptor); cysteine-aspartic proteases-2 (Caspase-2); PEG, polyethylene glycol; SV40,9 Simian virus 40; DPC, dynamic polyconjugate; SNALP, stable nucleic acid-lipid particle.

Table I.3: siRNA for non-cancer therapy applications that have reached the clinic. From Draz, et al. *Thernostics* **2014,** *4*, 872-892.

Thesis Organization

This thesis presents a nanoparticle siRNA delivery system based upon a cationic mucic acid polymer that attempts to overcome the challenges facing siRNA therapy for cancer treatment. These challenges, as mentioned earlier, include protecting the siRNA with the delivery system, increasing the siRNA nanoparticle circulation time, getting siRNA into cells, and allowing the siRNA to escape from the endosome to the cytosol for function.

Chapter 2 details the development of a cationic mucic acid polymer siRNA delivery system to achieve a long circulation time. Chapter 3 explores using targeting agents to

allow nanoparticle internalization: some antibodies have multiple functions which include an immune-mediated antibody-dependent cellular cytotoxicity (ADCC) effect, and we wanted to see whether this function is preserved when the antibody is attached to a nanoparticle to evaluate the value of using an antibody to target the nanoparticle with an added ADCC effect over using a protein or peptide without these immune effects to target the nanoparticle. Chapter 4 discusses achieving internalization of the cationic mucic acid polymer-based nanoparticle and endosomal escape. Finally, chapter 5 concludes with an outlook on the future of nanoparticle therapeutics and targeted cancer treatment.

References

1. Stricker, T.P.; Kumar, V. Neoplasia. In *Robbins Basic Pathology,* 8th Edition; Kumar, V.; Abbas, A.K., Fausto, N., Mitchell, R., Eds.; Elsevier Health Sciences: Philadelphia, 2007; pp 173-224.
2. Forman, D.; Ferlay, J. The global and regional burden of cancer. In *World Cancer Report 2014;* Stewart, B.W., Wild, C.P., Eds.; International Agency for Research on Cancer: Lyon, 2014; pp 15-76.
3. Sutcliffe, S.B. National cancer control plans. In *World Cancer Report 2014;* Stewart, B.W., Wild, C.P., Eds.; International Agency for Research on Cancer: Lyon, 2014; pp 529-536.
4. Fenn, J.E.; Udelsman, R. First use of intravenous chemotherapy cancer treatment: rectifying the record. *J. Am. Coll. Surg.* **2011,** *212,* 413-417.
5. Spain, P.D.; Kadan-Lottick, N. Observations of unprecedented remissions following novel treatment for acute leukemia in children in 1948. *J. R. Soc. Med.* **2012,** *105,* 177-181.
6. Stegmeier, F.; Warmuth, M.; Sellers, W.R.; Dorsch, M. Targeted cancer therapies in the twenty-first century: lessons from imatinib. *Clinical Pharmacology and Therapeutics* **2010,** *87,* 543-552.
7. Wu, K.; House, L.; Liu, W.; Cho, W.C.S. Personalized targeted therapy for lung cancer. *Int. J. Mol. Sci.* **2012,** *13,* 11471-11496.
8. Helfrich, B.A.; Raben, D.; Varella-Garcia, M.; et al. Antitumor activity of the epidermal growth factor receptor (EGFR) tyrosine kinase inhibitor gefitinib (ZD1839, Iressa) in non-

small cell lung cancer cell lines correlates with gene copy number and EGFR mutations but not EGFR protein levels. *Clin. Cancer Res.* **2006,** *12,* 7117-7125.

9. Cutsem, E.V.; Kohne, C.-H.; Hitre, E., et al. Cetuximab and chemotherapy as initial treatment for metastatic colorectral cancer. *N Engl J Med* **2009,** *360,* 1408-1417.
10. Sok, J.C.; Coppelli, F.M.; Thomas, S.M., et al. Mutant epidermal growth factor receptor (EGFRvIII) contributes to head and neck cancer growth and resistance to EGFR targeting. *Clin Cancer Res* **2006,** *12,* 5064-5073.
11. Patel, D.; Lahiji, A.; Patel, S.; Franklin, M.; Jimenez, X.; Hicklin, D.J.; Kang, X. Monoclonal antibody cetuximab binds to and down-regulates constitutively activated epidermal growth factor receptor vIII on the cell surface. *Anticancer Research,* **2007**, *27,* 3355-3366.
12. Diaz, L.A.; Williams, R.T.; Wu, J.; Kinde, I.; etc al. The molecular evolution of acquired resistance to targeted EGFR blockade in colorectal cancers. *Nature* **2012,** *486,* 537-540.
13. Hudis, C.A. Trastuzumab – Mechanism of action and use in clinical practice. *N Engl J Med* **2007,** *357,* 39-51.
14. Boku, N. HER2-positive gastric cancer. *Gastric Cancer* **2014,** *17,* 1-12.
15. Ruschoff, J.; Hanna, W.; Bilous, M.; et al. HER2 testing in gastric cancer: a practical approach. *Modern Pathology* **2013,** *25,* 637-650.
16. Brand, T.M.; Iida, M.; Wheeler, D.L. Molecular mechanisms of resistance to the EGFR monoclonal antibody cetuximab. *Cancer Biology & Therapy* **2011,** *11,* 777-792.
17. Kim, S.M.; Kim, J.S.; Kim, J.-H.; Yun, C.-O.; Kim, E.M.; Kim, H.K.; Solca, F.; Choi, S.-Y.; Cho, B.C. Acquired resistance to cetuximab is mediated by increased PTEN instability and leads cross-resistance to gefitinib in HCC827 NSCLC cells.
18. Bardelli, A.; Janne, P.A. The road to resistance: EGFR mutation and cetuximab. *Nature Medicine* **2012,** *18,* 199-200.
19. Cross, D.A.E.; Ashton, S.E.; Ghiorghiu, S. AZD9291, an irreversible EGFR TKI, overcomes T790M-mediated resistance to EGFR inhibitors in lung cancer. *Cancer Discov.* **2014,** *4,* 1046-1061.
20. Gibbons, D.L.; Byers, L.A. A HER 1-2 punch: dual EGFR targeting deals resistance a deadly blow. *Cancer Discov.* **2014,** *4,* 991-994.
21. Janjigian, Y.Y.; Smit, E.F.; Groen, H.J.M. Dual inhibition of EGFR with afatinib and cetuximab in kinase inhibitor-resistant EGFR-mutant lung cancer with and without T790M mutations. *Cancer Discov.* **2014,** *4,* 1036-1045.

22. Peddi, P.F.; Hurvitz, S.A. Trastuzumab emtansine: the first targeted chemotherapy for treatment of breast cancer. *Future Oncol.* **2013,** *9,* 319-326.
23. LoRusso, P.M.; Weiss, D.; Guardino, E. Trastuzumab Emtansine: A unique antibody-drug conjugate in development for human epidermal growth factor receptor 2-positive cancer. *Clin. Cancer Res.* **2011,** *17,* 6437-6447.
24. Barok, M.; Tanner, M.; Koninki, K.; Isola, J. Trastuzumab-DM1 causes tumour growth inhibition by mitotic catastrophe in trastuzumab resistant breast cancer cells *in vivo*. *Breast Cancer Research* **2011,** *13,* R46.
25. Junttila, T.T.; Li, G.; Parsons, K.; Phillips, G.L.; Sliwkowski, M.X. Trastuzumab-DM1 (T-DM1) retains all the mechanisms of trastuzumab and efficiently inhibits growth of lapatinib insensitive breast cancer. *Breast Cancer Res. Treat.* **2011,** *128,* 347-356.
26. Gwin, W.R.; Spector, N.L. Pertuzumab protects the Achilles' heel of trastuzumab-emtansine. *Clin. Cancer Res.* **2014,** *20,* 278-280.
27. Phillips, G.D.L.; Fields, C.T.; Li, G.; et al. Dual targeting of HER2-positive cancer with trastuzumab emtansine and pertuzumab: critical role for neuregulin in antitumor response to combination therapy. *Clin. Cancer Res.* **2014,** *20,* 456-468.
28. Mukherjee, S. *The emperor of all maladies: a biography of cancer.* Scribner: New York, 2010, p xiv.
29. Kamaly, N.; Xiao, Z.; Valencia, P.M.; Radovic-Moreno, A.F.; Farokhzad, O.C. Targeted polymeric therapeutic nanoparticles: design, development and clinical translation. *Chem. Soc. Rev.* **2012,** *41,* 2971-3010.
30. Egusquiaguirre, S.P.; Igartua, M.; Hernandez, R.M.; Pedraz, J.L. Nanoparticle delivery systems for cancer therapy: advances in clinical and preclinical research. *Clin. Transl. Oncol.* **2012,** *14,* 83-93.
31. Wang, A.Z.; Langer, R.; Farokhzad, O.C. Nanoparticle delivery of cancer drugs. *Annu. Rev. Med.* **2012,** *63,* 185-198.
32. Cheng, Z.; Al Zaki, A.; Hui, J.Z.; Muzykantov, V.R.; Tsourkas, A. Multifunctional nanoparticles: Cost versus benefit of adding targeting and imaging capabilities. *Science* **2012,** *338,* 903-910.
33. Clark, A.J.; Wiley, D.T.; Zuckerman, J.E.; Webster, P.; Chao, J.; Lin, J.; Yen, Y.; Davis, M.E. CRLX101 nanoparticles localize in human tumors and not in adjacent, nonneoplastic tissue after intravenous dosing. *PNAS* **2016,** *113,* 3850-3854.

34. Peer, D.; Karp, J.M.; Hong, S.; Farokhzad, O.C.; Margalit, R.; Langer, R. Nanocarriers as an emerging platform for cancer therapy. *Nature Nanotechnology* **2007,** *2,* 751-760.
35. Fire, A.; Xu, S.; Montgomery, M.K.; Kostas, S.A.; Driver, S.E.; Mello, C.C. Potent and specific genetic interference by double-stranded RNA in Caenorhabditis elegans. *Nature* **1998,** *19,* 806-811.
36. Bartlett, D.W.; Davis, M.E. Insights into the kinetics of siRNA-mediated gene silencing from live-cell and live-animal bioluminescent imaging. *Nucleic Acids Research* **2006,** *34,* 322-333.
37. Wu, S. Y., Lopez-Berestein, G., Calin, G. A., and Sood, A. K. RNAi Therapies: Drugging the Undruggable. *Sci. Transl. Med.* **2014,** *6,* 240ps7.
38. Tabernero, J.; Shapiro, G.I.; LoRusso, P.M; et al. First-in-man trial of an RNA interference therapeutic targeting VEGF and KSP in cancer patients with liver involvement. *Cancer Discovery* **2013,** *3,* 406-417.
39. Yuan, T.L.; Fellmann, C.; Lee, C.-S.; et al. Development of siRNA payloads to target KRAS-mutant cancer. *Cancer Discovery* **2014,** *4,* 1182-1197.
40. Ballarin-Gonzalez, B.; Howard, K.A. Polycation-based nanoparticle delivery of RNAi therapeutics: adverse effects and solutions. *Advanced Drug Delivery Reviews* **2012,** *64,* 1717-1729.
41. Zuckerman, J. E., Gritli, I., Tolcher, A., Heidel, J. D., Lim, D., Morgan, R., Chmielowski, B., Ribas, A., Davis, M. E., and Yen, Y. Correlating animal and human phase Ia/Ib clinical data with CALAA-01, a targeted, polymer-based nanoparticle containing siRNA. *Proc. Natl. Acad. Sci. U. S. A.* **2014,** *111*, 11449−11454.
42. Zuckerman, J. E., Choi, C. H. J., Han, H., and Davis, M. E. Polycation-siRNA nanoparticles can disassemble at the kidney glomerular basement membrane. *Proc. Natl. Acad. Sci. U. S. A.* **2012**, *109*, 3137−3142.
43. Naeye, B., Deschout, H., Caveliers, V., Descamps, B., Braeckmans, K., Vanhove, C., Demeester, J., Lahoutte, T., De Smedt, S. C., and Raemdonck, K. *In vivo* disassembly of IV administered siRNA matrix nanoparticles at the renal filtration barrier. *Biomaterials* **2013,** *34*, 2350−2358.
44. Christie, R. J., Matsumoto, Y., Miyata, K., Nomoto, T., Fukushima, S., Osada, K., Halnaut, J., Pittella, F., Kim, H. J., Nishiyama, N., et al. Targeted polymeric micelles for siRNA treatment of experimental cancer by intravenous injection. *ACS Nano* **2012**, *6*, 5174−5189.
45. Nelson, C. E., Kintzing, J. R., Hanna, A., Shannon, J. M., Gupta, M.K., and Duvall, C. L. Balancing cationic and hydrophobic contentof PEGylated siRNA polyplexes enhances

endosome escape, stability, blood circulation time, and bioactivity *in vivo*. *ACS Nano* **2013**, *7*, 8870−8880.

46. Barrett, S. E., Burke, R. S., Abrams, M. T., Bason, C., Busuek, M., Carlini, E., Carr, B. A., Crocker, L. S., Fan, H., Garbaccio, R. M., et al. Development of a liver-targeted siRNA delivery platform with a broad therapeutic window utilizing biodegradable polypeptide-based polymer conjugates. *J. Controlled Release* **2014**, *183*, 124−137.
47. Davis, M. E., Zuckerman, J. E., Choi, C. H. J., Seligson, D., Tolcher, A., Alabi, C. A., Yen, Y., Heidel, J. D., and Ribas, A. Evidence of RNAi in humans from systemically administered siRNA via targeted nanoparticles. *Nature* **2010**, *464*, 1067−1070.
48. Zuckerman, J.E.; Davis, M.E. Clinical experiences with systemically administered siRNA-based therapeutics in cancer. *Nature Reviews Drug Discovery* **2015,** *14,* 843-856.
49. Draz, M.S.; Fang, B.A.; Zhang, P.; et al. Nanoparticle-mediated systemic delivery of siRNA for treatment of cancers and viral infections. *Theranostics* **2014,** *4,* 872-892.
50. Bouchie, A. Companies in footrace to deliver RNAi. *Nature Biotechnology* **2012,** *12,* 1154-1157.
51. Young, S.W.S.; Stenzel, M.; Yang, J.-L. Nanoparticle-siRNA: A potential cancer therapy? *Critical Reviews in Oncology/Hematology* **2016,** *98,* 159-169.
52. Barros, S.A.; Gollob, J.A. Safety profile of RNAi nanomedicines. *Advanced Drug Delivery Reviews* **2012,** *64,* 1730-1737.

Chapter 2

Cationic mucic acid polymer-based siRNA delivery systems

This chapter has been published as:
Pan, D.W. and Davis, M.E. Cationic mucic acid polymer-based siRNA delivery systems. *Bioconjugate Chem.* **2015**, *26*, 1791-1803. doi : 10.1021/acs.bioconjchem.5b00324

Abstract

Nanoparticle (NP) delivery systems for small interfering RNA (siRNA) that have good systemic circulation and high nucleic acid content are highly desired for translation into clinical use. Here, a family of cationic mucic acid-containing polymers is synthesized and shown to assemble with siRNA to form NPs. A cationic mucic acid polymer (cMAP) containing alternating mucic acid and charged monomers is synthesized. When combined with siRNA, cMAP forms NPs that require steric stabilization by polyethylene glycol (PEG) that is attached to the NP surface via a 5-nitrophenylboronic acid linkage (5-nitrophenylboronic acid-PEGm (5-nPBA-PEGm)) to diols on mucic acid in the cMAP in order to inhibit aggregation in biological fluids. As an alternative, the cMAP is covalently conjugated with PEG via two methods. First, a copolymer is prepared with alternating cMAP-PEG units that can form loops of the PEG on the surface of the formulated siRNA-containing NPs. Second, an mPEG-cMAP-PEGm triblock polymer is synthesized that could lead to a PEG brush configuration on the surface of the formulated siRNA-containing NPs. The copolymer and triblock polymer are able to form stable siRNA-containing NPs without and with the addition of 5-nPBA-PEGm. Five formulations: (i) the cMAP with 5-nPBA-PEGm, (ii) cMAP-PEG copolymer both (a) with and (b) without 5-nPBA-PEGm, and (iii) mPEG-cMAP-PEGm triblock polymer both (a) with and (b) without 5-nPBA-

PEGm, are used to produce NPs in the 30-40 nm size range, and their circulation times evaluated in mice using tail vein injections. The mPEG-cMAP-PEGm triblock polymer provides the siRNA-containing NP with the longest circulation time (5-10% of the formulation remains in circulation at 60 min post-dosing), even when a portion of the excess cationic components used in the formulation are filtered away prior to injection. A NP formulation using the mPEG-cMAP-PEGm triblock polymer that is free of excess components could contain as much as ca. 30wt% siRNA.

INTRODUCTION

Therapeutics that use RNA interference (RNAi) as their mechanism of action have great promise for the treatment of human disease. For example, siRNA has attractive features for use as a therapeutic, including: (i) the ability to target essentially any gene (thus, all targets are in principle druggable), (ii) potent, single-digit, picomolar IC_{50}'s (concentration required for 50% inhibition) for mRNA inhibition in well-designed siRNAs, (iii) chemical modifications and sequence designs that can minimize off-target effects and immune stimulation without compromising potency and target specificity, and (iv) a catalytic RNAi mechanism of action, resulting in extended siRNA inhibition of mRNA target expression. Although a major obstacle to the translation of siRNA into an effective and efficient therapeutic is the delivery of the nucleic acid to the target, siRNA-based experimental therapeutics have reached the clinic.[1]

Therapeutics investigated for cancer treatment are primarily administered systemically and use some type of synthetic compounds (positively charged lipids or polymers) in their formulations to deliver siRNA.[2] A number of these formulations are now called nanoparticles (NPs). CALAA-01 was the first siRNA-based therapeutic to reach the

clinic for the treatment of cancer.[3-5] This targeted NP contains a cyclodextrin-based polycation (CDP) that assembles with siRNA via electrostatic interactions between positive charges on the polymer and negative charges on the siRNA backbone. CALAA-01 was able to deliver siRNA to solid tumors in patients and release functional siRNA that inhibited the target using an RNAi mechanism (the first example in a human).[4,5] While CALAA-01 revealed several positive attributes, one of its shortcomings is that it has a very limited circulation time. The fast clearance of CALAA-01 that is observed in animals (mice, rats, dogs, and non-human primates) is also observed in humans.[5] We have investigated the origin of this short circulation time, and have shown that CALAA-01 disassembles at the glomerular basement membrane (GBM) in the kidney.[6] We speculated that this clearance mechanism may affect any NP formulation that is primarily assembled through electrostatic interactions between cationic delivery components and anionic nucleic acids.[6] Other siRNA delivery systems that use either cationic polymers or lipids have shown similar short circulation times and renal clearance.[7-10]

A number of the current polymeric and liposomal systems used to deliver siRNA *in vivo* contain excess cationic components in their formulations (positive to negative charge ratios are commonly greater than 1), in addition to a large amount of material, e.g., polyethylene glycol (PEG), used to sterically stabilize the formed NPs. Excess cationic components can have unwanted side effects *in vivo*, causing adverse reactions such as platelet aggregation, complement activation, and inflammatory reactions.[9,11-14]

The development of a polymer system for siRNA delivery that both increases the circulation time of siRNA-containing NPs and decreases the amount of non-siRNA components within the formulation would be advantageous. Here, we present efforts to

address this need. We have created a family of cationic mucic acid-based polymers (cMAP) for siRNA delivery *in vivo*. This polymer delivery system has some features analogous to the CDP system, since the latter system did function in humans.[4,5] The cationic polymer developed here uses a simpler sugar, mucic acid, than the cyclodextrin, and enables an alternative strategy for surface functionalization. Instead of NP surface functionalization via inclusion complex formation (CDP) with adamantane (AD), the cMAP contains vicinal diols that are binding sites for boronic acids which can be used to PEGylate and target the cMAP-based NPs. (NPs formed with mucic acid containing polymers for the delivery of small molecule drugs have incorporated targeting agents via this method of assembly.[15,16]) The basic cMAP was also further reacted with functionalized PEG into linear block copolymers. Reaction at the end-groups of cMAP with either a di-activated, carboxylic acid-PEG or an activated, carboxylic acid-PEG-methoxy (PEGm) leads to two possible copolymers: a cMAP-PEG copolymer or an mPEG-cMAP-PEGm triblock polymer. The cMAP-PEG copolymer can assemble with siRNA to form PEG loops on the surface to stabilize the NP, while the mPEG-cMAP-PEGm triblock can form a PEG brush configuration on the NP surface. The latter triblock approach has been explored previously with CDP and plasmid DNA (pDNA), and that triblock polymer did not have the ability to encapsulate the pDNA.[17] It has been shown that polymers that encapsulate pDNA may not be good at condensing siRNA and vice versa.[18,19] Here, we demonstrate that the mPEG-cMAP-PEGm triblock polymer is able to form siRNA-containing NPs (which can have ca. 30 wt% of the formulation being siRNA) with increased circulation times in mice. Additionally, the NPs can be easily assembled directly in phosphate buffered saline (PBS) without any additional 5-nPBA-PEGm to stabilize the NPs.

RESULTS AND DISCUSSIONS

cMAP Synthesis, NMR Characterization, and End-Group Determination. A cationic mucic acid polymer (cMAP) was synthesized by using the series of reactions schematically illustrated in Scheme II.1. The mucic acid and the intermediate reaction products leading to the preparation of mucic acid ethylenediamine were fully characterized (Supporting Information: Figures II.S1-II.S7, Structure II.S1, and Table II.S1). The condensation reaction between mucic acid ethylenediamine and DMS yielded the cMAP material. Because DMS can hydrolyze at conditions like those used for the polymerization, we investigated the reaction pathway for this reaction and the products formed (Supporting Information: Table II.S2, Structures II.S2-II.S4, Figures II.S8-II.S13). This information assisted in the characterization of the cMAP product.

NMR analysis of cMAP (Supporting Information: Structure II.S5, Figures II.S14-II.S20, and Tables II.S3-II.S7) enabled the assignment of all resonances to the various carbon and hydrogen environments in the polymer. Of importance was the identification of the end group composition of cMAP, as these functionalities are utilized in subsequent reactions with functionalized PEG to form cMAP-PEG copolymers or mPEG-cMAP-PEGm triblock polymers.

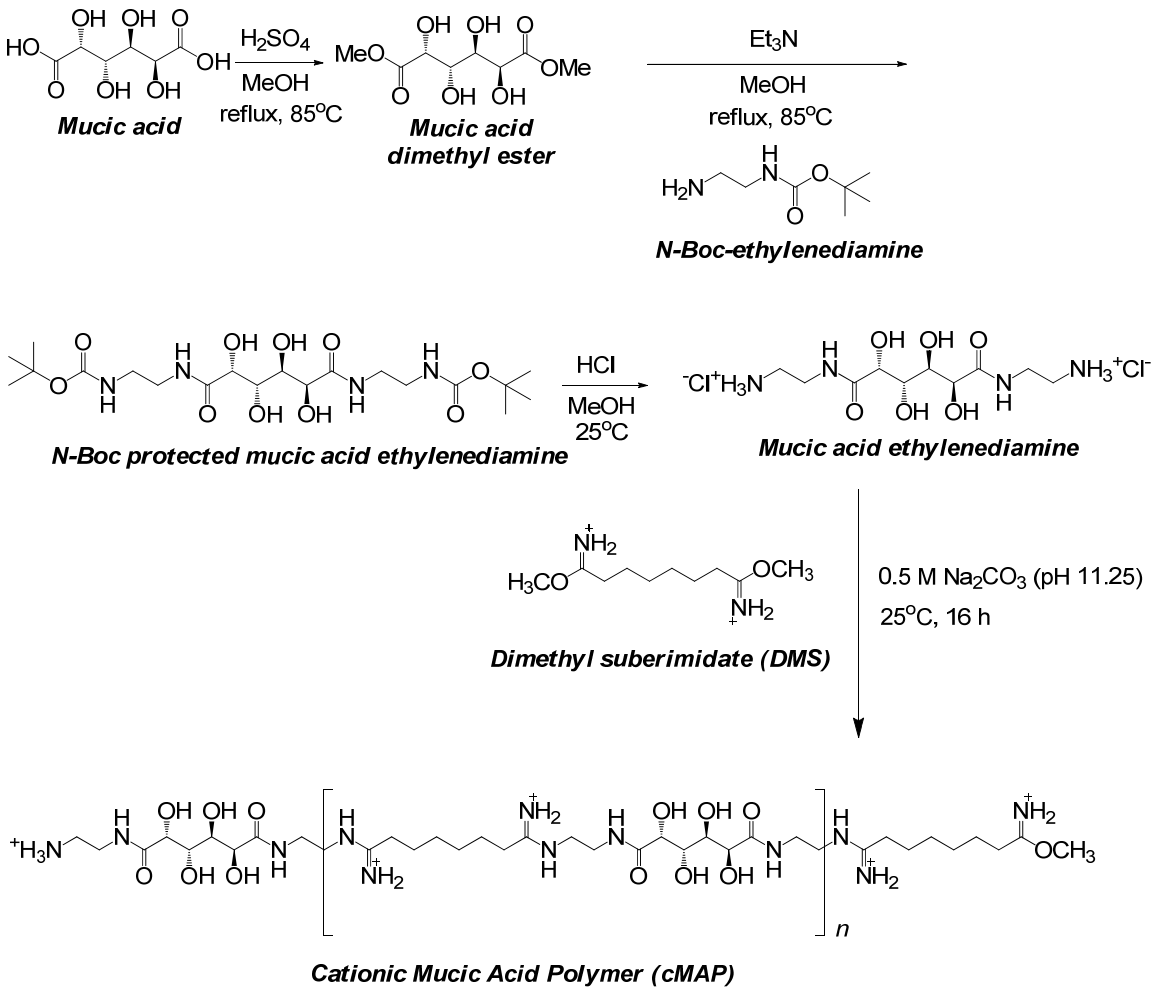

Scheme II.1. Synthesis of cationic Mucic Acid Polymer (cMAP).

The cMAP end groups include methoxy of a methoxy ester, amine, and small amounts of carboxylic acid (Figure II.1). ^{1}H NMR analysis of cMAP shows the presence of a characteristic sharp methoxy peak at 3.55 ppm (Figure II.2), and this assignment is supported by ^{1}H-^{13}C HSQC NMR measurements (Supporting Information: Figure II.S16). The methoxy group originates from the loss of ammonia from the imidate group of the DMS through hydrolysis (Supporting Information: Table II.S2, Structures II.S2-II.S4, Figures II.S8-II.S13), and had been previously reported.[20] The methylene group adjacent to the methoxy can be observed as a triplet at 2.25 ppm in the ^{1}H NMR spectrum (Figure II.2). The amine end group that originates from the mucic acid ethylenediamine

cannot be directly observed with ^{1}H NMR. However, analysis of the NMR spectrum of the monomer (Supporting Information: Figure II.S4-5) and the HMBC NMR spectrum of cMAP (Supporting Information: Figure II.S18) enabled assignment of the triplet at 2.85 ppm to be from a methylene group adjacent to the amine functional group. Additionally, a TNBSA assay for primary amines was positive, thus confirming that the cMAP has a terminal primary amine as an end group. Lastly, there was a small amount of carboxylic acid as an end group that arises from complete hydrolysis of the methyl ester or as an impurity in the starting DMS. The methylene group adjacent to the carboxylic acid is observed as a small triplet at 2.00 ppm in the ^{1}H NMR spectrum (Figure II.2). The ratios of these end groups in a batch of cMAP can be determined by comparing the integrations of the triplets at 2.85 (amine), 2.25 (methoxy), and 2.00 (carboxylate) ppm, and are shown for 8 batches in Supplementary Information, Table II.S8. The average values for the % amine, % methoxy, and % carboxylate are 49%, 42%, and 9%, respectively.

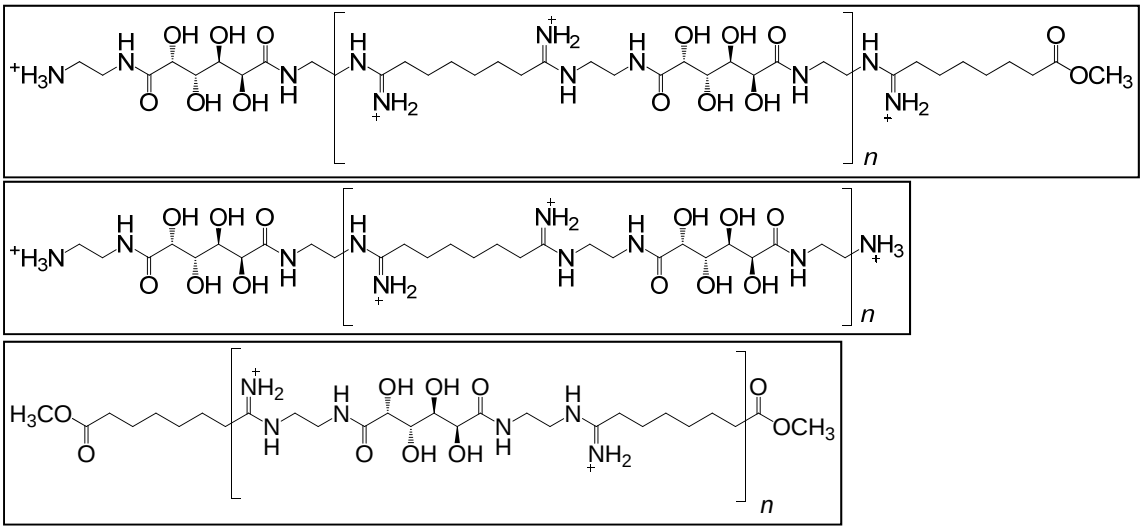

Figure II.1. End groups of cMAP. Polymers can have one amine and one methoxy (top), both amine (middle), or both methoxy (bottom) end groups. A small amount of carboxylic acid is also observed and would be generated from hydrolysis of one end of DMS.

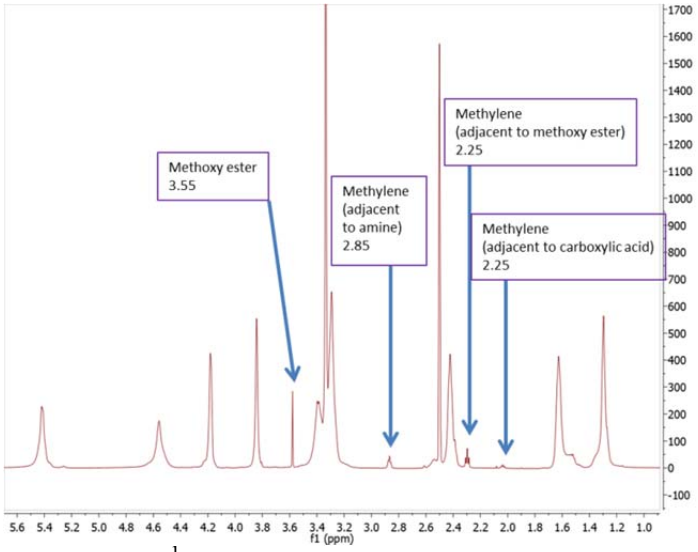

Figure II.2. ^{1}H NMR (600 MHz) of cMAP showing resonances from the methoxy group and methylene groups adjacent to the end group functionalities.

cMAP-PEG Copolymer and mPEG-cMAP-PEGm Triblock. cMAP was reacted with activated carboxylic acid end groups on PEG, such as succinimidyl propionic acid ester (SPA) or succinimidyl valeric acid ester (SVA). cMAP reacted with di-SPA-PEG or mPEG-SVA generated copolymers or triblock polymers, respectively, with PEG lengths of 2, 3.4, or 5 kD (NMR data from these polymers are provided in the Supporting Information: Figures II.S21-II.S27).

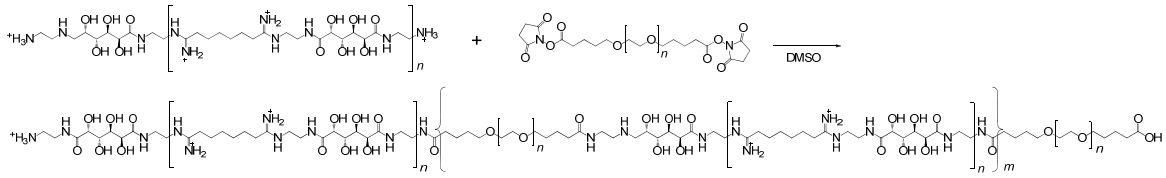

Scheme II.2: Synthesis of cMAP-PEG copolymer.

Because a significant amount of diamine terminated polymer chains exist in the cMAP mixture, reaction with di-SPA-PEG (Scheme II.2) resulted in cMAP-PEG copolymers with large size distributions (copolymers ranged from a diblock cMAP-PEG copolymer just slightly larger than 10 kD, to a cMAP-PEG-cMAP triblock polymer terminated by a methyl ester or carboxylic acid on the cMAPs, to a long polymer of over

100 kD; size distributions reported in Supporting Information: Table II.S9-10 are from the polymer yields obtained by fractionating the crude polymer through sequentially smaller molecular weight cutoff centrifugal spin filters). Because a polymer with such a large molecular weight could pose substantial toxicity *in vivo*, in an effort to synthesize a well-defined polymer with a reasonable length, the cMAP-PEG-cMAP triblock polymer species was isolated from the copolymer using this fractionation method. Other triblock polymers of this repeat structure of a cationic polymer flanking a PEG or PLA polymer has been explored previously for gene and iron oxide-carbon nanotube delivery.[21-23]

Reacting cMAP with mPEG-SVA limited the structure of the resulting product to the mPEG-cMAP-PEGm triblock polymer (Scheme II.3) (NMR characterizations provided in Supporting Information: Figures II.S28-II.S33). Some cMAP-PEGm diblock polymer was also present and separated from the desired triblock by fractionation.

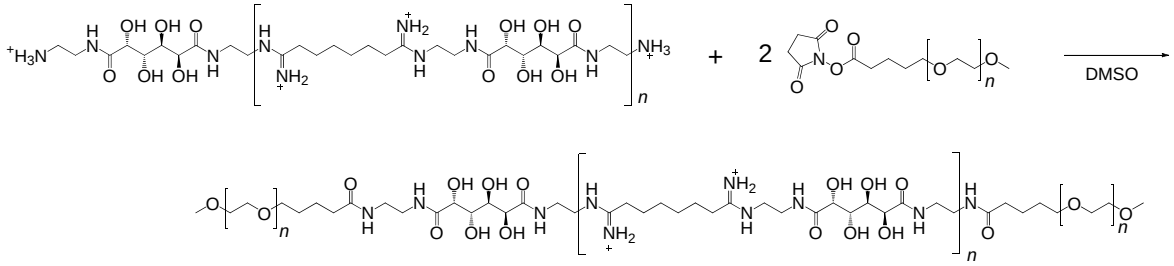

Scheme II.3: Synthesis of mPEG-cMAP-PEGm triblock polymer.

Molecular Weights of Polymers by GPC. Gel permeation chromatography was used to characterize the molecular weight of cMAP. Though the elution time of the polymer can be correlated to its size, with new cationic polymers there are no ideal size standards for calibration. Therefore, we determined the absolute molecular weight of the polymers using a multi-angle light scattering detector. The advantage of this method is its dependence only on the polymer's scattering ability and its concentration; it does not require a standard for comparison. The differential refractive index with respect to concentration, *dn/dc*, of cMAP

was determined (Table II.1) and used to measure molecular weight. The average molecular weight of 9 batches of cMAP was around 6 kD with a polydispersity index (PDI) of less than 1.1 (Table II.1). The results from the individual batches can be found in Supporting Information: Table II.S11. Using a similar method, the 5k cMAP-PEG copolymer had a larger size distribution with a PDI of 1.4, and an Mw of 42 kD and Mn of 29 kD (Table II.1). The 5k mPEG-cMAP-PEGm triblock was about 21 kD with a PDI of less than 1.1 (Table II.1). Additionally, results for the 3.4 kD PEG cMAP-PEG copolymer and the 2 kD PEG mPEG-cMAP-PEGm triblock, as well as the cMAP-PEG-cMAP triblocks derived from fractionating the cMAP-PEG copolymer are all reported in Supporting Information: Table II.S12.

Polymer	dn/dc (mL/g)	Mn (kD)	Mw (kD)	PDI (Mw/Mn)
cMAP (9 batches ± std. error)	0.1806 ± 0.0002	6.30 ± 0.40	6.76 ± 0.40	1.08 ± 0.01
cMAP-PEG5k copolymer (2 batches ± std. error)	0.1660 ± 0.0003	28.72 ± 4.55	41.49 ± 14.65	1.40 ± 0.29
mPEG5k-cMAP-PEG5km (3 batches ± std. error)	0.1420 ± 0.0004	20.98 ± 0.67	21.95 ± 0.67	1.05 ± 0.02

Table II.1. Molecular weights of cMAP-based polymers.

siRNA Encapsulation by cMAP-based Polymers. The ability of cMAP, cMAP-PEG copolymer, and mPEG-cMAP-PEGm triblock polymer to encapsulate siRNA was confirmed using both a RiboGreen assay and a gel retardation assay. cMAP is able to encapsulate siRNA at a charge ratio (+/-) of 1+/-, and the cMAP-PEG5k copolymer and the mPEG5k-cMAP-PEG5km triblock both are able to fully encapsulate siRNA by a charge ratio of 3 or 2, respectively, using the fluorescent RiboGreen assay (Figure II.3). Similar siRNA encapsulation data is reported for copolymers and triblock polymers of the other

PEG lengths in Supporting Information: Figures II.S42-II.S43. The results of the RiboGreen assay are perhaps more sensitive, but comparable to those from a gel retardation assay (shown for cMAP and cMAP-PEG copolymer in Supporting Information: Figures II.S39-II.S41).

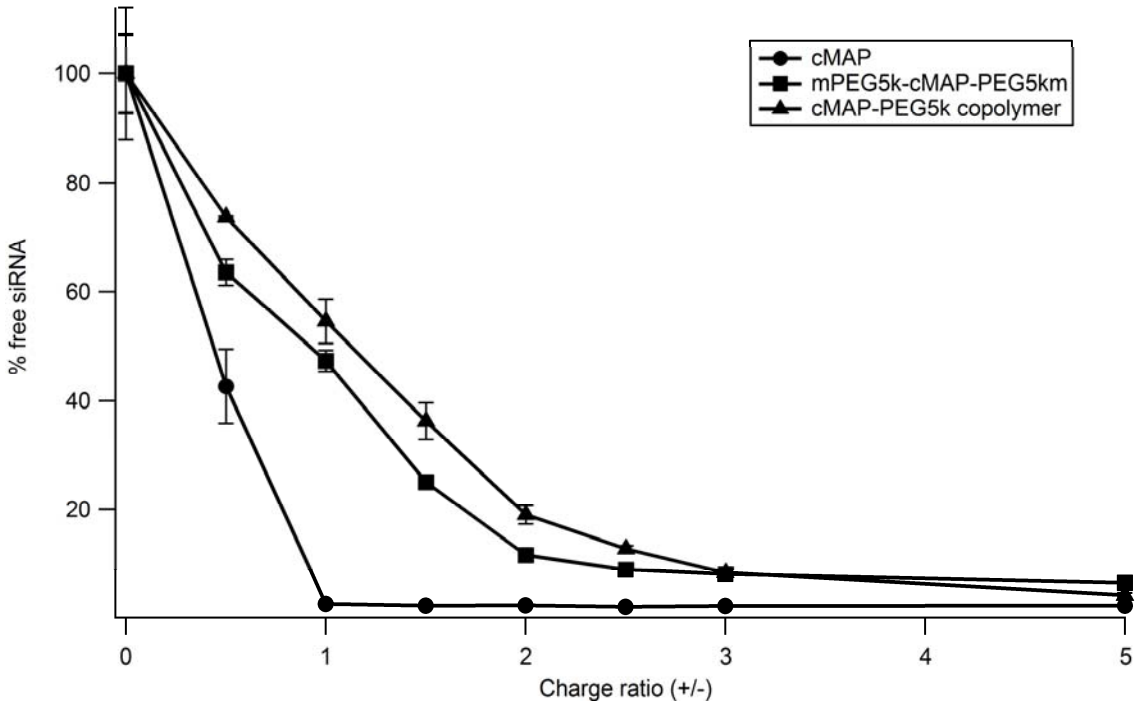

Figure II.3. Percentage of siRNA encapsulated by cMAP, cMAP-PEG5k copolymer, and mPEG5k-cMAP-PEG5km triblock polymer using the RiboGreen assay.

Nanoparticle Formulations and Properties.

*Formulations***.** 5-nitrophenyl boronic acid-PEGm (5-nPBA-PEGm), synthesized as shown in Scheme II.4, contains a boronic acid group that allows one end of this 5kD PEG to bind to vicinal diol groups on mucic acid[15,16] in cMAP at a pH above 6.8 to provide steric stabilization of the siRNA-containing NPs, as illustrated in Scheme II.5. The various NP formulations using cMAP, cMAP-PEG copolymer, and mPEG-cMAP-PEGm triblock polymer with or without extra 5-nPBA-PEGm are shown in Scheme II.6. A NP prepared by mixing cMAP and siRNA at a 3+/- charge ratio without the addition of 5-nPBA-PEGm,

while stable in water, is unstable in PBS (one 5-nPBA-PEGm per diol added to the formulation, Supporting Information: Figure II.S44).

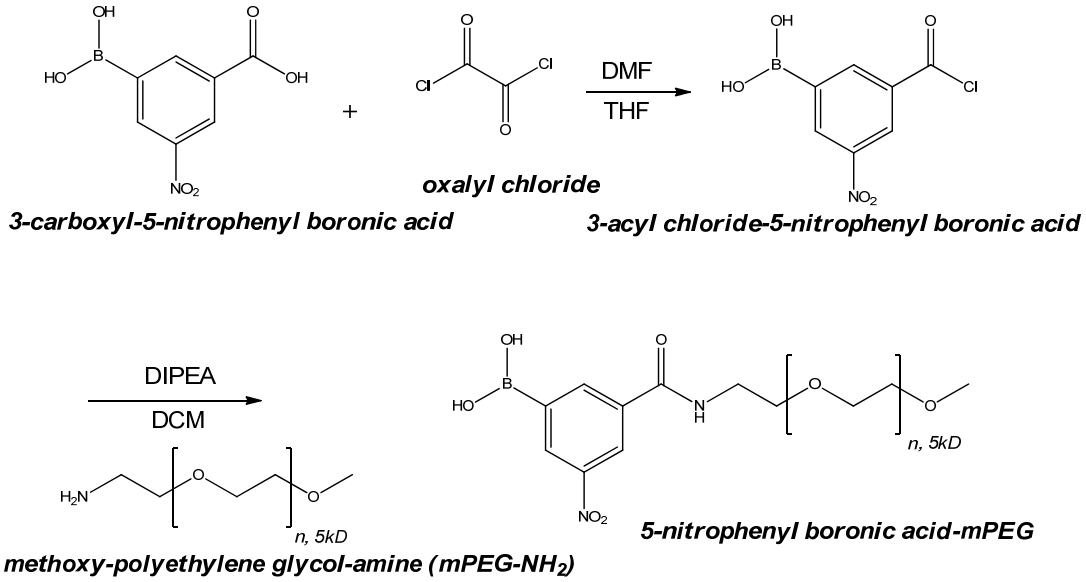

Scheme II.4. Synthesis of 5-nitrophenylboronic acid-PEGm.

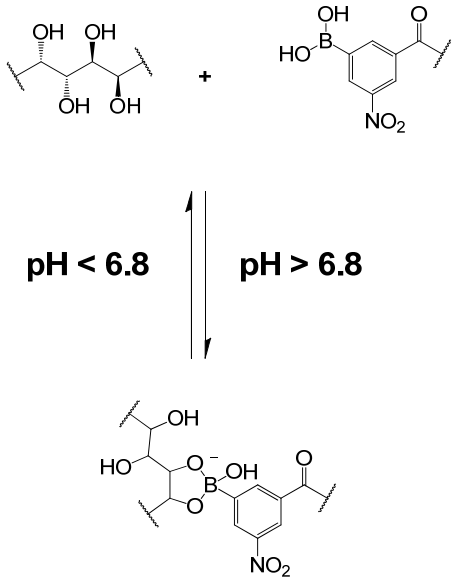

Scheme II.5. pH dependence of 5-nitrophenylboronic acid-PEGm which forms the boronic acid ester with vicinal diols on cMAP at a physiological pH of around 7.4, but which will dissociate at acidic pH.

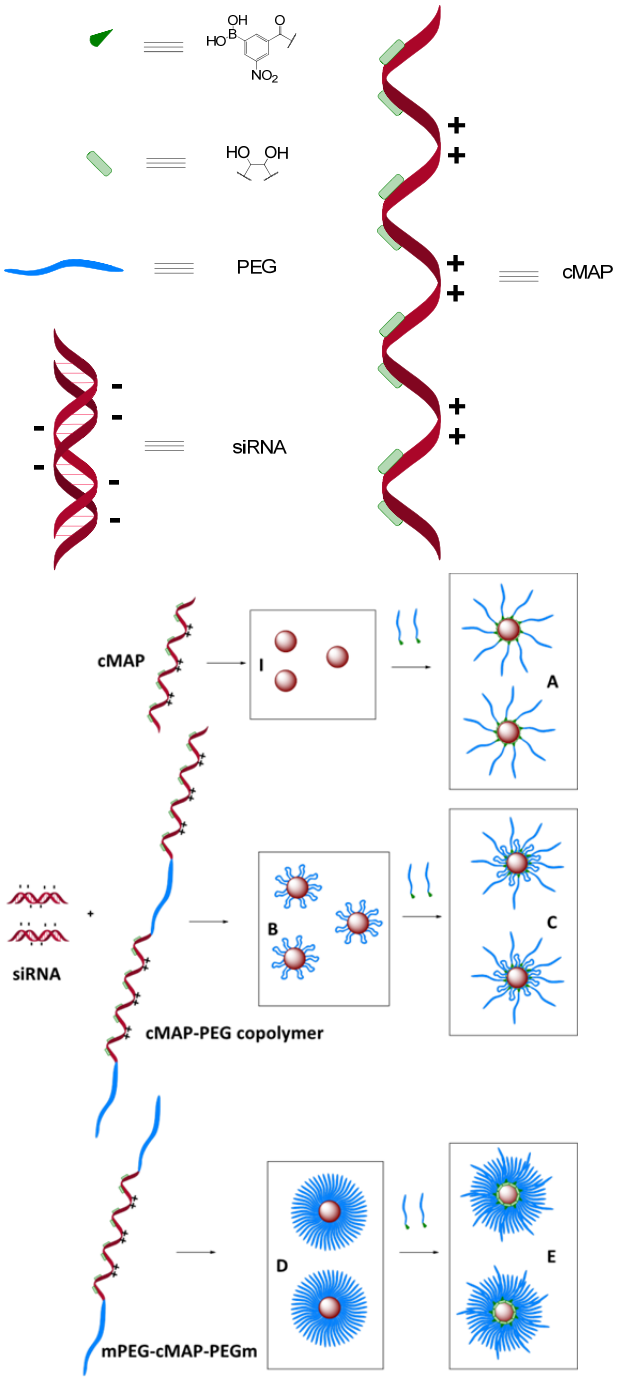

Scheme II.6. Diagram showing the various NPs with siRNA that were formed: cMAP (I, not stable and not injected), cMAP + 5-nPBA-PEGm (A), cMAP-PEG copolymer (B), cMAP-PEG copolymer + 5-nPBA-PEGm (C), mPEG-cMAP-PEGm triblock (D), and mPEG-cMAP-PEGm triblock + 5-nPBA-PEGm (E). (Note: Illustration is not drawn to scale or stoichiometry and doesn't reflect how particles are formulated – e.g. in PEGylated formulations the PEG is added to the polymer first, before the siRNA is added).

In contrast to cMAP alone, cMAP-PEG copolymer and mPEG-cMAP-PEGm triblock polymer are able to form stable particles without additional 5-nPBA-PEGm. However, the pure cMAP-PEG-cMAP triblock polymer isolated from the cMAP-PEG copolymer was not able to form stable siRNA-containing NPs without added 5-nPBA-PEGm, perhaps because it does not contain enough PEG to fully shield and sterically stabilize the NP (Supporting Information: Table II.S13 and Figures II.S45-II.S47).

Although the cMAP-PEG copolymer and mPEG-cMAP-PEGm triblock polymer form stable NPs in PBS, formulations with additional 5-nPBA-PEGm were also prepared to test whether the extra PEG offered greater steric stability to the NPs when tested *in vivo*. The amount of PEG bound to the NPs is approximately 20% (Table II.2). The polymeric components of the NP were mixed together with an equal volume of siRNA to form NPs at concentrations of 0.8 – 1 mg siRNA/mL. Furthermore, the cMAP-PEG copolymer and mPEG-cMAP-PEGm triblock polymers were able to formulate stable NPs directly in PBS, eliminating the need to first formulate stable particles in a low salt buffer followed by addition of PBS (required by the cMAP).

Formulation	% 5-nPBA-PEGm bound to NP	% cationic polymer bound to NP
cMAP	N/A	33.0 ± 0.2
cMAP + 5-nPBA-PEG5km	34.2 ± 8.7	N/A
cMAP-PEG5k copolymer	N/A	46.1 ± 1.3
cMAP-PEG5k copolymer + 5-nPBA-PEG5km	21.5 ± 1.7	N/A
mPEG5k-cMAP-PEG5km	N/A	34.4 ± 0.8
mPEG5k-cMAP-PEG5km + 5-nPBA-PEG5km	18.4 ± 4.5	N/A

Table II.2. Nanoparticle composition for NPs formulated at a charge ratio of 3+/-. Mean +/- S.E.M. of 3 runs (for PEG) or 2 runs (for polymer).

Formulation	Hydrodynamic Diameter by DLS (nm)	Diameter by CryoTEM (nm)	Zeta potential (mV) in 10 mM phosphate buffer, pH 7.4	Zeta potential (mV) in 1 mM KCl, pH 5.5
cMAP + 5-nPBA-PEG5km	40.9 ± 8.9	29.3 ± 12.8	-3.14 ± 0.56	0.76 ± 0.37
cMAP-PEG5k copolymer	25.1 ± 5.6	27.0 ± 7.9	0.69 ± 0.71	1.77 ± 0.76
cMAP-PEG5k copolymer + 5-nPBA-PEG5km	38.1 ± 15.3	34.4 ± 19.7	-2.25 ± 0.64	0.70 ± 0.74
mPEG5k-cMAP-PEG5km	36.8 ± 20.2	33.6 ± 16.7	0.42 ± 0.73	0.40 ± 0.64
mPEG5k-cMAP-PEG5km + 5-nPBA-PEG5km	29.8 ± 9.2	27.8 ± 12.9	-0.36 ± 0.64	1.44 ± 0.83

Table II.3. Size and surface charge of formulated NPs.

Nanoparticle Size. The sizes of the formulated NPs were characterized by dynamic light scattering (DLS) and cryo-transmission electron microscopy (CryoTEM). The diameters of these NPs are all ca. 30-40 nm as determined by both DLS and CryoTEM (Table II.3). The NPs have a spherical morphology (CryoTEM imaging, shown in Figure II.4). Additional images and the distributions of sizes by both DLS and CryoTEM are reported in Supporting Information: Figures II.S48-II.S62.

Nanoparticle Zeta potential. The zeta potential of the NPs (a measure of the NP surface charge), was measured in two solutions of different pH: 10 mM phosphate buffered at pH 7.4, when 5-nPBA-PEGm would be bound to the vicinal diols on cMAP; and 1 mM KCl at pH 5.5, when 5-nPBA-PEGm would dissociate from the diols of the mucic acid. cMAP-siRNA NPs with 5-nPBA-PEGm have a slightly negative zeta potential at -3 mV in pH 7.4 phosphate buffer when 5-nPBA-PEGm is present on the NP. However, when these NPs are placed in 1 mM KCl at pH 5.5, the zeta potential is about +1 mV. These results are consistent with the boronic acid binding to diols on the mucic acid to form a tetrahedral boronate complex at pH 7.4 that shields the positive charge on cMAP, and with the boronic acid dissociating from the NP at acidic pH 5.5. Similar effects are observed with the cMAP-PEG copolymer and mPEG-cMAP-PEGm triblock polymer with and without 5-nPBA-PEGm (Table II.3).

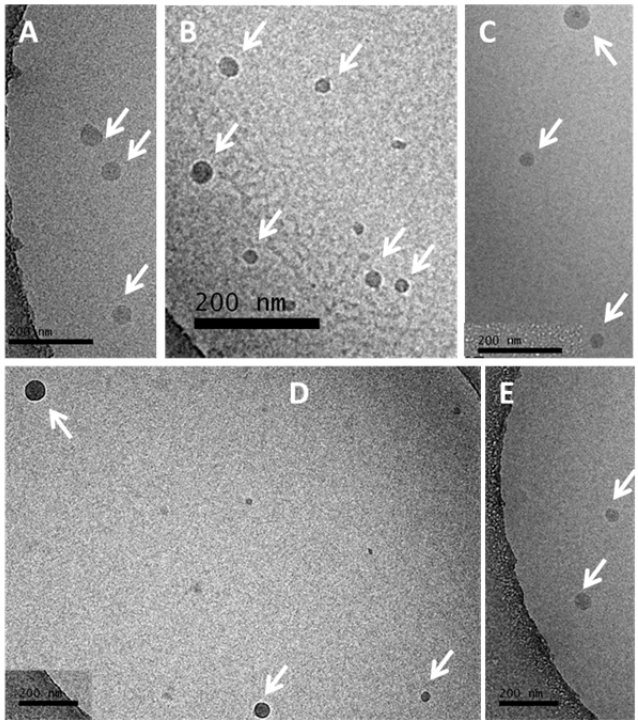

Figure II.4. CryoTEM images of NP formulations: cMAP + 5-nPBA-PEG5km (A), cMAP-PEG5k copolymer (B), cMAP-PEG5k copolymer + 5-nPBA-PEG5km (C), mPEG5k-cMAP-PEG5km (D), and mPEG5k-cMAP-PEG5km + 5-nPBA-PEG5km (E).

*Nanoparticle Stoichiometry***.** The amount of cMAP and copolymers bound to the NPs is shown in Table II.2. For all three polymers (cMAP, cMAP-PEG copolymer, and mPEG-cMAP-PEGm triblock polymer), approximately 33% of the total polymer used for formulation is bound for an effective NP charge ratio of 1+/-. The amount of 5-nPBA-PEGm present on the NP formulations containing excess PEG for stabilization is also shown in Table II.2. The amount of 5-nPBA-PEGm bound to the cMAP + 5-nPBA-PEGm NP is about 34%, or one PEG per diol (Table II.2). About 20% of the PEG was found to be bound to the NP for the cMAP-PEG copolymer and the mPEG-cMAP-PEGm triblock polymer NP formulations. Considering the excess cationic polymer present when the particles were formulated at a 3 +/- charge ratio and because the effective NP charge ratio is 1+/-, this means that a little less than 1 PEG per diol is present on the NP. Virtually all of the siRNA is encapsulated in the NPs, as was shown above in the data on siRNA encapsulation (Figure II.3).

***In vivo* Pharmacokinetic Studies in Mice.**

Stable formulations of NPs were tested *in vivo* via tail vein injection into Balb/c mice. At the doses injected, no toxicities (no visible signs of distress and no deaths) were observed from any formulation. The pharmacokinetics (PKs) of the various NPs were measured, and the results are illustrated in Figure II.5.

A NP composed of the cMAP polymer and siRNA mixed at a 3+/- charge ratio and stabilized with 5-nPBA-PEGm was tested, as this NP formulation is analogous to the CDP formulation that was used for clinical studies (CALAA-01).[3-5] The cMAP-based NP has slightly longer circulation times than CALAA-01 (Figure II.5A). Because CALAA-01 uses an inclusion complex for the interaction of CDP and adamantane-PEG (AD-PEG), the AD-

PEG can detach from the NP during circulation to cause the NP to lose stability. Han[24] and Eriksen[25] have synthesized AD_2-PEG, and have shown that this compound has greater ability to stabilize CDP-based NPs than the AD-PEG in the original CALAA-01 formulation. This is due to the enhanced binding of the two adamantanes per PEG (into two CDs) that therefore results in more steric stabilization during circulation (Figure II.5A).[24,25] With the cMAP boronic acid system, the interaction between the PEG compound and the polymer is through a boronic acid ester that is formed from the boronic acid and diols on the polymer, with ca. 30% of the PEG bound to the NP. Because only 1/3 of the cMAP used to formulate the NP is bound to the particle (Table II.2), this is roughly equivalent to one PEG present per diol. We believe that the boronic acid-diol interaction is stronger than the inclusion complex between adamantine and cyclodextrin, so that the 5-nPBA-PEGm is able to stay attached to cMAP longer than AD-PEG to CDP to result in greater steric stabilization and improved circulation time.

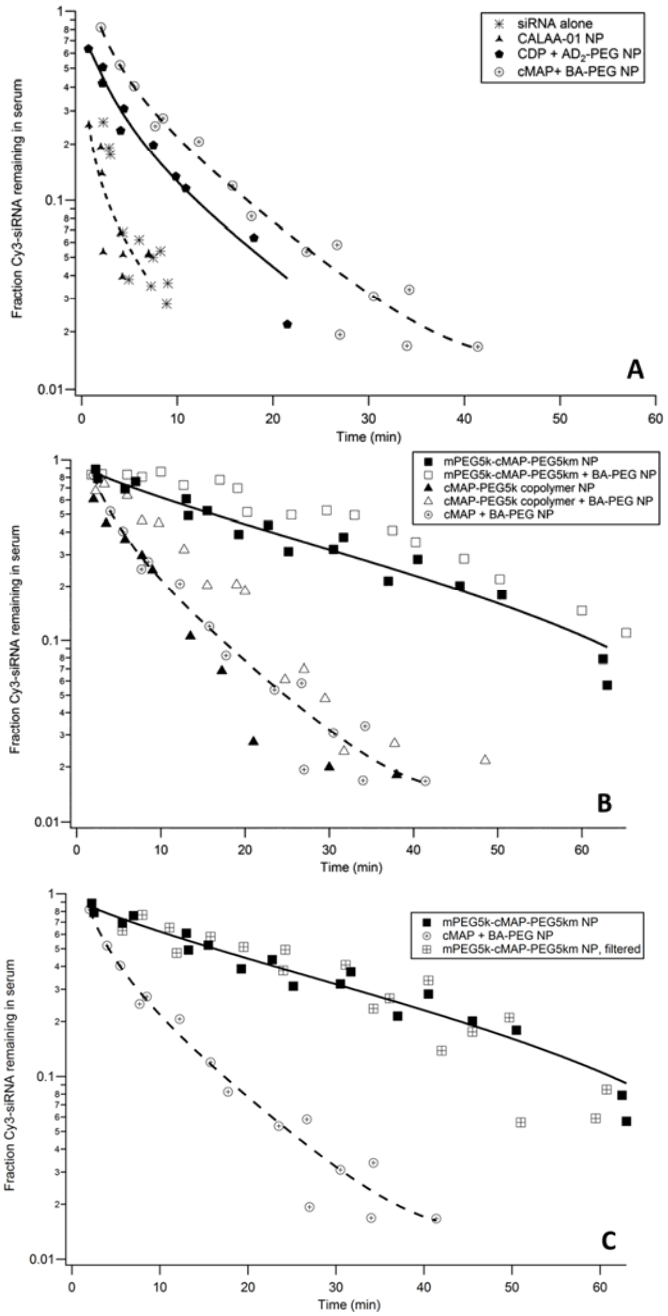

Figure II.5. PK of formulated siRNA NPs compared to siRNA alone. (A) Comparison of siRNA alone with CALAA-01, the CDP system with AD_2-PEG for stabilization, and cMAP + 5-nPBA-PEGm, the latter of which shows greater stability than CDP with AD_2-PEG and CALAA-01. (B) Comparison of cMAP + 5-nPBA-PEGm to the copolymer and triblock formulations. (C) Comparison of cMAP + 5-nPBA-PEGm to the triblock formulation with excess components filtered away. n=3 mice.

NPs formed using the cMAP-PEG copolymer can be stably formulated with siRNA in PBS at a 3+/- charge ratio into a NP without the use of 5-nPBA-PEGm (vide supra). The PEG in the cMAP-PEG copolymer is thought to form PEG loops (hypothesized by Zhong, et al.[21] with a PEI-PEG-PEI polymer condensing pDNA) to shield the NP core. Additional 5-nPBA-PEGm can be used for further stabilization of the NPs. The zeta potential switching from negative at pH 7.4 to positive at pH 5.5, in addition to the 20% PEG bound to the particles by measuring the amount of excess PEG filtered away, show that the 5-nPBA-PEGm is able to interact with the cMAP-PEG copolymer in the NP formulations. The NPs formulated with cMAP-PEG copolymer did not provide for longer circulation times over the cMAP:5-nPBA-PEGm-based NPs whether or not 5-nPBA-PEGm is added (Figure II.5B).

NPs formed using the mPEG-cMAP-PEGm triblock form stable NPs in PBS (vide supra), and should have a brush-like configuration of the PEG on the surface of the NPs. As shown by the data provided in Figure II.5B, injection of these NPs into mice resulted in an improved PK profile compared to all other cMAP-based NPs, with approximately 5-10% of the NPs remaining in mouse circulation after 60 minutes (other formulations were below the limit of detection by 60 minutes). Similar results are observed with this formulation in nude mice (Supporting Information: Figure II.S63). These longer circulation times are consistent with the NPs having a greater degree of steric stabilization that is presumably from a PEG polymer brush configuration on the surface of the NPs.[26,27] The addition of 5-nPBA-PEGm to the triblock polymer-siRNA NP did not provide for improvements in the circulation time (Figure II.5B). Furthermore, a siRNA-containing NP formulation with a charge ratio of 2+/- that was obtained by removing some of the 66%

excess triblock polymer from the 3+/- NP formulation by spin filtering the formulation with a 30 kD MWCO membrane did not result in a decrease in circulation time (Figure II.5C). Using this method of purification, it is difficult to remove all of the excess polymer. These results suggest that the polymer that is not contained within the NP does not alter the PK.

Of the polymer variations investigated here, the mPEG-cMAP-PEGm NP provides for the longest circulation time and the circulation time does not increase with additional bound 5-nPBA-PEGm. Although the 5-nPBA-PEGm interaction with the diols on cMAP are likely stronger than the interactions between adamantane and CDP, there is still likely to be some amount of PEG shedding from the NP. On the other hand, the triblock polymer, with 2 PEGs per cMAP unit, may be able to achieve a PEG density on the NP surface required for a good brush layer. However, the amount of PEG covalently linked on this triblock polymer is less than that on the cMAP + 5-nPBA-PEGm NP. The PK data from these systems suggest that the PEG shedding during circulation still occurs, but is less than what happens with the CDP-adamantane system. Previously, Han and Davis showed with an antibody targeting agent bound to a mucic acid polymer based NP containing a small molecule drug via the same 5-nPBA-PEG linkage, that some of the targeting agent stays on the NP in circulation as the presence of the targeting agent on the NP led to greater sequestration of the NPs in the spleen (function of the humanized antibody) and altered the distribution of the NPs in the tumor.[16] Thus, some of the 5-nPBA-PEGm must be staying on the NPs during the circulation.

In order to provide further evidence that the NPs are remaining intact during circulation, serum collected from mice 20 minutes post-dosing was run on a gel and the siRNA visualized by either ethidium bromide or the fluorophore-tagged siRNA on a

Typhoon imager. Results from these experiments are presented in the Supporting Information: Figures II.S64-II.S67, and they show that the siRNA and fluorescently tagged siRNA remain in intact NPs while circulating *in vivo*.

Summary

A new cationic polymer that possesses repeat units based on mucic acid and dimethyl suberimidate was synthesized and denoted cMAP. Further modification of cMAP into a triblock polymer with mPEG flanking cMAP, mPEG-cMAP-PEGm, resulted in a well-defined polymer with a molecular weight of ca. 20 kD. This triblock polymer was able to fully encapsulate siRNA at charge ratios of 2 +/- or greater. Stable NPs composed of this triblock polymer and siRNA can be formulated directly in PBS with diameters of ca. 30 nm (by both DLS and CryoTEM), and slightly positive surface charge of ca. 0.4 mV in both 10 mM phosphate buffer pH 7.4 and 1 mM KCl pH 5.5. Upon injection into mice, these NPs formed with the mPEG-cMAP-PEGm triblock polymer showed prolonged circulation compared to NPs formulated with cMAP and cMAP-PEG copolymer, with 5-10% of the formulation remaining in the circulation after 1 hour. The circulation time remained the same when a portion of the excess triblock polymer is removed from the formulation. The absence of any excess cationic polymer will be advantageous to minimize any adverse effects that these entities cause *in vivo*. Future work with this NP formulation will involve *in vivo* anti-tumor studies in immunocompromised mice.

EXPERIMENTAL PROCEDURES

General.

Mucic acid and oxalyl chloride were purchased from Sigma-Aldrich, N-boc-ethylenediamine from AK Scientific, dimethyl suberimidate from Thermo Fisher Scientific or Sigma-Aldrich, and 3-carboxyl-5-nitrophenyl boronic acid from Alfa-Aesar. Polyethylene glycol reagents were purchased from either Jenkem Technology USA or Laysan Bio, Inc.

Nuclear magnetic resonance (NMR) spectra were acquired on Varian 300 MHz, 500 MHz, or 600 MHz instruments at 25 degrees Celsius, without spinning, at 500 or 600 MHz. For most ^{1}H proton spectra, a delay time of 1-1.5 s was used; for quantitative integration of the polymer, a 25 s delay was used. ^{13}C carbon spectra were acquired at 500 MHz with default settings. ^{1}H-^{13}C heteronuclear single quantum coherence (HSQC), ^{1}H-^{1}H correlation spectroscopy (COSY), and ^{1}H-^{13}C heteronuclear multiple-bond correlation spectroscopy (HMBC) spectra using default VNMRJ3.0 HSQCAD, COSY, and HMBC settings were acquired. Additionally, diffusion ordered spectroscopy (DOSY) spectra using the bipolar pulse pair stimulated echo with convection compensation (Dbppste_cc) method in VNMRJ3.0 with diffusion gradient length of 4.0 ms and diffusion delay of 100.0 ms was acquired for synthesized polymers. Acquisition parameters are listed on each spectrum in Supporting Information.

Electrospray ionization masses of small molecules were acquired using a Finnigan LCQ ion trap mass spectrometer. Matrix-assisted laser desorption/ionization-time of flight (MALDI-TOF) mass spectra for polymers were acquired on an Applied Biosystems Voyager DE-PRO using a 10 mg/mL alpha-cyano-4-hydroxycinnamic acid matrix.

Synthesis of the Mucic Acid Containing Polymers.

1. *Synthesis of cationic Mucic Acid Polymer (cMAP) (Scheme II.1).* Methanol (360 mL) was added to **mucic acid** (15 g, 71 mmol, 1 equiv) in a 500 mL round bottom flask containing a stir bar. Concentrated sulfuric acid (1.2 mL, 22.5 mmol, 0.3 equiv) was added to this suspension, which was then stirred overnight and refluxed at 85^{o}C. The mixture was cooled to room temperature and filtered through a Buchner funnel using Whatman #5 filter paper. The solid was washed with 600 mL of methanol and then returned to the 500 mL round bottom flask. 240 mL of methanol and 1.5 mL of triethylamine were added and the solid was recrystallized at 85^{o}C reflux for 1 h. The mixture was cooled to room temperature, filtered through a Buchner funnel, and washed with 600 mL of methanol. The solid was dried under vacuum at 75^{o}C overnight to afford **mucic acid dimethyl ester** (13.72 g, 80% yield), a white solid. ^{1}H NMR (300 MHz, DMSO-*d*6): 4.91 (d, 2H), 4.80 (q, 2H), 4.29 (d, 2H), 3.76 (q, 2H), 3.62 (s, 6H).

Methanol (220 mL) was added to **mucic acid dimethyl ester** (13.72 g, 57.6 mmol, 1 equiv) in a 500 mL round bottom flask containing a stir bar. Triethylamine (20.9 mL, 150 mmol, 2.6 equiv) was added and the mixture was stirred and refluxed at 85^{o}C for 30 min, during which time a yellow suspension formed. N-boc-ethylenediamine (23.7 mL, 150 mmol, 2.6 equiv) in methanol (55 mL) was added to the suspension and stirring and refluxing at 85^{o}C was resumed overnight. The mixture was cooled to room temperature and filtered through a Buchner funnel using Whatman #5 filter paper. The solid was washed with methanol (750 mL) and recrystallized with methanol (350 mL) at 85^{o}C for 1.5 h. The mixture was again cooled to room temperature, filtered through a Buchner funnel, and washed with methanol (750 mL). The solid was dried under vacuum at 75^{o}C overnight to

afford **N-boc protected mucic acid ethylenediamine** (19.27 g, 68% yield), a white solid. ^{1}H NMR (300 MHz, DMSO-*d*6): 7.71 (t, 2H), 6.81 (t, 2H), 5.13 (d, 2H), 4.35 (q, 2H), 4.10 (d, 2H), 3.77 (q, 2H), 3.13 (m, 4H), 2.97 (m, 4H), 1.36 (s, 18H). ESI 495.1 $[M+H]^+$, 517.4 $[M+Na]^+$.

N-boc protected mucic acid ethylenediamine (19.2 g) in a 500 mL round bottom flask with a stir bar was placed in a water bath. Methanol (260 mL), followed by concentrated 12 N hydrochloric acid (65 mL), was added to the flask to make 3 N HCl in methanol. The reaction flask was sealed with a septum and vented with a needle. The water bath was set to 25^{o}C and the suspension was stirred for 6-8 h. The reaction was monitored by thin layer chromatography (TLC) with a mobile phase of 1% methanol in CH_2Cl_2 and the spots were visualized in an iodine tank. Reaction completion was also confirmed by ESI. The slurry was filtered through a glass frit with a fine grain and washed with methanol (750 mL) until the filtrate was close to a neutral pH. The solid was dried under vacuum at 80^{o}C overnight to afford **mucic acid ethylenediamine** (12.96 g, 91% yield) as a white solid. ^{1}H NMR (500 MHz, DMSO-*d*6): 7.97-7.83 (m, 8H), 5.30 (d, 2H), 4.55 (d, 2H), 4.16 (d, 2H), 3.82 (m, 2H), 2.85 (m, 4H). ^{13}C NMR (125 MHz, DMSO-*d*6): 174.79, 71.39, 70.98, 39.25, 36.76. ESI 295.1 $[M+H]^+$, 588.93 $[2M+H]^+$.

Mucic acid ethylenediamine (100 mg, 0.3 mmol, 1 equiv) was added to a 4 mL glass vial with a stir bar. 0.5 M sodium carbonate solution in nanopure water (1 mL) was added to the vial and the solution was stirred for 5 min. Dimethyl suberimidate (DMS) (74.4 mg, 0.3 mmol, 1 equiv) was then added to the mixture and the reaction was stirred for 16 h overnight at 25^{o}C. The reaction was diluted with nanopure water (10 mL) and 1N HCl was added drop wise to adjust the pH to 4. The resulting solution was dialyzed with a 15

mL Amicon Ultra 3 kD spin filter against nanopure water until the filtrate pH was neutral. The solution of polymer was concentrated to 3-4 mL, filtered through a 0.2 um PVDF syringe filter into a pre-weighed 20 mL glass vial, and lyophilized to dryness to afford **cationic mucic acid polymer** (29.2 mg, 16% yield) as a white solid, which was stored under argon at -20^{o}C. ^{1}H NMR (600 MHz, DMSO-*d*6): 9.59-8.74, 7.92, 5.40, 4.53, 4.16, 3.82, 3.55, 3.26, 2.86-2.00, 1.60, 1.28. ^{13}C NMR (125 MHz, DMSO-*d*6): 174.61, 168.12, 71.19, 70.96, 51.67, 42.09, 36.71, 32.48, 27.84, 26.65.

2. *Synthesis of cMAP-PEG copolymer (Scheme II.2).* Starting materials were equilibrated to room temperature for 1 h after removing them from the -20^{o}C freezer. **cMAP** (50 mg, 0.009 mmol, 2 equiv) and di-SPA-PEG-3.4kD (succinimidyl propionic acid ester, 15.7 mg, 0.0046 mmol, 1 equiv) were weighed into an oven-dried 10 mL flask with stir bar. The flask was capped with a septum, the two solids were dried under vacuum for 1 h, and then the flask was filled with argon. Anhydrous DMSO (2 mL) was added using a needle and syringe to dissolve the two white solids, and the solution was stirred for 24 h. Nanopure water (20 mL) was added to dilute the DMSO, and the solution was dialyzed against nanopure water using a 10kD MWCO Amicon Ultra filter >8 times. The retentate, **cMAP-PEG3.4k copolymer**, was filtered through a 0.2 um PVDF membrane and lyophilized to a white powder (29.6 mg, 45% yield). ^{1}H NMR (600 MHz, DMSO-*d*6): 9.84-8.48, 7.90, 5.41, 4.53, 4.15, 3.82, 3.55, 3.49 (PEG), 3.26, 2.86-2.00, 1.59, 1.27. ^{13}C NMR (125 MHz, DMSO-*d*6): 174.66, 168.17, 71.24, 71.00, 70.24, 67.22, 51.69, 42.11, 36.75, 32.58, 27.89, 26.66. A similar procedure was followed using 5 kD di-SVA-PEG (succinimidyl valeric acid ester) to synthesize **cMAP-PEG5k copolymer** using a 15 kD SpectraPor 7 MWCO membrane (Spectrum Labs) for dialysis.

The **cMAP-PEG-cMAP Triblock Polymer** was isolated from the **cMAP-PEG** copolymer by fractionation through centrifugal spin filters of various MWCO. cMAP-PEG3.4k copolymer was dialyzed using a 20 kD MWCO centrifugal spin filter, and the filtrate was then dialyzed through a 10 kD MWCO spin filter to isolate cMAP-PEG3.4K-cMAP, which was filtered through a 0.2 um PVDF membrane and lyophilized to a white powder (10.6 mg, 16% yield). cMAP-PEG5k-cMAP was isolated in the same way.

3. *Synthesis of mPEG-cMAP-PEGm triblock polymer (Scheme II.3*). Starting materials were equilibrated to room temperature for 1 h after removing them from the -20^{o}C freezer. **cMAP** (40 mg, 0.006 mmol, 2 equiv) and mPEG5k-SVA (85.7 mg, 0.017 mmol, 3 equiv) were weighed into an oven-dried 10 mL flask with stir bar. The flask was capped with a septum, the two solids were dried under vacuum for 1 h, and then the flask was filled with argon. Anhydrous DMSO (4 mL) was added using a needle and syringe to dissolve the two white solids, and the solution was stirred for 48 h. Nanopure water (40 mL) was added to dilute the DMSO, and the solution was dialyzed against nanopure water using a 20kD MWCO centrifugal spin filter >8 times. The retentate, **mPEG5k-cMAP-PEG5km**, was filtered through a 0.2 um PVDF membrane and lyophilized to a white powder (11.3 mg, 9% yield). ^{1}H NMR (600 MHz, DMSO-*d*6): 9.84-8.48, 7.90, 5.41, 4.53, 4.15, 3.82, 3.55, 3.49 (PEG), 3.26, 3.20, 2.86-2.00, 1.59, 1.27.

A similar procedure was followed using 2 kD mPEG-SVA to synthesize mPEG-cMAP-PEGm with 2 kD blocks. For 2 kD PEG, a 10 kD MWCO centrifugal spin filter was used to isolate the triblock polymer.

Synthesis of 5-nitrophenylboronic acid-PEGm (5-nPBA-PEGm) (Scheme II.4).

3-carboxyl-5-nitrophenylboronic acid (200 mg, 0.95 mmol, 1 equiv) was added to an oven-dried 2-necked 10 mL round bottom flask containing a dry stir bar. The flask was vented with argon and sealed with a rubber septum. Anhydrous tetrahydrofuran with BHT inhibitor (5 mL) was added to dissolve the boronic acid, followed by anhydrous DMF (14.7 uL, 0.19 mmol, 0.2 equiv). The flask was cooled to 0^{o}C in an ice-water bath. Oxalyl chloride (195.4 uL, 2.28 mmol, 2.4 equiv) was then added drop wise to the reaction mixture. The ice-water bath was removed after oxalyl chloride addition was complete, and the reaction continued stirring for 2 hours at room temperature, with an argon vent to allow for the escape of volatiles. Solvent and DMF was removed via rotary evaporator and then under vacuum for 2 days under dark to afford **3-acyl chloride-5-nitrophenyl boronic acid** (217.5 mg, 100% yield) as a yellow solid.

3-acyl chloride-5-nitrophenylboronic acid (27.5 mg, 0.12 mmol, 2 equiv) was added to an oven-dried 25 mL round bottom flask containing a dry stir bar. The flask was sealed with a rubber septum, vented with argon, and cooled to 0^{o}C in an ice-water bath. Anhydrous dichloromethane (4 mL) was added to dissolve the boronic acid. 5 kD mPEG-amine (300 mg, 0.06 mmol, 1 equiv) in an oven-dried 10 mL round bottom flask vented with argon, dissolved in anhydrous dichloromethane (5 mL) and diisopropylethylamine (DIPEA, 20.9 uL, 0.12 mmol, 2 equiv) dried with activated molecular sieves, was slowly added to the boronic acid solution. The reaction flask was left in the ice-water bath to slowly warm up to room temperature, and the reaction was stirred overnight under dark. The solvent and DIPEA was removed via rotary evaporator and then under vacuum for 2 days under dark. The solid residue was reconstituted in 0.5 N HCl (5 mL) and stirred for 15

min. The resulting suspension was filtered through a 0.2 um Supor syringe filter, and the resulting clear solution was dialyzed with a 15 mL Amicon Ultra 3 kD spin filter against nanopure water until the pH was constant. The solution of polymer was concentrated to 3-4 mL, filtered through a 0.2 um PVDF syringe filter into a pre-weighed 20 mL glass vial, and lyophilized to dryness to afford **5-nitrophenylboronic acid-PEGm** (219.2 mg, 70% yield) as a fluffy white solid. ^{1}H NMR (600 MHz, DMSO-*d6*): 8.89 (t, 1H), 8.72 (m, 1H), 8.68 (m, 1H), 8.64 (m, 1H), 8.60 (s, 2H), 3.5 (s - PEG, 510H), 3.22 (s, 3H). ^{11}B NMR (160 MHz, 10 mM phosphate buffer, pH 7.4 in D_2O): 11.26 (broad s). MALDI: 5825.5.

Polymer Characterization

*1. Gel Permeation Chromatography***.** An Agilent 1100 HPLC with binary pump and injector was connected to a Tosoh TSKgel G3000PWXL-CP size exclusion column with Wyatt DAWN HELEOS light scattering and Wyatt Optilab Rex refractive index detection. Lyophilized polymer was dissolved at six different concentrations in 0.1 M NaNO3 and injected into the refractive index detector directly via a syringe pump for *dn/dc* determination. For absolute molecular weight determination by light scattering, 100 uL of polymer solution was injected onto the column and the detected polymer peak analyzed using ASTRA V software.

2. TNBSA assay of cMAP for primary amines. The instructions provided by Thermo Scientific with the 2,4,6-trinitrobenzene Sulfonic Acid 5% w/v in methanol stock solution were followed, with modifications as described next. Briefly, cMAP and glycine were each dissolved in the reaction buffer and serially diluted for a concentration range of 2 to 0.0039 mg/mL and 20 to 0.00195 mg/mL, respectively. 100 uL of each sample concentration and 50 uL of TNBSA working solution were added to a 96-well plate in triplicates and briefly

shaken. The absorbance was read on a Tecan infinite M200 plate reader at a wavelength of 335 nm, incubated at 37 degrees Celsius for 2 h, and read again. Glycine was used as a positive control.

3. Polymer siRNA encapsulation assays. The ability of the cMAP polymers to encapsulate siRNA was analyzed using two methods: a gel retardation assay and a RiboGreen assay. For the gel retardation assay, increasing volumes of 0.5 mg/mL polymer was mixed with 1 uL of 1 mg/mL siRNA at (+/-) charge ratios of 0, 0.5, 1, 1.5, 2, 2.5, 3, and 5 in water for a total volume of 15 uL. The mixtures were briefly vortexed, centrifuged down, and allowed to sit for 15 min at room temperature. 3 uL of 6X DNA loading dye was added to each mixture, which was then loaded onto a 1 wt% agarose gel and run at 95V for 1.5 h in 0.5x TBE buffer. The gel was imaged on a UVP BioDoc-It Imaging System.

The RiboGreen assay was performed in a similar manner to the gel retardation assay, except using increasing volumes of 0.1 mg/mL polymer and 1 uL of 0.1 mg/mL siRNA in water for a total volume of 100 uL in 96-well plate. To each of these mixtures, 100 uL of the Quant-iT RiboGreen RNA reagent working solution, prepared according to the kit's protocol, was added. The plate was briefly shaken, incubated in the dark for 5 min at room temperature, and the fluorescence intensity read on a Tecan infinite M200 plate reader at an excitation wavelength of 480 nm and an emission wavelength of 520 nm. Measurements were done in triplicate.

Nanoparticle formulation and characterization.

1. Nanoparticle formulation. cMAP NPs were formulated by first mixing a 1:1 molar ratio of cMAP vicinal diols to 5-nPBA-PEGm (1 mg cMAP to 22 mg 5-nPBA-PEGm) in 10 mM phosphate buffer pH 7.4, briefly vortexing, centrifuging down, and letting the mixture

sit for 15 min at room temperature. siRNA in an equivalent volume of RNAse-free water was then added at a 3:1 charge ratio of cMAP to siRNA, and at a concentration of up to 0.8 mg/mL siRNA. cMAP-PEG copolymer, cMAP-PEG-cMAP triblock, and mPEG-cMAP-PEGm triblock formulations were made in a similar fashion, though the charge ratio was varied from 3:1 down to a 1:1 charge ratio of polymer to siRNA, and at a concentration of up to 1 mg/mL siRNA. For formulations without any 5-nPBA-PEGm, the polymer and siRNA in equal volumes were simply mixed at an appropriate charge ratio. For injection into mice, 0.1 volumes of 10X phosphate buffered saline (PBS) were added to attain a 1X PBS solution, with a final concentration of 0.73 mg/mL siRNA. For the cMAP-PEG copolymer and mPEG-cMAP-PEGm NPs which were formulated in PBS, both the polymer and siRNA solutions were in PBS, and then mixed together; this was able to be directly injected into mice. For removal of excess components (i.e., polymer, PEG), the NP formulation was placed in a 0.5 mL 30 kD MWCO Amicon Ultra spin filter and dialyzed with PBS at 2,000 rpm for 10 min 5-10 times.

2. Nanoparticle size and zeta potential. NP size was determined using two different methods: dynamic light scattering (DLS) and cryo-transmission electron microscopy (cryoTEM). DLS was performed on a Brookhaven Instruments Corporation (BIC) Zeta-PALS with BIC Particle Sizing Software. The particles were diluted down to a concentration of 0.2 mg/mL siRNA or less, depending on the formulation, until a stable size was recorded for ten 1-minute measurements. The results of at least 10 measurements were averaged.

CryoTEM imaging was performed on particles in solution that were frozen on R2/2 Quantifoil grids in liquid ethane after blotting with filter paper using an FEI Mark IV

Vitrobot with a 2 s blot time (blot force 6) and a 1 s drain time. Images were collected on a Tecnai 120-keV transmission electron microscope equipped with a Gatan 2k x 2k UltraScan CCD camera and Serial EM automated software. Acquired images were analyzed using ImageJ software to measure NP diameter.

The NPs' surface charge, or zeta potential, was measured using the same Zeta-PALS used for DLS, with the addition of a Brookhaven aqueous electrode assembly. 10 uL of particle formulation was mixed with 1.5 mL of either 10 mM phosphate buffer, pH 7.4 or 1 mM potassium chloride, pH 5.5 in a cuvette. The electrode was inserted into the cuvette and zeta potential measured using BIC PALS Zeta Potential Analyzer software with a target residual of 0.012. The results of at least 10 measurements were averaged.

Nanoparticle Stoichiometry.

1. Quantification of 5-nPBA-PEGm bound to NP. NPs were formulated with 5-nPBA-PEGm and excess components were removed as described above. 50 uL of filtrate from the 30 kD MWCO spin filter (containing excess components) were injected on an Agilent 1200 HPLC with quaternary pump and autosampler connected to a Phenomenex Gemini C18 reverse phase column and multiple wavelength detector. The absorbance at 254 nm was recorded and compared with a calibration curve of 5-nPBA-PEGm.

2. Quantification of cationic polymer bound to NP. NPs were formulated in the absence of 5-nPBA-PEGm. For cMAP, excess cationic polymer was removed from aggregated NPs as described above. The cationic polymer bound to the NP was directly quantitated by taking the retentate from the 30 kD MWCO spin filter containing the NPs, and disassembling and sequestering the siRNA using BcMag^{TM} SAX (Strong Anion Exchange) magnetic beads (Bioclone Inc). 50 uL of the liquid containing cMAP was injected onto the GPC setup

described above and the amount of polymer bound to the NP was directly determined using the refractive index signal as compared to a cMAP calibration curve. For cMAP-PEG copolymer and mPEG-cMAP-PEGm, 50 uL of the formulation was injected onto the GPC setup described above. The refractive index signal corresponding to polymer not bound to the NP was recorded and compared with a calibration curve of the same cationic polymer. This amount was subtracted from the total amount of polymer used for the formulation to determine the percent of polymer bound to the NP.

***In vivo* mouse pharmacokinetic (PK) studies.**

All animal studies were approved by the Institutional Animal Care and Use Committee at Caltech. NPs were formulated as described above, except 20% of the siRNA was substituted with a Cy3-fluorophore tagged siRNA. The NP formulation was injected intravenously via the mouse tail vein at a dose of 5 mg siRNA per kg mouse. The hind legs of Balb/c mice (Taconic and Jackson Labs) were shaved for blood collection from the saphenous vein in red top clot activator containing Sarstedt Microvette CB300 capillary tubes. Blood was collected at various time points starting at 2 min after NP injection, with up to six points per mouse. The tubes were centrifuged at 14,000x*g* for 15 min at 4^{o}C and the serum at the top of the tube used for analysis of Cy3 fluorescence, with excitation wavelength 530 nm and emission wavelength 570 nm, as compared to a standard curve of the NP formulation in mouse serum. The fraction of Cy3-siRNA remaining in serum was calculated using the serum volume based on mouse weight and the amount of formulation injected. Data points are from 3 mice per formulation.

Acknowledgements

We thank Alasdair McDowell and David VanderVelde for assistance with CryoTEM imaging and NMR spectroscopy, respectively. This project was financially supported by the National Cancer Institute Grant CA 151819, and a donation from Avidity NanoMedicines.

Supporting Information

Table of Contents

I. cMAP precursors: NMR and mass spectra

Mucic acid dimethyl ester.

Figure II.S1: 1H NMR Spectrum of mucic acid dimethyl ester.

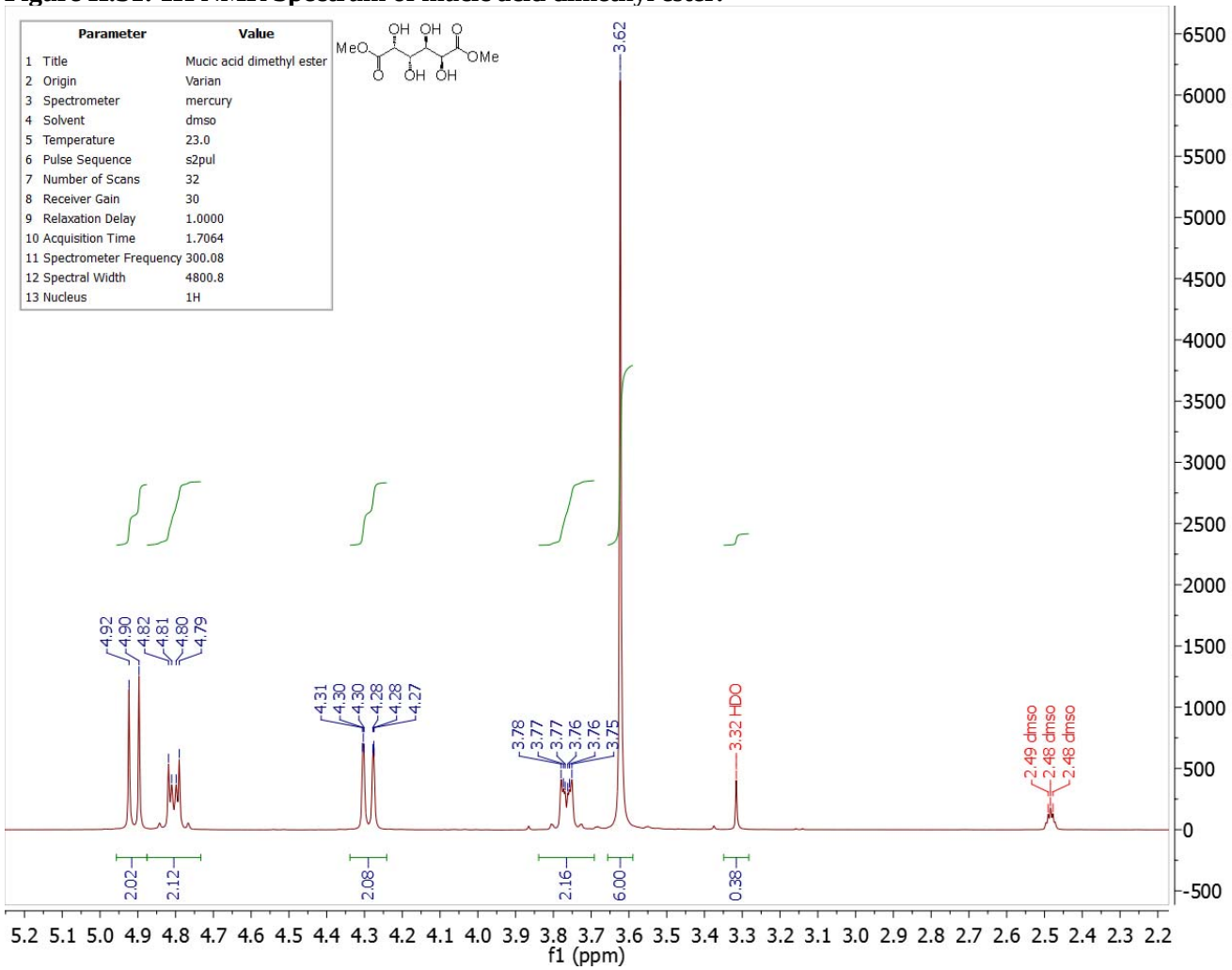

N-boc protected mucic acid ethylenediamine.

Figure II.S2: 1H NMR Spectrum of N-boc protected mucic acid ethylenediamine.

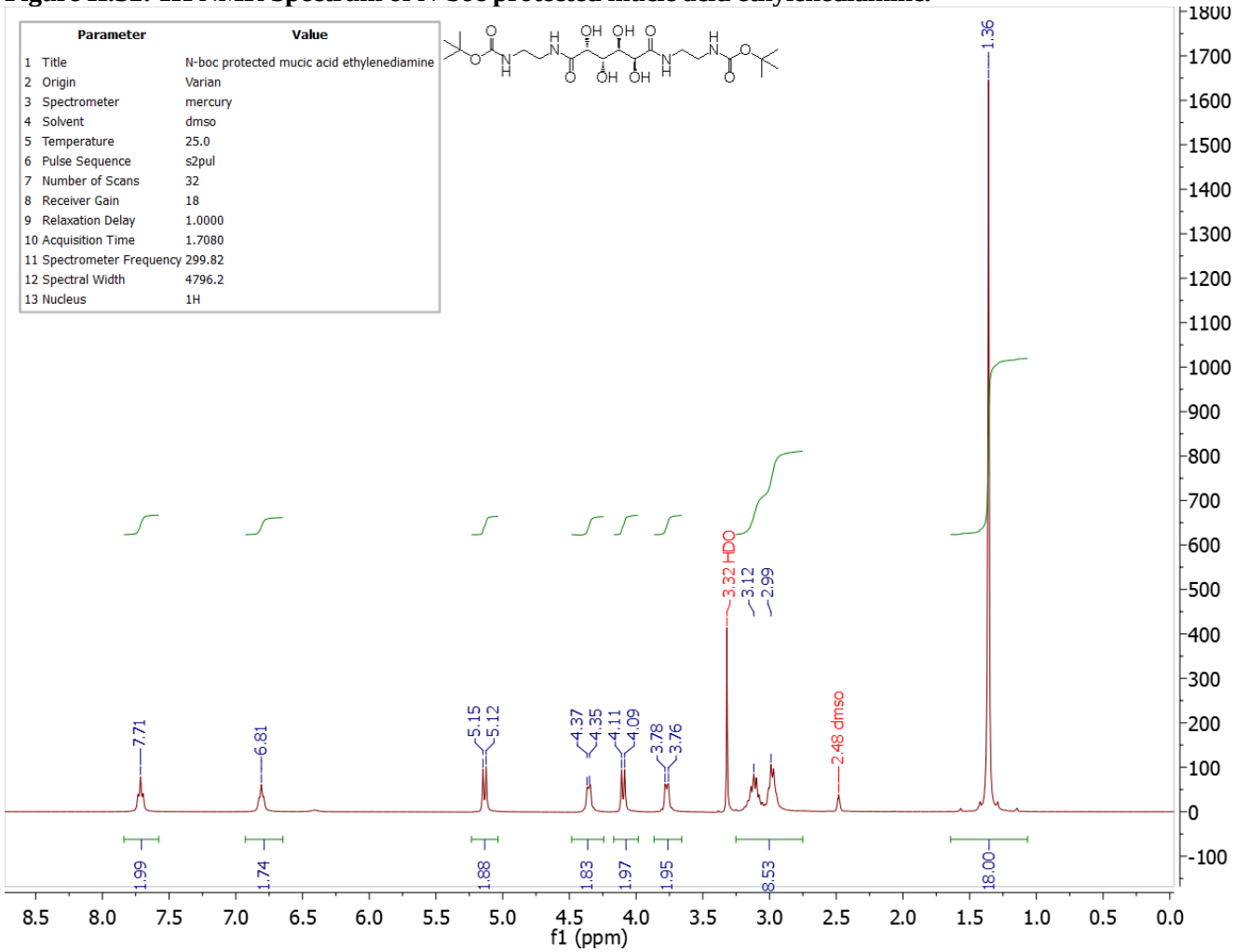

Figure II.S3: Electrospray Ionization (ESI) Mass Spectrum of N-boc protected mucic acid ethylenediamine.

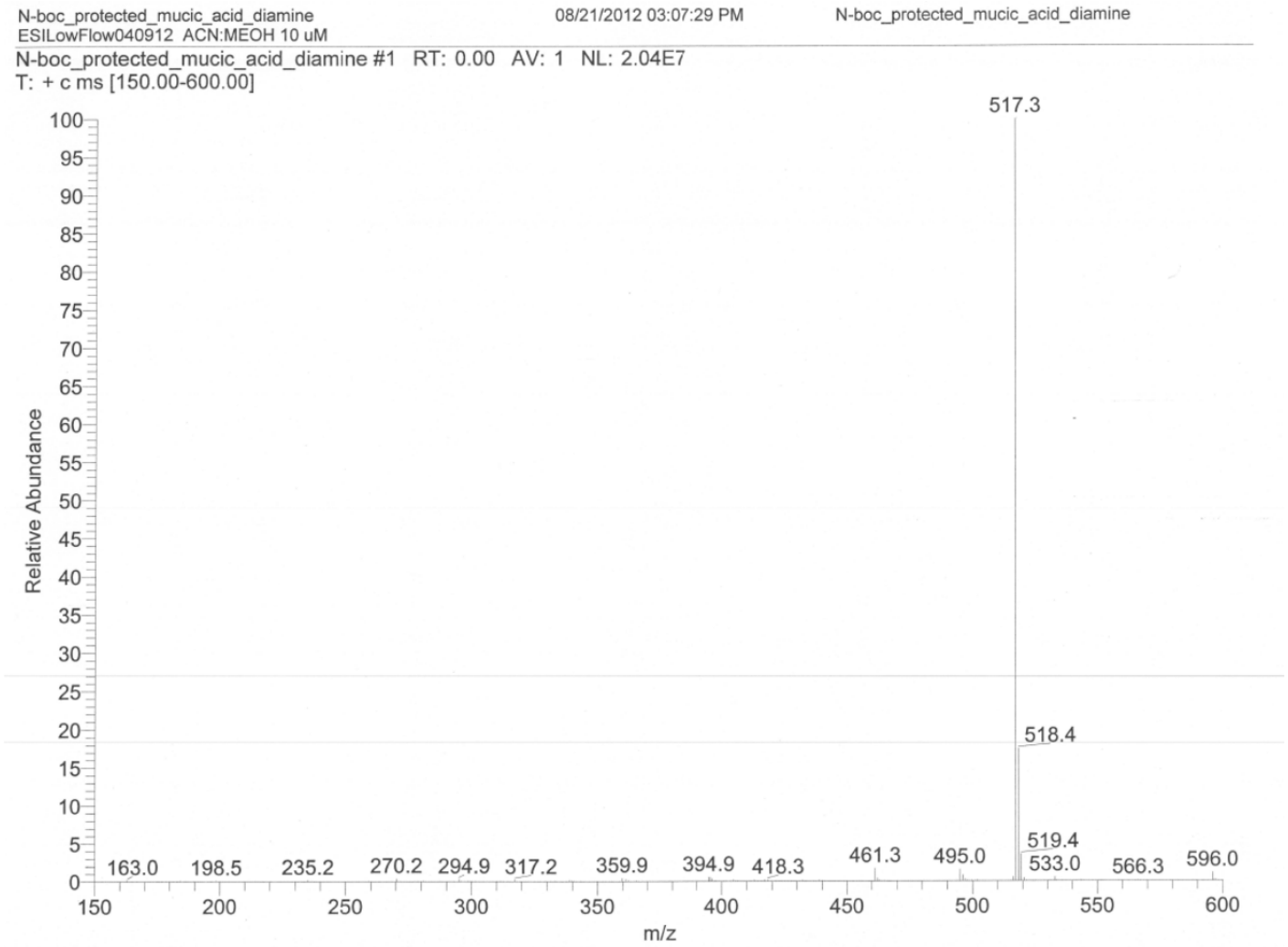

Mucic acid ethylenediamine.

Structure II.S1: Mucic Acid Ethylenediamine.

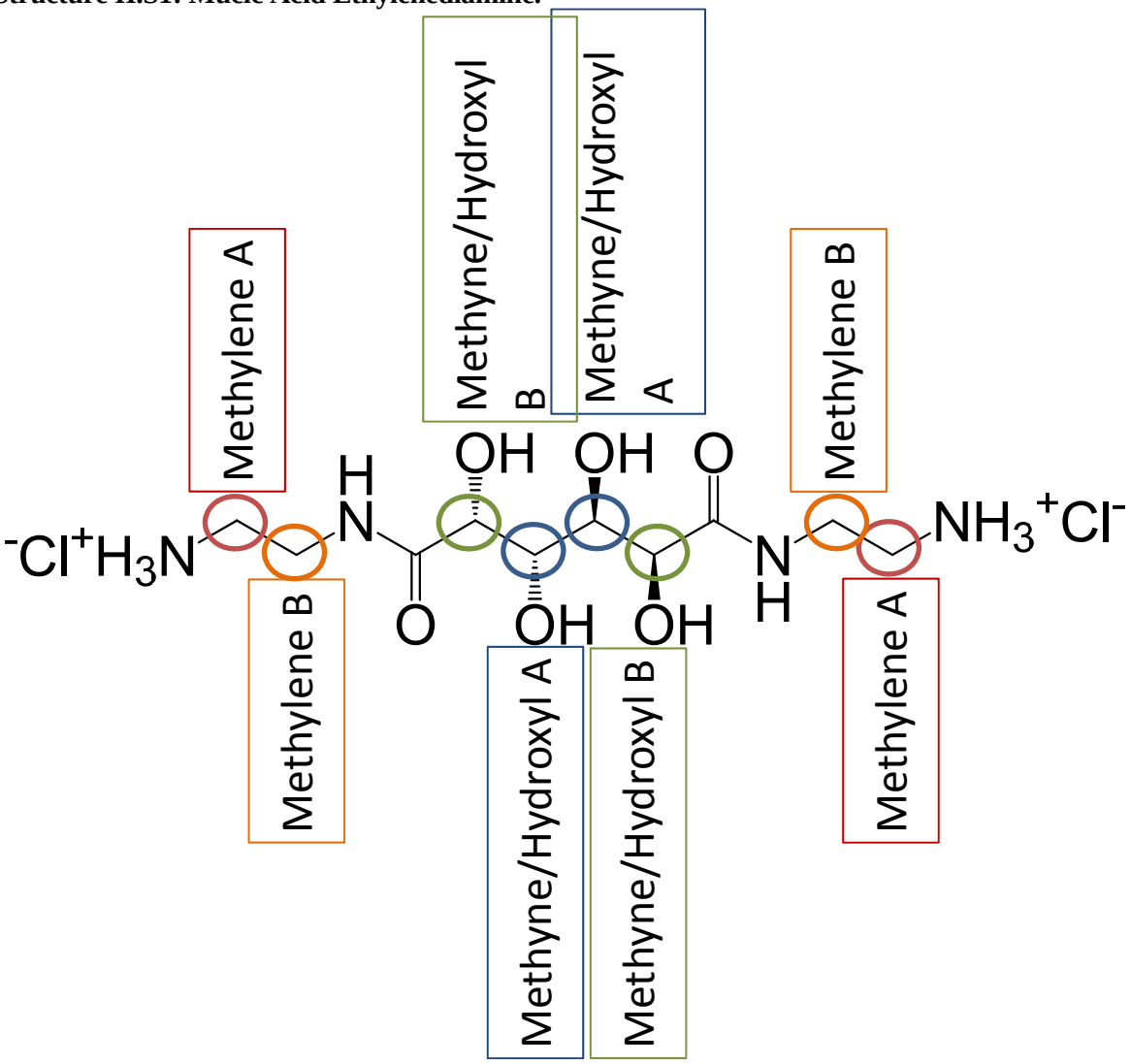

Mucic acid ethylenediamine

Figure II.S4: 1H NMR Spectrum of Mucic Acid Ethylenediamine in D_2O.

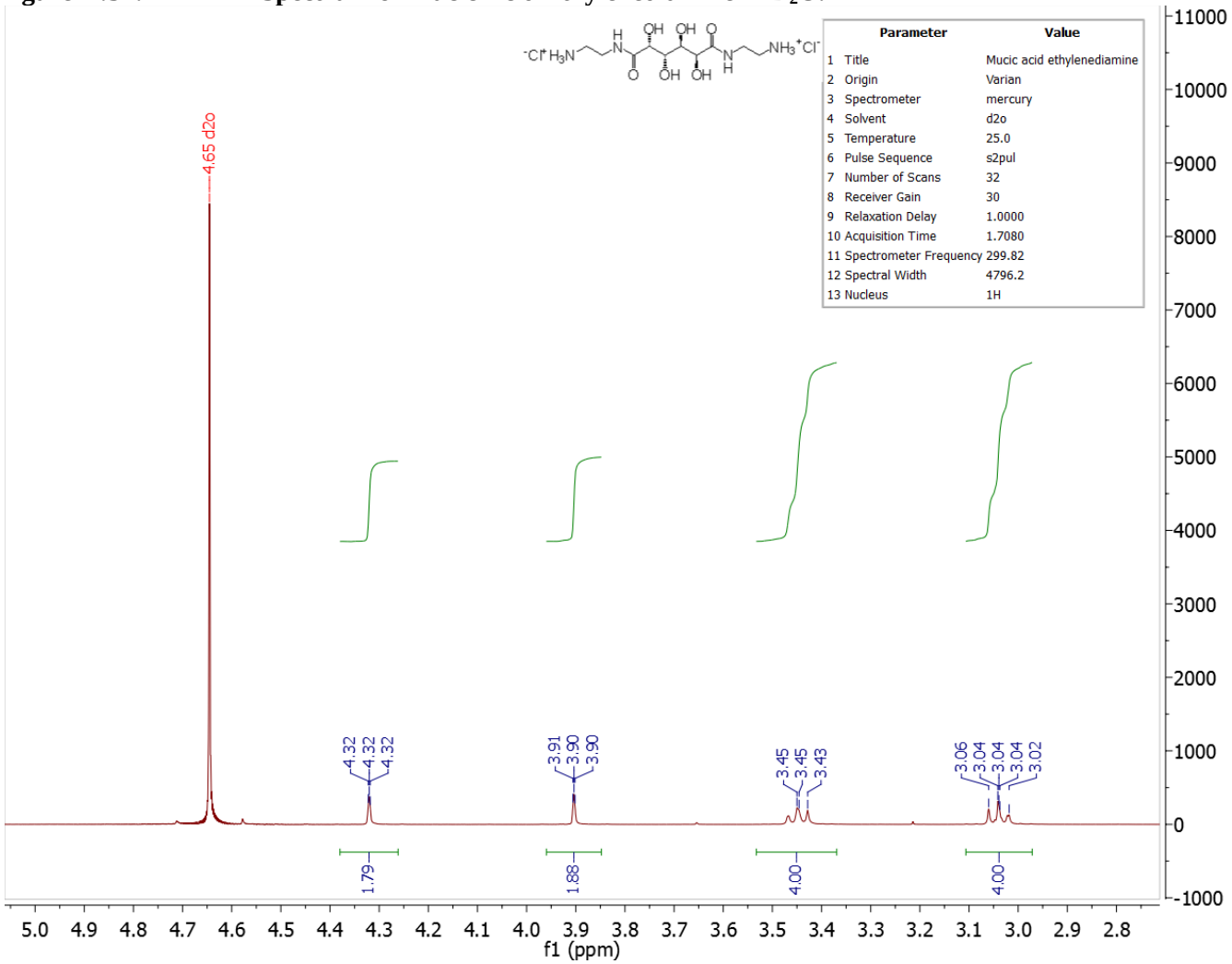

	Parameter	Value
1	Title	Mucic acid ethylenediamine
2	Origin	Varian
3	Spectrometer	mercury
4	Solvent	d2o
5	Temperature	25.0
6	Pulse Sequence	s2pul
7	Number of Scans	32
8	Receiver Gain	30
9	Relaxation Delay	1.0000
10	Acquisition Time	1.7080
11	Spectrometer Frequency	299.82
12	Spectral Width	4796.2
13	Nucleus	1H

Figure II.S5: 1H NMR Spectrum of Mucic Acid Ethylenediamine in DMSO.

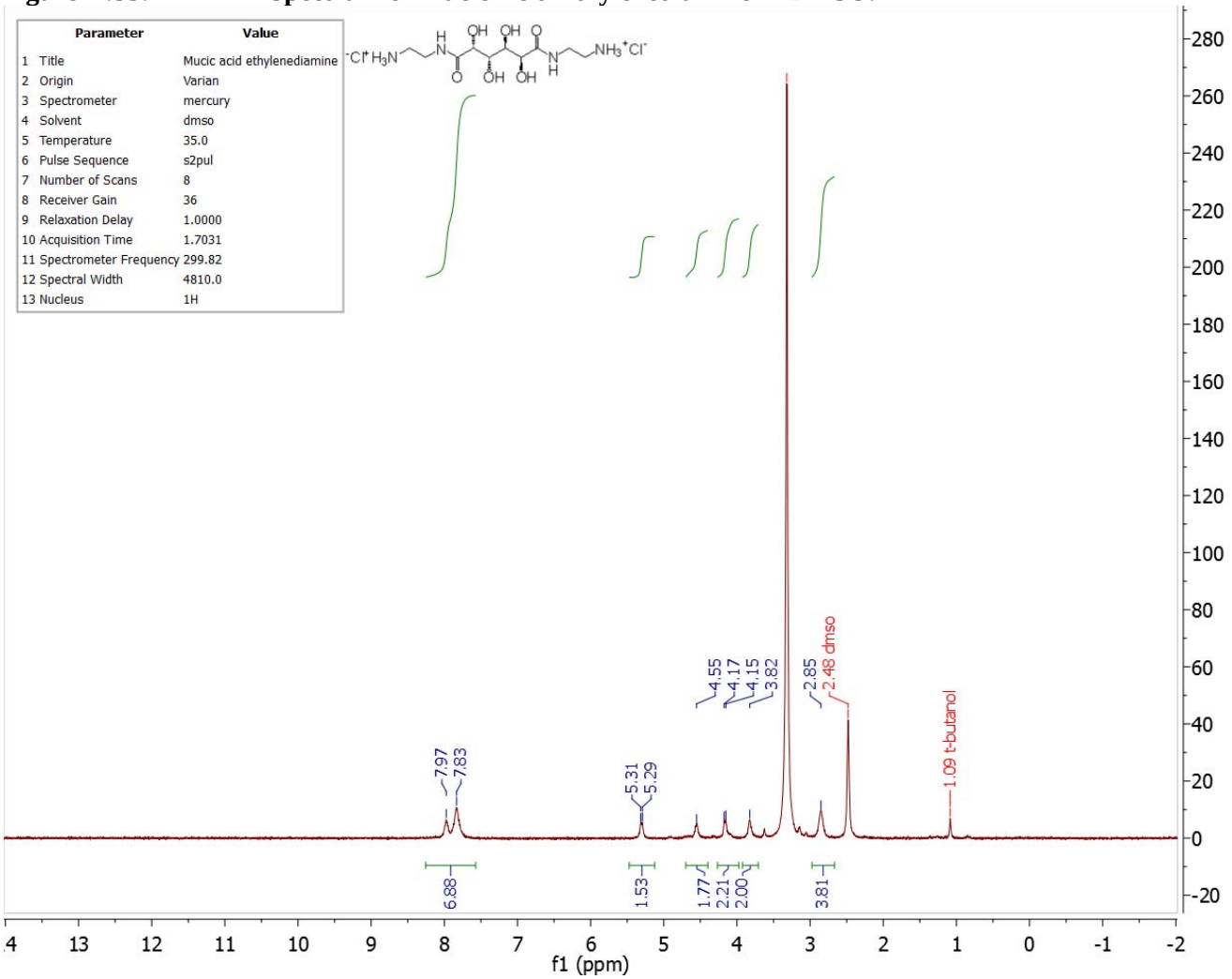

Figure II.S6: 13C NMR Spectrum of Mucic Acid Ethylenediamine in DMSO.

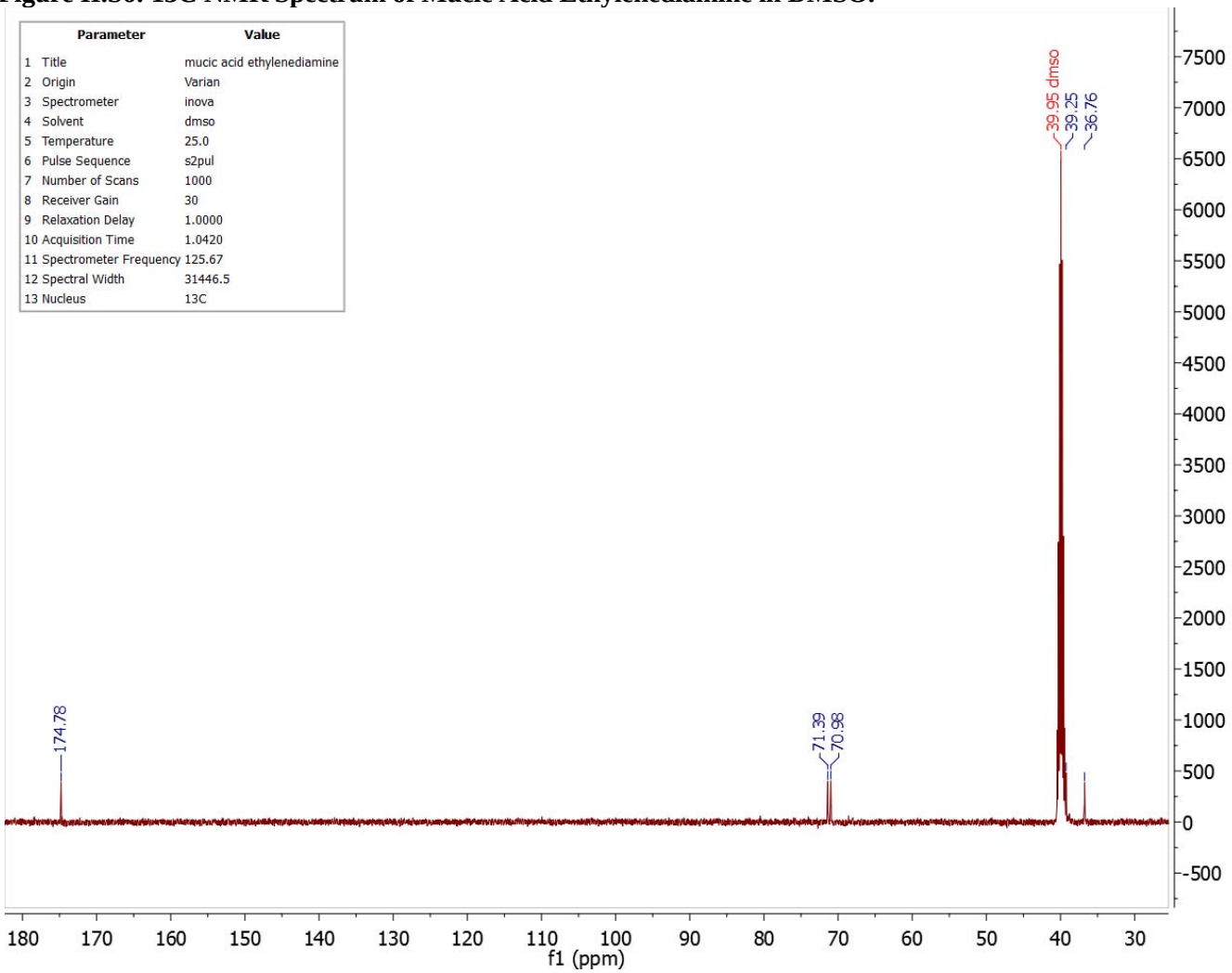

Table II.S1: 1H and 13C NMR peak assignments for Mucic Acid Ethylenediamine.

	1H in D_2O Chemical Shift (ppm)	1H in DMSO Chemical Shift (ppm)	13C in DMSO Chemical Shift (ppm)
Methylene A	3.04	2.85	36.76
Methylene B	3.45	Covered by H2O	39.25
Methyne A	3.90	3.82	70.98
Methyne B	4.32	4.15	71.39
Hydroxyl A	Not observed	4.55	N/A
Hydroxyl B	Not observed	5.30	N/A
Amide and amines	Not observed	7.83, 7.97	N/A
Amide Carbonyl carbon	N/A	N/A	174.78

Figure II.S7: ESI Mass Spectrum of Mucic Acid Ethylenediamine.

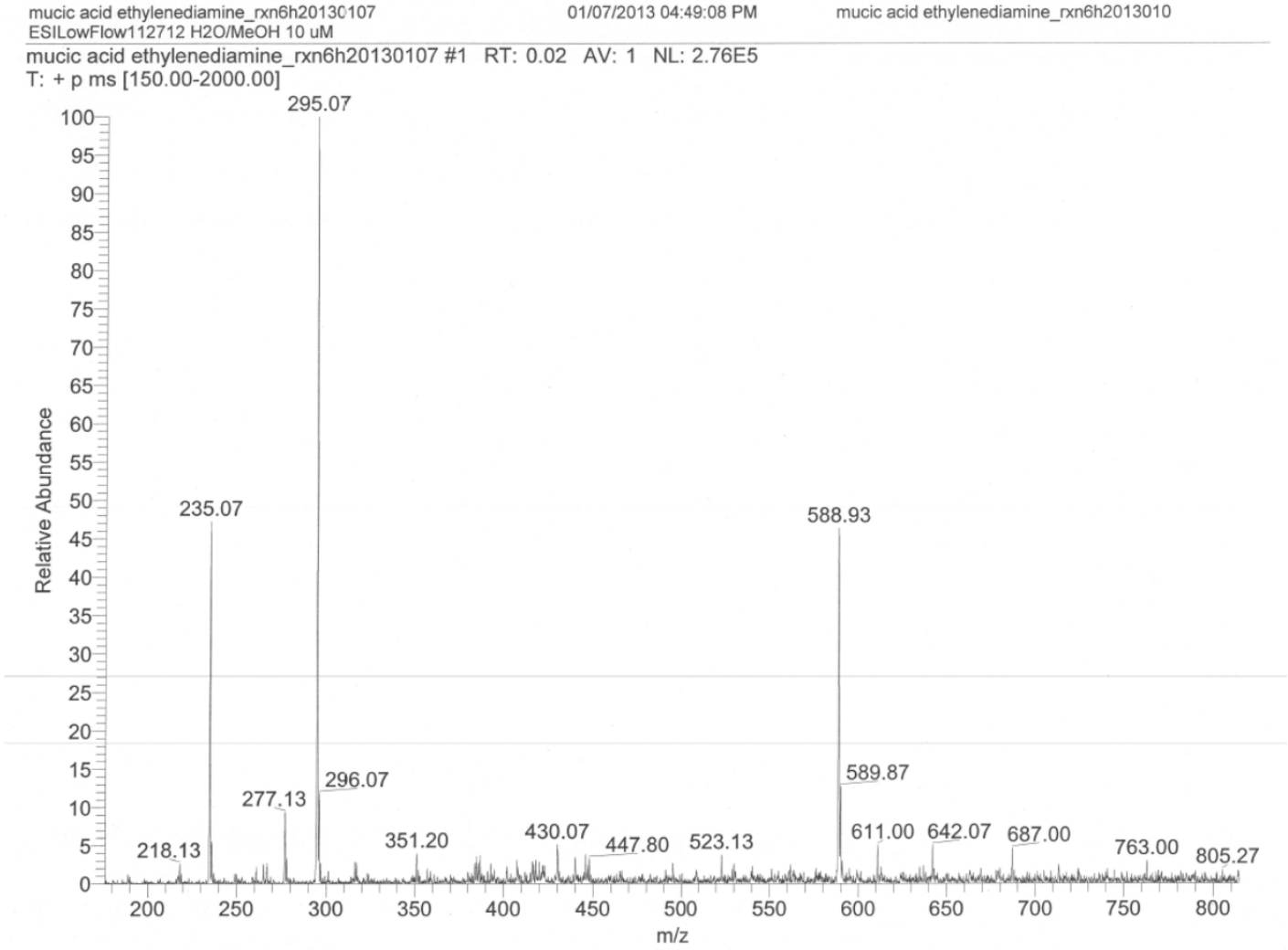

2. Dimethyl Suberimidate (DMS) and DMS hydrolysis: NMR and mass spectra

Dimethyl Suberimidate (DMS).

Dimethyl suberimidate, the charged monomer with which mucic acid ethylenediamine was polymerized, was used as purchased from Thermo Scientific or Sigma-Aldrich. In order to assign peaks in the proton and carbon spectra of cMAP, NMR spectra of dimethyl suberimidate were acquired. Both proton and carbon NMR spectra of DMS were more complex than expected, suggesting that some hydrolysis was present in a freshly opened bottle. For example, the three protons of the methoxy peak for DMS have a chemical shift of 4.08 ppm, which completely shift to 3.55 ppm in a sample hydrolyzed in D_2O. Similarly, the methylene peak adjacent to the methoxy (methylene A) has a chemical shift of 2.64 ppm in DMS, which when hydrolyzed shifts more upfield to 2.25 ppm.

Additionally there was the presence of dimethyl suberimidate containing one methoxy group which was completely hydrolyzed to a carboxylate group, as determined by both the ESI mass spectrum peak at *m/z* of 187.9 and the ^{1}H-^{13}C HMBC NMR spectrum. The methylene A peak in this case was present on ^{1}H NMR with a chemical shift of 2.01 ppm.

Table II.S2: 1H NMR peak assignments for Dimethyl Suberimidate with varying degrees of hydrolysis.

	Methoxy	Methylene A	Methylene B	Methylene C
Dimethyl suberimidate	4.08	2.64	1.60	1.30
Dimethyl suberimidate hydrolyzed to the dimethyl ester	3.55	2.25	1.45	1.20
Dimethyl suberimidate hydrolyzed to carboxylate	None	2.01	1.46	1.20

Structure II.S2: Dimethyl Suberimidate.

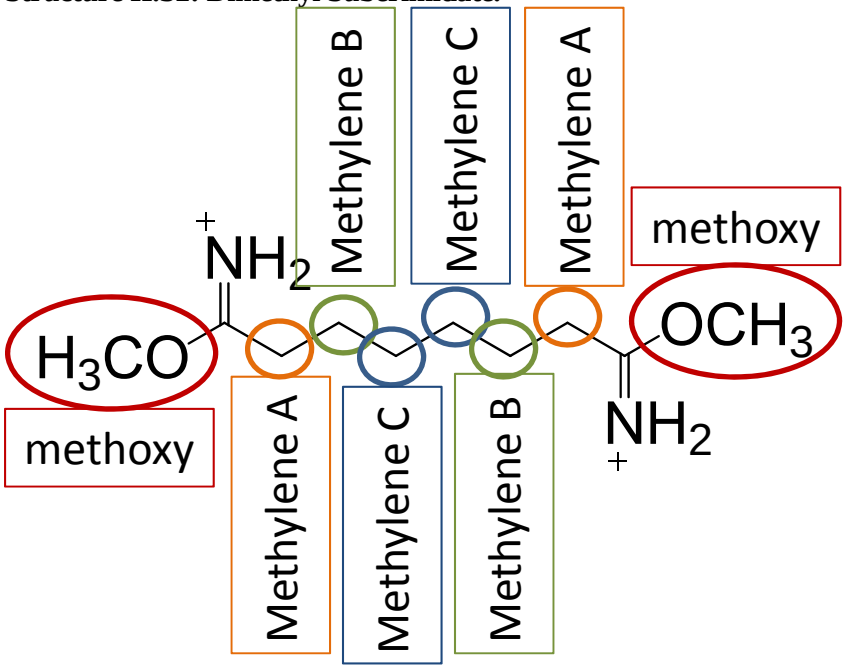

Dimethyl Suberimidate

Structure II.S3: Dimethyl Suberimidate hydrolyzed to the dimethyl ester.

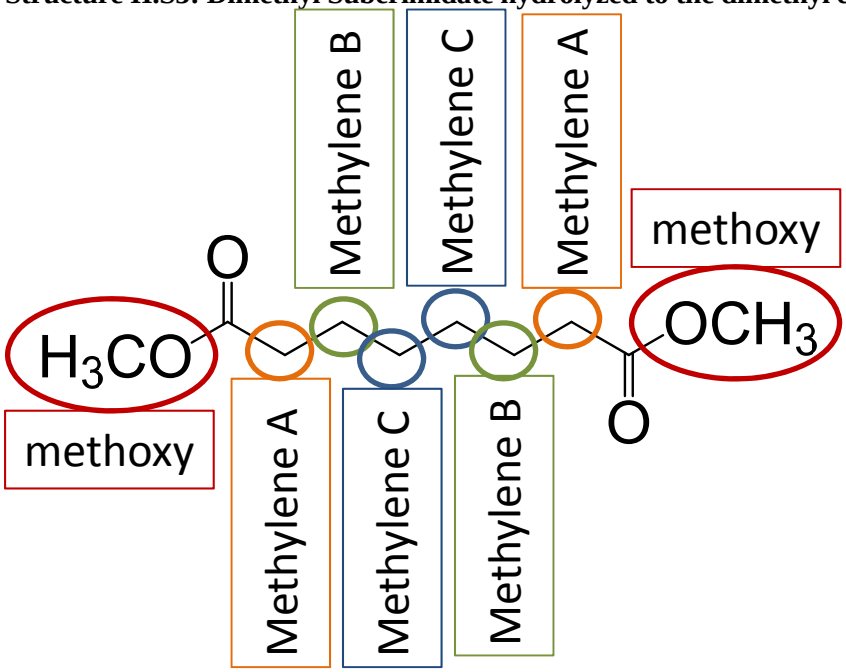

Dimethyl Suberimidate - hydrolyzed

Structure II.S4: Dimethyl Suberimidate with one side hydrolyzed to the carboxylate.

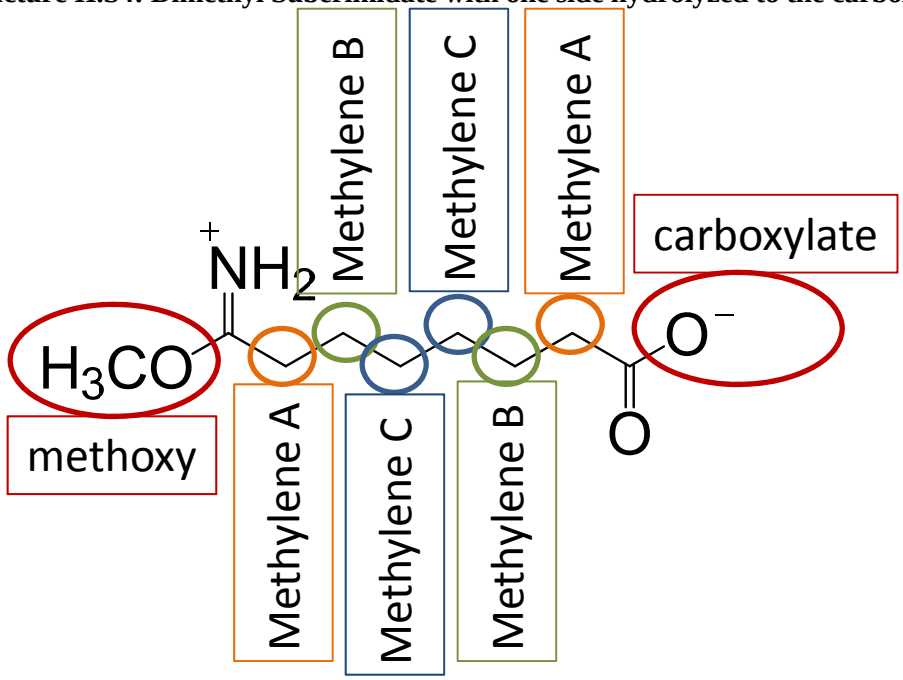

Dimethyl Suberimidate – hydrolyzed to carboxylate

Figure II.S8: 1H NMR Spectrum of Dimethyl Suberimidate.

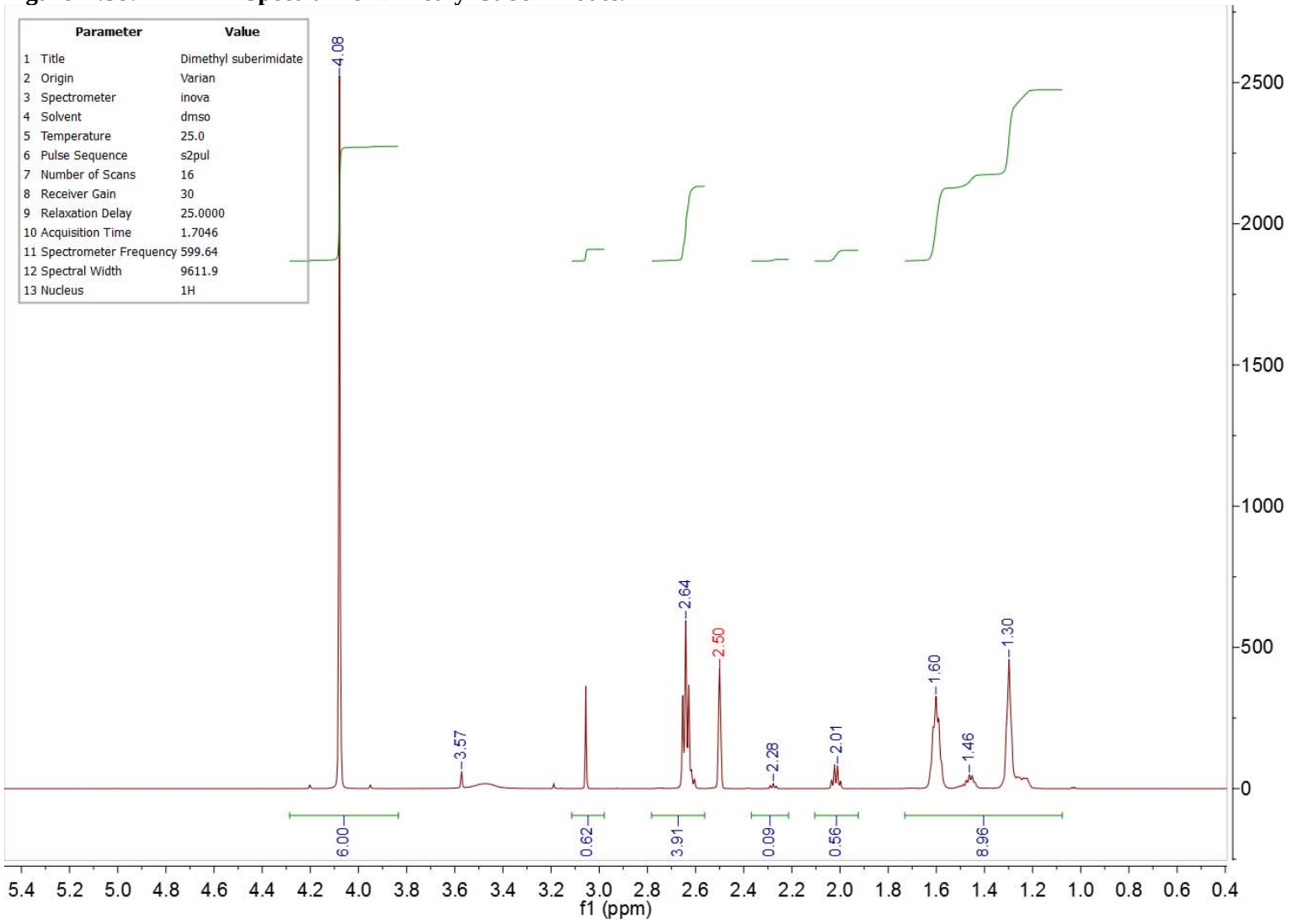

Figure II.S9: 13C NMR Spectrum of Dimethyl Suberimidate.

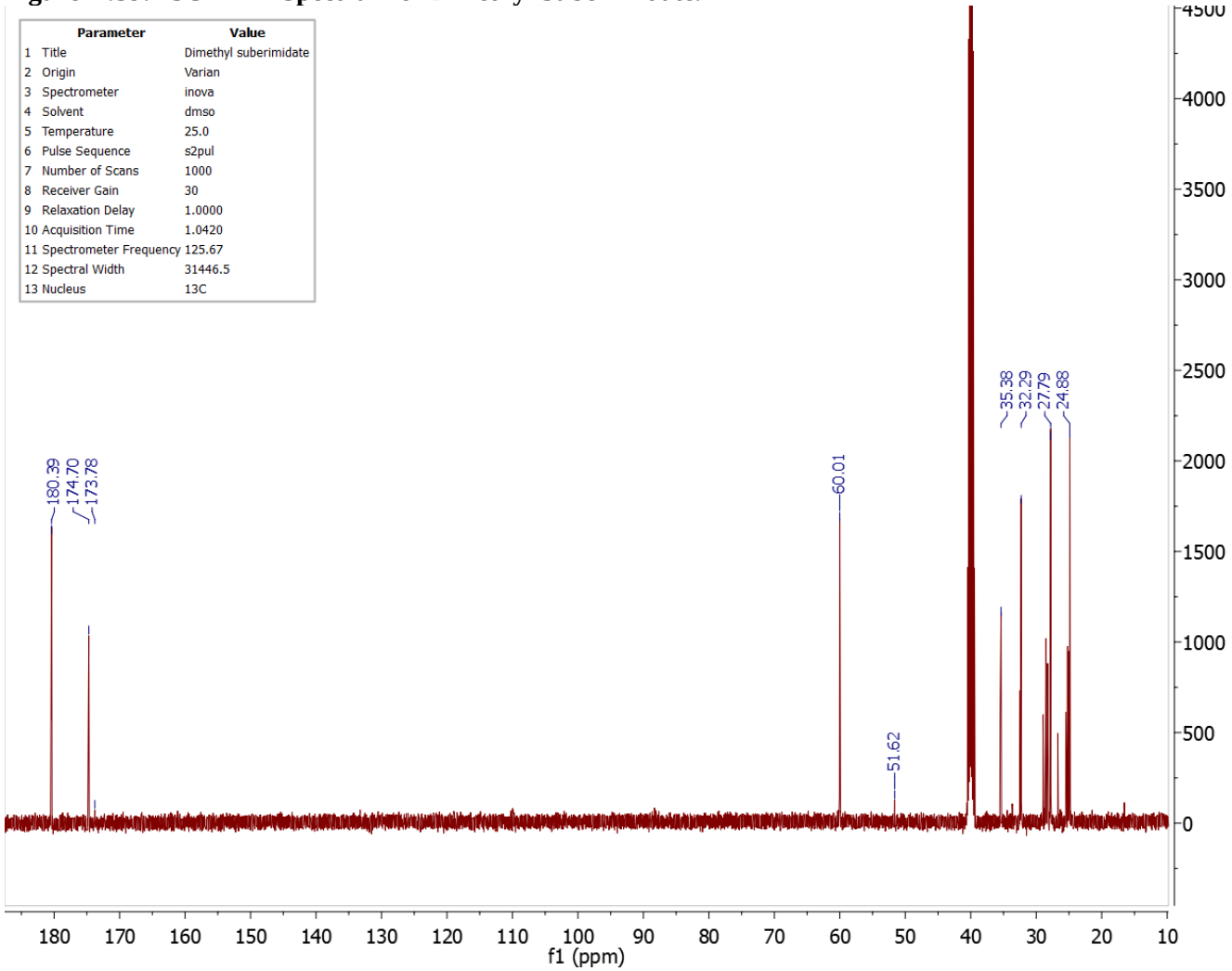

Figure II.S10: 1H-13C HMBC Spectrum of Dimethyl Suberimidate.

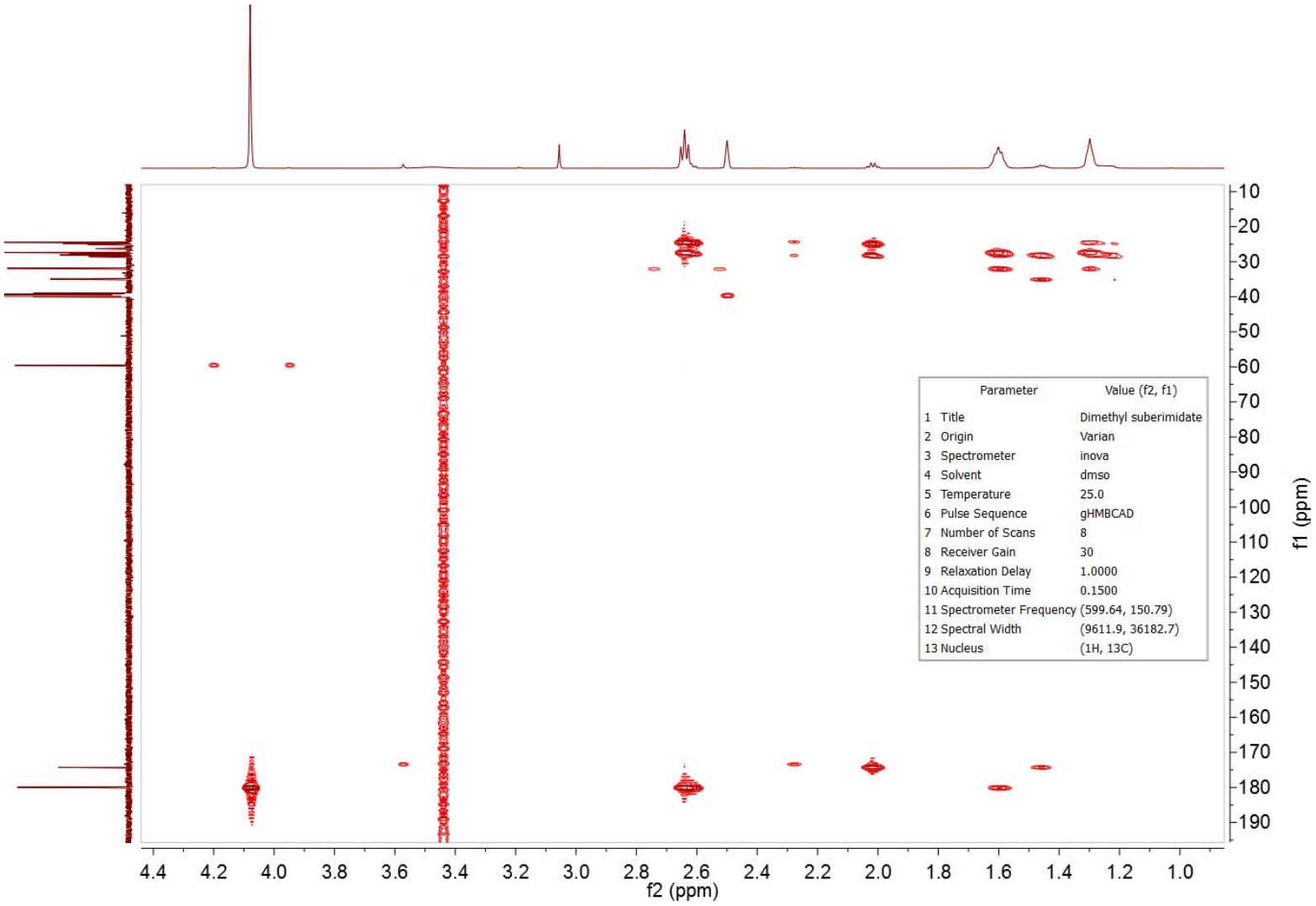

Figure II.S11: 1H NMR Spectrum of Dimethyl Suberimidate hydrolyzed to the dimethyl ester.

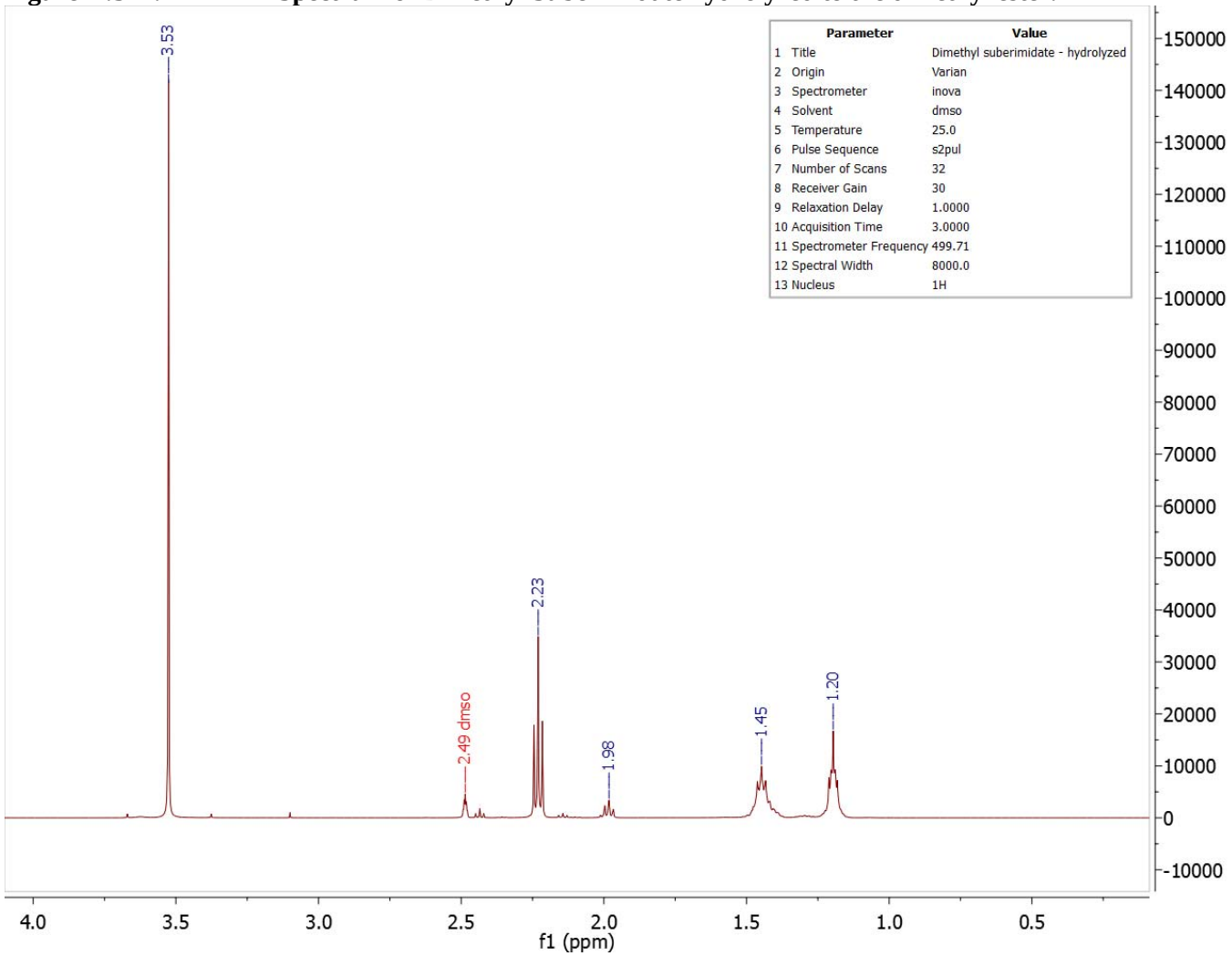

Parameter	Value
1 Title	Dimethyl suberimidate - hydrolyzed
2 Origin	Varian
3 Spectrometer	inova
4 Solvent	dmso
5 Temperature	25.0
6 Pulse Sequence	s2pul
7 Number of Scans	32
8 Receiver Gain	30
9 Relaxation Delay	1.0000
10 Acquisition Time	3.0000
11 Spectrometer Frequency	499.71
12 Spectral Width	8000.0
13 Nucleus	1H

Figure II.S12: 13C NMR Spectrum of Dimethyl Suberimidate hydrolyzed to the dimethyl ester.

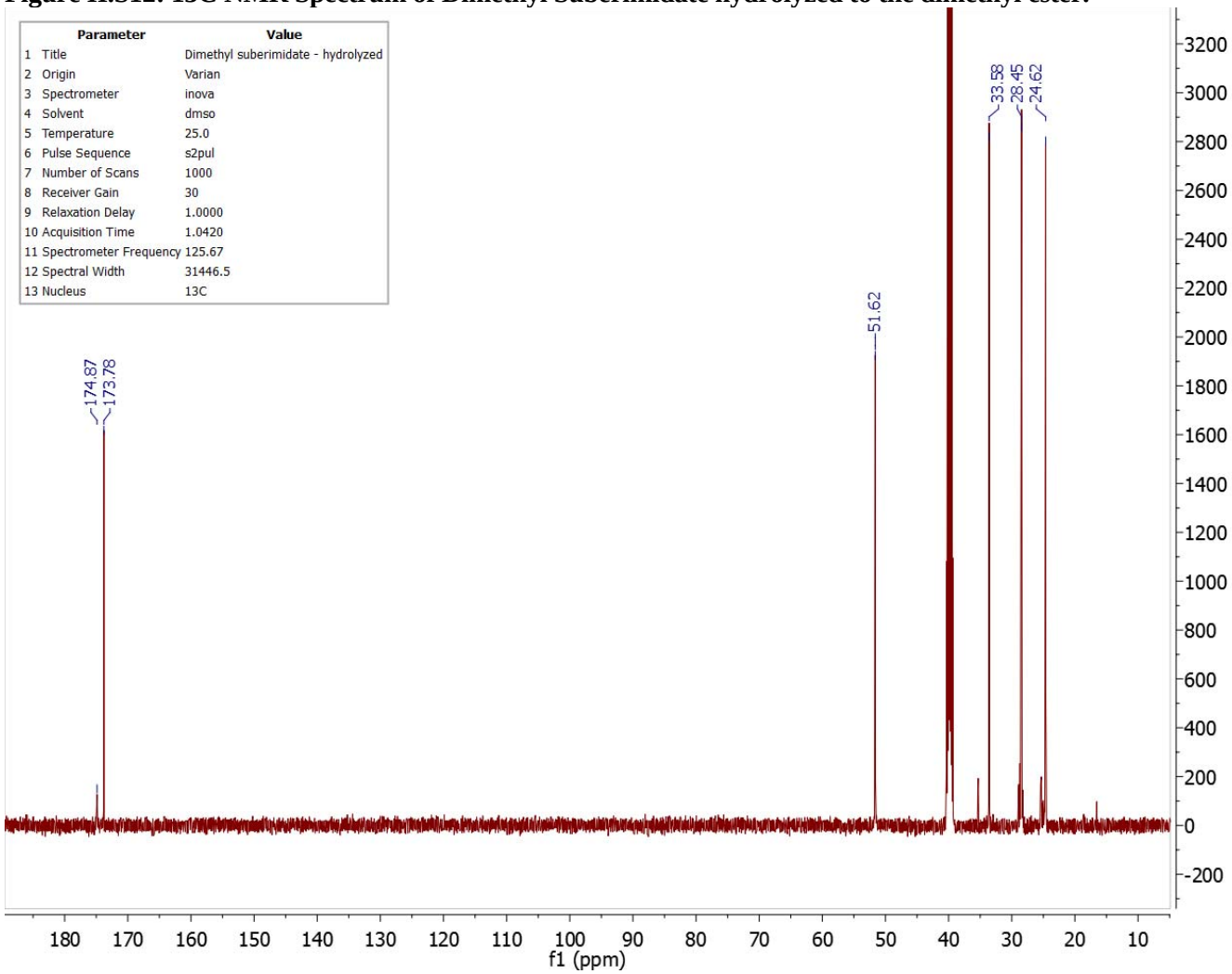

Figure II.S13: ESI Mass Spectrum of Dimethyl Suberimidate hydrolyzed to the dimethyl ester (*m/z* 202.9). Dimethyl suberimidate with one end hydrolyzed to the carboxylate is the peak with *m/z* 187.9. Dimethyl suberimidate with both ends hydrolyzed to the carboxylate is the peak with *m/z* 170.8.

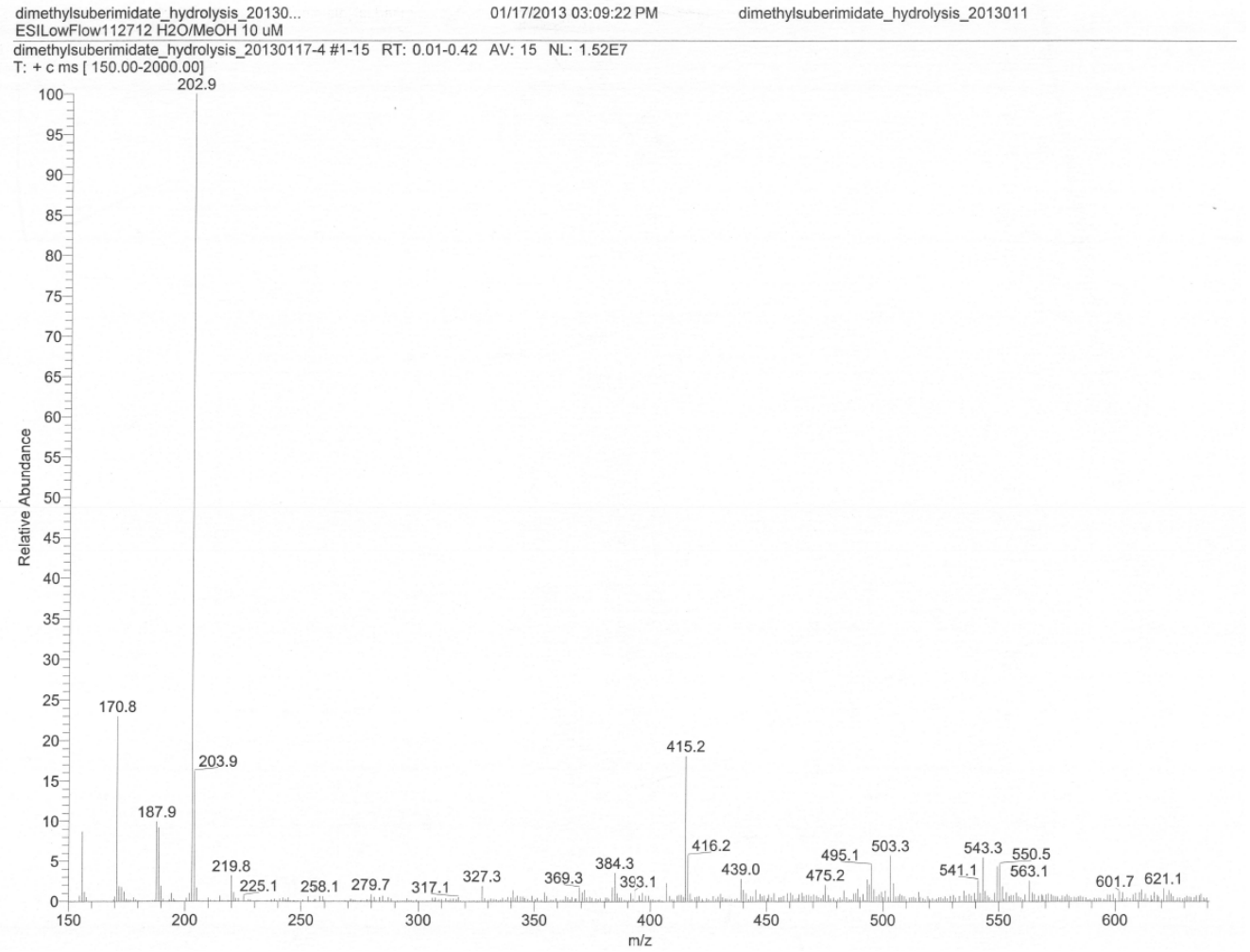

3. cMAP: NMR spectra

cationic Mucic Acid Polymer (cMAP).

Structure II.S5: cMAP.

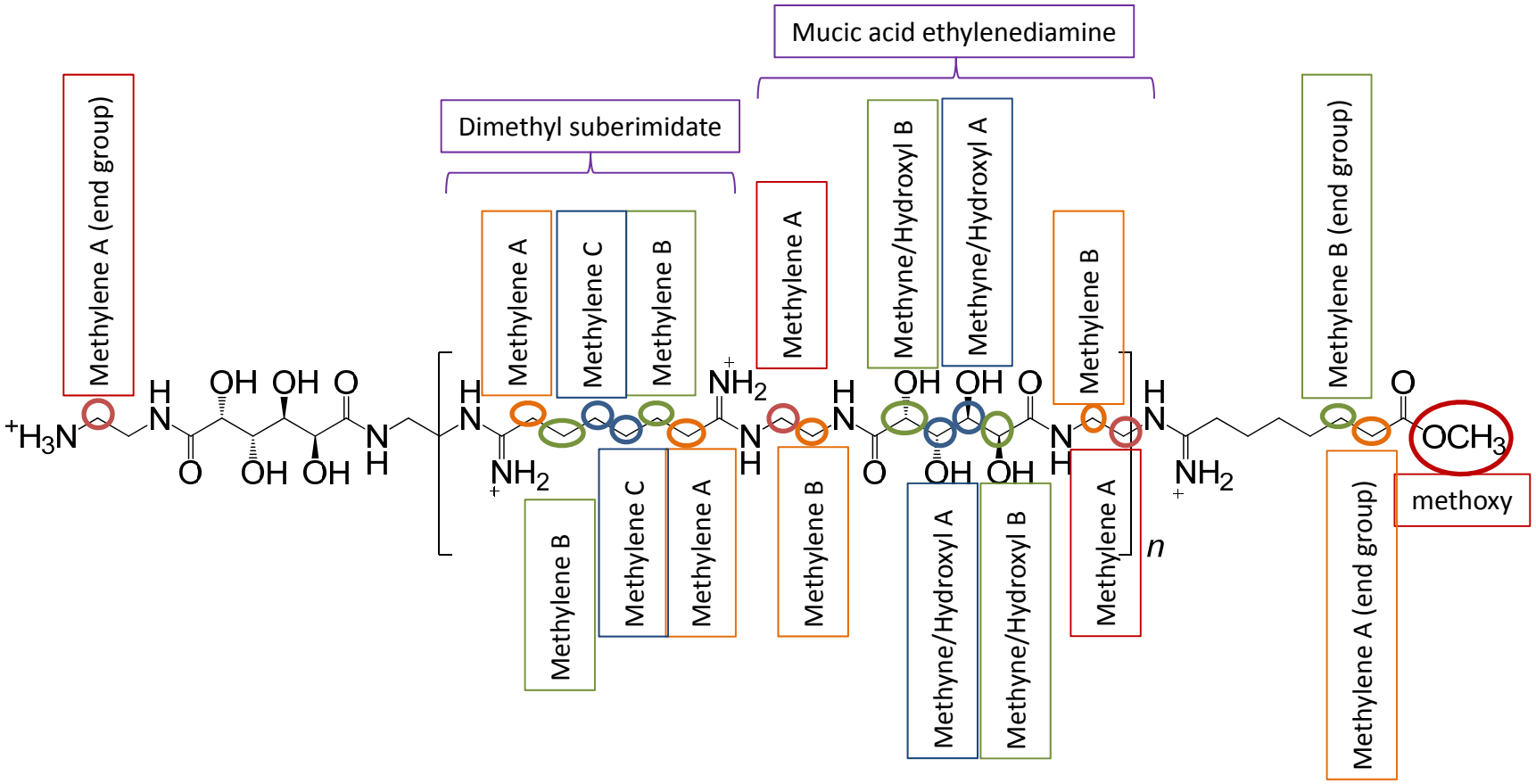

Figure II.S14: 1H NMR Spectrum of cMAP.

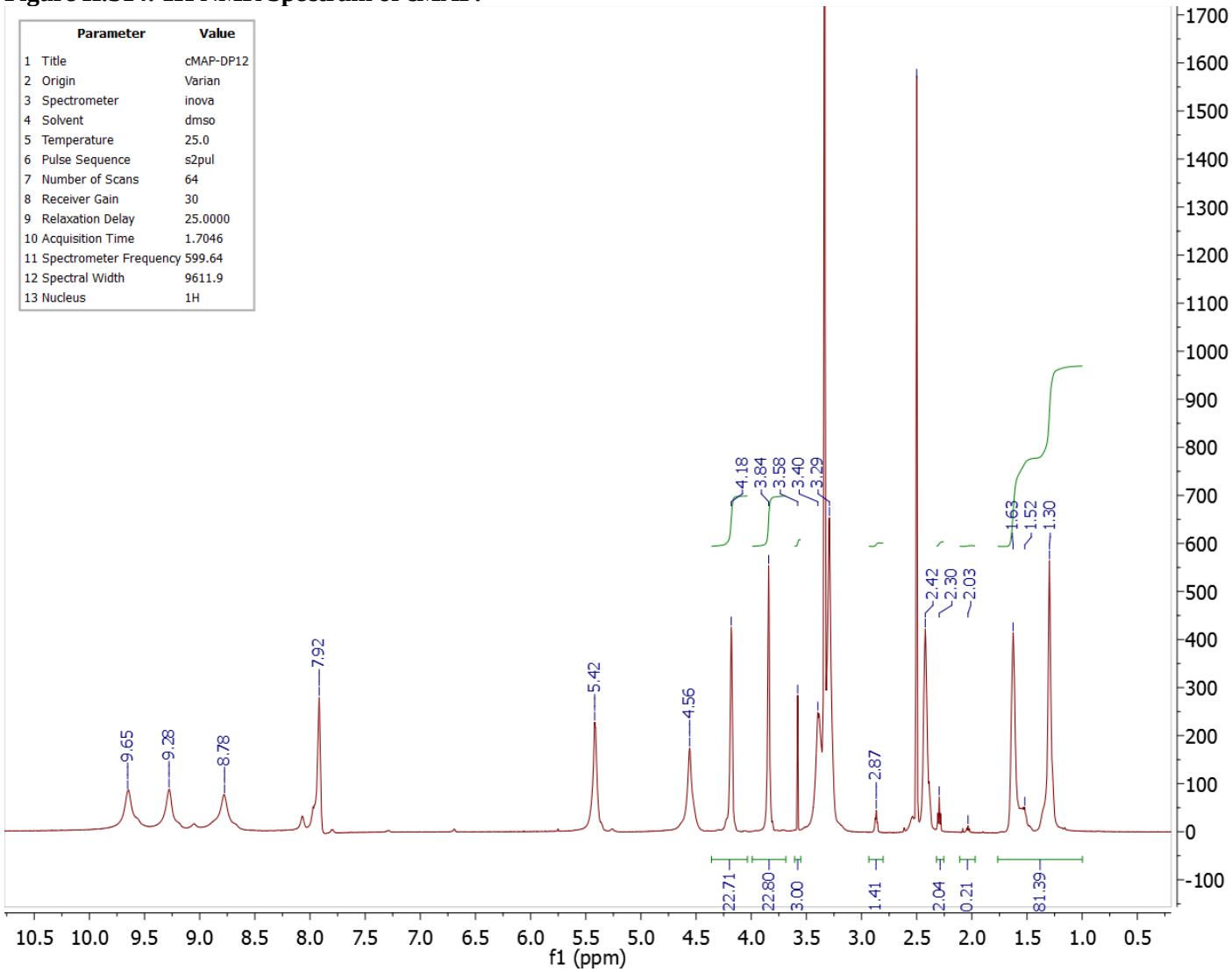

Table II.S3: 1H NMR peak assignments for cMAP.

	Originating Monomer	1H in DMSO Chemical Shift (ppm)
Amidine	Mucic acid and dimethyl suberimidate	9.65
Amidine	Mucic acid and dimethyl suberimidate	9.28
Amidine	Mucic acid and dimethyl suberimidate	8.78
Amide	Mucic acid and dimethyl suberimidate	7.92
Hydroxyl B	Mucic acid	5.42
Hydroxyl A	Mucic acid	4.56
Methyne B	Mucic acid	4.18
Methyne A	Mucic acid	3.84
Methoxy (end group)	Dimethyl suberimidate	3.58
Methylene B	Mucic acid	3.40
Methylene A	Mucic acid	3.29
Methylene A (end group)	Mucic acid	2.87
Methylene A	Dimethyl suberimidate	2.42
Methylene A (end group)	Dimethyl suberimidate	2.30
Methylene A (end group)	Dimethyl suberimidate – hydrolyzed to carboxylate	2.03
Methylene B	Dimethyl suberimidate	1.63
Methylene B (end group)	Dimethyl suberimidate	1.52
Methylene C	Dimethyl suberimidate	1.30

Figure II.S15: 13C NMR Spectrum of cMAP.

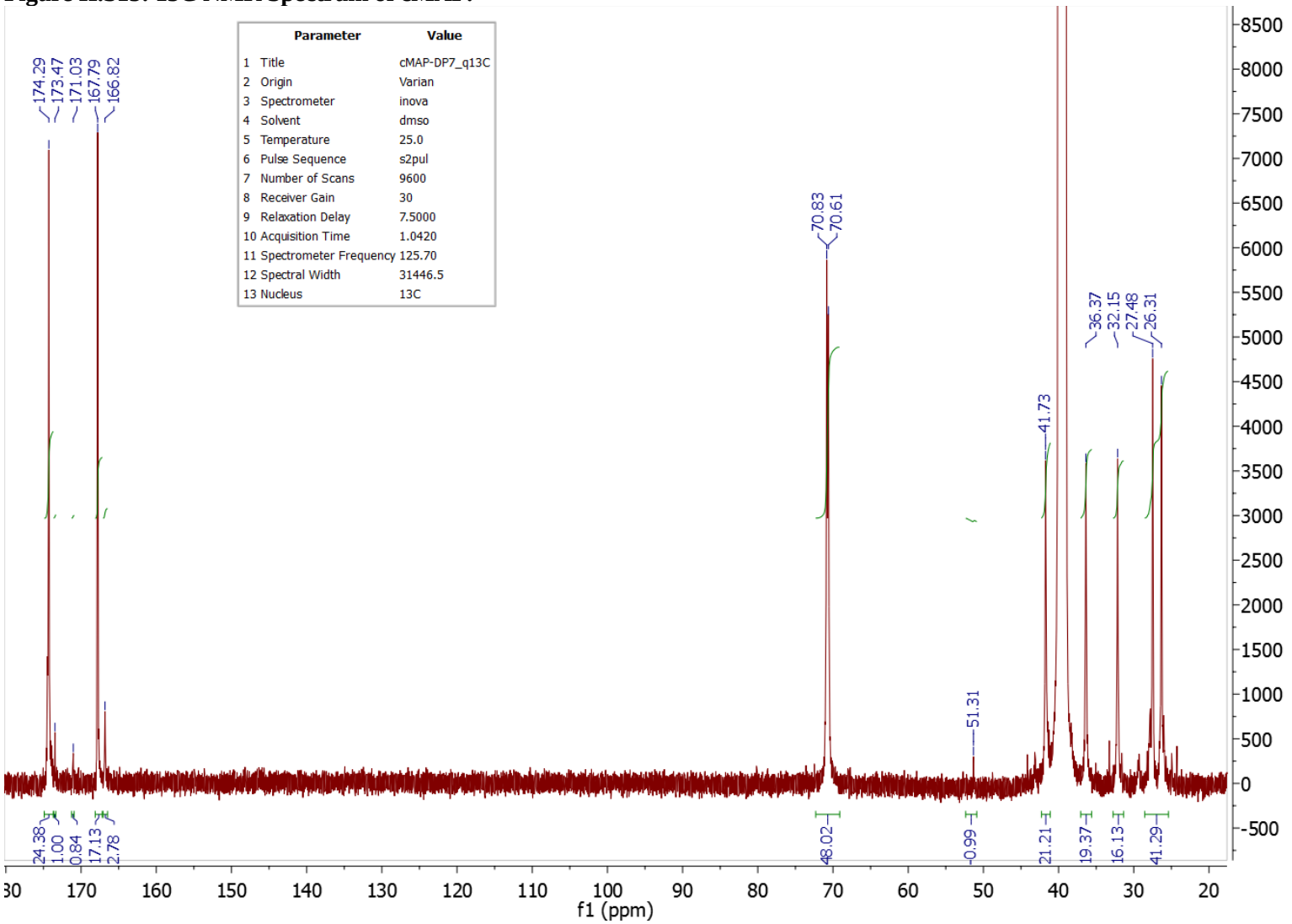

Table II.S4: 13C NMR peak assignments for cMAP.

	Originating Monomer	13C in DMSO Chemical Shift (ppm)
Amide Carbonyl	Mucic acid	174.29
Methoxy Carbonyl (end group)	Dimethyl suberimidate	173.47
Amide Carbonyl (end group)	Mucic acid	171.03
Amidine Carbonyl	Dimethyl suberimidate	167.79
		166.82
Methyne B	Mucic acid	70.83
Methyne A	Mucic acid	70.61
Methoxy (end group)	Dimethyl suberimidate	51.31
Methylene A	Mucic acid	41.73
Methylene B	Mucic acid	36.37
Methylene A	Dimethyl suberimidate	32.15
Methylene C	Dimethyl suberimidate	27.48
Methylene B	Dimethyl suberimidate	26.31
Methylene A (end group)	Dimethyl suberimidate – hydrolyzed to carboxylate	35.06
Methylene A (end group)	Dimethyl suberimidate	33.22
Methylene B (end group)	Dimethyl suberimidate	24.23

Figure II.S16: 1H-13C HSQC Spectrum of cMAP used to correlate proton and carbon chemical shifts.

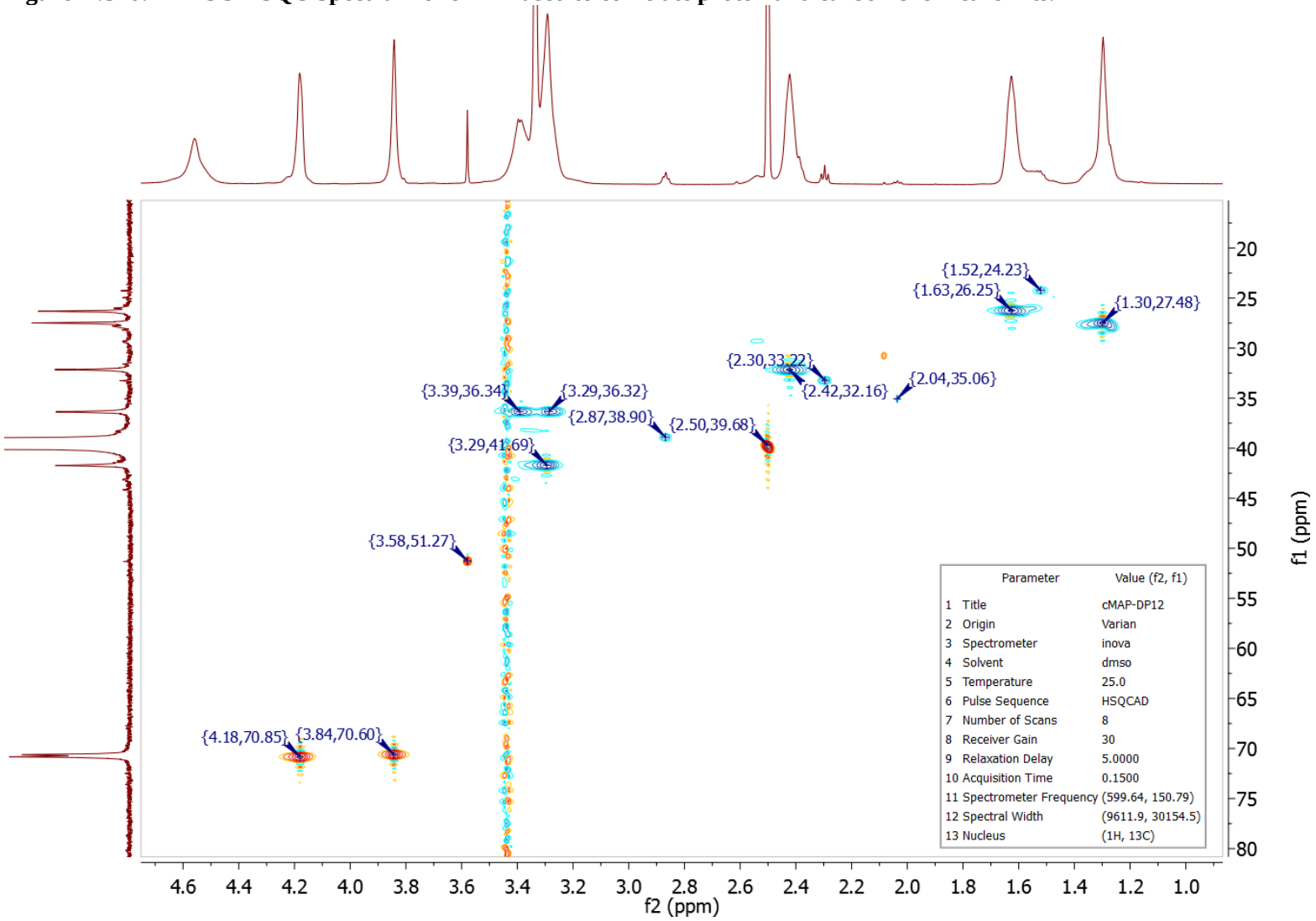

Table II.S5: 1H-13C HSQC NMR peak assignments for cMAP.

	Originating Monomer	1H Chemical Shift (ppm)	13C Chemical Shift (ppm)
Methyne B	Mucic acid	4.18	70.85
Methyne A	Mucic acid	3.84	70.60
Methoxy (end group)	Dimethyl suberimidate	3.58	51.27
Methylene A	Mucic acid	3.29	41.69
DMSO	(Solvent)	2.50	39.68
Methylene A (end group)	Mucic acid	2.87	38.90
Methylene B	Mucic acid	3.39	36.34
Methylene A	Mucic acid	3.29	36.32
Methylene A (end group)	Dimethyl suberimidate (hydrolyzed to carboxylate)	2.04	35.06
Methylene A (end group)	Dimethyl suberimidate	2.30	33.22
Methylene A	Dimethyl suberimidate	2.42	32.16
Methylene C	Dimethyl suberimidate	1.30	27.48
Methylene B	Dimethyl suberimidate	1.63	26.25
Methylene B (end group)	Dimethyl suberimidate	1.52	24.23

Figure II.S17: 1H-1H COSY Spectrum of cMAP used to correlate protons to nearby protons more than one bond away.

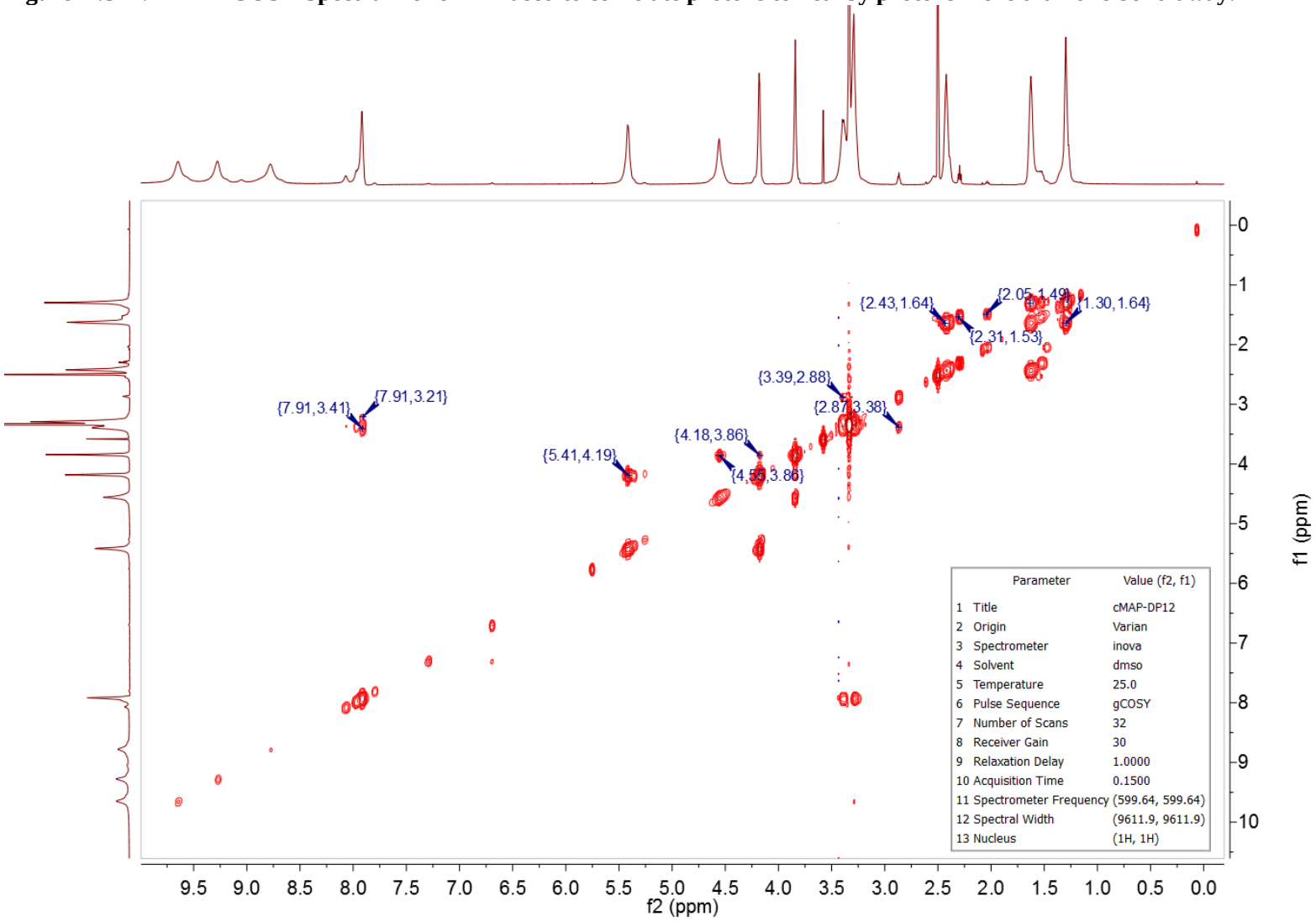

Table II.S6: 1H-1H COSY NMR peak assignments for cMAP.

Correlation		1H Chemical Shift (ppm)	1H Chemical Shift (ppm)
Methyne B	Hydroxyl B	4.19	5.41
Methyne B	Methyne A	3.86	4.18
Methyne A	Hydroxyl A	3.86	4.55
Methylene B (mucic acid)	Amide	3.41	7.91
Methylene B (mucic acid)	Methylene A (end group, mucic acid)	3.38	2.87
Methylene A (mucic acid)	Amide	3.21	7.91
Methylene A (end group, mucic acid)	Methylene B (mucic acid)	2.88	3.39
Methylene B (DMS)	Methylene A (DMS)	1.64	2.43
Methylene B (DMS)	Methylene C (DMS)	1.64	1.30
Methylene B (end group, DMS)	Methylene A (end group, DMS)	1.53	2.31
Methylene B (end group, DMS)	Methylene A (end group, DMS hydrolyzed to carboxylate)	1.49	2.05
Methylene C (DMS)	Methylene B (DMS)	1.31	1.63

Figure II.S18: 1H-13C HMBC Spectrum of cMAP used to correlate protons to carbons more than one bond away.

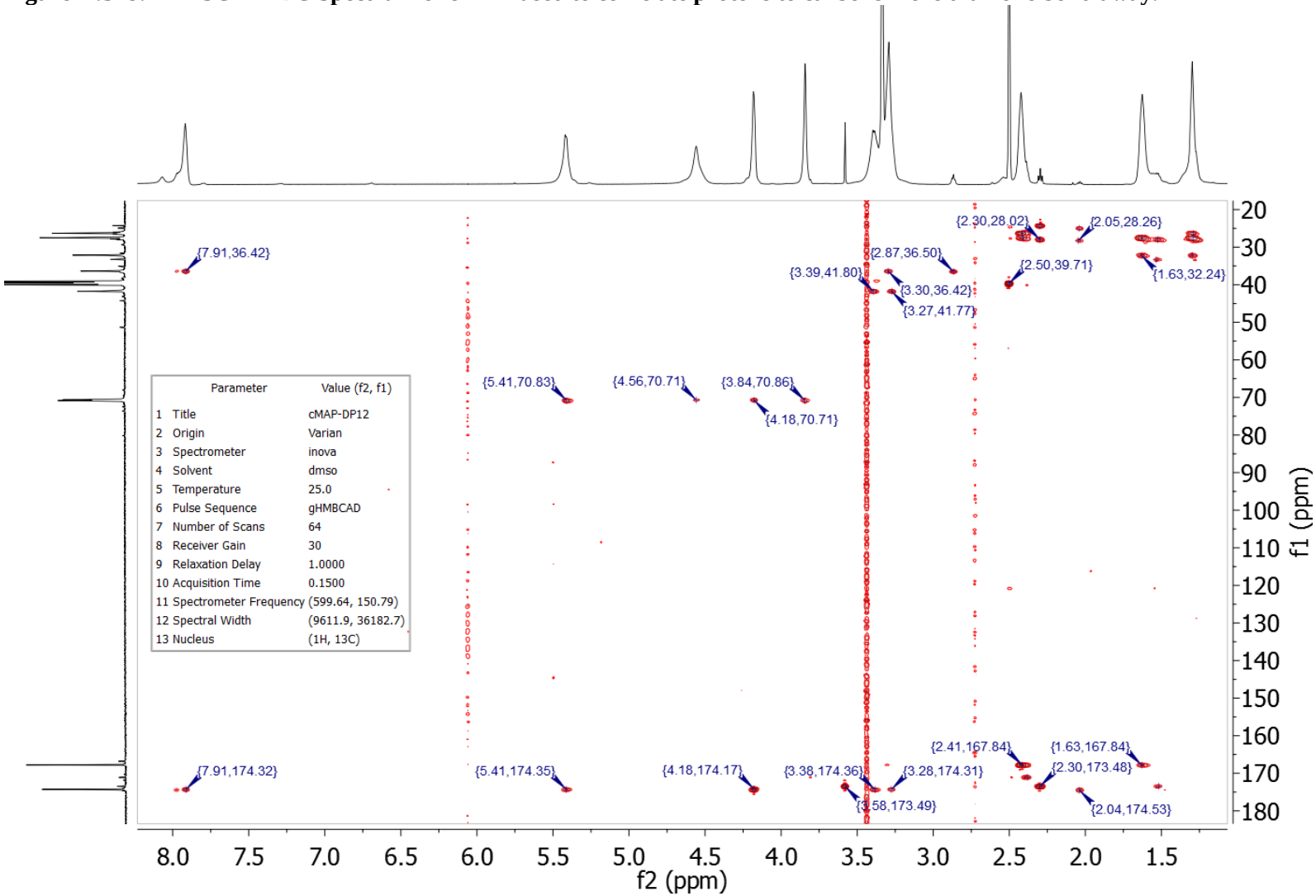

Table II.S7: 1H-13C HMBC NMR peak assignments for cMAP.

Correlation		13C Chemical Shift (ppm)	1H Chemical Shift (ppm)
Carbonyl Carbon (DMS hydrolyzed to carboxylate)	Methylene A (end group, DMS hydrolyzed to carboxylate)	174.53	2.04
Amide Carbonyl (mucic acid)	Methylene B (mucic acid)	174.36	3.38
Amide Carbonyl (mucic acid)	Hydroxyl B (mucic acid)	174.35	5.41
Amide Carbonyl (mucic acid)	Amide proton (mucic acid)	174.32	7.91
Amide Carbonyl (mucic acid)	Methylene A (mucic acid)	174.31	3.28
Amide Carbonyl (mucic acid)	Methyne B (mucic acid)	174.17	4.18
Methyl ester carbonyl (DMS)	Methoxy (DMS)	173.49	3.58
Methyl ester carbonyl (DMS)	Methylene A (end group, DMS)	173.48	2.30
Methyl ester carbonyl (DMS)	Methylene B (end group, DMS)	173.44	1.52
Amide Carbonyl (end group)	Methylene B (end group, mucic acid)	171.09	2.38
Amidine Carbonyl	Methylene A (DMS)	167.84	2.41
Amidine Carbonyl	Methylene B (DMS)	167.84	1.63
Methyne B (mucic acid)	Methyne A (mucic acid)	70.86	3.84
Methyne B (mucic acid)	Hydroxyl B (mucic acid)	70.83	5.41
Methyne A (mucic acid)	Methyne B (mucic acid)	70.71	4.18
Methyne A (mucic acid)	Hydroxyl A (mucic acid)	70.71	4.56
Methylene A (mucic acid)	Methylene B (mucic acid)	41.80	3.39
Methylene A (mucic acid)	Methylene A (mucic acid)	41.77	3.27
DMSO	DMSO	39.71	2.50
Methylene B (mucic acid)	Methylene A (end group, mucic acid)	36.50	2.87
Methylene B (mucic acid)	Amide Proton (mucic acid)	36.42	7.91
Methylene B (mucic acid)	Methylene A (mucic acid)	36.42	3.30
Methylene A (end group, DMS)	Methylene B (end group, DMS)	33.33	1.53
Methylene A (DMS)	Methylene B (DMS)	32.24	1.63
Methylene A (DMS)	Methylene C (DMS)	32.24	1.30
Methylene B (end group, DMS)	Methylene A (end group, DMS hydrolyzed to carboxylate)	28.26	2.05
Methylene B (end group, DMS)	Methylene A (end group, DMS)	28.02	2.30
Methylene B (end group, DMS)	Methylene B (end group, DMS)	28.00	1.52
Methylene C (DMS)	Methylene C (DMS)	27.61	1.29
Methylene C (DMS)	Methylene A (DMS)	27.61	2.41
Methylene C (DMS)	Methylene B (DMS)	27.57	1.63
Methylene B (DMS)	Methylene C (DMS)	26.41	1.29
Methylene B (DMS)	Methylene A (DMS)	26.34	2.42
Methylene C (end group, DMS hydrolyzed to carboxylate)	Methylene A (end group, DMS hydrolyzed to carboxylate)	25.00	2.04
Methylene B (end group, DMS)	Methylene A (end group, DMS)	24.33	2.30

Figure II.S19: 1H stacked DOSY Spectrum of cMAP showing that all the peaks on the cMAP polymer, including the small end group peaks, diffuse at the same rate. H_2O and DMSO diffuse much faster as shown by their quick disappearance after the first spectrum (bottom).

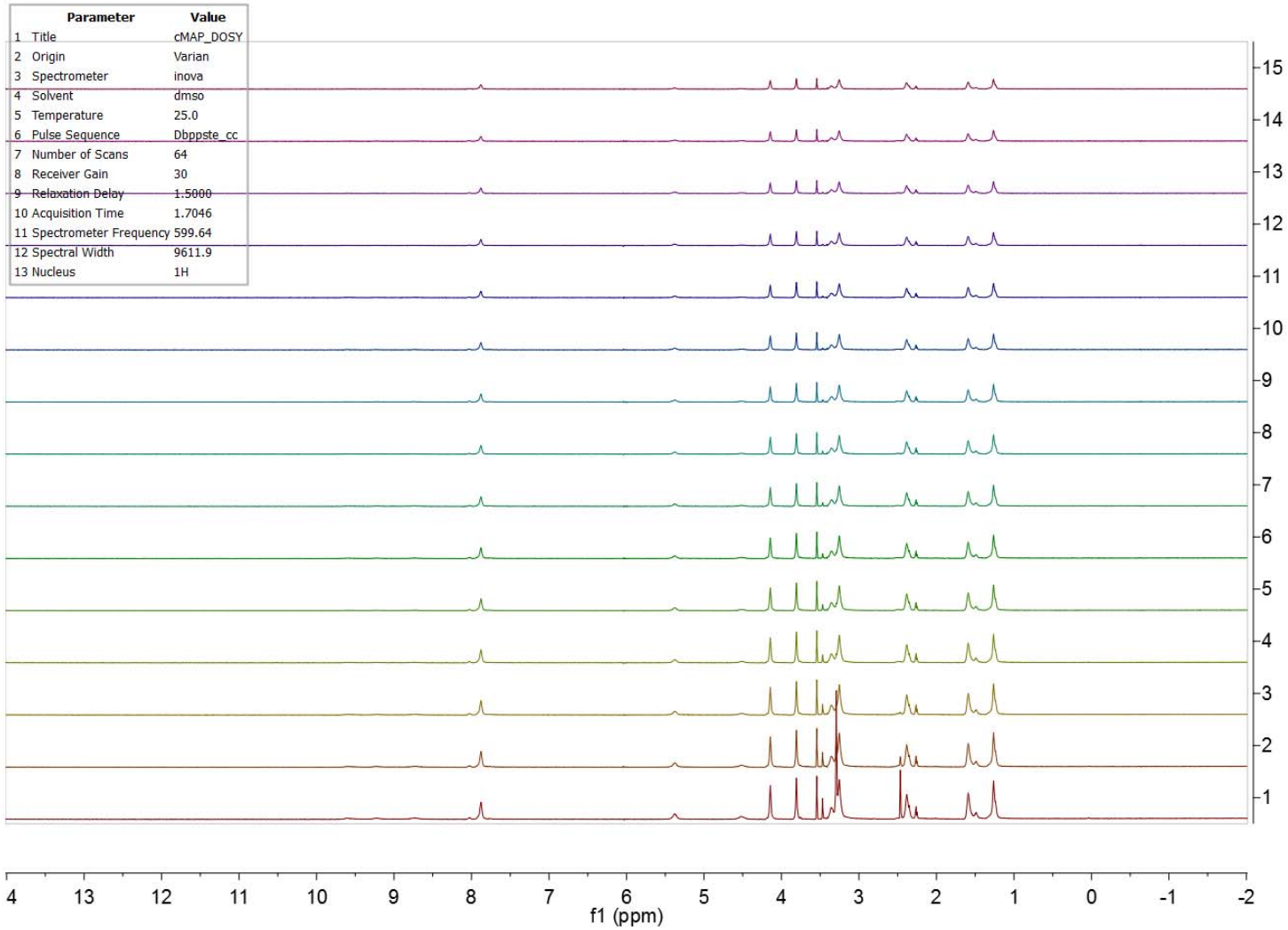

Figure II.S20: 1H transformed DOSY Spectrum of cMAP showing that all the peaks on the cMAP polymer, including the small end group peaks, diffuse at the same rate. H_2O and DMSO diffuse much faster.

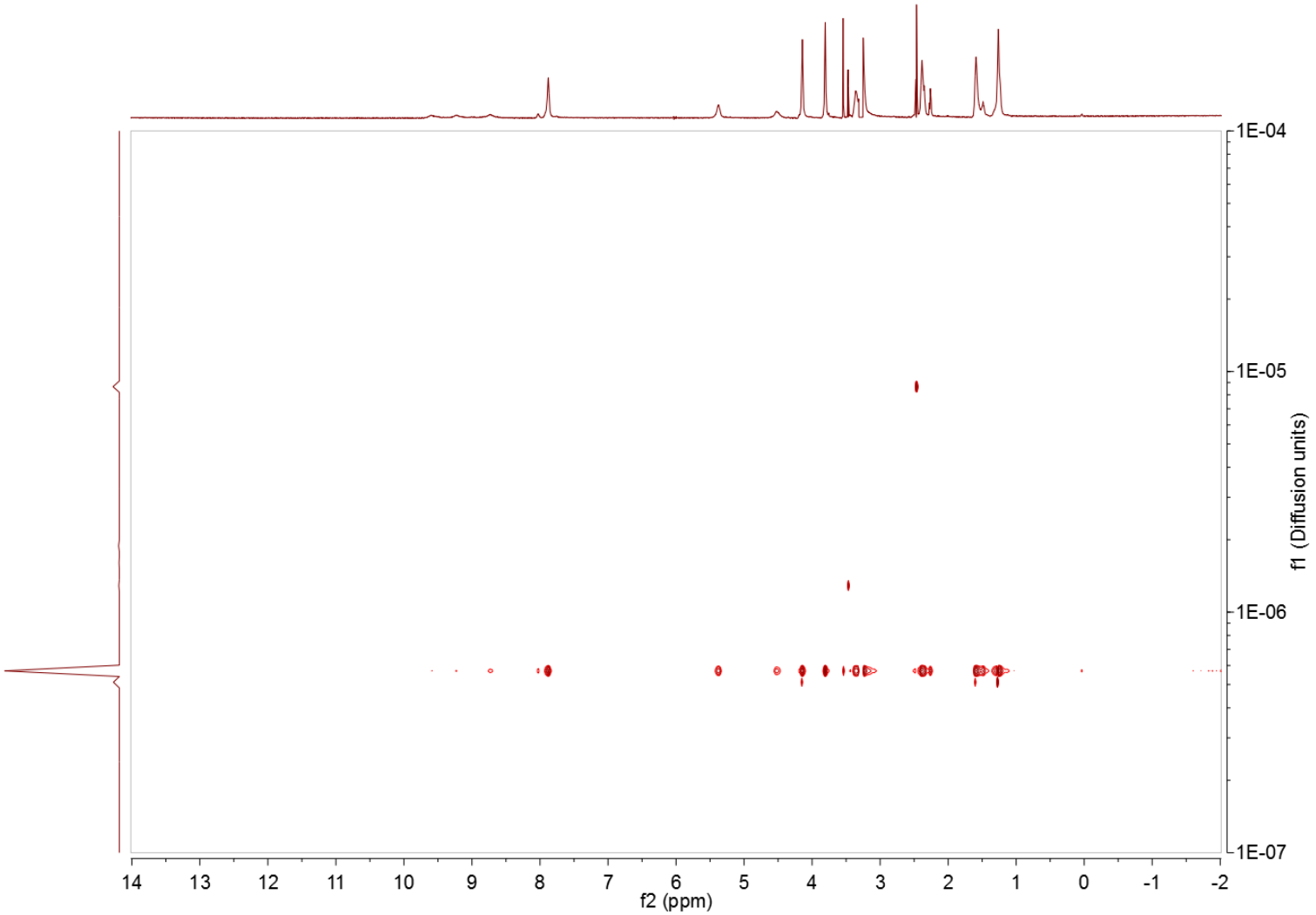

4. cMAP: End group ratios

Table II.S8: Ratios of amine: methoxy: carboxylate end groups in 8 batches of cMAP by comparing NMR integrations.

Batch	% amine	% methoxy	% carboxylate
11	52.52	33.96	13.52
12	38.45	54.15	7.40
13	48.58	45.89	5.53
14	47.07	45.71	7.22
15	47.75	51.17	1.08
16	55.58	37.14	7.28
17	63.22	29.92	6.86
18	38.76	39.50	21.75
Average	48.99 ± 2.93	42.18 ± 2.99	6.22 ± 2.20

5. cMAP-PEG copolymer: NMR spectra

Figure II.S21: 1H NMR of cMAP-PEG5k copolymer. The large resonance at 3.5 ppm corresponds to the PEG block.

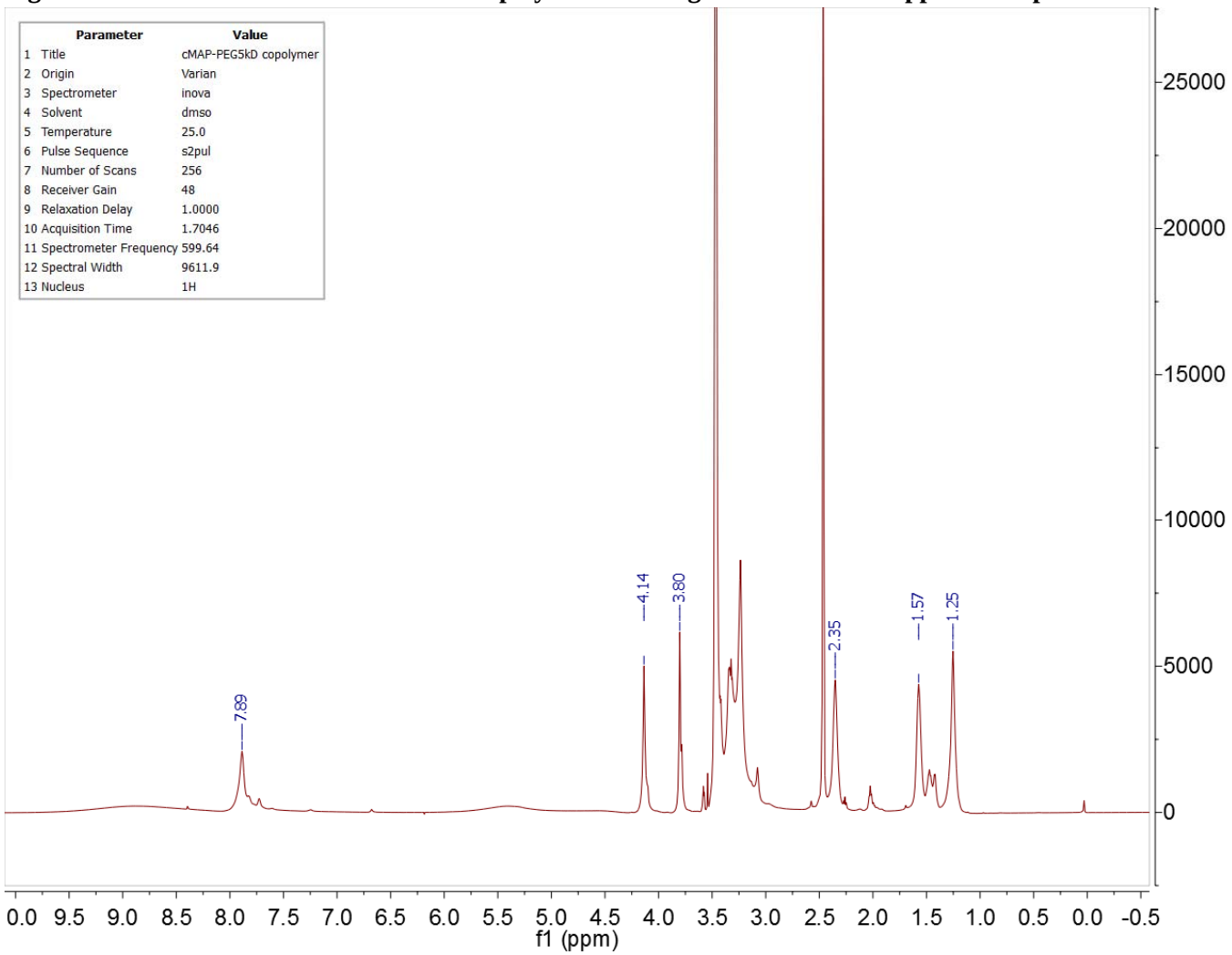

Figure II.S22: 1H-13C HSQC spectrum of cMAP-PEG5k copolymer.

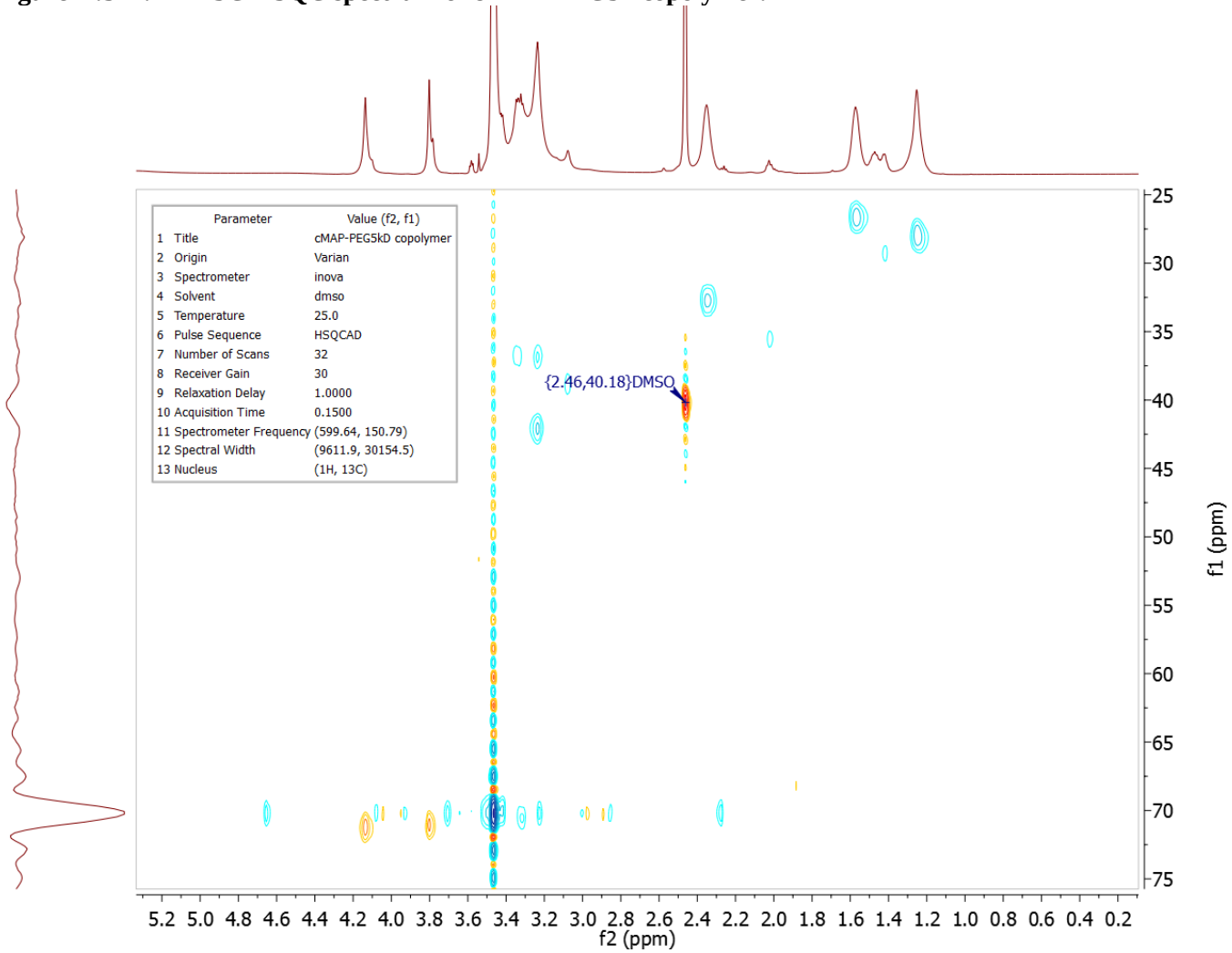

Figure II.S23: 1H DOSY transformed spectrum of cMAP-PEG5k copolymer.

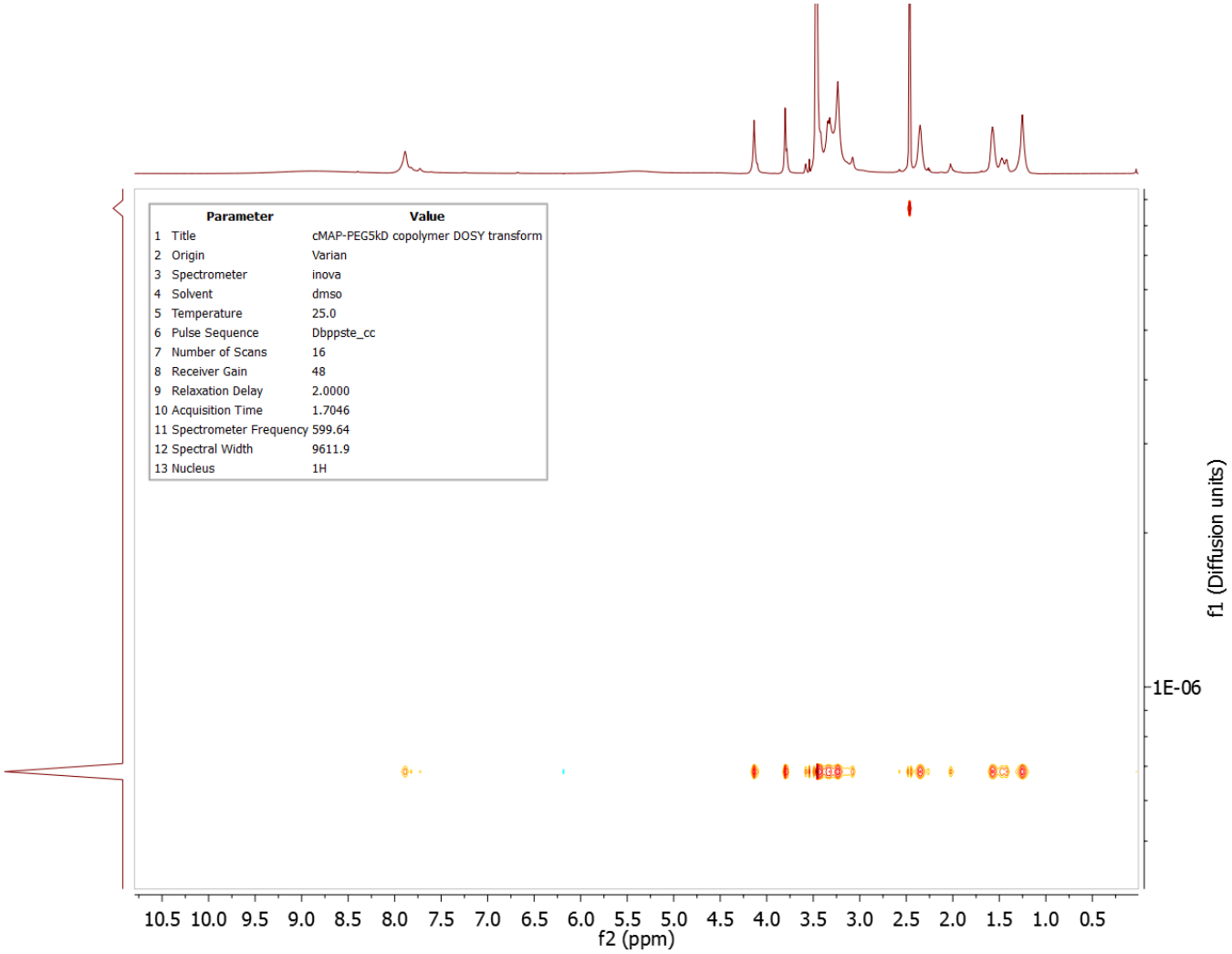

Figure II.S24: 1H NMR of cMAP-PEG3.4k copolymer.

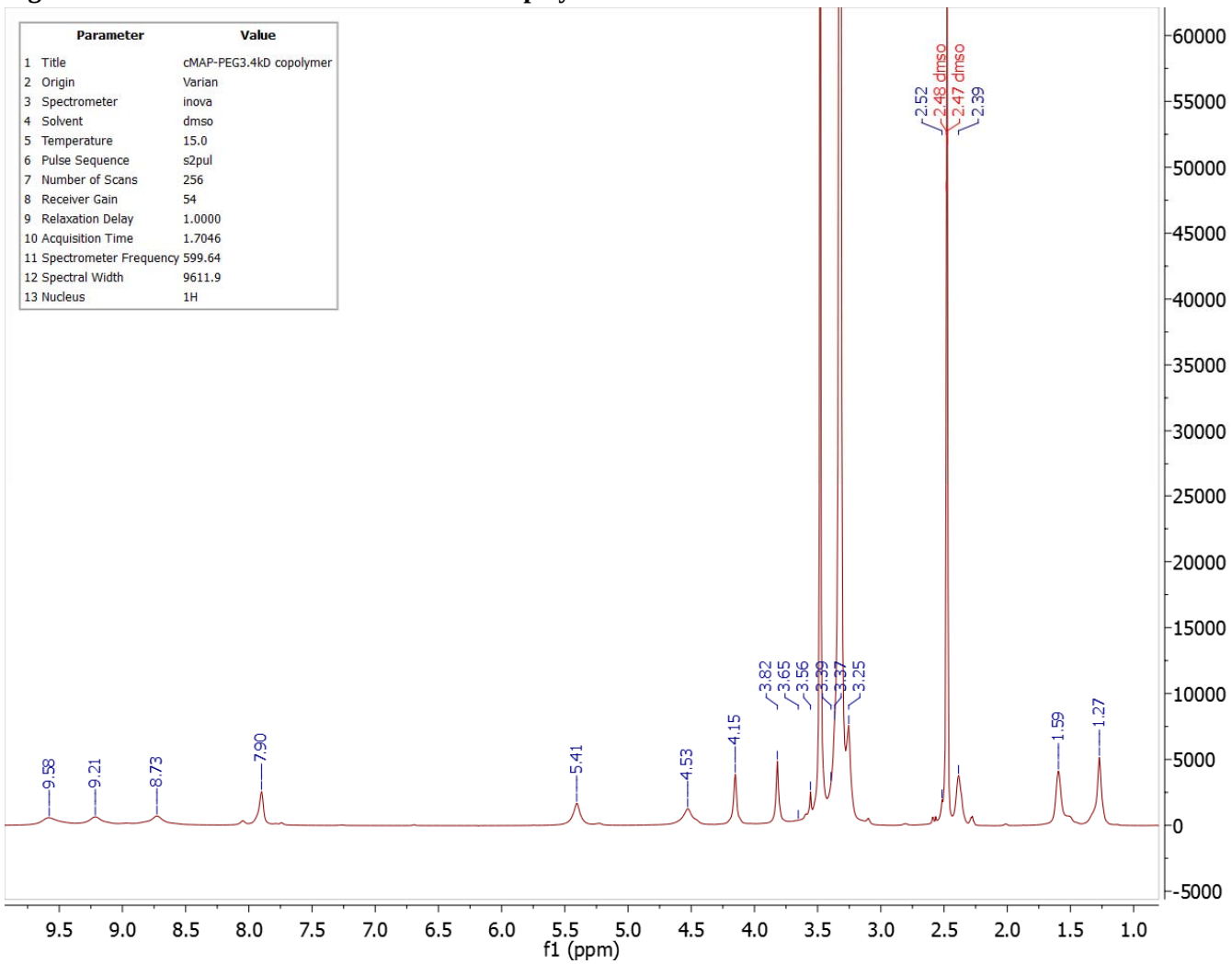

Figure II.S25: 13C NMR of cMAP-PEG3.4k copolymer.

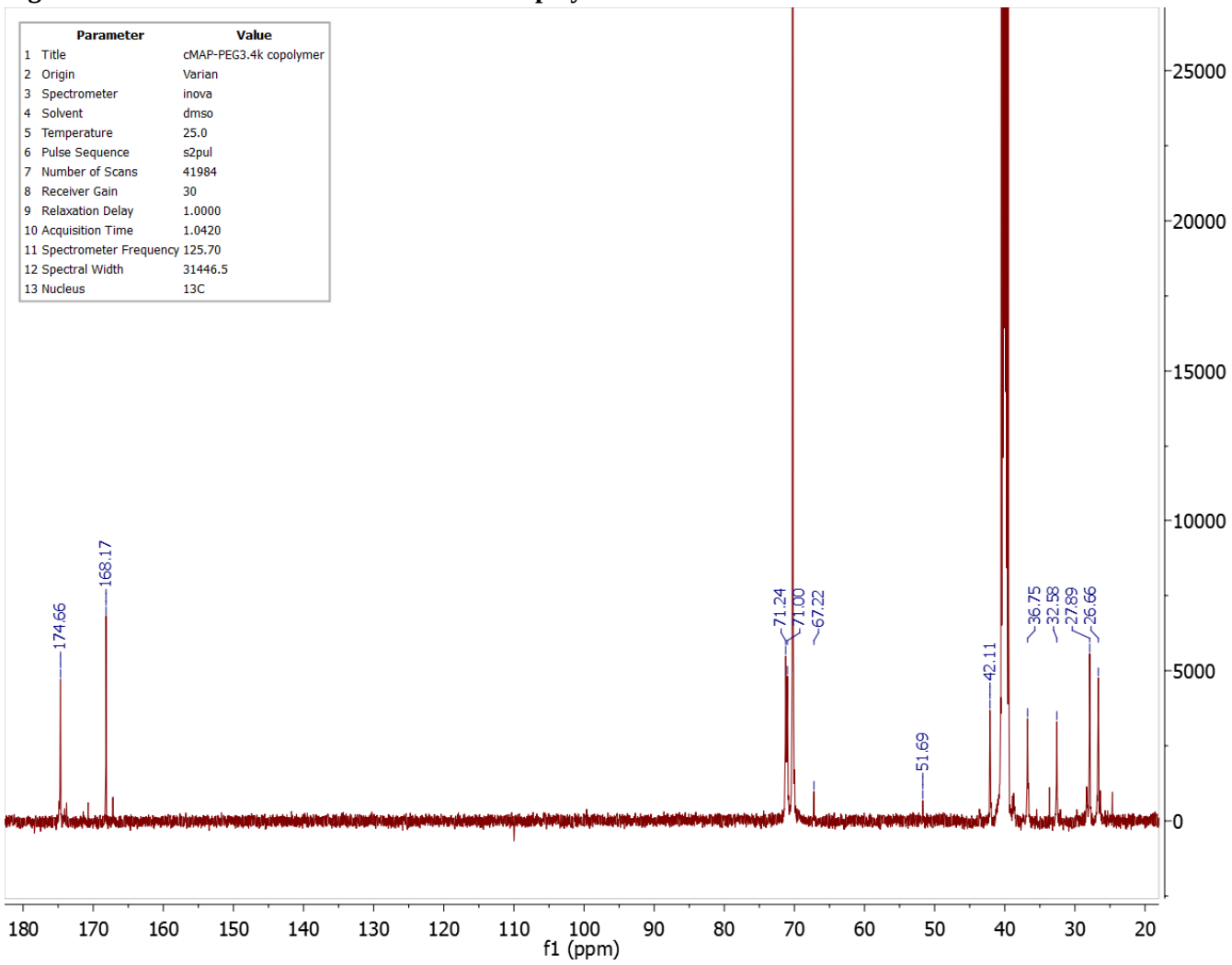

Figure II.S26: 1H-13C HSQC spectrum of cMAP-PEG3.4k copolymer.

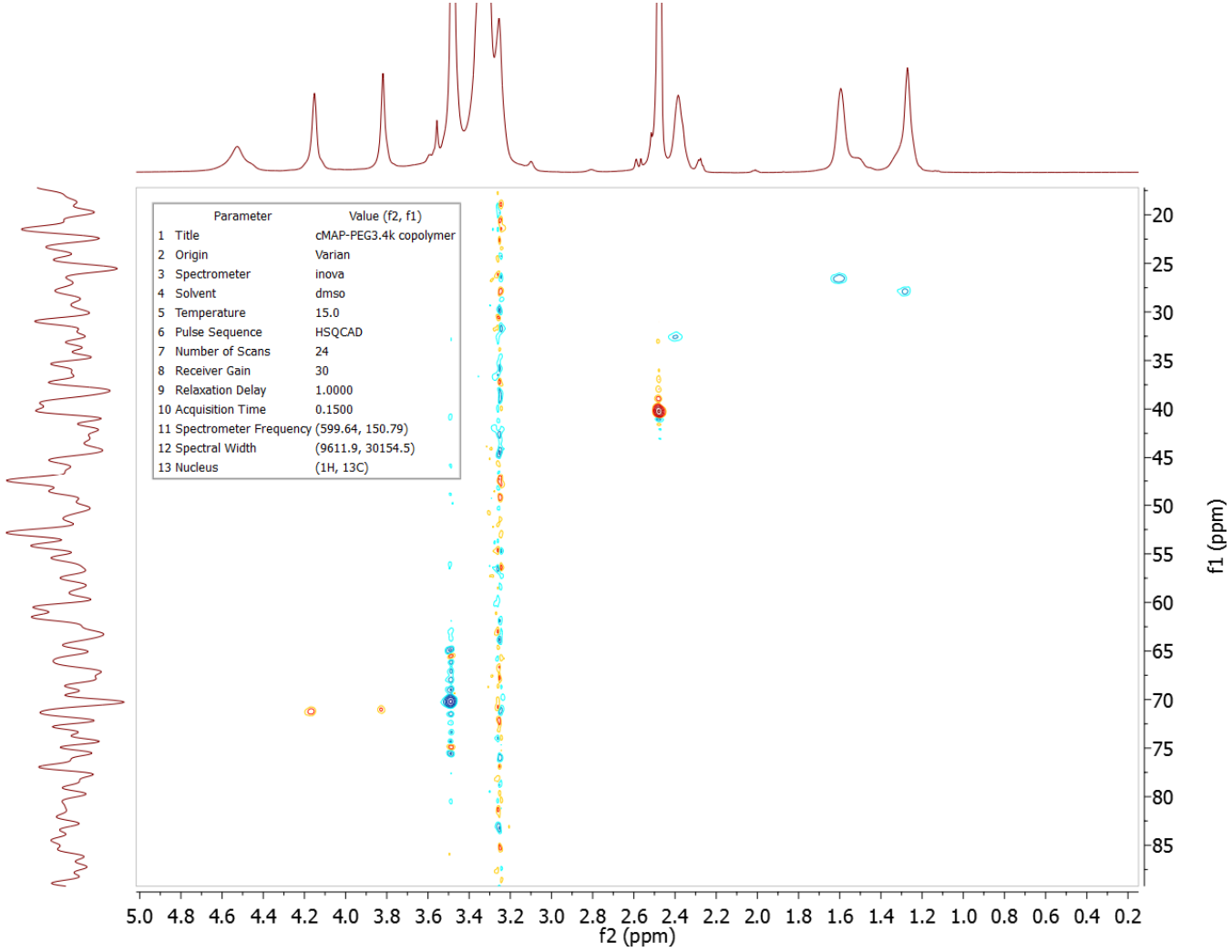

Figure II.S27: 1H DOSY transformed spectrum of cMAP-PEG3.4k copolymer.

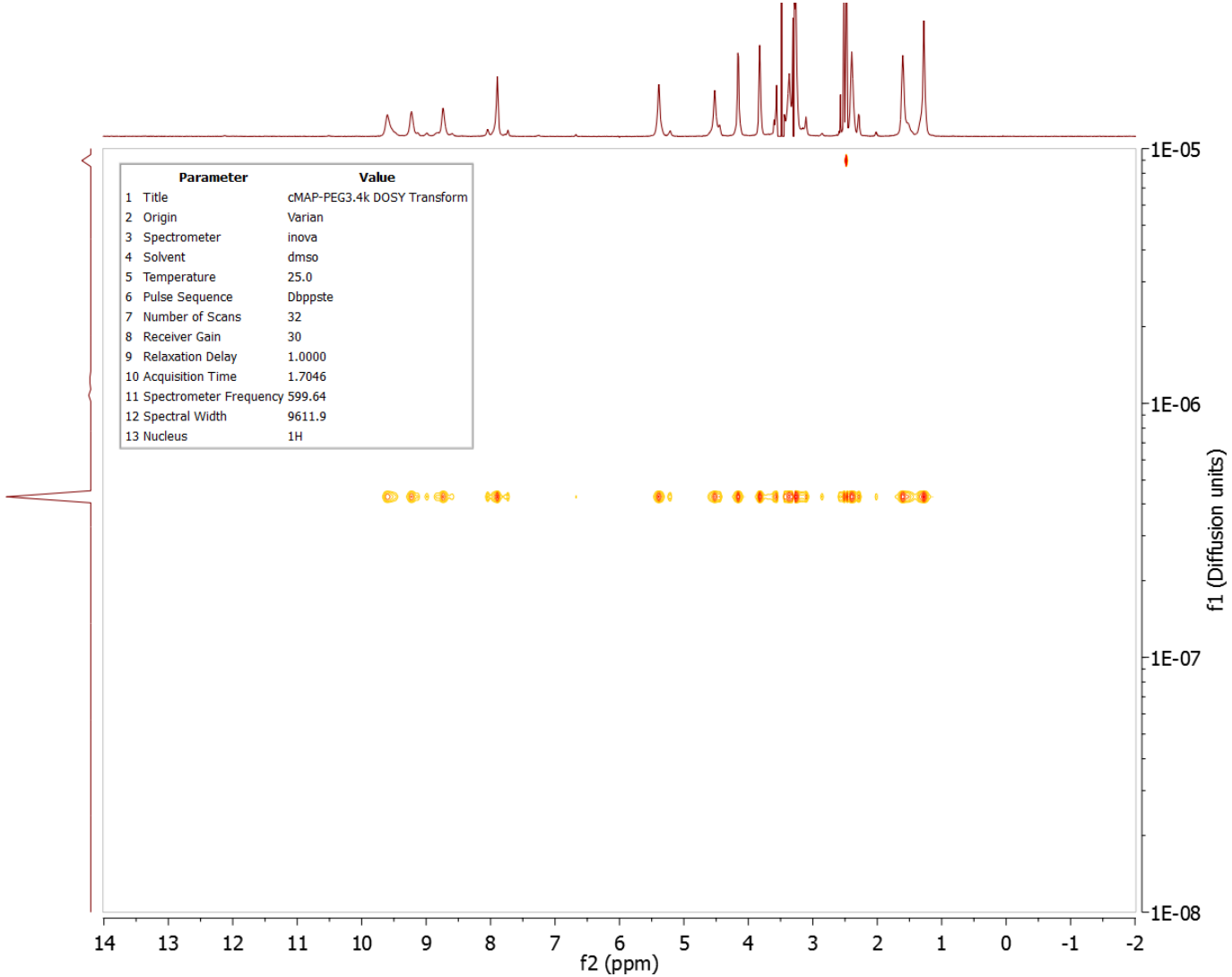

6. cMAP-PEG copolymer fractionation yields

A reaction was started with 50 mg of cMAP and 16.5 mg di-SPA-PEG3.4k. After stirring for 24 hours, the reaction was diluted in water and filtered through sequentially smaller molecular weight cutoff (MWCO) Amicon centrifugal spin filters. Some material loss does occur onto the filter membrane and during transfer steps, but the retained material on each of these filters after lyophilization to dryness is shown in the table below. A significant amount of high molecular weight cMAP-PEG3.4k copolymer is formed in the synthesis due to the presence of diamine end groups on cMAP.

Table II.S9: Retained mass on each MWCO filter after fractionating crude cMAP-PEG3.4k copolymer.

MWCO (kD)	Mass (mg)	Comment
100	9.5	High molecular weight cMAP-PEG copolymer
50	3.4	High molecular weight cMAP-PEG copolymer
30	5	High molecular weight cMAP-PEG copolymer
20	12.3	
10	10.6	**Pure cMAP-PEG-cMAP triblock**
3	13.2	Unreacted cMAP, excess PEG
Total	54	

Similarly, a reaction was started with 50 mg of cMAP and 22.3 mg di-SVA-PEG5k. After stirring for 24 hours, the reaction was diluted in water and filtered through sequentially smaller molecular weight cutoff (MWCO) Amicon centrifugal spin filters. Some material loss does occur onto the filter membrane and during transfer steps, but the retained material on each of these filters after lyophilization to dryness is shown in the table below. A significant amount of higher molecular weight cMAP-PEG5k copolymer is formed in this synthesis similar to the analogous reaction above.

Table II.S10: Retained mass on each MWCO filter after fractionating crude cMAP-PEG5k copolymer.

MWCO (kD)	Mass (mg)	Comment
30	18.3	High molecular weight cMAP-PEG copolymer
20	20.8	
10	12	**Pure cMAP-PEG-cMAP triblock** + cMAP-PEG diblock
Total	51.1	

7. mPEG-cMAP-PEGm NMR spectra

Figure II.S28: 1H NMR of mPEG5k-cMAP-PEG5km. The resonance at 3.5 ppm corresponds to the PEG blocks, and the resonance at 3.2 ppm is that of the methoxy end group on PEGm.

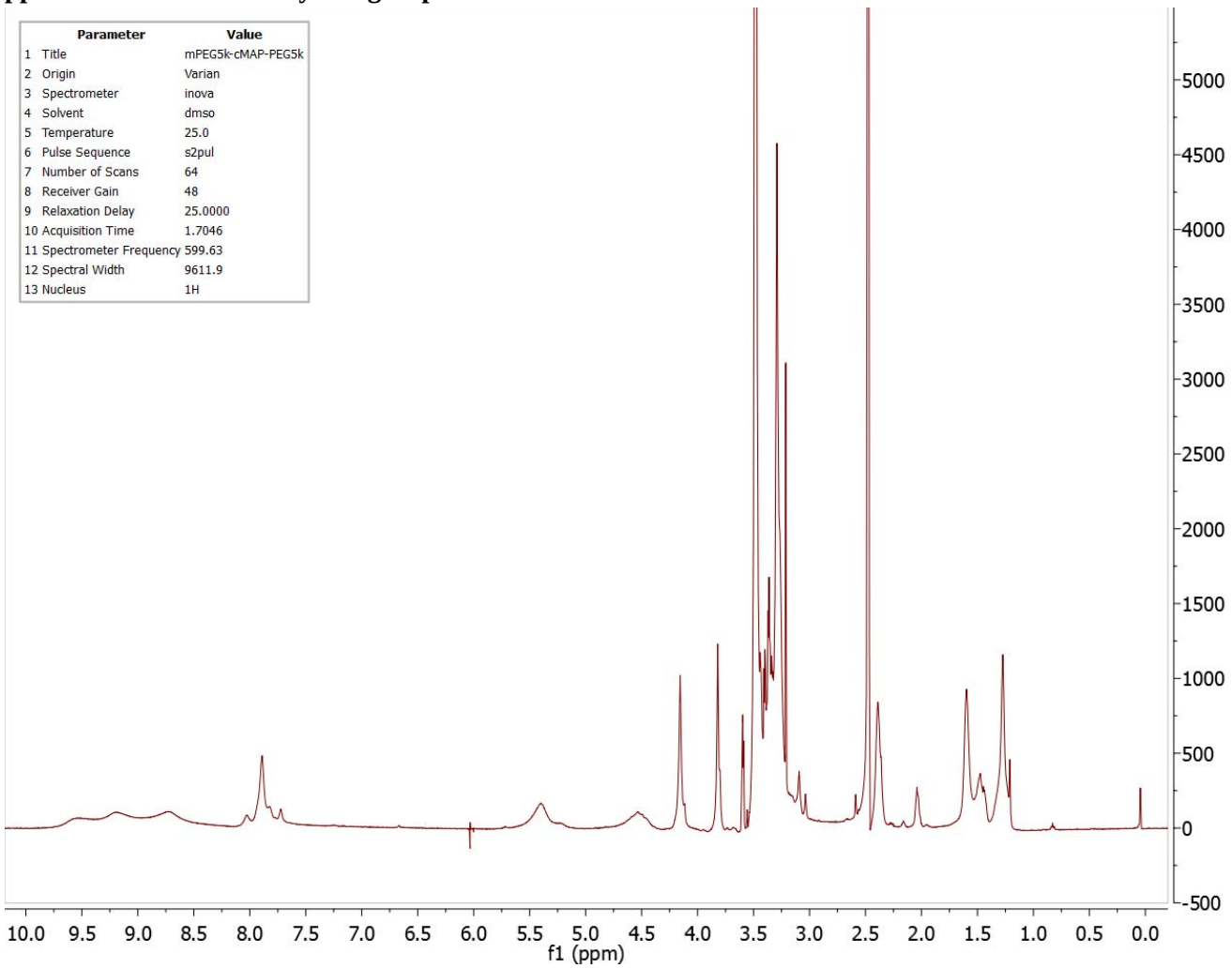

Figure II.S29: 1H-13C HSQC of mPEG5k-cMAP-PEG5km.

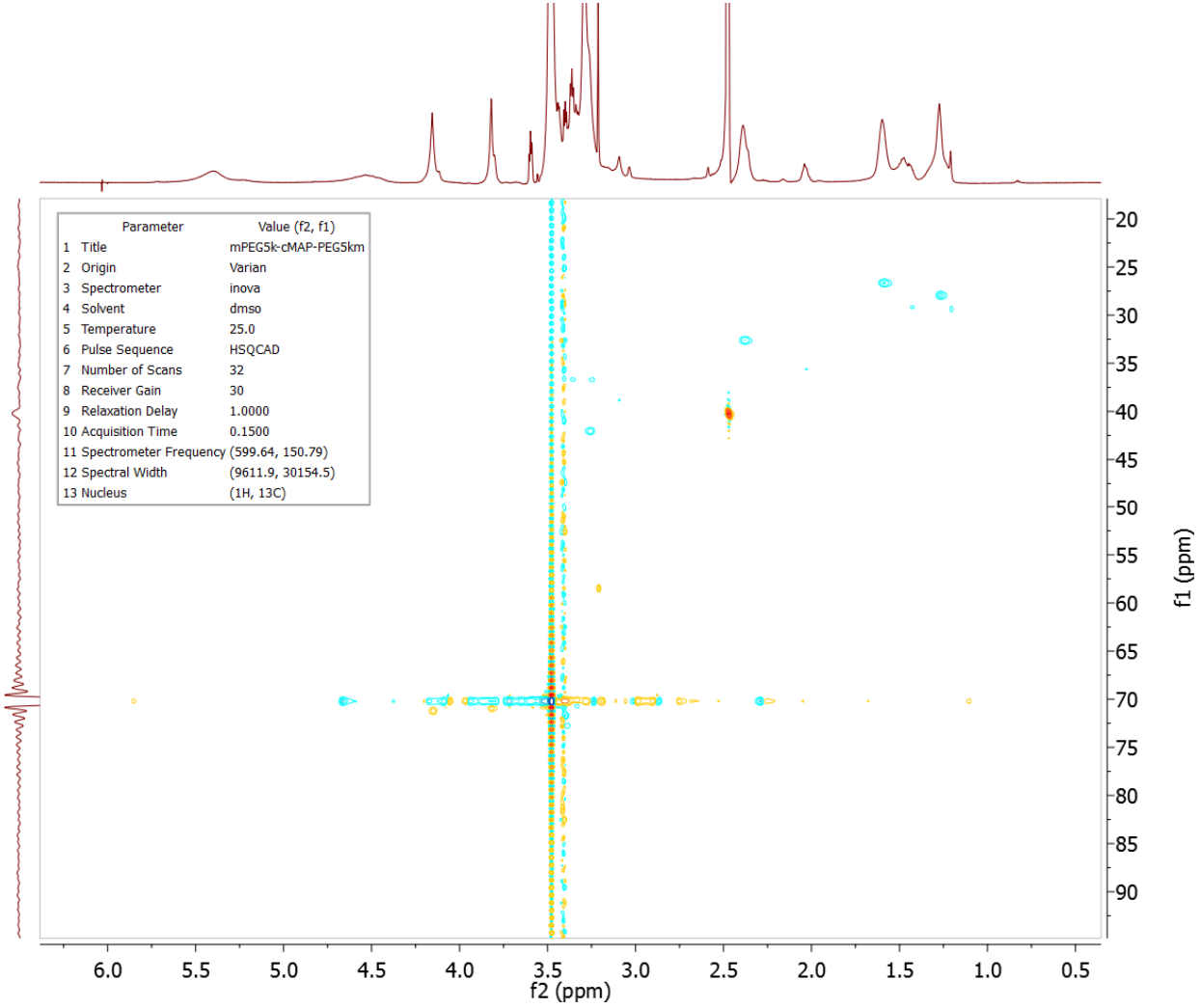

Figure II.S30: 1H DOSY transform of mPEG5k-cMAP-PEG5km.

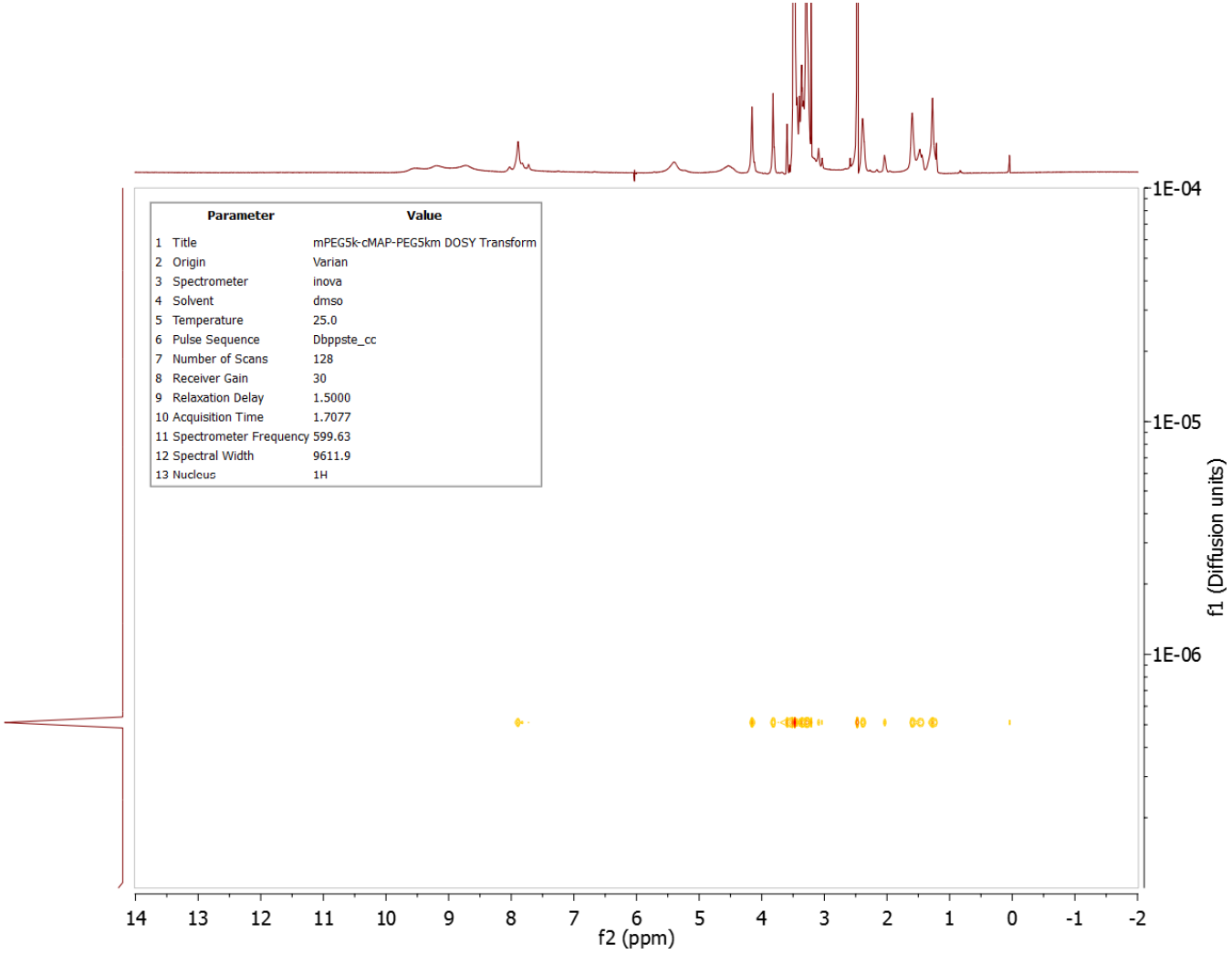

Figure II.S31: 1H NMR of mPEG2k-cMAP-PEG2km.

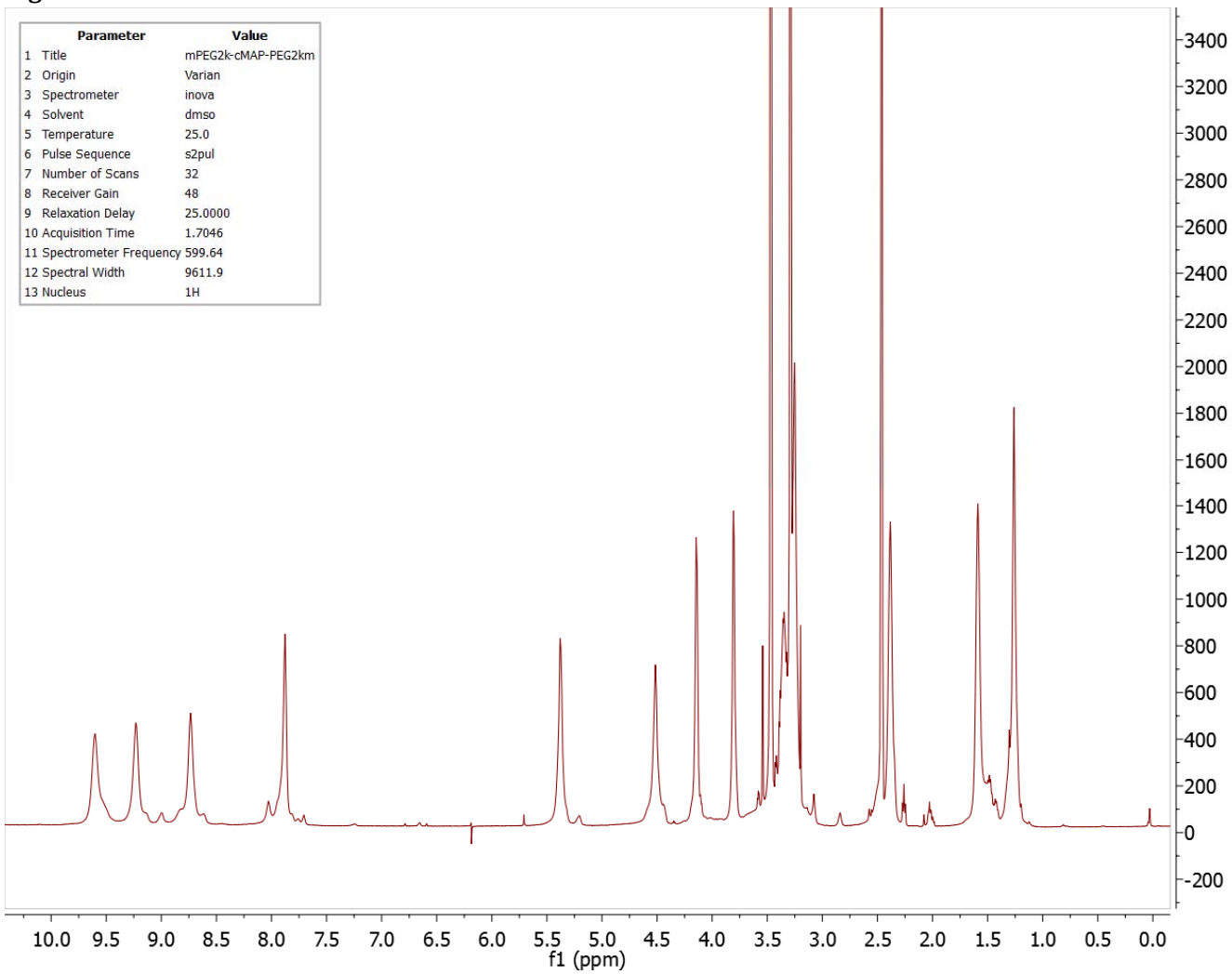

Figure II.S32: 1H-13C HSQC of mPEG2k-cMAP-PEG2km.

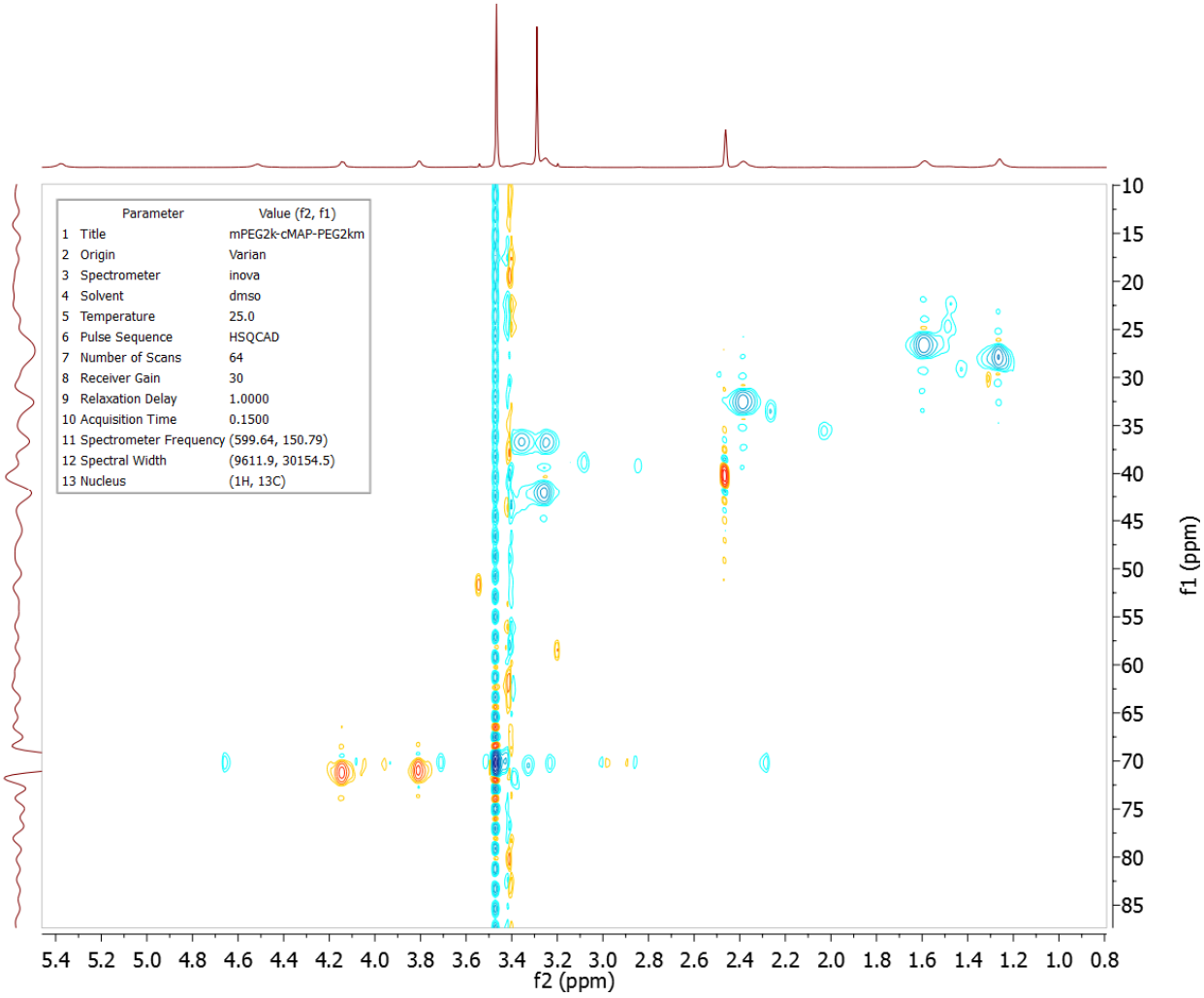

Figure II.S33: 1H DOSY transform of mPEG2k-cMAP-PEG2km.

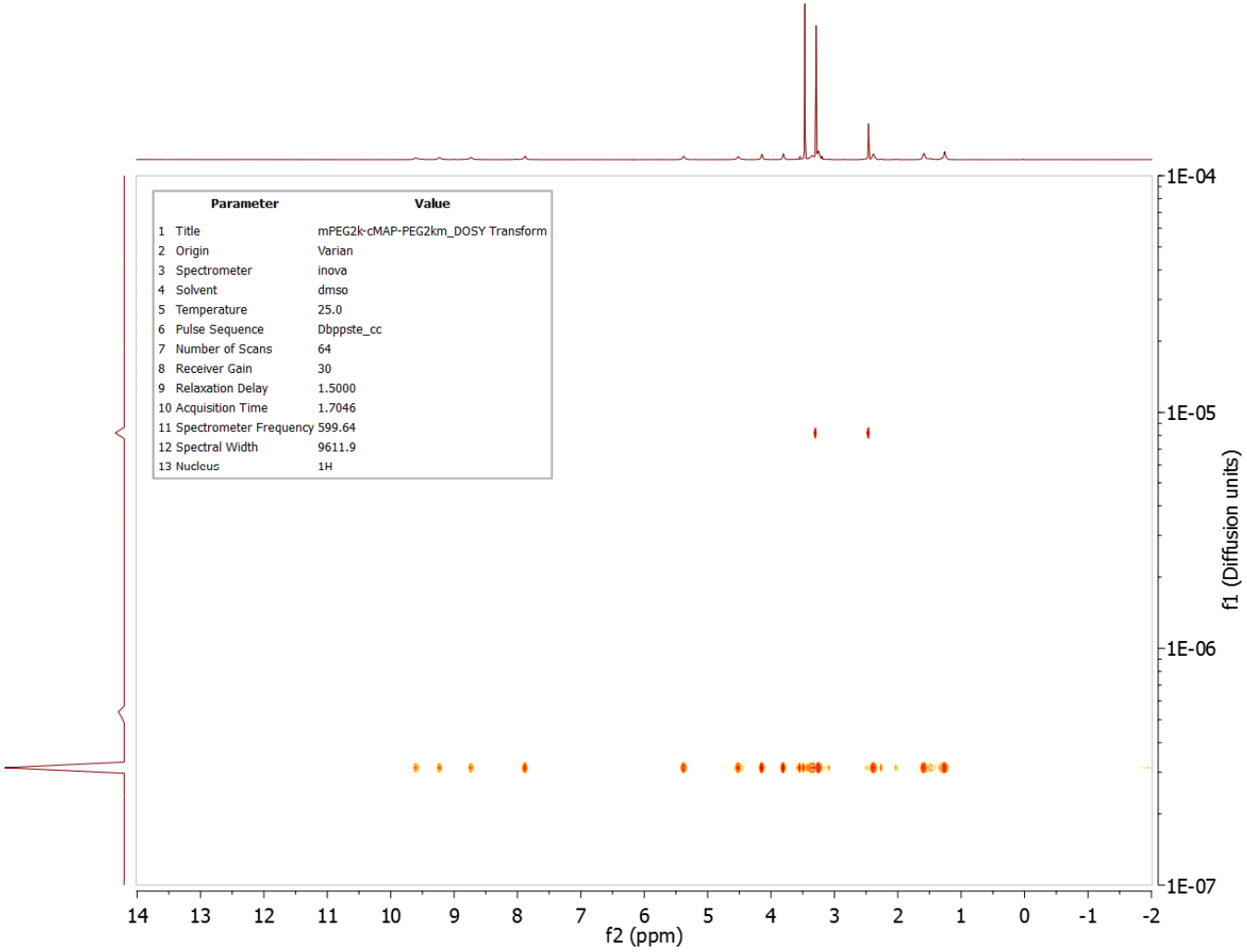

8. 5-nitrophenylboronic acid-PEGm NMR and MALDI spectra

Figure II.S34: 1H NMR of 5-nPBA-PEGm.

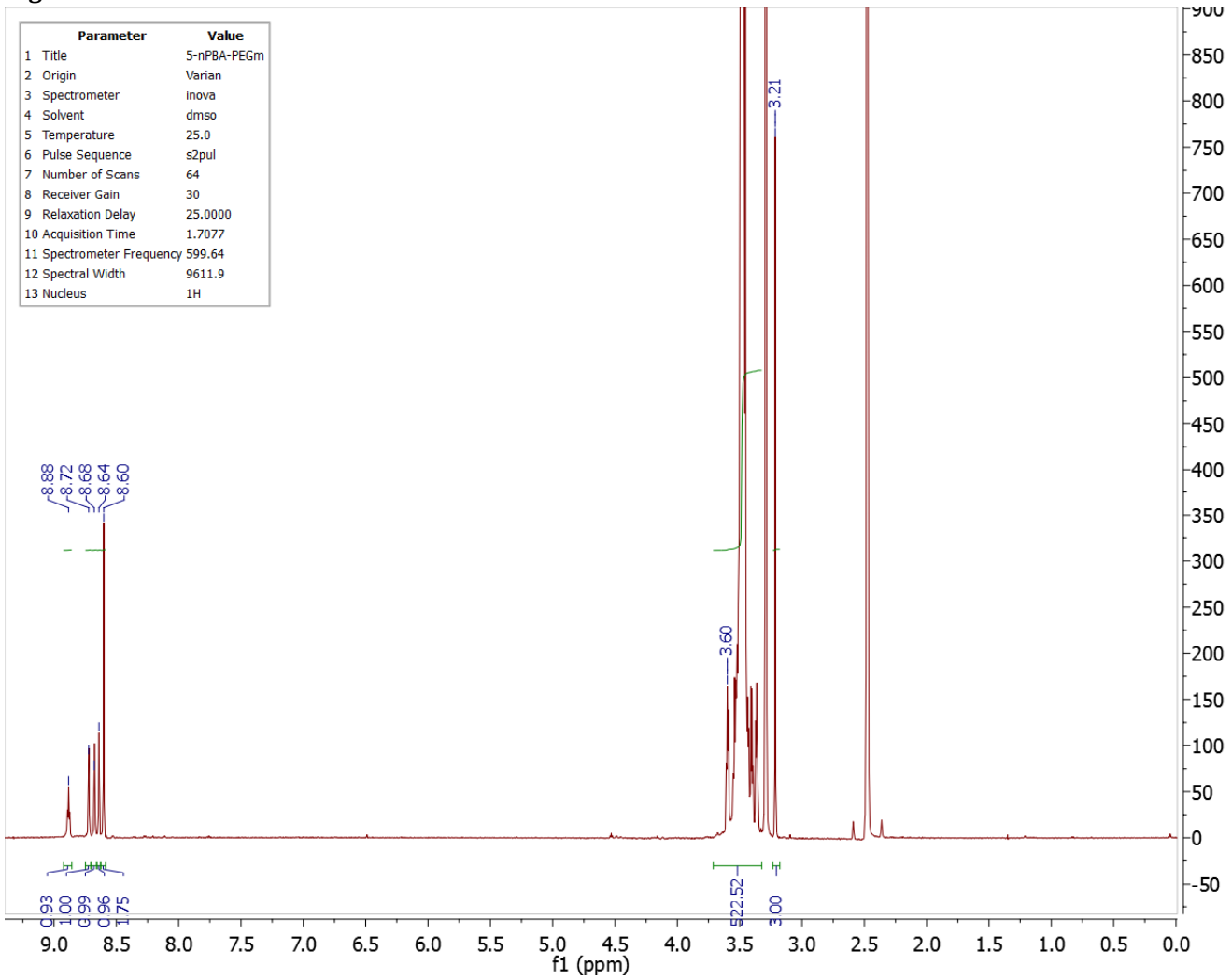

Figure II.S35: 1H DOSY of 5-nPBA-PEGm showing that the 5-nitrophenylboronic acid group is attached to PEGm by the downfield protons' persistence with PEG throughout the gradient sequence (compared to DMSO and H_2O, which disappear after the first gradients applied).

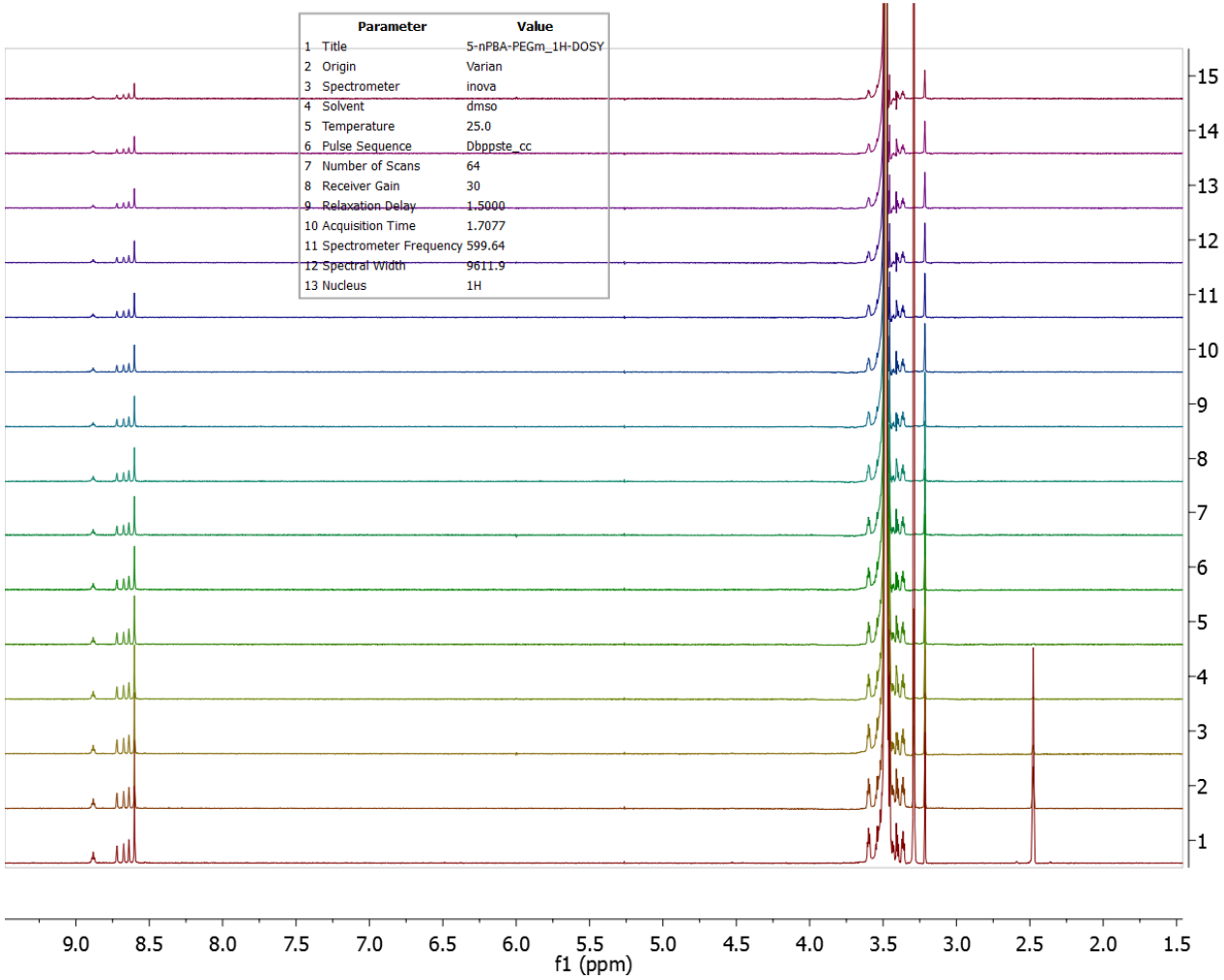

Figure II.S36: 1H DOSY transform of 5-nPBA-PEGm showing that the downfield 5-nitrophenylboronic acid peaks diffuse at the same rate as the PEG peaks.

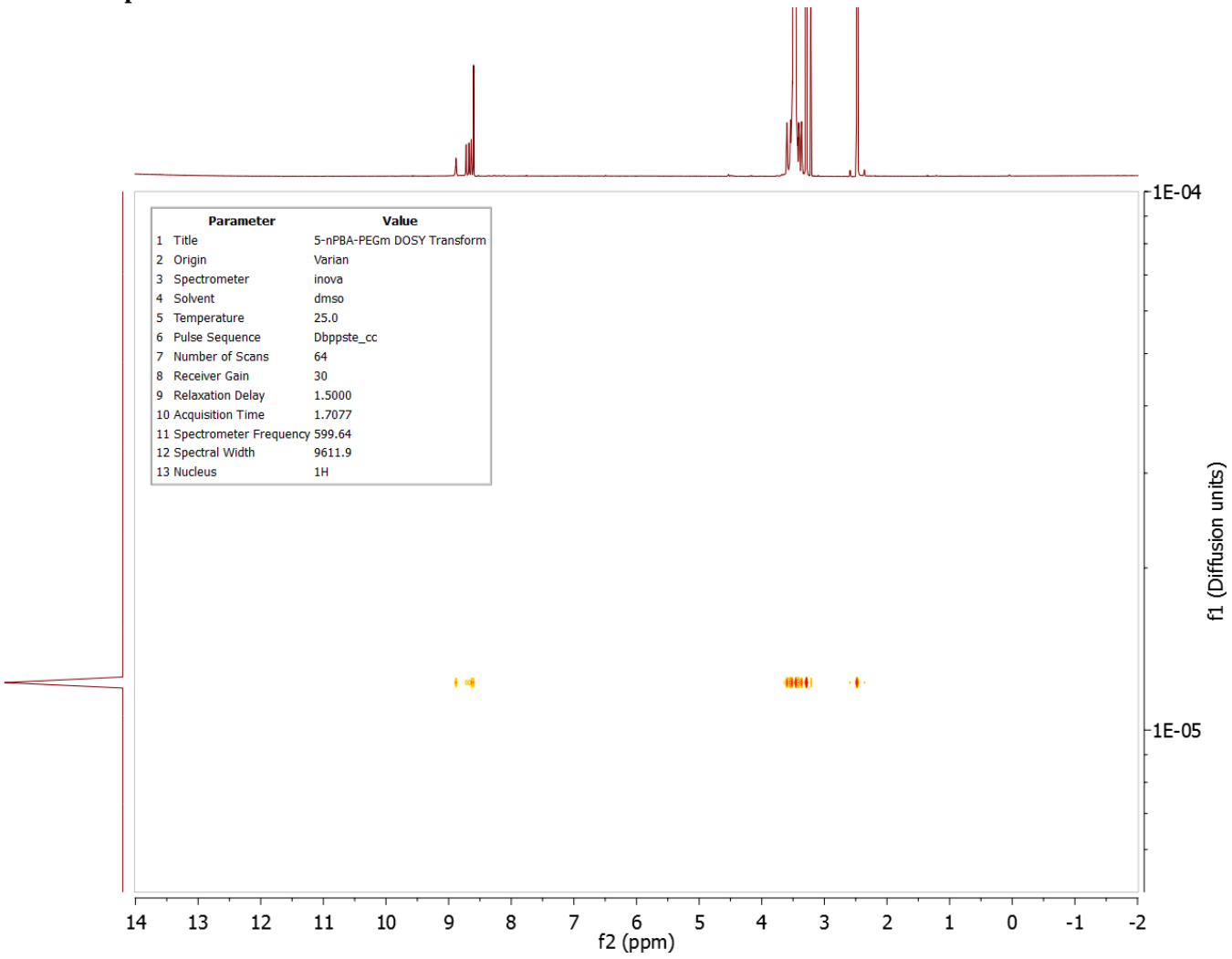

Figure II.S37: 11B NMR of 5-nPBA-PEGm. 11.26 ppm is the boronic acid peak. 19.54 ppm is boric acid (impurity).

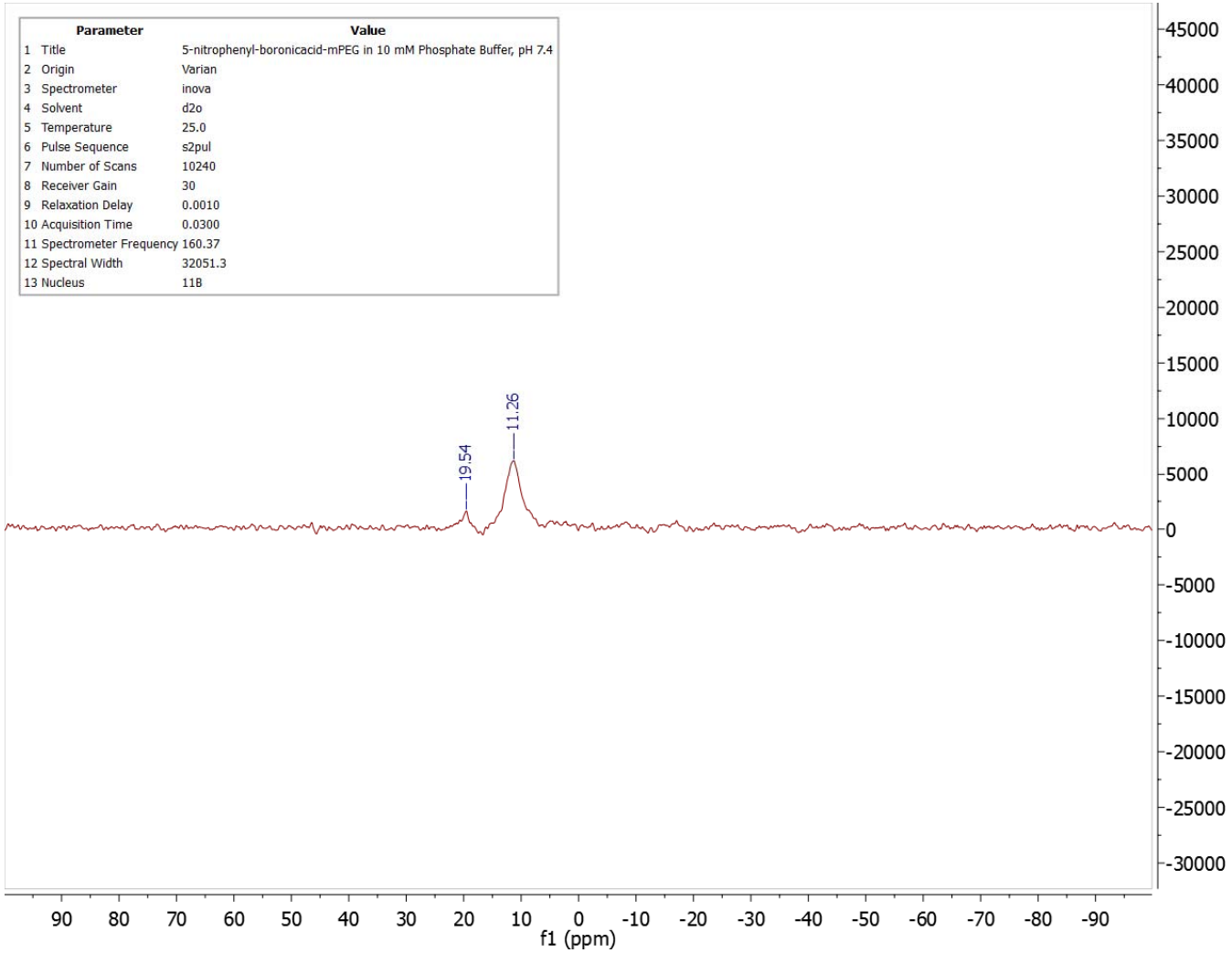

Figure II.S38: MALDI mass spectrum of 5-nPBA-PEGm.

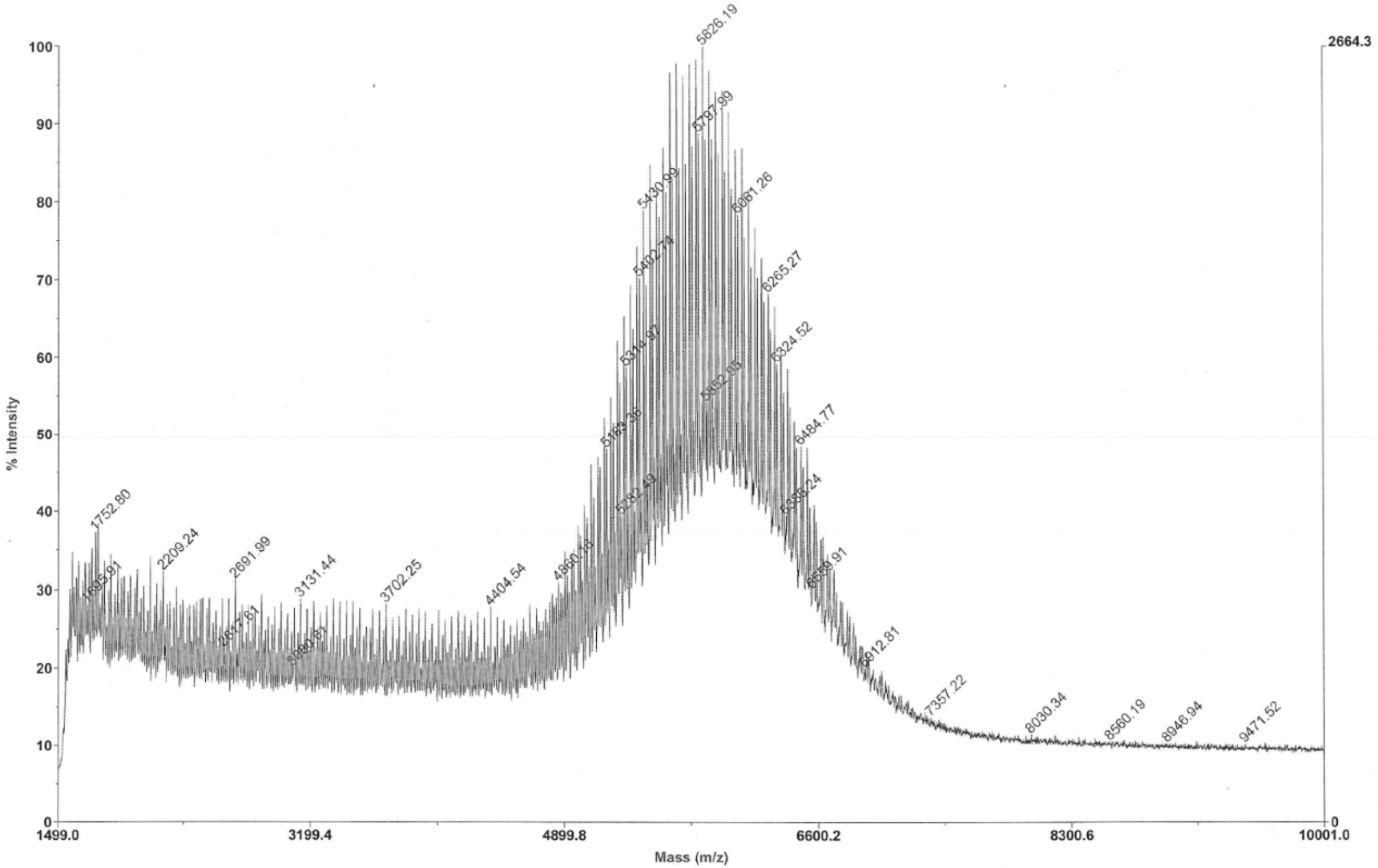
% Intensity
Mass (m/z)
100
90
80
70
60
50
40
30
20
10
0
1499.0
3199.4
4899.8
6600.2
8300.6
10001.0
2664.3
1752.80
1805.91
2209.24
2691.99
2817.61
3131.44
3080.81
3702.25
4404.54
4860.16
5163.36
5282.49
5314.97
5430.99
5492.74
5652.05
5797.99
5826.19
6061.26
6265.27
6324.52
6484.77
6636.24
6659.91
6812.81
7357.22
8030.34
8560.19
8946.94
9471.52

9. GPC: cMAP individual batch MW.

Table II.S11: Gel Permeation Chromatography Analysis of cMAP Batches.

Sample	Mn	Mw	Mw/Mn (PDI)
cMAP-DP11	5323	6068	1.14
cMAP-DP12	5213	5839	1.12
cMAP-DP13	5936	6365	1.07
cMAP-DP14	5747	5940	1.03
cMAP-DP15	5050	5568	1.10
cMAP-DP16	6102	6357	1.04
cMAP-DP17	7712	8235	1.07
cMAP-DP18	7313	7524	1.03
cMAP-DP19	8353	8984	1.08

Values are reported as the average of 3 runs.

10. GPC: other PEG length copolymer and triblock MW.

Table II.S12: GPC Analysis of cMAP copolymers and triblocks (other than 5 kD PEG reported in main article text).

Polymer	dn/dc (mL/g)	Mn (kD)	Mw (kD)	PDI (Mw/Mn)
cMAP-PEG3.4k Copolymer	0.1660	128.30	289.25	2.27
cMAP-PEG3.4k -cMAP	0.1660 used (not for pure triblock)	12.89	14.20	1.10
cMAP-PEG5k-cMAP	0.1660 used (not for pure triblock)	24.17	26.84	1.11
mPEG2k-cMAP-PEG2km	0.1654	9.75	9.81	1.01

11. siRNA encapsulation: Gel Retardation images

Figure II.S39. cMAP gel retardation showing complete siRNA encapsulation at a charge ratio of 1+/-.

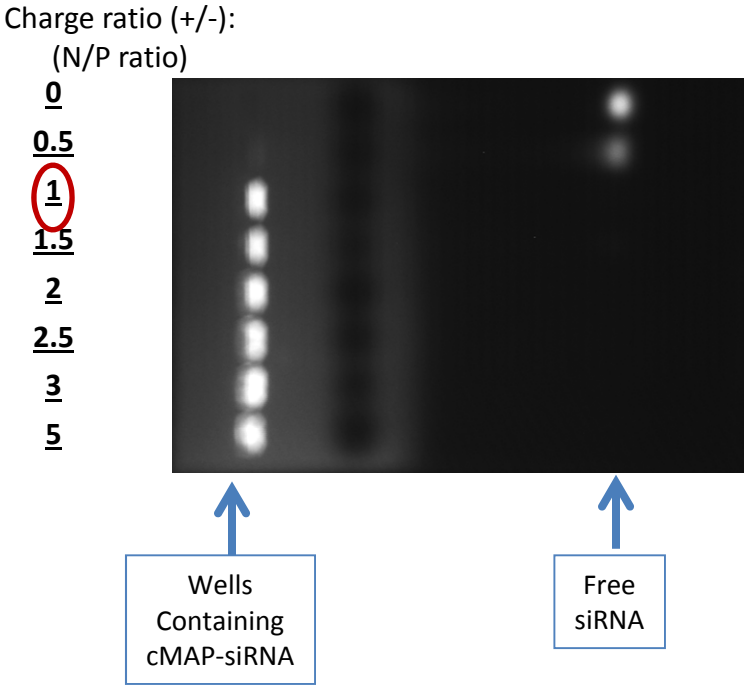

Figure II.S40. cMAP-PEG3.4k copolymer gel retardation assay showing siRNA encapsulation at a charge ratio of 1+/- .

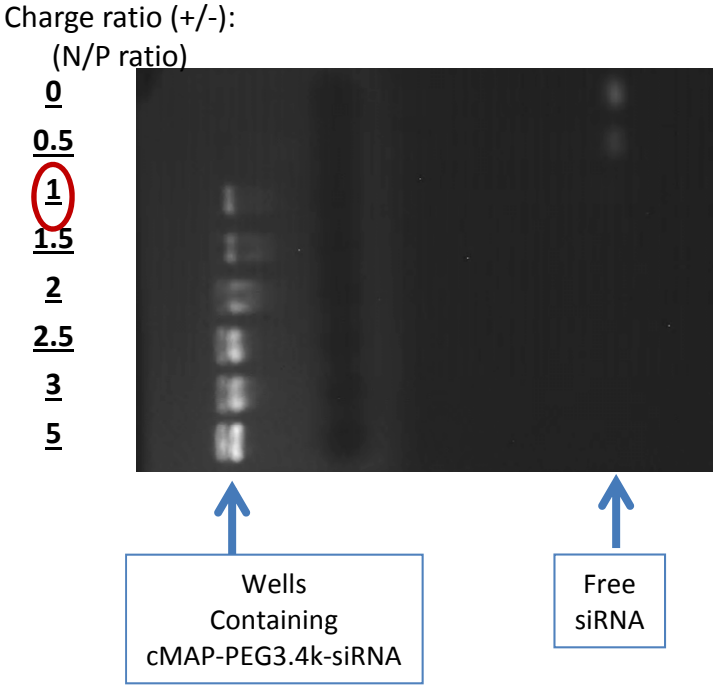

Figure II.S41. cMAP-PEG5k copolymer gel retardation assay showing siRNA encapsulation at a charge ratio of 2+/- .

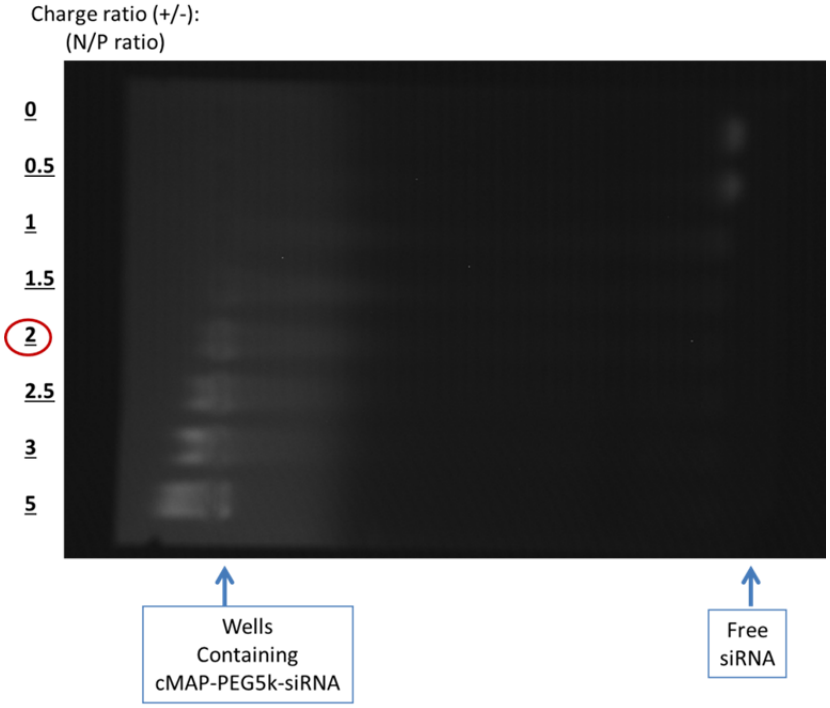

12. siRNA encapsulation: RiboGreen comparing PEG lengths for copolymer and triblock

Figure II.S42. cMAP-PEG copolymer RiboGreen assay showing siRNA encapsulation by a charge ratio of 3+/- for 3.4k and 5k PEG blocks.

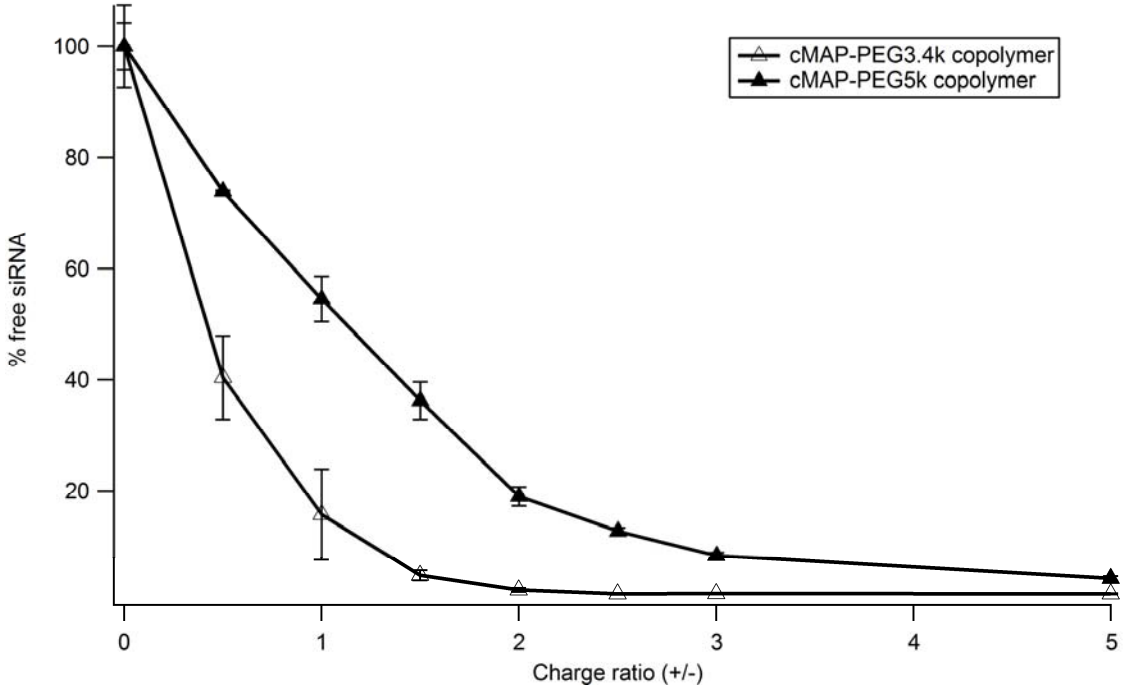

Figure II.S43. mPEG-cMAP-PEGm triblock RiboGreen assay showing siRNA encapsulation by a charge ratio of 3+/- for 2k and 5k PEG blocks.

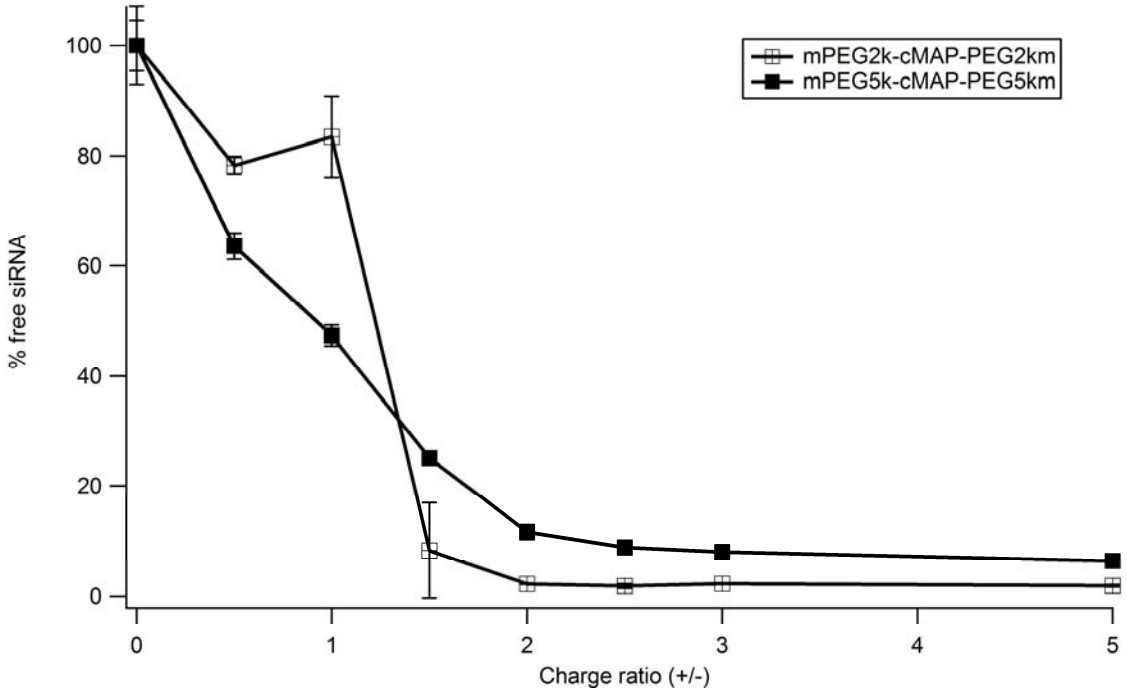

13. cMAP siRNA NP Salt Stability

Figure II.S44. Without PEG, the cMAP-siRNA NP is unstable once in 1X PBS, but is stable for 2 days when 5-nPBA-PEGm is used to stabilize the NP.

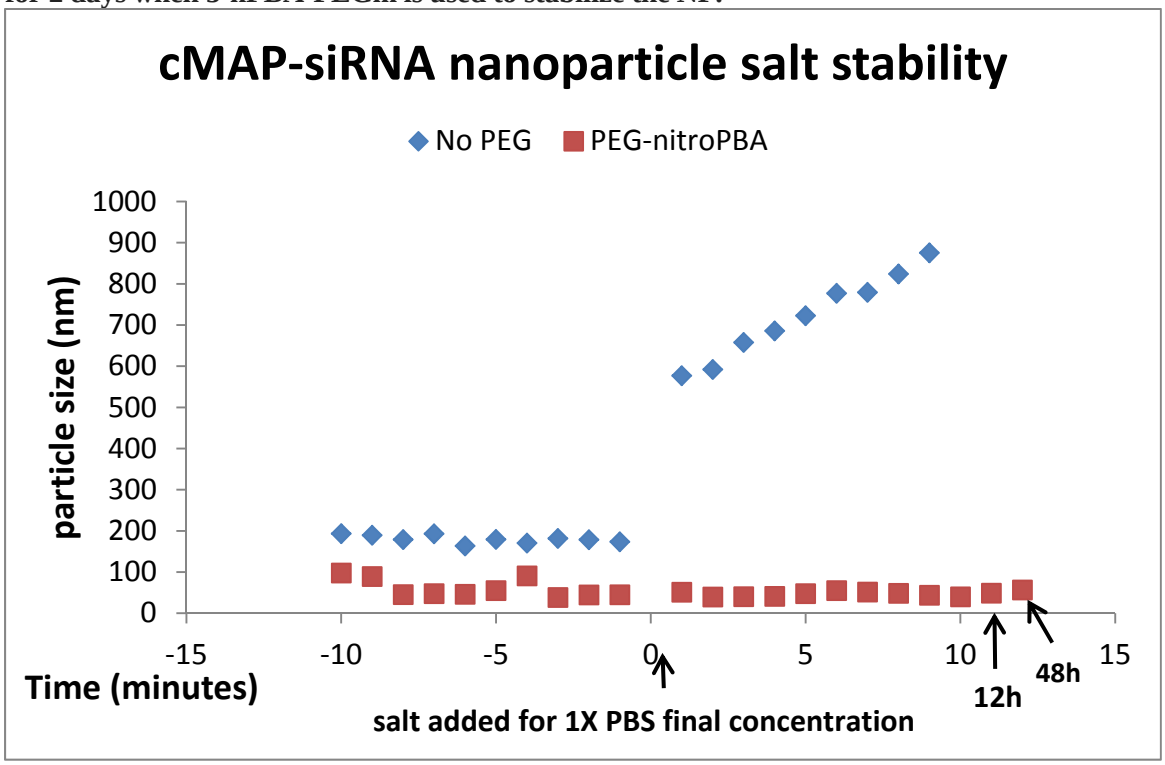

14. cMAP-PEG-cMAP pure triblock siRNA NP Salt Stability

Table II.S13: NPs formed without extra 5-nPBA-PEGm using cMAP-PEG-cMAP triblock isolated from cMAP-PEG copolymer aggregates in 1X PBS, but is stable when at least one PEG per 2 diol groups is added to the formulation. The average sizes of the data presented in the following figures are shown.

Formulation	10 mM phosphate buffer	PBS
	Avg. size (nm)	Avg. size (nm)
3.4k triblock, 1:1, 0 PEG	176.6 ± 1.0	aggregates
3.4k triblock, 1:1, 0.5 PEG	100.1 ± 0.8	57.9 ± 0.9
3.4k triblock, 1:1, 1 PEG	149.5 ± 1.6	56.5 ± 1.5
3.4k triblock, 1:1, 2 PEG	85.9 ± 2.0	74.5 ± 3.4
3.4k triblock, 3:1, 0 PEG	392.3 ± 5.0	aggregates
3.4k triblock, 3:1, 0.5 PEG	42.8 ± 2.0	47.3 ± 2.0
3.4k triblock, 3:1, 1 PEG	61.3 ± 2.3	55.7 ± 1.2
3.4k triblock, 3:1, 2 PEG	115.9 ± 11.4	96.6 ± 1.6
5k triblock, 1:1, 0 PEG	165.2 ± 4.7	aggregates
5k triblock, 1:1, 0.5 PEG	141.3 ± 5.2	99.8 ± 3.8
5k triblock, 1:1, 1 PEG	109.2 ± 3.6	97.5 ± 4.2
5k triblock, 1:1, 2 PEG	179.1 ± 19.9	143.5 ± 5.4

Figure II.S45. Without added 5-nPBA-PEGm, the cMAP-PEG3.4k-cMAP siRNA NP formulated at a 1+/- charge ratio aggregates once in 1X PBS, but is stable when at least one 5-nPBA-PEGm per two diol groups (0.5 PEG) on cMAP is added to the formulation.

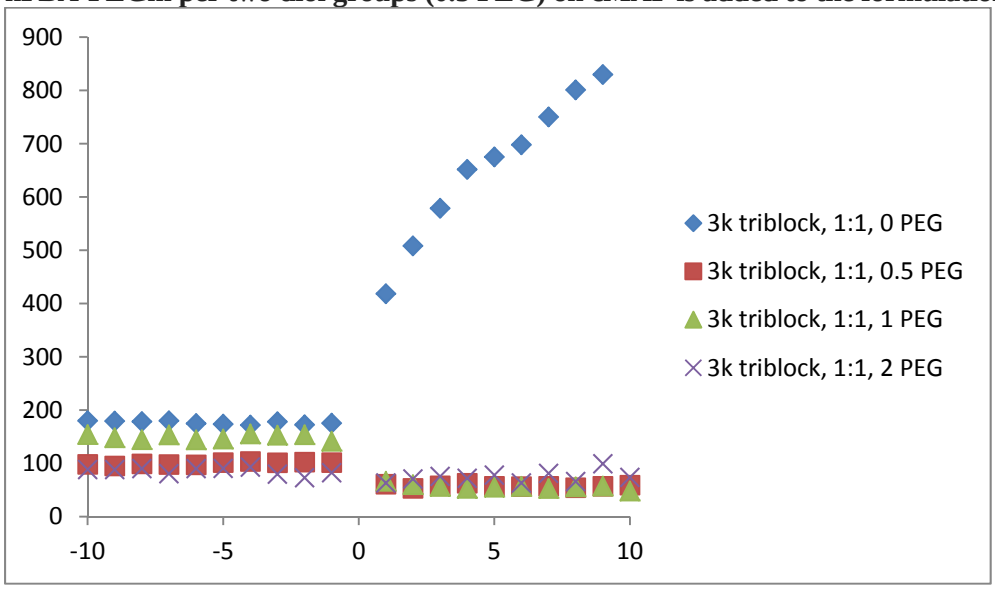

Figure II.S46. Without added 5-nPBA-PEGm, the cMAP-PEG3.4k-cMAP siRNA NP formulated at a 3+/- charge ratio aggregates once in 1X PBS, but is stable when at least one 5-nPBA-PEGm per two diol groups (0.5 PEG) on cMAP is added to the formulation.

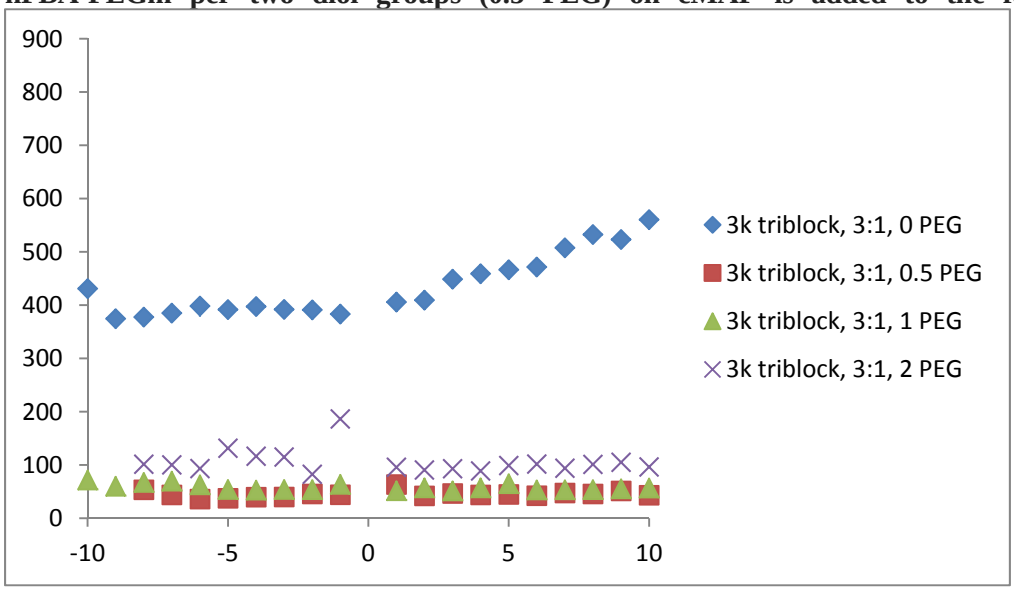

Figure II.S47. Without added 5-nPBA-PEGm, the cMAP-PEG5k-cMAP siRNA NP formulated at a 1+/- charge ratio aggregates once in 1X PBS, but is stable when at least one 5-nPBA-PEGm per two diol groups (0.5 PEG) on cMAP is added to the formulation.

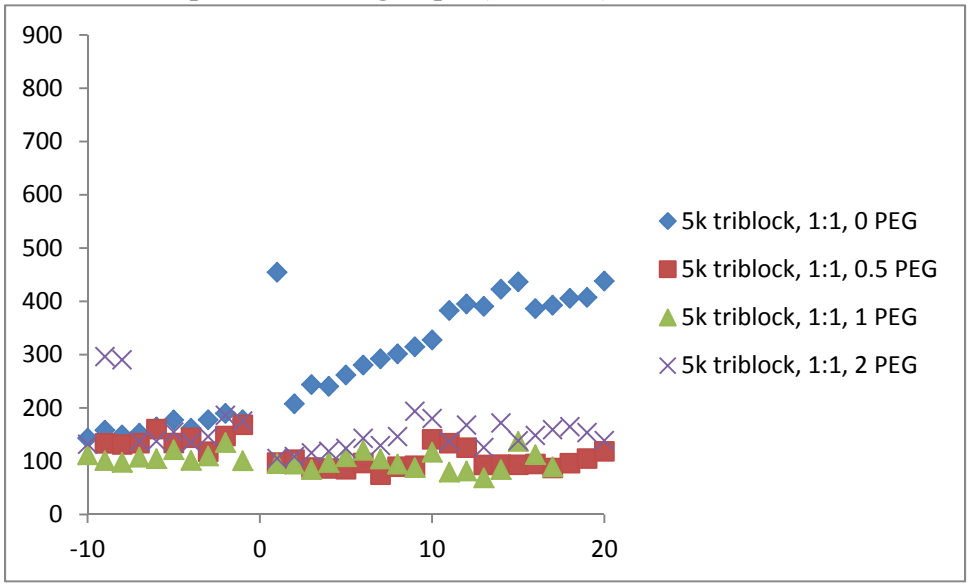

15. DLS Nanoparticle Size Distributions

Figure II.S48: Lognormal size distribution by DLS for the cMAP + 5-nPBA-PEGm NP.

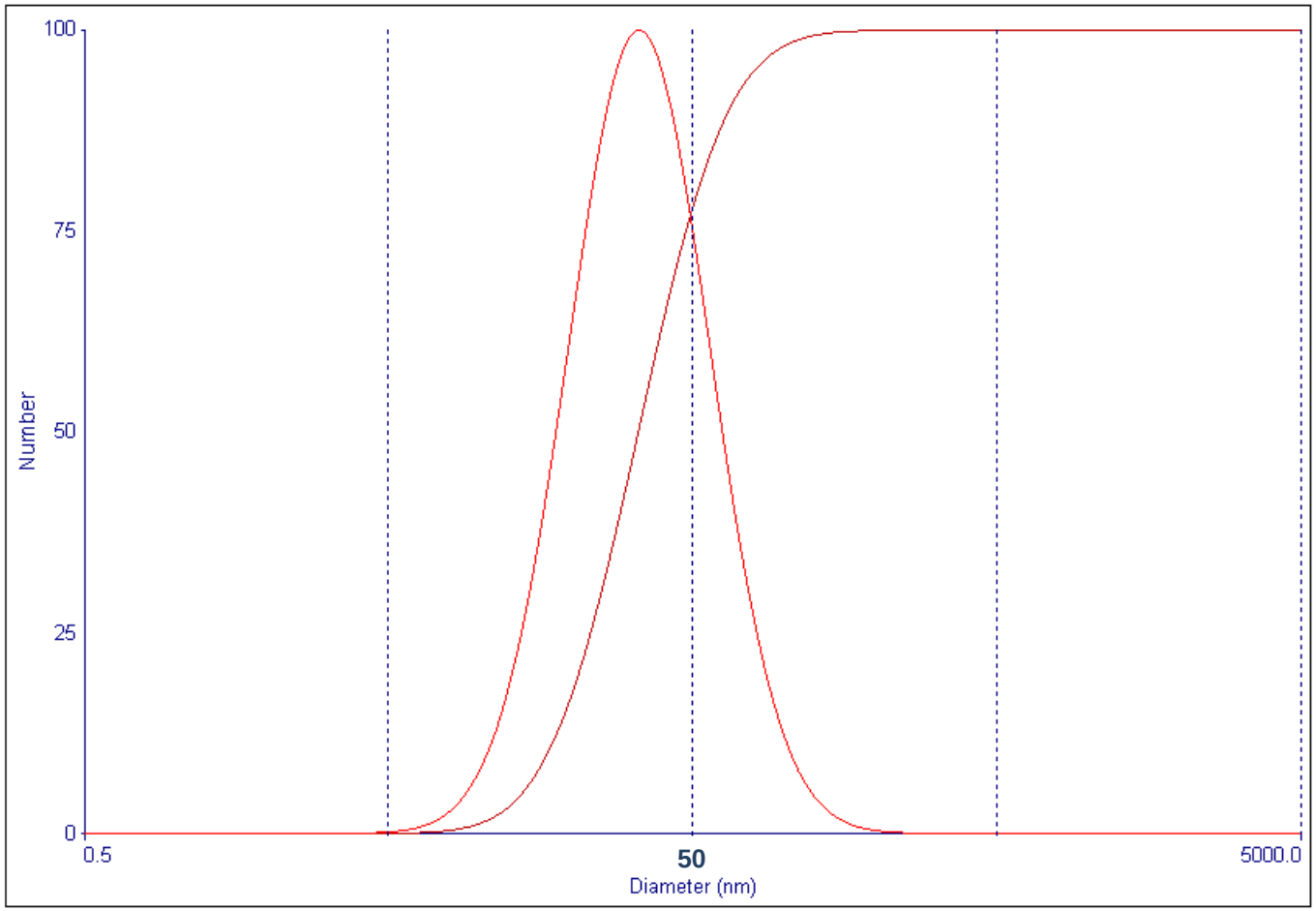

Figure II.S49: Lognormal size distribution by DLS for the cMAP-PEG copolymer NP.

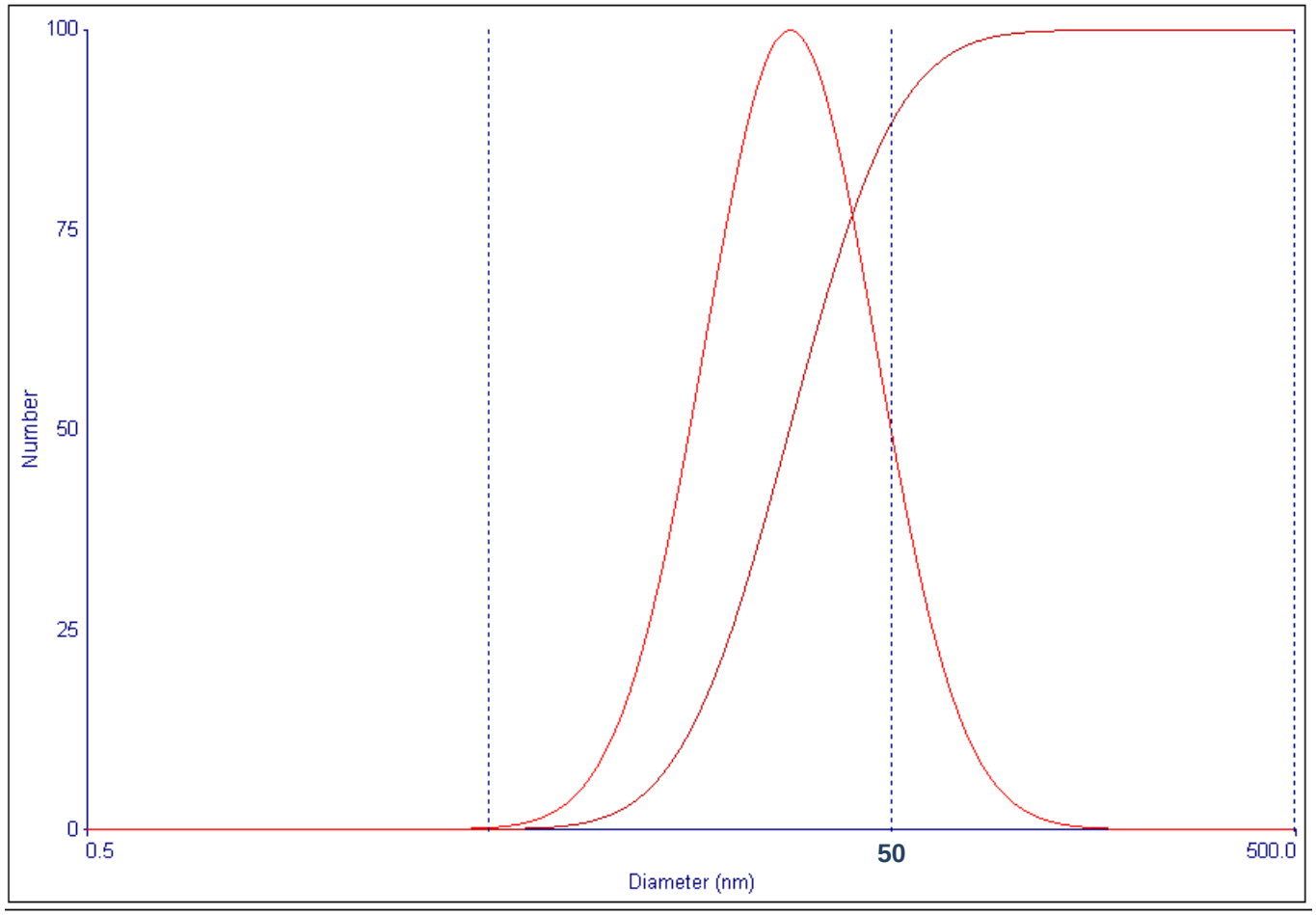

Figure II.S50: Lognormal size distribution by DLS for the cMAP-PEG copolymer + 5-nPBA-PEGm NP.

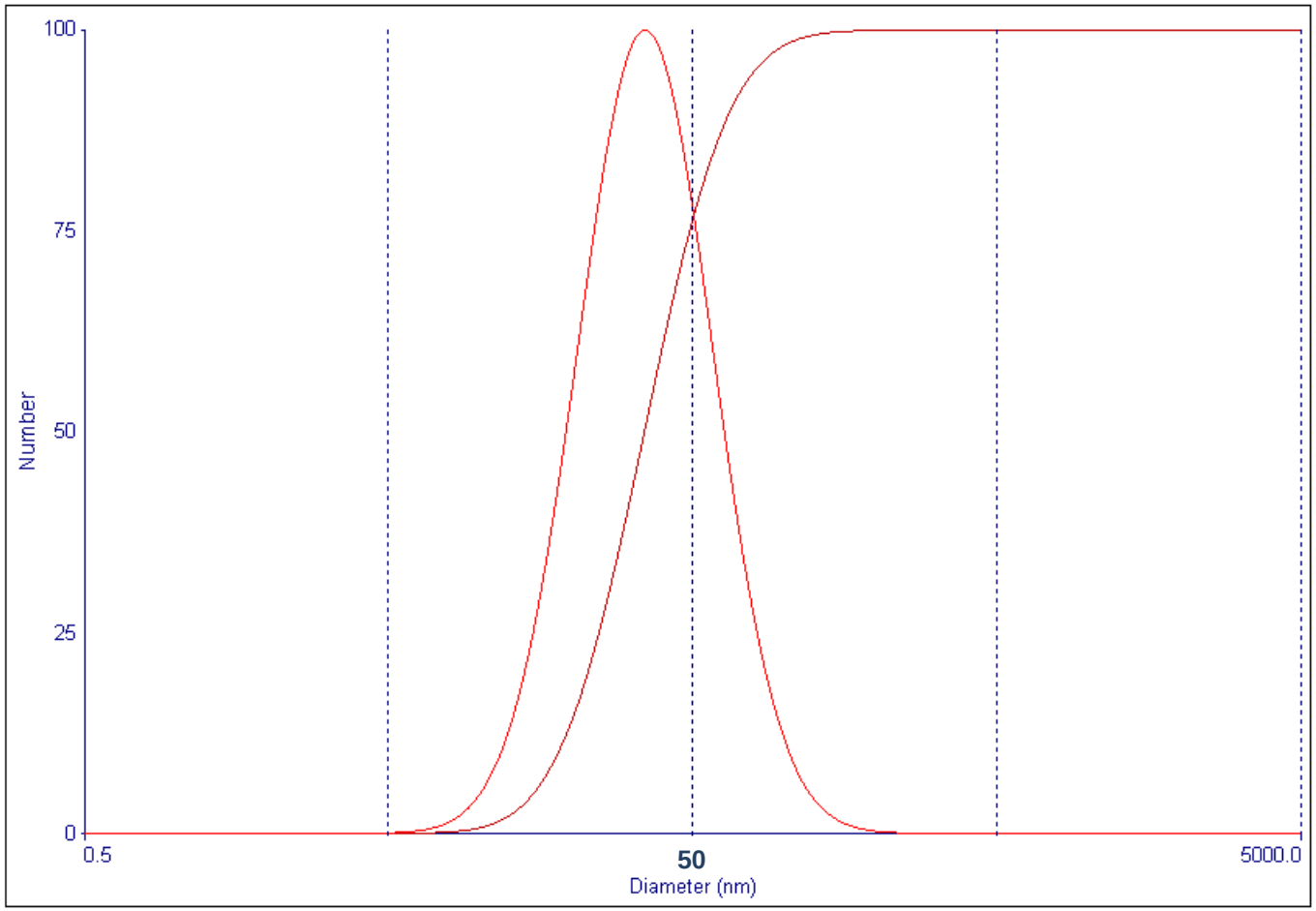

Figure II.S51: Lognormal size distribution by DLS for the mPEG-cMAP-PEGm NP.

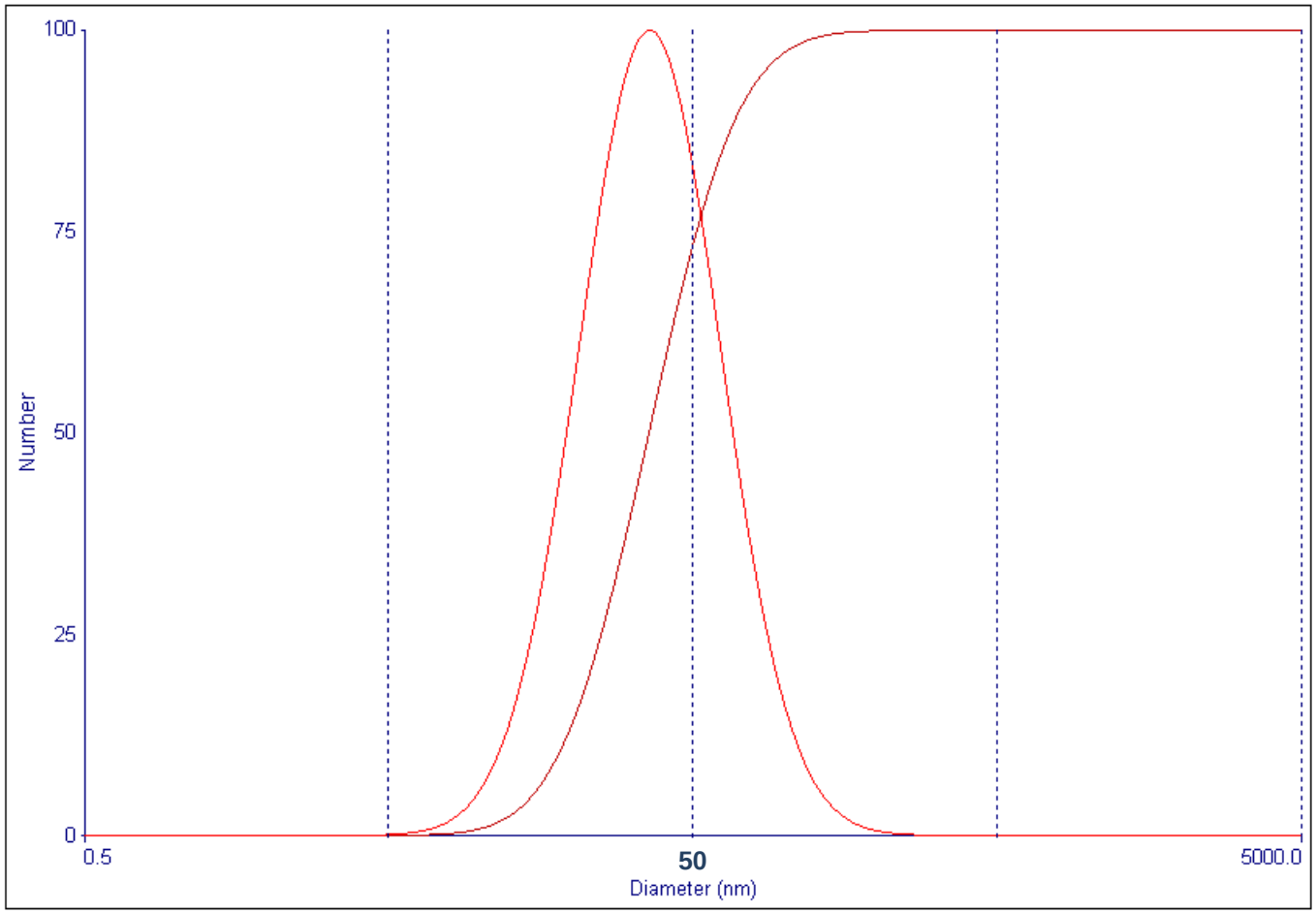

Figure II.S52: Lognormal size distribution by DLS for the mPEG-cMAP-PEGm + 5-nPBA-PEGm NP.

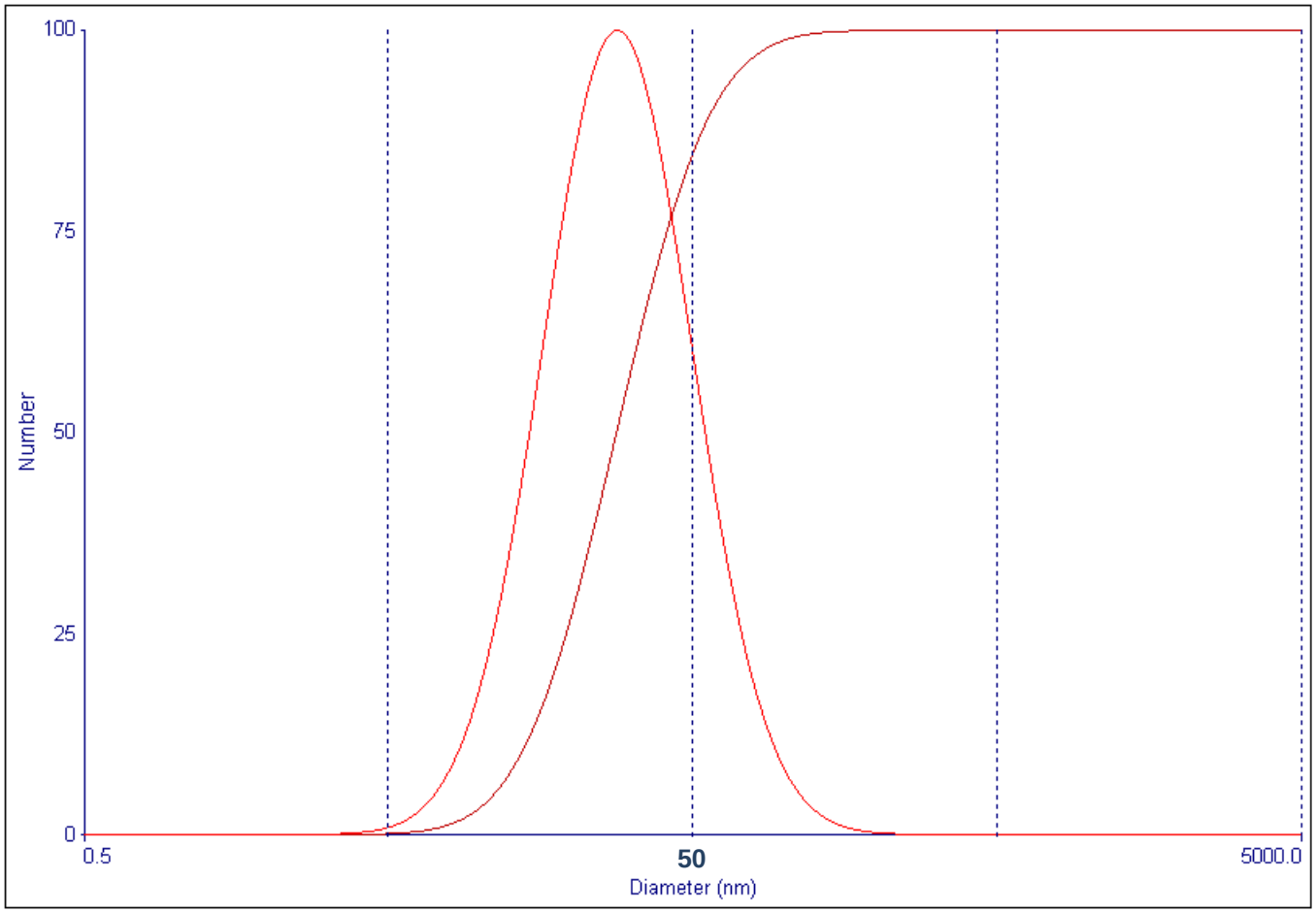

16. CryoTEM Nanoparticle Size Distributions and additional images

Figure II.S53: Size distribution by CryoTEM for the cMAP + 5-nPBA-PEGm NP.

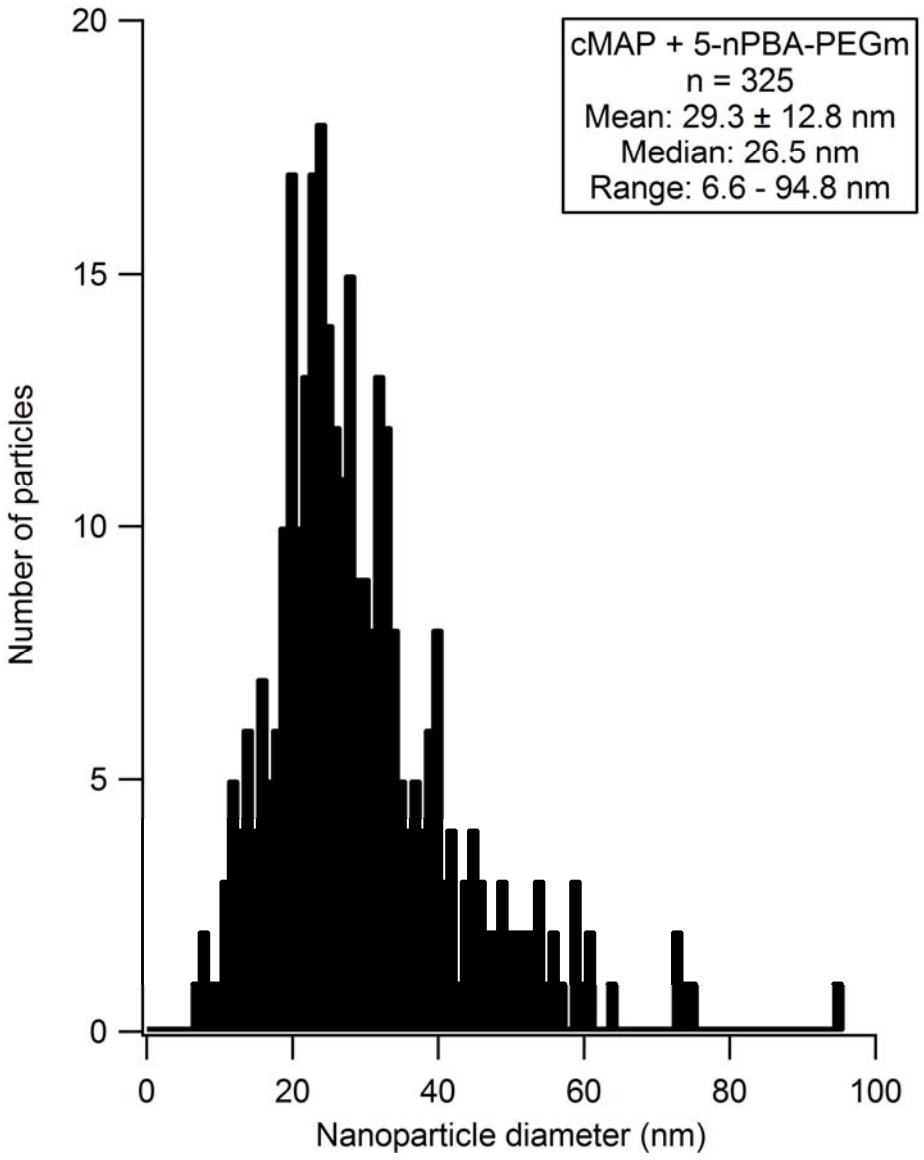

Figure II.S54: Additional CryoTEM images for the cMAP + 5-nPBA-PEGm NP.

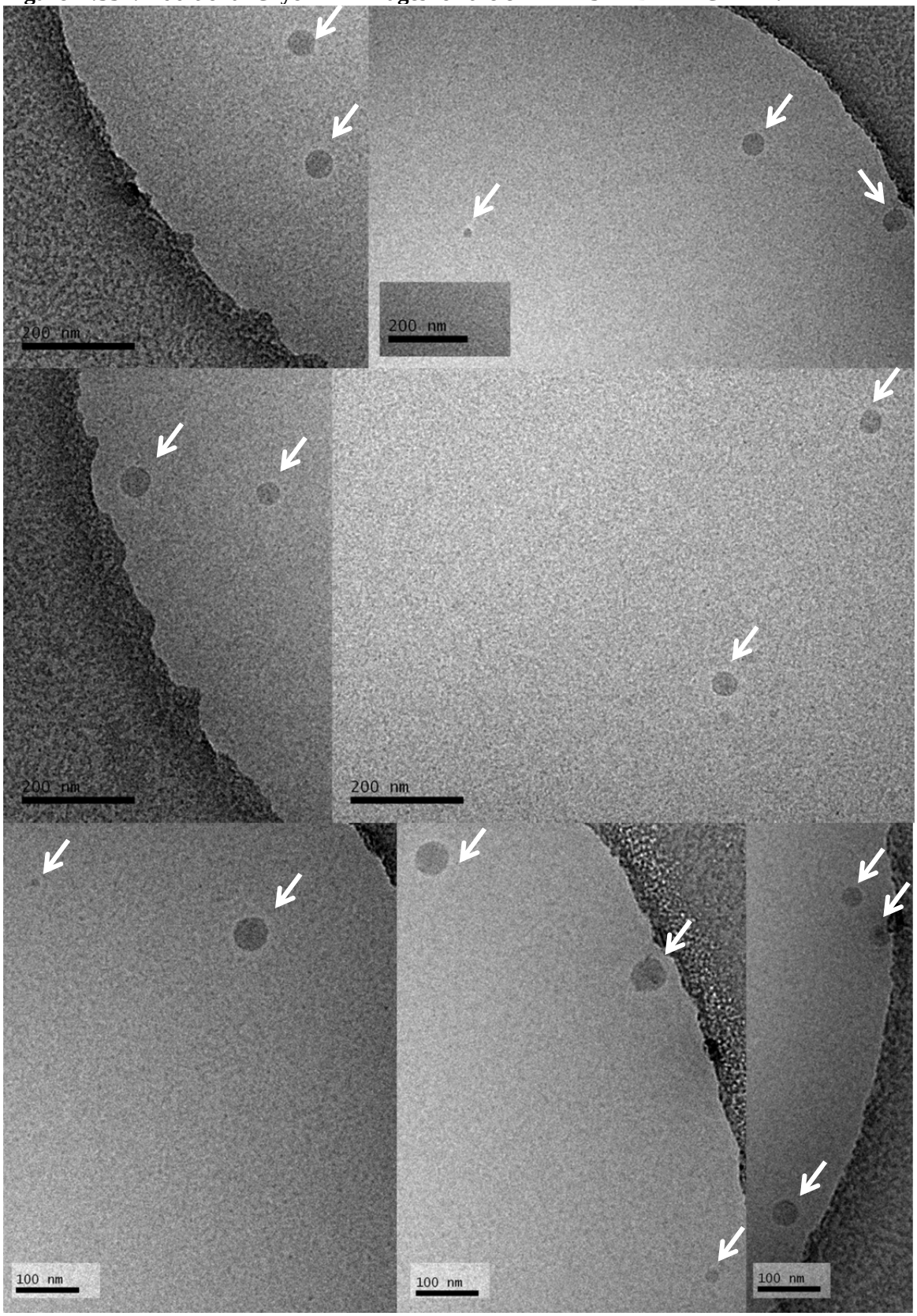

Figure II.S55: Size distribution by CryoTEM for the cMAP-PEG copolymer NP.

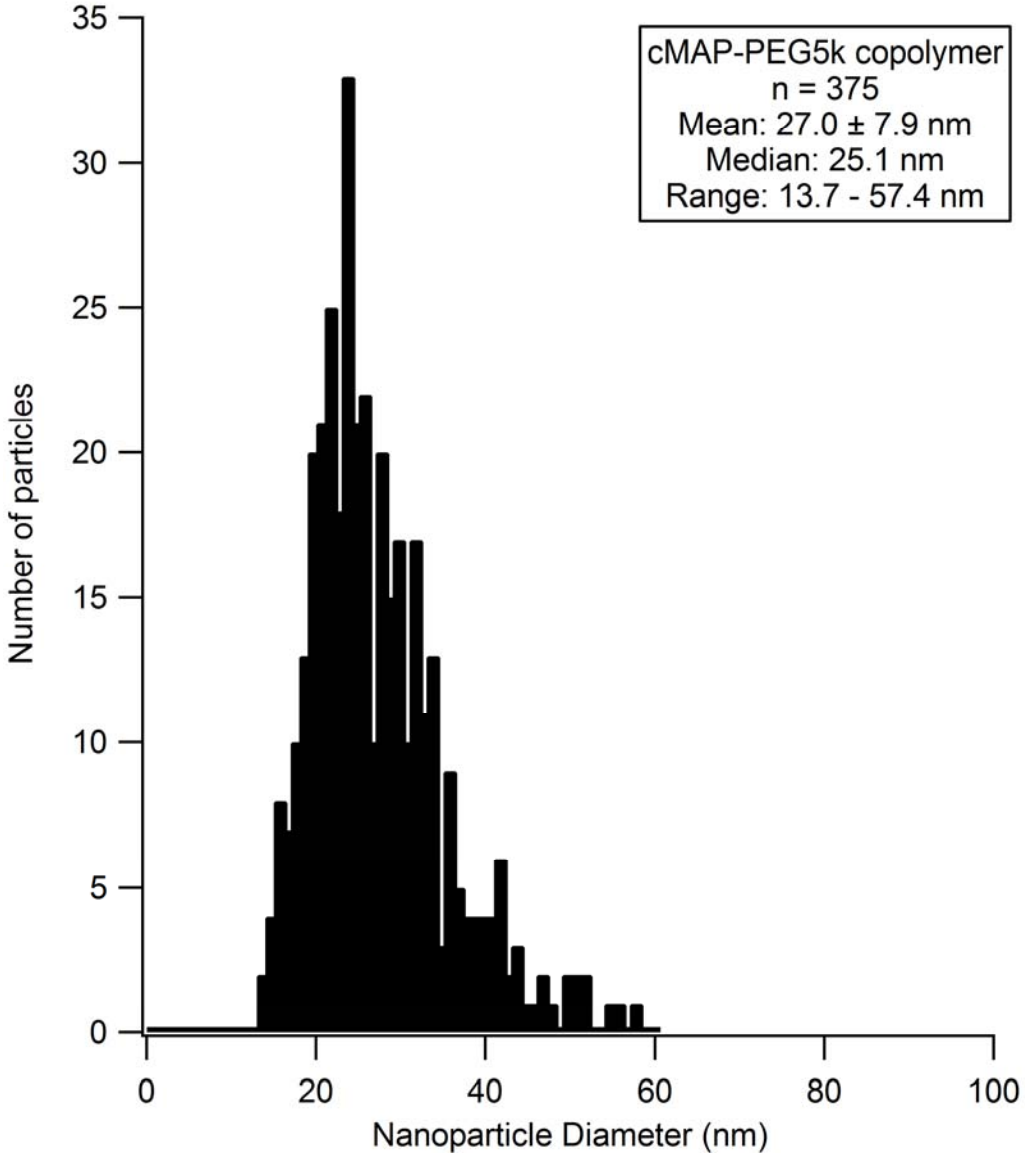

Figure II.S56: Additional CryoTEM images for the cMAP-PEG copolymer NP.

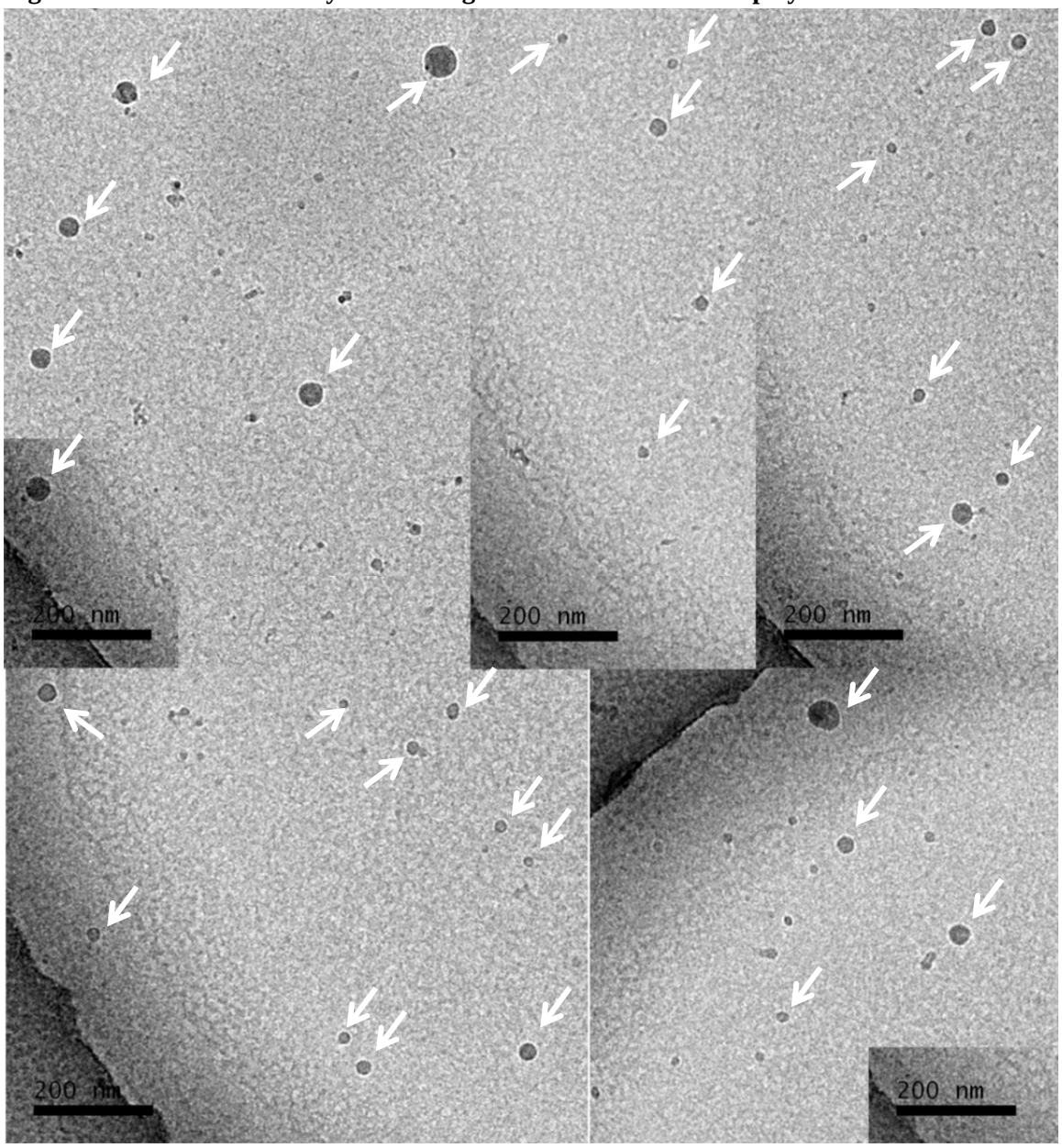

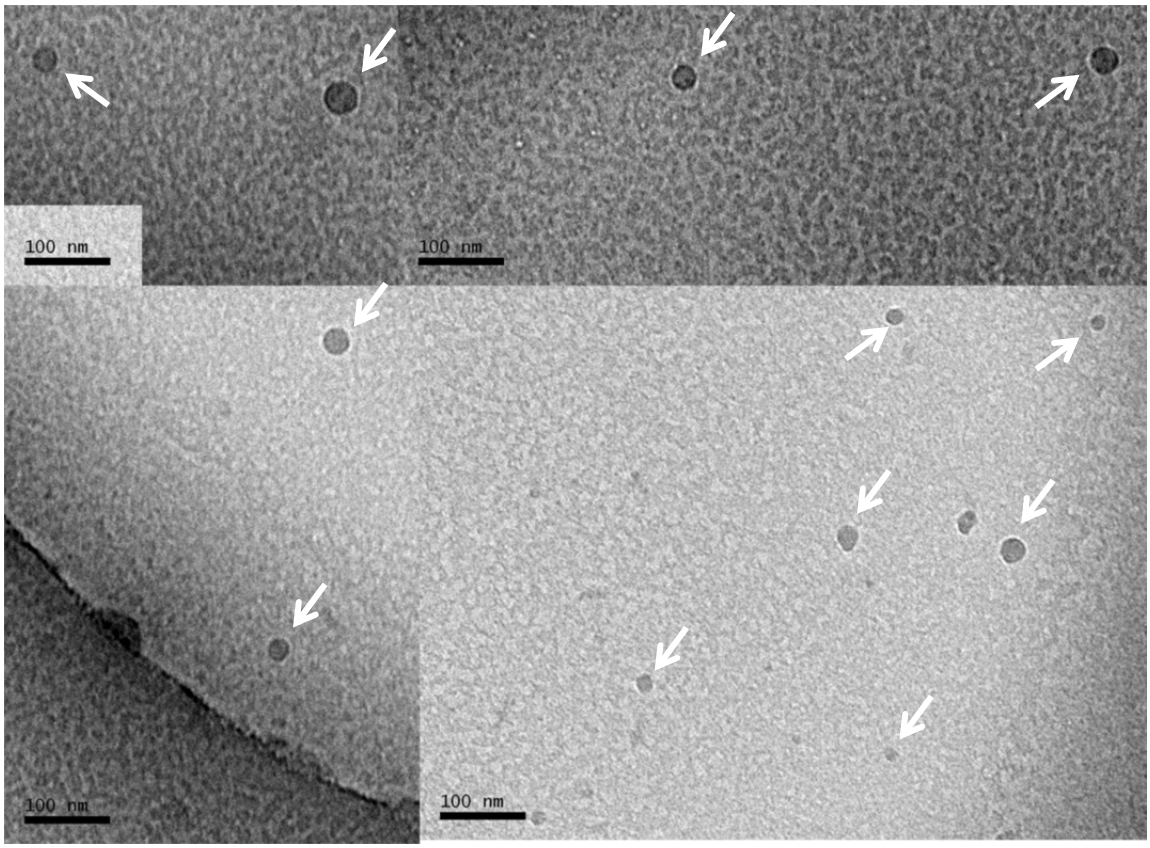
100 nm
100 nm
100 nm
100 nm

Figure II.S57: Size distribution by CryoTEM for the cMAP-PEG copolymer + 5-nPBA-PEGm NP.

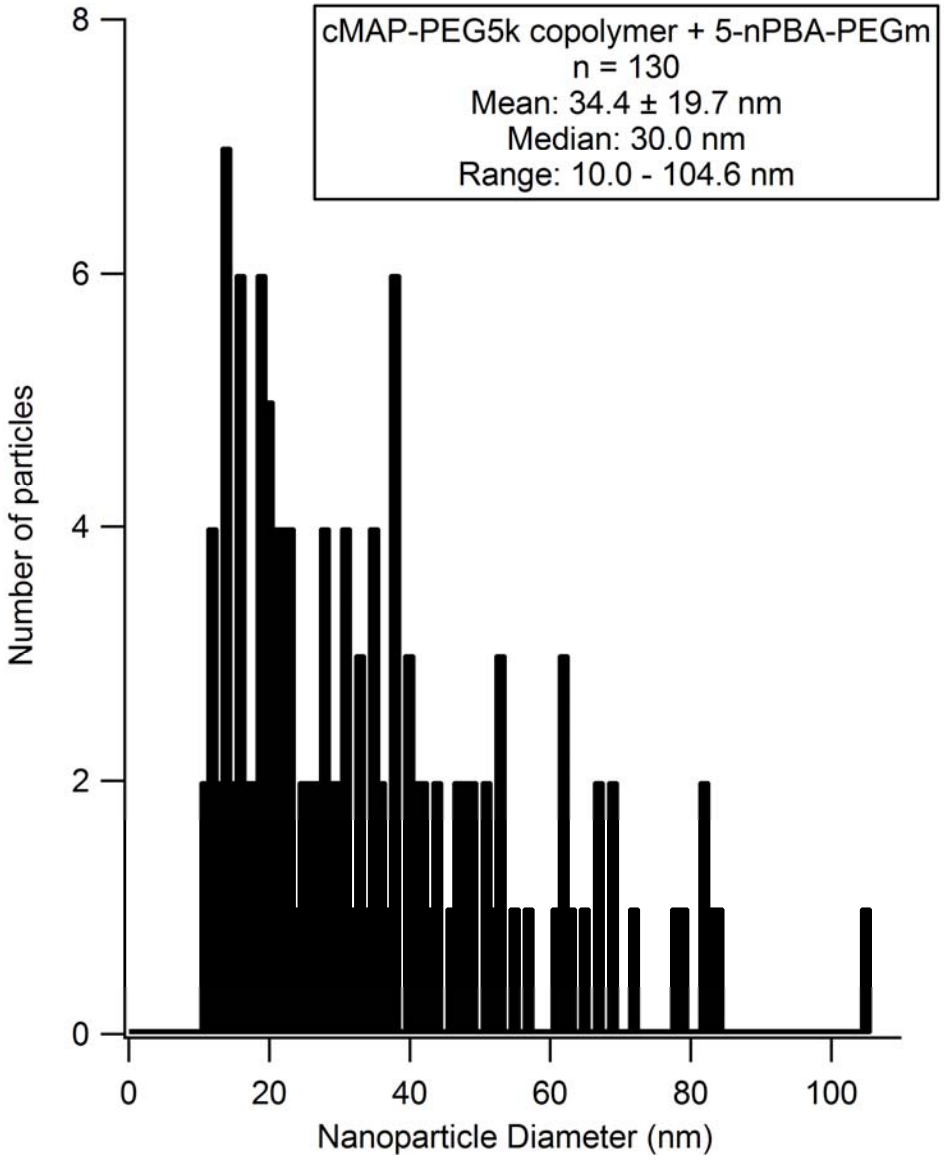

Figure II.S58: Additional CryoTEM images for the cMAP-PEG copolymer + 5-nPBA-PEGm NP.

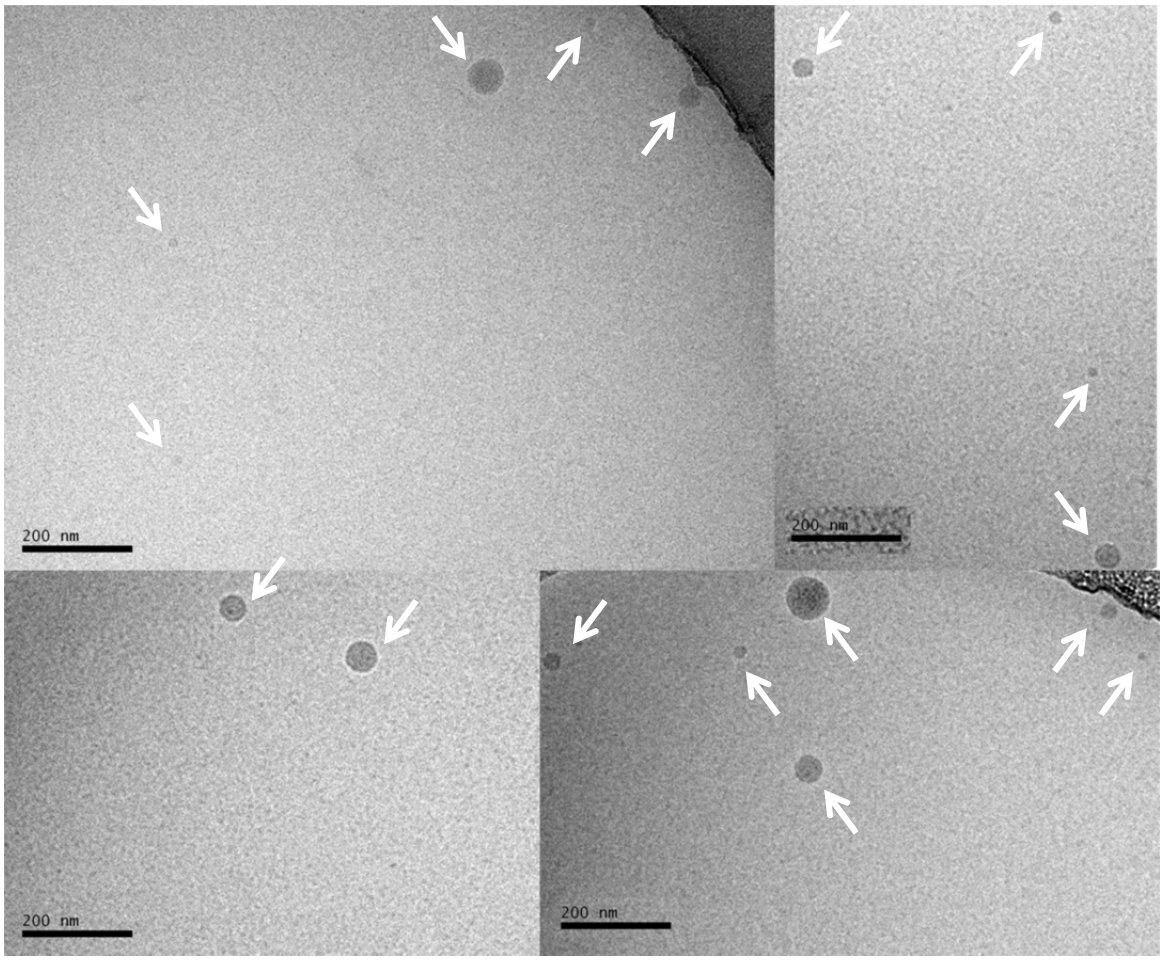

Figure II.S59: Size distribution by CryoTEM for the mPEG-cMAP-PEGm NP.

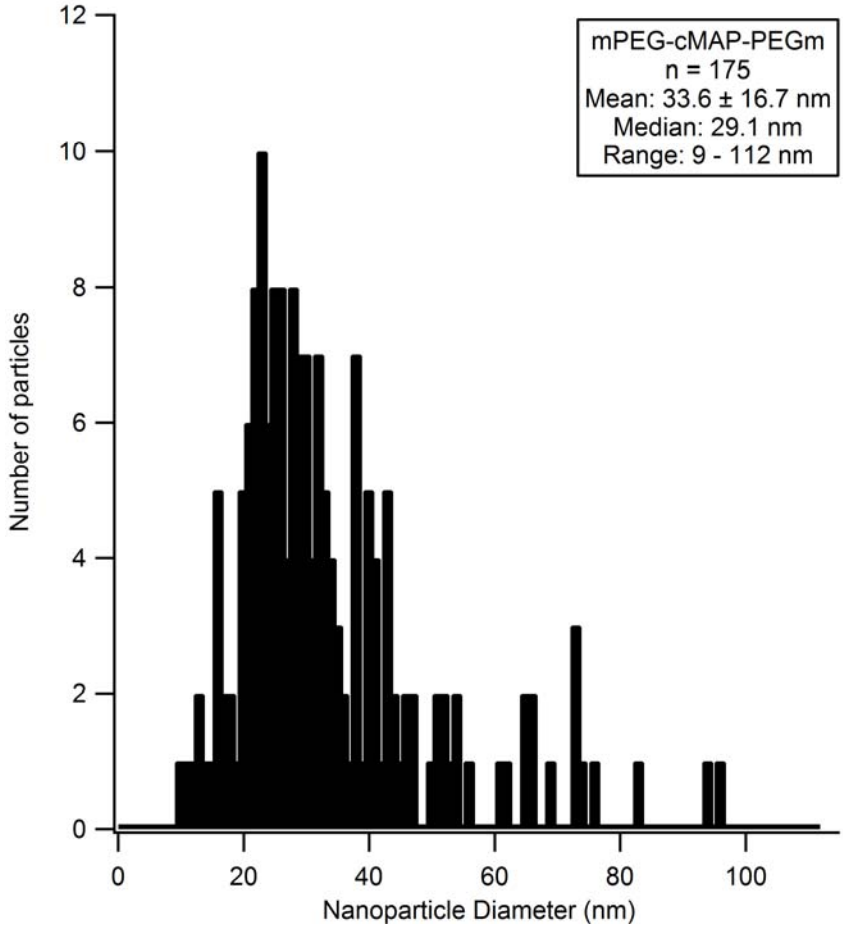

Figure II.S60: Additional CryoTEM images for the mPEG-cMAP-PEGm NP.

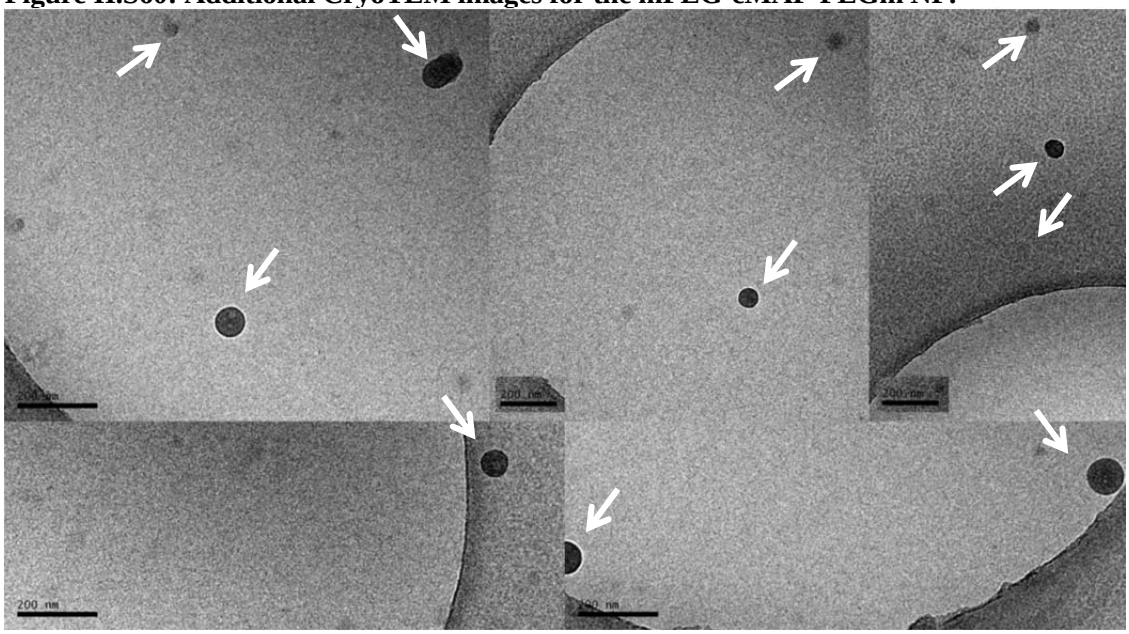

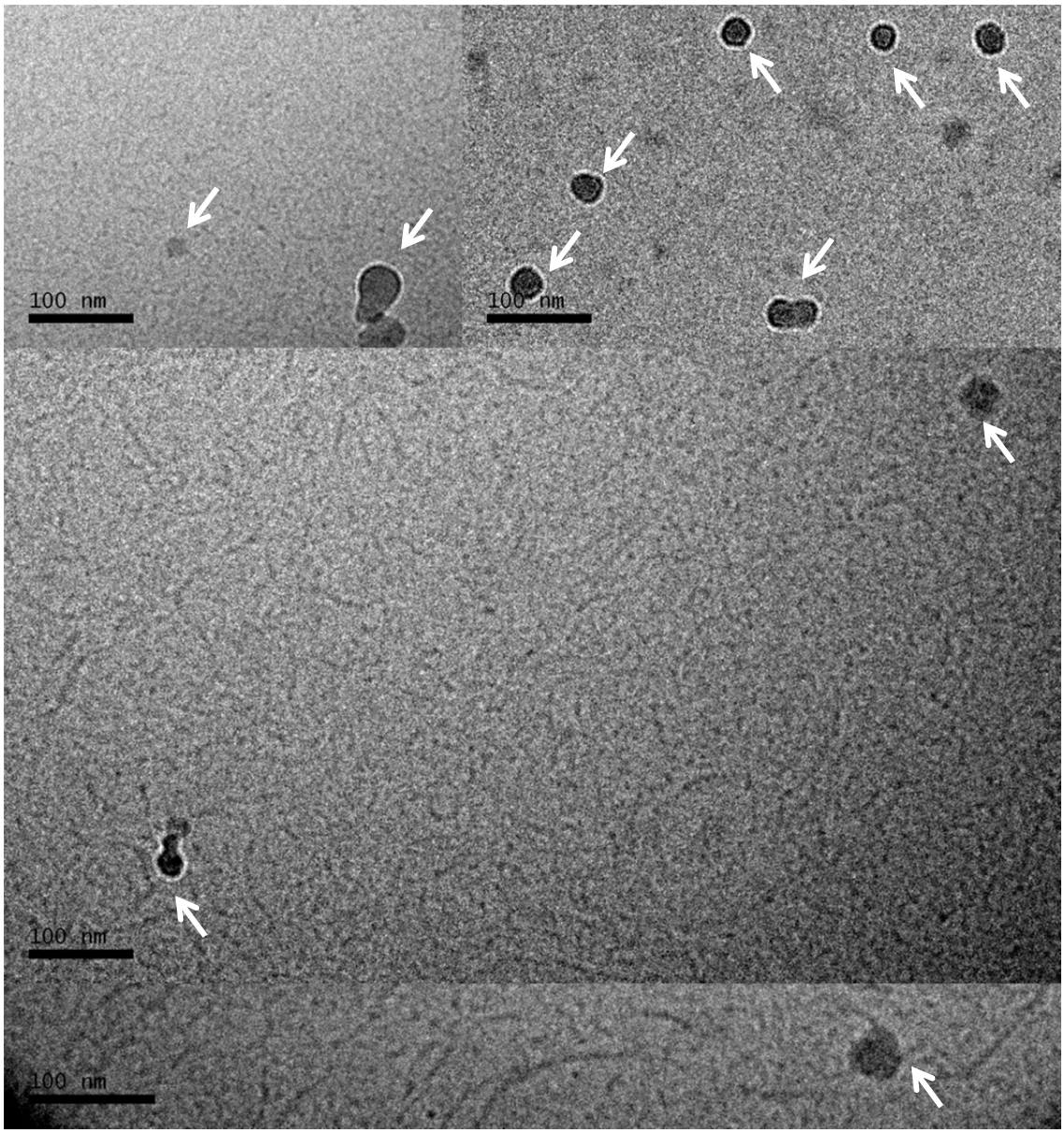
100 nm
100 nm
100 nm
100 nm

Figure II.S61: Size distribution by CryoTEM for the mPEG-cMAP-PEGm + 5-nPBA-PEGm NP.

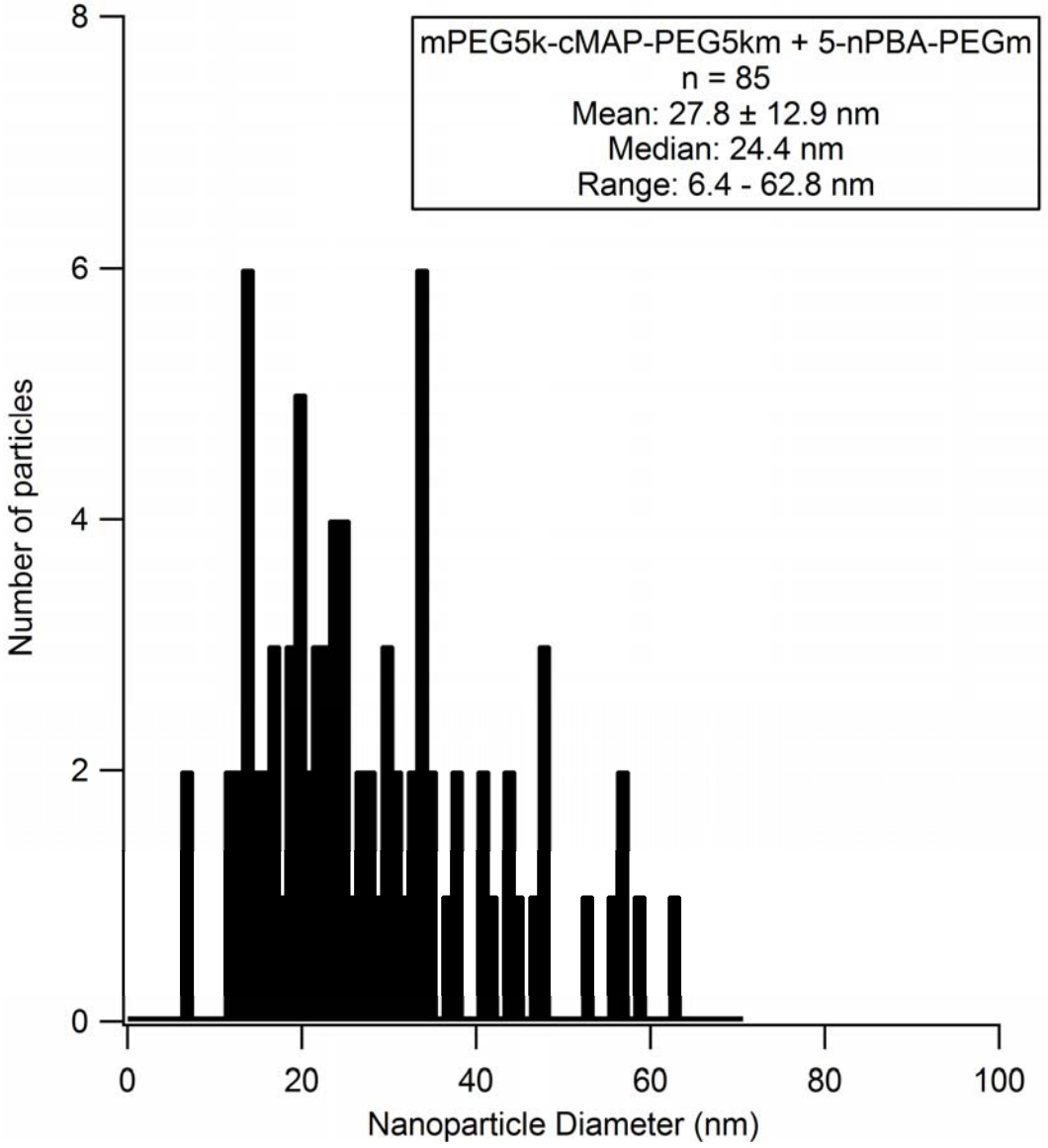

Figure II.S62: Additional CryoTEM images for the mPEG-cMAP-PEGm + 5-nPBA-PEGm NP.

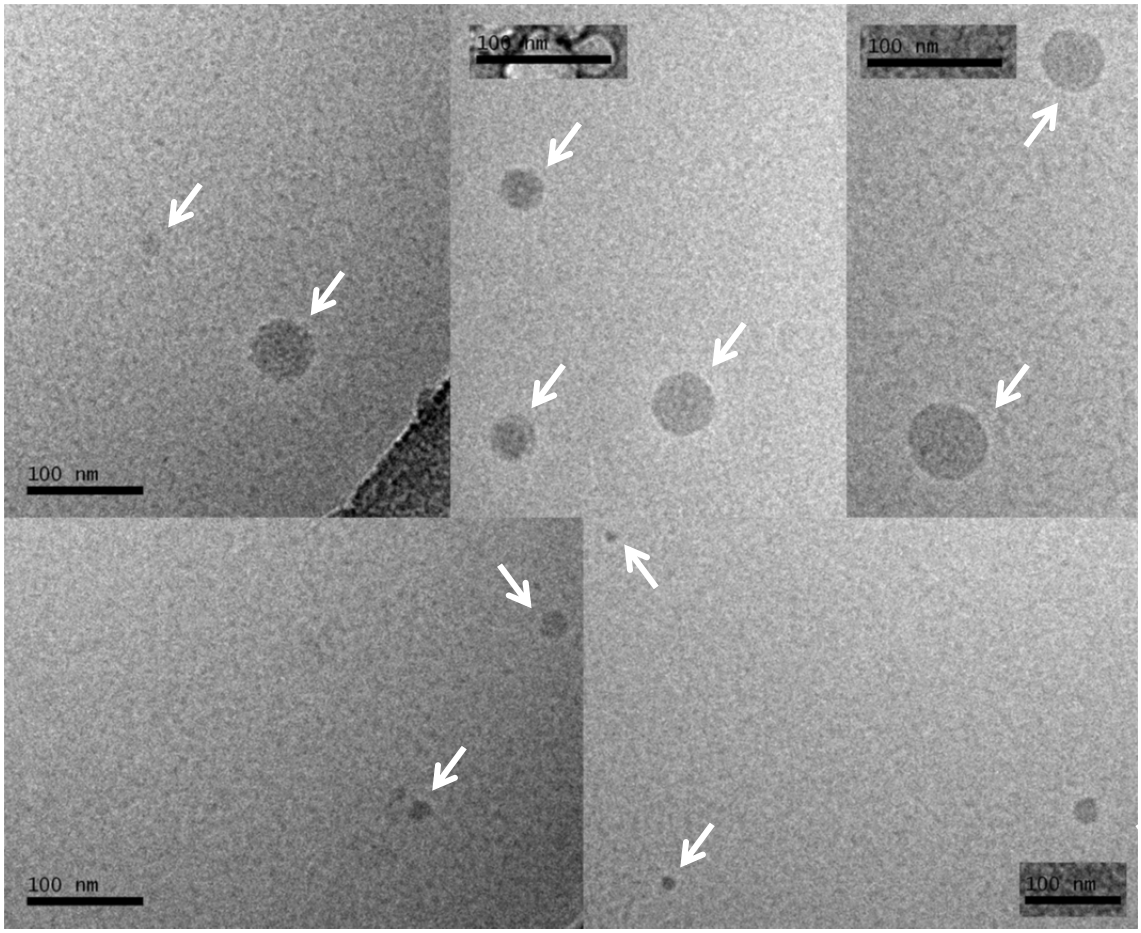
100 nm
100 nm
100 nm
100 nm
100 nm

17. Phamacokinetics of mPEG-cMAP-PEGm NP in Balb/c vs. nude mice

Figure II.S63: The circulation time of the mPEG-cMAP-PEGm siRNA NP is similar in Balb/c and nude mice. n=3 mice.

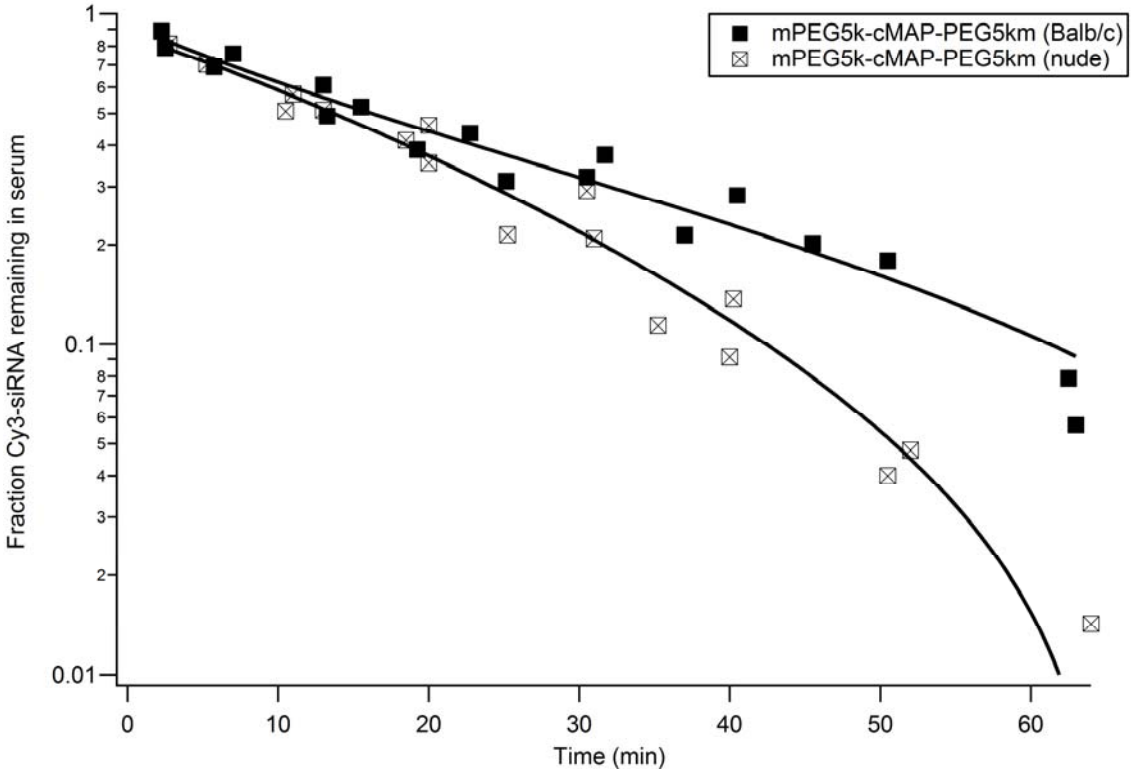

18. Gel images of mPEG-cMAP-PEGm NP in mouse serum

Figure II.S64: This gel shows mPEG-cMAP-PEGm NPs with and without 5-nPBA-PEGm in mouse serum. The samples are run on a 0.5% agarose gel in Tris-Borate-EDTA buffer (pH 8) at 90V, and are detected by the Cy3 fluorophore labeled siRNA on a Typhoon gel scanner with laser excitation 532 nm, emission 580 nm. Lanes are labeled as follows. This shows that the NPs shift further down the gel due to protein adsorption but are intact in mouse serum. SDS dissociates the nanoparticle allowing the siRNA to run down the gel.

1. mPEG-cMAP-PEGm NP
2. mPEG-cMAP-PEGm NP in mouse serum
3. mPEG-cMAP-PEGm NP in mouse serum + SDS
4. mPEG-cMAP-PEGm + 5-nPBA-PEGm NP
5. mPEG-cMAP-PEGm + 5-nPBA-PEGm NP in mouse serum
6. mPEG-cMAP-PEGm + 5-nPBA-PEGm NP in mouse serum + SDS
7. siRNA in mouse serum
8. siRNA in mouse serum + SDS

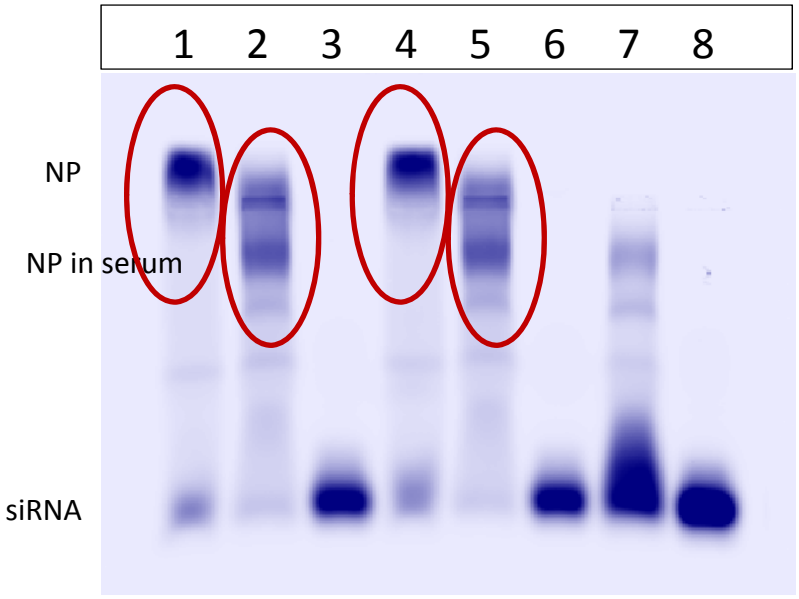

Figure II.S65: A 0.5% agarose gel (made as described in Figure II.S64) is detected by ethidium bromide intercalating siRNA on a Biodocit gel imager. Lanes are labeled as follows. SDS dissociates the NP so the siRNA runs down the gel. This shows that the mPEG-cMAP-PEGm NP is intact in mouse serum, including in serum after 20 minutes of circulation post-injection.

1. Mouse Serum
2. Mouse Serum + SDS
3. siRNA
4. siRNA + SDS
5. mPEG-cMAP-PEGm NP
6. mPEG-cMAP-PEGm NP + SDS
7. Serum collected at 20 min after mPEG-cMAP-PEGm NP injection
8. Serum collected at 20 min after mPEG-cMAP-PEGm NP injection + SDS

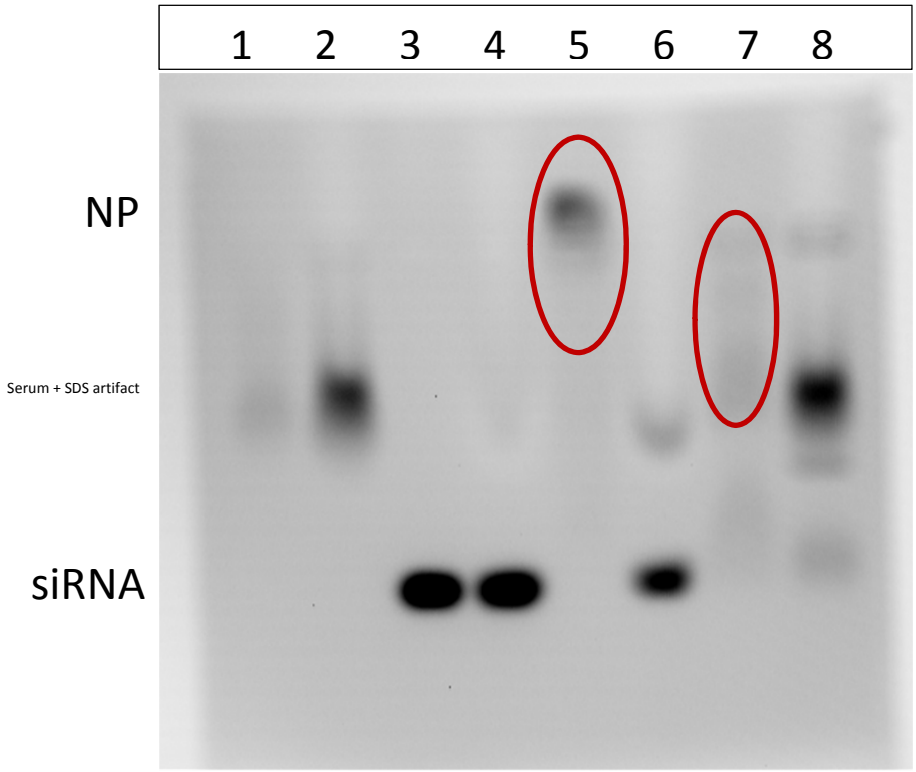

Figure II.S66: This is the same gel as in Figure II.S65, but detected by the Cy3 fluorophore labeled siRNA on a Typhoon gel scanner with laser excitation 532 nm, emission 580 nm. Lanes are labeled as follows. SDS dissociates the NP. The bands detected by fluorescence line up well with the bands detected by ethidium bromide staining. This shows that the mPEG-cMAP-PEGm NP is intact in mouse serum, including in serum after 20 minutes of circulation after injection.

1. Mouse Serum
2. Mouse Serum + SDS
3. siRNA
4. siRNA + SDS
5. mPEG-cMAP-PEGm NP
6. mPEG-cMAP-PEGm NP + SDS
7. Serum collected at 20 min after mPEG-cMAP-PEGm NP injection
8. Serum collected at 20 min after mPEG-cMAP-PEGm NP injection + SDS

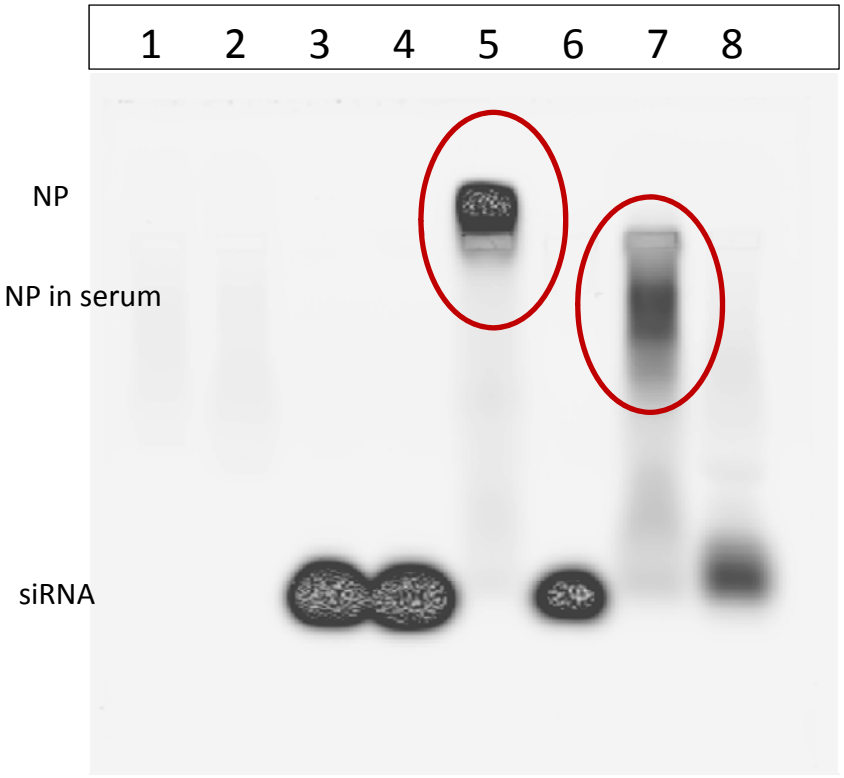

Figure II.S67: This gel is detected by the Cy3 fluorophore labeled siRNA on a Typhoon gel scanner with laser excitation 532 nm, emission 580 nm. Lanes are labeled as follows. SDS dissociates the NP. This shows that the mPEG-cMAP-PEGm NP is intact in mouse serum, including in serum after 20 minutes of circulation after injection.

1. Mouse Serum
2. mPEG-cMAP-PEGm NP
3. mPEG-cMAP-PEGm NP in mouse serum
4. mPEG-cMAP-PEGm NP in mouse serum + SDS
5. Serum collected at 20 min after mPEG-cMAP-PEGm NP injection
6. siRNA
7. siRNA in mouse serum
8. siRNA in mouse serum + SDS

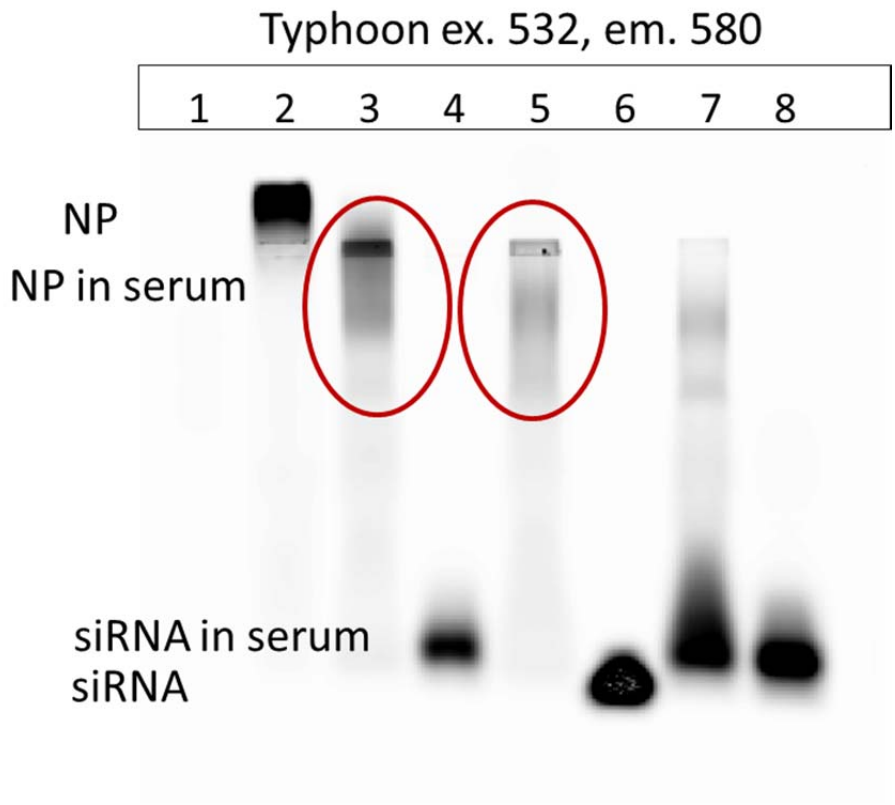

References

1. Wu, S. Y., Lopez-Berestein, G., Calin, G. A., and Sood, A. K. (2014) RNAi Therapies: Drugging the Undruggable. *Science Transl. Med. 6*, 240ps7.
2. Kanasty, R., Dorkin, J. R., Vegas, A., and Anderson, D. (2013) Delivery materials for siRNA therapeutics. *Nat. Mater. 12*, 967–977.
3. Davis, M. E. (2009) The First Targeted Delivery of siRNA in Humans via a Self-Assembling Cyclodextrin Polymer-Based nanoparticle: From Concept to Clinic. *Mol. Pharm. 6*, 659-668.
4. Davis, M. E., Zuckerman, J. E., Choi, C. H. J., Seligson, D., Tolcher, A., Alabi, C. A., Yen, Y., Heidel, J. D., and Ribas, A. (2010) Evidence of RNAi in humans from systemically administered siRNA via targeted nanoparticles. *Nature 464*, 1067–1070.
5. Zuckerman, J. E., Gritli, I., Tolcher, A., Heidel, J. D., Lim, D., Morgan, R., Chmielowski, B., Ribas, A., Davis, M. E., and Yen, Y. (2014) Correlating animal and human phase Ia/Ib clinical data with CALAA-01, a targeted, polymer-based nanoparticle containing siRNA. *Proc. Natl. Acad. Sci. USA 111*, 11449-11454.
6. Zuckerman, J. E., Choi, C. H. J., Han, H., and Davis, M. E. (2012) Polycation-siRNA nanoparticles can disassemble at the kidney glomerular basement membrane. *Proc. Natl. Acad. Sci. USA 109*, 3137-3142.
7. Naeye, B., Deschout, H., Caveliers, V., Descamps, B., Braeckmans, K., Vanhove, C., Demeester, J., Lahoutte, T., De Smedt, S. C., and Raemdonck, K. (2013) *In vivo* disassembly of IV administered siRNA matrix nanoparticles at the renal filtration barrier. *Biomaterials 34*, 2350-2358.
8. Christie, R. J., Matsumoto, Y., Miyata, K., Nomoto, T., Fukushima, S., Osada, K., Halnaut, J., Pittella, F., Kim, H. J., Nishiyama, N., *et al*. (2012) Targeted polymeric micelles for siRNA treatment of experimental cancer by intravenous injection. *ACS Nano. 6,* 5174-5189.
9. Nelson, C. E., Kintzing, J. R., Hanna, A., Shannon, J. M., Gupta, M. K., and Duvall, C. L. (2013) Balancing cationic and hydrophobic content of PEGylated siRNA polyplexes enhances endosome escape, stability, blood circulation time, and bioactivity *in vivo*. *ACS Nano. 7,* 8870-8880.
10. Barrett, S. E., Burke, R. S., Abrams, M. T., Bason, C., Busuek, M., Carlini, E., Carr, B. A., Crocker, L. S., Fan, H., Garbaccio, R. M., *et al*. (2014) Development of a liver-

targeted siRNA delivery platform with a broad therapeutic window utilizing biodegradable polypeptide-based polymer conjugates. *J. Control. Release 183,* 124-137.

11. Gallas, A., Alexander, C., Davies, M. C., Puri, S., and Allen, S. (2012) Chemistry and formulations for siRNA therapeutics. *Chem. Soc. Rev. 42,* 7983-7997.
12. Barros, S. A., and Gollob, J. A. (2012) Safety profile of RNAi nanomedicines. *Adv. Drug Deliver. Rev. 64,* 1730-1737.
13. Ballarin-Gonzalez, B., and Howard, K. A. (2012) Polycation-based nanoparticle delivery of RNAi therapeutics: Adverse effects and solutions. *Adv. Drug Deliver. Rev. 64,* 1717-1729.
14. Gomes-da-Silva, L. C., Simoes, S., and Moreira, J. N. (2013) Challenging the future of siRNA therapeutics against cancer: the crucial role of nanotechnology. *Cell. Mol. Life. Sci. 71,* 1417-1438.
15. Han, H., and Davis, M. E. (2013) Targeted nanoparticles assembled via complexation of boronic acid-containing targeting moieties to diol-containing polymers. *Bioconjugate Chem. 24,* 669-677.
16. Han, H., and Davis, M. E. (2013) Single-Antibody, Targeted Nanoparticle Delivery of Camptothecin. *Mol. Pharm. 10*, 2558-2567.
17. Pun, S. H., and Davis, M. E. (2002) Development of a nonviral gene delivery vehicle for systemic application. *Bioconjugate Chem. 13,* 630-639.
18. Brissault, B., Leborgne, C., Scherman, D., Guis, C., and Kichler, A. (2011) Synthesis of poly(propylene glycol)-*block*-polyethylenimine tri block copolymers for the delivery of nucleic acids. *Macromol. Biosci. 11,* 652-661.
19. Xue, L., Ingle, N. P., and Reineke, T. M. (2013) Highlighting the role of polymer length, carbohydrate size, and nucleic acid type in potency of glycopolycation agents for pDNA and siRNA delivery. *Biomacromolecules 14,* 3903-3915.
20. Yuthavong, Y., Feldman, N., and Boyer, P. (1975) Some chemical characteristics of dimethylsuberimidate and its effect on sarcoplasmic reticulum vesicles. *Biochim. Biophys. Acta 382,* 116-124.
21. Zhong, Z., Feijen, J., Lok, M. C., Hennink, W. E., Christensen, L. V., Yockman, J. W., Kim, Y.-H., and Kim, S. W. (2005) Low molecular weight linear polyethyleneimine-*b*-poly(ethylene glycol)-*b*-polyethyleneimine triblock copolymers: Synthesis, characterization, and *in vitro* gene transfer properties. *Biomacromolecules 6,* 3440-3448.
22. Adeli, M., Ashiri, M., Chegeni, B. K., and Sasanpour, P. (2013) Tumor-targeted drug delivery systems based on supramolecular interactions between iron oxide-carbon

nanotubes PAMAM-PEG-PAMAM linear-dendritic copolymers. *J. Iran. Chem. Soc. 10,* 701-708.

23. Zhu, Y., Sheng, R., Luo, T., Li, H., Sun, W., Li, Y., and Cao, A. (2011) Amphiphilic cationic [dendritic poly(L-lysine)]-*block*-poly(L-lactide)-*block*-[dendritic poly(L-lysine)]s in aqueous solution: Self-aggregation and interaction with DNA as gene delivery carries. *Macromol. Biosci. 11,* 174-186.
24. Han, H. Development of targeted, polymeric delivery vehicles for camptothecin and siRNA via boronic acid-diol complexation. Ph.D. Thesis, California Institute of Technology, Pasadena, CA, 2012.
25. Eriksen, F. Relationship between *in vitro* stability and *in vivo* pharmacokinetic behavior of a polymeric gene delivery system. M.S. Thesis, ETH, Zurich, Switzerland, 2011.
26. Sato, A., Choi, S. W., Hirai, M., Yamayoshi, A., Moriyama, R., Yamano, T., Takagi, M., Kano, A., Shimamoto, A., and Maruyama, A. (2007) Polymer brush-stabilized polyplex for a siRNA carrier with long circulatory half-life. *J. Control. Release 122,* 209-216.
27. D'Addio, S. M., Saad, W., Ansell, S. M., Squiers, J. J., Adamson, D. H., Herrera-Alonso, M., Wohl, A. R., Hoye, T. R., Macosko, C. W., Mayer, L. D., *et al*. (2012) Effects of block copolymer properties on nanocarrier protection from *in vivo* clearance. *J. Control. Release 162,* 208-217.

C h a p t e r 3

Lack of *in vivo* antibody dependent cellular cytotoxicity with antibody containing gold nanoparticles

This chapter has been published as:
Ahmed, M., Pan, D.W., and Davis, M.E. Lack of *in vivo* antibody dependent cellular cytotoxicity with antibody containing gold nanoparticles. *Bioconjugate Chem.* **2015**, *26*, 812-816. doi : 10.1021/acs.bioconjchem.5b00139

Abstract:

Antibody-dependent cellular cytotoxicity (ADCC) is a cytolytic mechanism that can elicit *in vivo* antitumor effects, and can play a significant role in the efficacy of antibody treatments for cancer. Here, we prepared cetuximab, panitumumab, and rituximab containing gold nanoparticles, and investigated their ability to produce an ADCC effect *in vivo*. Cetuximab treatment of EGFR-expressing H1975 tumor xenografts showed significant tumor regression due to the ADCC activity of the antibody *in vivo*, while the control antibody, panitumumab, did not. However, all three antibody containing nanoparticles are not able to suppress tumor growth in the same *in vivo* mouse model. The antibody containing nanoparticles localized in the tumors and did not suppress the immune function of the animals, so the lack of tumor growth suppression of the cetuximab containing nanoparticle suggests that immobilizing antibodies onto a nanoparticle significantly decreases the ability of the antibody to promote an ADCC response.

Introduction

A number of targeted nanoparticles have now been investigated in human clinical trials.[1,2] At this time, there is no clinical example of a full antibody targeted nanoparticle. Since immunotherapies are finding increased importance in cancer, the use of a full antibody targeted nanoparticle could be interesting. This type of therapeutic could potentially elicit immunotherapeutic functions such as antibody-dependent cellular cytotoxicity (ADCC) and complement dependent cytotoxicity (CDC) in addition to targeting the nanoparticles to cancer cell surface receptors and blocking cell signaling from those receptors. While antibody fragments can elicit the latter two functions, they do not stimulate immunotherapeutic pathways.

Numerous preclinical studies utilize full antibody targeted nanoparticles. However, only one investigation has specifically explored the possibility of stimulating an ADCC response.[3] Rituximab is an IgG1 antibody that binds to the CD20 receptor, and rituximab containing lipid nanoparticles were investigated both *in vitro* and *in vivo* for their ability to elicit ADCC. Rituximab nanoparticles exhibited ADCC cell lysis *in vitro*, but the observed *in vivo* therapeutic efficacy of the antibody-lipid conjugates could not be ascribed to ADCC function.[3]

Natural killer (NK) cell based immunotherapies have shown considerable potential for cancer therapy in the clinic.[4,5] ADCC is an immune mechanism dependent on the activity of $CD56^{dim}$ CD^{16+} NK cells. Transgenic mouse models deficient in the CD16 receptor, also known as the activating Fcγ (FcγRIIIa/CD16) receptor are unable to inhibit tumor growth in the presence of IgG1 antibodies that primarily work by inducing an ADCC response.[6] Various types of peripheral blood mononuclear cells (PBMCs) have been

studied for their anti-tumor ADCC activities *in vitro*, and NK cells have been found to induce the most potent ADCC response.[7]

Cetuximab and panitumumab are two antibodies that specifically target the epidermal growth factor receptor I (EGFRI), and possess similar EGFR binding affinities.[8,9] In contrast to cetuximab, panitumumab is not able to elicit an ADCC response.[10] Here, we address the question as to whether full antibodies that are displayed on the surface of nanoparticles can elicit an ADCC response *in vivo*. In order to observe antitumor effects that would be specific to an ADCC response, we selected a lung cancer cell line (H1975) that does not show any *in vitro* anti-proliferative effects upon treatment with either cetuximab or panitumumab. Thus, any anti-tumor behavior observed *in vivo* can be ascribed to an ADCC function (positive for cetuximab and negative for panitumumab). Since gold nanoparticles will not have antitumor effects, antibody containing gold nanoparticles were prepared using cetuximab, panitumumab, and rituximab (negative control), and investigated *in vivo* with xenografts of the EGFR-expressing H1975 lung cancer cell line in athymic nude mice. While cetuximab alone reveals significant ADCC dependent anti-tumor behavior, the lack of anti-tumor function with the cetuximab containing gold nanoparticles shows that the ADCC function from antibody containing nanoparticles maybe be difficult to achieve *in vivo*.

Results and Discussion

Assembly of antibody containing gold nanoparticle:

The assembly of the antibody containing gold nanoparticles was accomplished as follows. Conjugates of polyethylene glycol (PEG) and cetuximab, panitumumab, and rituximab were prepared by antibody reaction with NHS-PEG-OPSS (reacts with amine groups of

antibodies to yield antibody-PEG conjugates through amide bond formation (Scheme III.1)). High pressure liquid-phase chromatography (HPLC) purified antibody-PEG conjugates were analyzed by MALDI-TOF-MS and confirmed to be mono-PEGylated. 50 nm gold nanoparticles (AuNPs) were then functionalized with the mono-PEGylated antibody-PEG conjugates and mPEG-SH (Scheme III.1), and were analyzed for their average hydrodynamic diameter and surface charge (Table III.1). The quantitative number of antibodies per nanoparticle was obtained using two different methods. The results from the two were consistent with each other (Supporting Information, Table III.S1), and the mean values obtained from the two methods are presented in Table III.1. PEGylated AuNPs containing ca. 15-20 antibodies per particle have negative zeta potential values and are stable in deionized water and saline solutions.

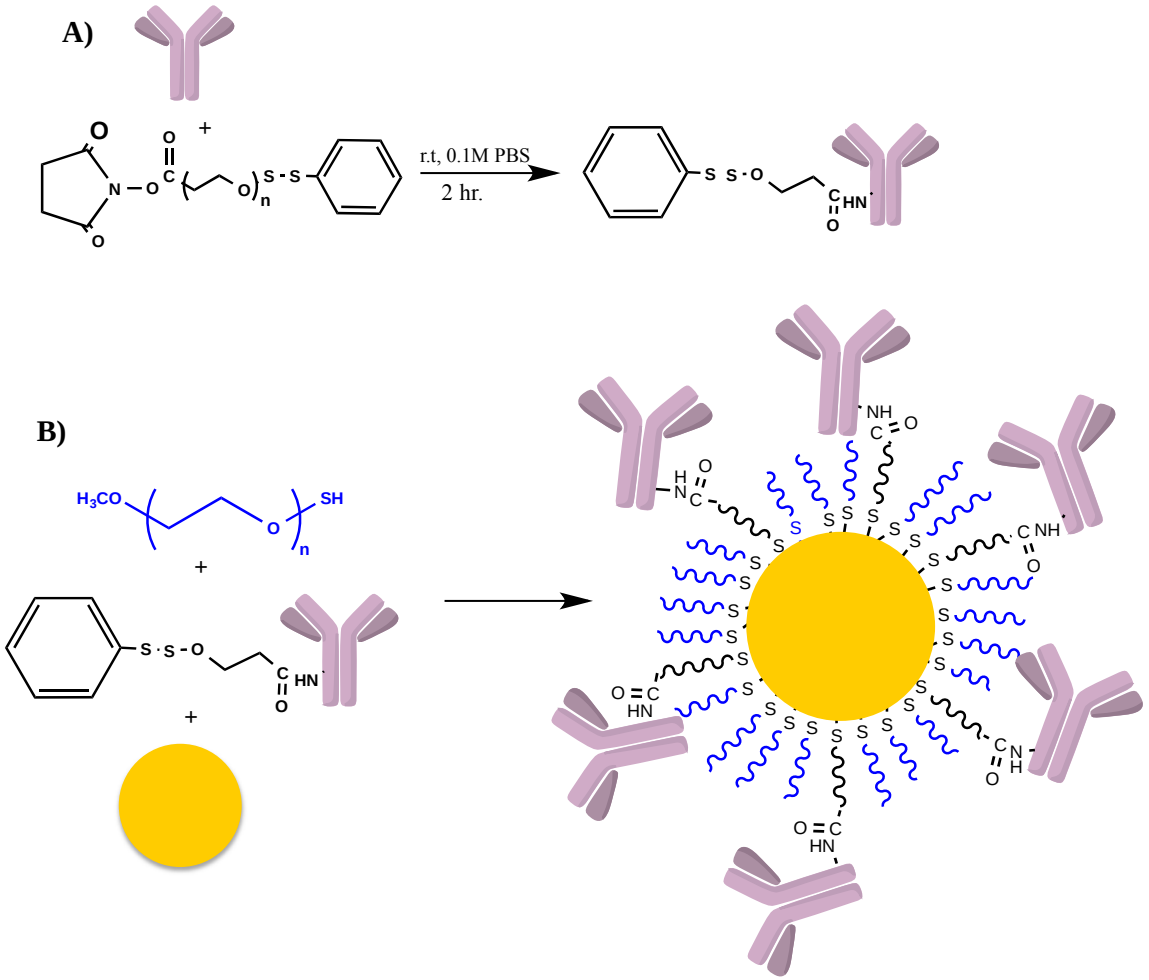

Scheme III.1: Assembly of antibody containing gold nanoparticles. A) Antibodies first reacted with the NHS-PEG-OPSS and then purified. B) In a second step, the antibody conjugates were then combined with mPEG-SH and assembled onto the surface of the gold nanoparticles.

Sample	Size (nm) in PBS by DLS[a]	Size (nm) by NTA[b]	Zeta Potential (mV)[c]	Number of Antibodies on surface
Cetuximab-AuNPs	79.5±4	72.6±0.4	-18.7±1	19±6
Panitumumab-AuNPs	72.8±1.9	74.8±1.6	-19.2±2.1	20±5
Rituximab-AuNPs	82.5±5.5	73.2±1.3	-20.5±1.7	17±3
mPEG-AuNPs	64.1±9.5	72.3±0.9	-19.4±4.3	0

Table III.1: Properties of antibody containing AuNPs. [a]DLS (Dynamic Light Scattering), measured in phosphate buffered saline (PBS). [b]NTA (Nanoparticle Tracking Analysis), measured in deionized water). [c]Measured in 1 mM KCl solution in deionized water.

In vitro Cytotoxicity of Antibodies and Antibody-functionalized Gold Nanoparticles:

The H1975 cell line harbors a double mutation in the kinase domain of EGFR that makes these cells insensitive to treatments with tyrosine kinase inhibitors (TKIs). Also, EGFR specific monoclonal antibodies do not produce anti-proliferative effects with the H1975 cells *in vitro*.[11] The *in vivo* anti-tumor effects observed with cetuximab are thought to be associated with the ADCC activity of the antibody. Here, the anti-proliferative effects of the antibodies cetuximab, panitumumab, and rituximab, and the corresponding antibody containing AuNPs were investigated with the EGFR-TKI resistant H1975 lung cancer cell line via a cell viability assay. The H1975 cells remained viable in the presence of all antibodies and antibody containing AuNPs (Supporting Information, Figure III.S1) 72 hours post-treatment. The results are consistent with previous reports that show no *in vitro* cell death upon exposure of H1975 lung cancer cells to cetuximab or panitumumab,[10] and

reveal that multiple antibodies on the surface of the AuNPS also do not produce any anti-proliferative effects *in vitro*.

Anti-Tumor Effects of Antibodies and Antibody Containing AuNPs:

To investigate the role of ADCC *in vivo,* mice bearing established H1975 xenograft tumors were dosed twice a week for two weeks, and tumor growth was measured over a period of two months. Cetuximab treated mice showed significant tumor regression while panitumumab treated mice did not (Figure III.1). Thus, cetuximab treatments inhibit *in vivo* H1975 tumor growth, and these results are consistent with literature reports.

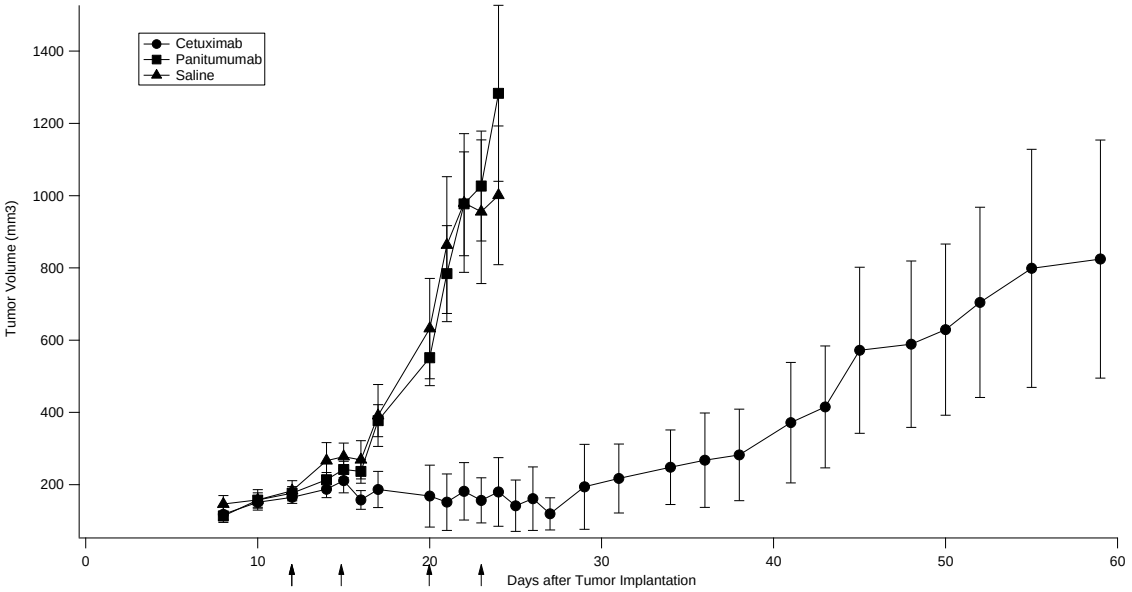

Figure III.1: Effects of antibody treatment on H1975 xenograft tumors in nude mice. Mice treated with panitumumab (squares), cetuximab (diamonds) or saline (triangles) as a negative control. Arrows indicate the days treatment occurred.

Antibody containing AuNPs were investigated for their anti-tumor activities in nude mice bearing H1975 tumor xenografts in order to compare to the results from treatments with the antibodies alone. The data illustrated in Figure III.2 show that neither the cetuximab nor panitumumab containing AuNPs produced an anti-tumor effect *in vivo* (compared to saline, rituximab containing AuNPs, and AuNPs with no antibody). These

results show that attaching the antibody to the surface of the AuNPs abolished cetuximab's ADCC activity *in vivo.*

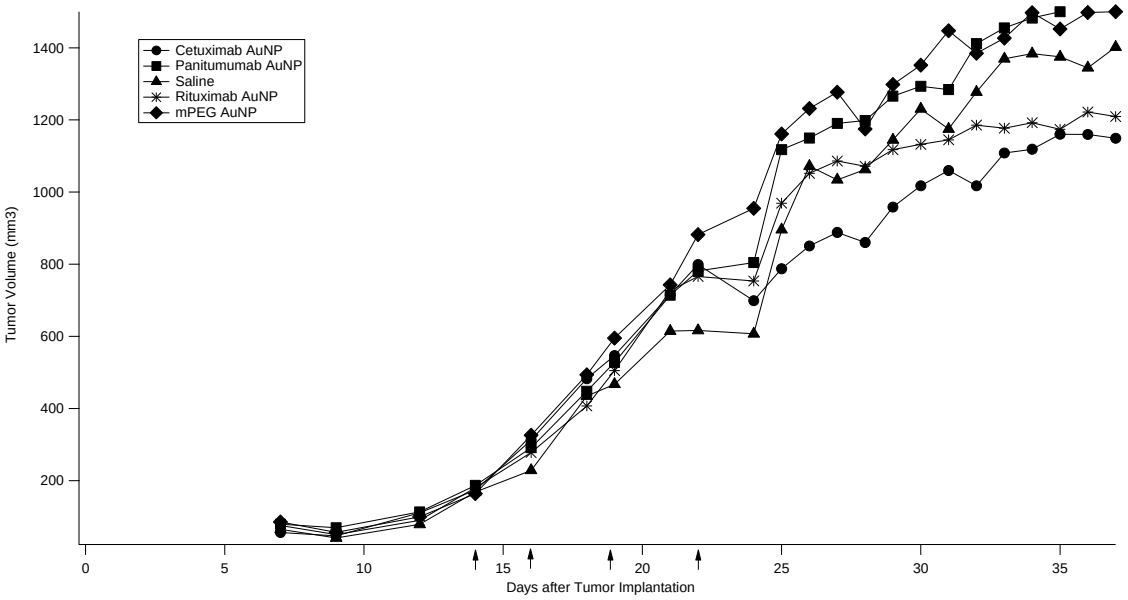

Figure III.2: H1975 xenograft tumor growth in mice treated with antibody containing AuNPs. Non-antibody containing AuNPs, rituximab containing AuNPs and saline used as negative controls. Arrows indicate the days treatment occurred.

Lack of ADCC with cetuximab containing AuNPs is not due to loss of tumor accumulation or presence of immune cells:

The strong tumor regression observed in cetuximab treated mice (Figure III.1) is attributed to the ADCC activity of cetuximab. As expected, no anti-tumor effects are observed with panitumumab, which does not elicit an ADCC effect. This difference in the anti-tumor effect between the two antibodies was completely abolished when they were attached to the AuNPs (Figure III.2). Unfortunately, we were not able to construct an *in vitro* model system for testing the ADCC activity of cetuximab or panitumumab. However, we were able to do so for trastuzumab using the BT474M1 cell line and immortalized NK cells (Supporting Information, Materials and Methods). These model data show that trastuzumab and trastuzumab AuNPs give an *in vitro* ADCC response (Supporting

Information, Figure III.S2). Since we used the same conjugation chemistry with cetuximab and panitumumab as with trastuzumab, we assume that at least some fraction of the antibodies displayed on the surfaces of the nanoparticles are able to bind to their cancer cell surface receptors and stimulate an ADCC response *in vitro*. Thus, in order to better understand the factors that cause the *in vivo* loss in antitumor effects for the cetuximab that is contained on the AuNPs, we must first prove that the AuNPs are in fact reaching the tumors and that these tumors possess immune cells.

AuNPs in tissue can be visualized by silver staining and imaging by light microscopy. Images of silver stained tissues harvested from mice treated with antibody containing AuNPs (Supporting Information, Figure III.S3) show the presence of AuNPs in all treated tumor tissues, as well as in liver, spleen, and small amounts in kidney (non-tumor organs were imaged to confirm that the AuNPs were reaching all organs expected with NPs). No staining was evident for tissues from mice treated with saline (negative control). Thus, the AuNPs are localizing to the tumors in these mice. The presence of immune cells within the tumor tissue was investigated by staining for CD45 (pan-leukocyte) and CD11b (NK) immune cell markers. In comparison to saline treated tumors, no significant difference in the presence of immune cells in tumor sections was found for antibody or antibody containing AuNP treated mice (Supporting Information, Figures III.S4 and III.S5).

Lack of ADCC with cetuximab containing AuNPs is due to loss of ADCC function:

The *in vivo* anti-tumor data shown here reveal that an antibody that can elicit an ADCC effect when used alone loses this function when it is conjugated onto a nanoparticle. Cetuximab injected at 9.3 mg/kg showed significant tumor regression due to an ADCC

effect, while cetuximab containing AuNPs dosed at 0.44 mg of antibody/kg did not show any anti-tumor effects. It should be noted that cetuximab maintains anti-tumor activities in nude mice over the range of 0.4-40 mg/kg.[12]

The mice dosed with 0.44 mg/kg of cetuximab containing AuNPs (0.299 nmoles of gold/gram of body weight) showed significant accumulation of AuNPs in dermis, spleen, liver, and kidney, as revealed by sharp changes in skin color and silver staining of tissues from treated mice. Similar deposition of targeted and non-targeted PEGylated AuNPs in mouse dermis and lymph nodes was previously observed when studied at a much lower dose of AuNPs per mouse.[13] Most importantly, the AuNPs also trafficked to the tumors (Supporting Information, Figure III.S3). Thus, the lack of anti-tumor effects with the cetuximab containing AuNPs is not because the NPs did not reach the tumor.

It has been argued that introducing NPs into animals can modify their immune response via secretion of anti- or pro-inflammatory cytokines, which in turn has an impact on immune cell surveillance in tumor tissues.[14-16] Here, the presence of immune cells in tumor tissues was studied using antibodies against CD45 (for all leukocytes) and CD11b (for mouse NK cells). Immune cell surveillance in the tumors used here was not significantly different regardless of treatment (Supporting Information, Figures III.S4 and III.S5). CD45 and CD11b labeled immune cells were abundant in H1975 tumor xenografts, indicating that the inability of the cetuximab containing AuNPs to show an anti-tumor effect *in vivo* was not due to a suppression of the animal's immune response.

The results presented here lead to the conclusion that covalent immobilization of an antibody on a nanoparticle surface can eliminate the ADCC function of the antibody. Here, we conjugated the antibody to PEG via reactions with amines on the antibody. Due to the

presence of several amines on the antibody, the conjugation of the PEG component will occur at various sites on the antibody. The antibody-PEG conjugates were purified by HPLC to obtain a mono-PEGylated fraction for attachment to the nanoparticle surface. However, the orientation and distribution of antibodies on the nanoparticle surface, such as whether the Fc region is accessible to immune cell binding may play an important role in eliminating the ADCC effects *in vivo*. At this time, the mechanistic origin of the loss in ADCC with nanoparticle containing antibodies remains unknown. Results from a model *in vitro* system suggest that at least a fraction of the antibodies that are contained on the surfaces of the gold nanoparticles can bind to the appropriate cancer cell surface receptor and stimulate an *in vitro* ADCC response. Thus, at this time, the mechanistic origin of the *in vivo* loss in ADCC with nanoparticle containing antibodies remains unknown. The ability to perform site-specific conjugation to the antibody like what is presently done with antibody drug conjugates[17] may help resolve some of these issues.

Supporting Information:

Table of Contents:

Materials and Methods:

Synthesis of antibody-PEG conjugates:

Cetuximab, rituximab, panitumumab, and trastuzumab were obtained from Dr. Yun Yen at the City of Hope. Antibody-PEG-OPSS conjugates were prepared by reacting amine groups of antibodies with NHS-PEG-OPSS (5kDa, Nanocs) at a 5:1 PEG to antibody ratio in 0.1 M phosphate buffer, pH 7.4. The conjugates were purified by high performance liquid chromatography (HPLC) using 0.1 M phosphate buffered saline (PBS), pH 7.4, as the elution buffer. Collected fractions were analyzed by

matrix assisted laser desorption ionization-time of flight mass spectrometry (MALDI-TOF-MS).

Synthesis of antibody-functionalized gold nanoparticles:

50 nm gold nanoparticles (AuNPs) (Ted Pella) were surface functionalized with mPEG-SH (5 kDa, Nanocs) and antibody-PEG-OPSS conjugates by mixing 50:10:1 molar ratios of Au:mPEG:antibody-PEG in deionized water. AuNPs were stirred at room temperature for 2 hours. Surface functionalized AuNPs were centrifuged at 14,000 *g* for 10 minutes, the supernatant was removed, and AuNPs were washed with deionized water three times. The purified nanoparticles were re-suspended in deionized water or buffer solution for further characterization. The concentration of antibody-functionalized AuNPs was determined by nanoparticle tracking analysis (NTA) using a Nanosight NS500 system.

Physiochemical Characterization of AuNPs:

mPEG-AuNPs and antibody functionalized AuNPs were pelleted and were re-suspended in saline and deionized water. The hydrodynamic diameter and zeta potential (ζ) of mPEG-AuNPs and antibody functionalized AuNPs were measured using ZetaPALS (Brookhaven Instruments Corporation). Hydrodynamic diameter was also measured by nanoparticle tracking analysis (NTA) using a Nanosight NS500 system.

Quantification of Antibodies per Particle:

Fluorescent Labeling of Antibody-PEG conjugates: Dylight-650 (Pierce) labeled fluorescent antibody-PEG conjugates were prepared according to the manufacturer's protocol. Antibody coated gold nanoparticles were synthesized using the experimental

conditions described above. The amount of antibody in the supernatant of AuNPs was estimated by measuring the fluorescence of the labeled antibody using an Infinite M200 microplate reader (Tecan). The fluorescence of the antibody in the supernatant was subtracted from the original fluorescence values measured in the feed amount of antibody per sample.

Ortho-Phthaldehyde Assay (OPA):

Antibody-PEG conjugates bearing a base labile linker, (Bis[2-(succinimidooxycarbonyloxy)ethyl]sulfone) (BSCOES), were prepared by mixing antibody:NH_2- PEG-SH:BSCOES at molar ratios of 1:10:25, respectively, in 0.1 M PBS, pH 7.4. The conjugates were purified by HPLC. Antibody-functionalized gold nanoparticles were prepared, as described above. The purified antibody-functionalized AuNPs were dispersed in 8 mM boric acid buffer (pH 10.8) containing 3.5% Birj-35 and were incubated at 37°C overnight. The supernatant was collected and was reacted with 0.06M OPA in the presence of 0.025M 2- mercaptoethanol, and fluorescence was measured using an excitation λ=340 nm and an emission λ=450 nm using an Infinite M200 microplate reader (Tecan). The amount of antibody on the AuNP surface was determined, using a calibration curve of antibody-PEG conjugates.

Cell Line:

H1975 (ATCC) was cultured in RPMI-1640 media (ATCC) containing 10% fetal bovine serum (FBS) in a humidified atmosphere at 37°C with 5% CO_2.

Cell Viability Assay:

H1975 cells were seeded at 5,000 cells per well in 96-well plates and were treated with antibodies and antibody-functionalized gold nanoparticles for 72 hours. H1975 cell viability was evaluated using the MTS assay (Promega).

In vitro Antibody Dependent Cell Cytotoxicity (ADCC) assay:

The H1975 cell line was unable to provide satisfactory cell lysis results even with the cetuximab antibody alone using NKL-cells (DFCI, Boston MA), an immortalized NK cell line, and the lactate dehydrogenase (LDH) assay to measure ADCC *in vitro*. Therefore, another model using the BT474M1 cell line and trastuzumab to see whether ADCC occurs with the antibody, antibody-PEG conjugates, and antibody-functionalized AuNPs was developed. In addition to the Fab fragment of trastuzumab, which does not have the Fc region to which NK cells bind, rituximab was used as a negative control.

Trastuzumab-Fab Synthesis:

Trastuzumab IgG was incubated with a papain-modified agarose gel slurry (Pierce) at 37°C for 8 hours. The enzyme to substrate ratio was 1:160 weight/weight. The digested IgG was neutralized, and free IgG and Fc segments were removed using a protein A column. The purified Fab was analyzed using sodium dodecyl sulfate poly acrylamide gel electrophoresis (SDS PAGE).

Cell Lines:

NKL-cells (DFCI, Boston MA) were cultured in the presence of IL-2 (Peprotech) and 10% heat inactivated FBS (Invitrogen). BT474M1 cells (UCSF) were maintained in RPMI-1640 media (Invitrogen) containing 10% ultra-low IgG FBS (Invitrogen) in

humidified chambers at 37°C with 5% CO_2. The cells were sub-cultured twice a week and were seeded in 96-well tissue culture plates.

ADCC Assay:

The cells were treated with varying concentrations of antibodies (10-0.001 μM), Fab, antibody- PEG conjugates, and antibody-conjugated gold nanoparticles at a 10:1 ratio of NKL to BT474M1 cells. ADCC was evaluated 3 hours post-treatment using a lactate dehydrogenase (LDH) (Roche) assay according to the manufacturer's protocol. Because the same chemistry was used for antibody-PEG coupling and AuNP synthesis, the same phenomenon observed with trastuzumab and trastuzumab-AuNPs on the BT474M1 cell line should hold true for cetuximab and cetuximab-AuNPs on the H1975 cell line.

Xenograft Experiments:

All mouse experiments were approved by the California Institute of Technology Institutional Animal Care and Use Committee. $1x10^7$ H1975 cells, suspended in 0.2 mL of serum-free RPMI-1640 media, were injected subcutaneously into the left rear flank of each 8-week old athymic NCr nude mouse (Taconic Biosciences, Inc). Xenograft tumor size was monitored daily or every other day using electronic calipers starting 7 days post-implantation. Tumor volume was calculated using the equation $V = W^2 \times L / 2$, where W is the shortest tumor dimension and L is the longest tumor dimension. When tumors reached 200 mm^3, mice were divided into groups of 7 mice and treated via tail vein IV injection with either saline, cetuximab, or panitumumab at a dose of 9.34 mg/kg, or saline, cetuximab-AuNP, panitumumab-AuNP, rituximab-AuNP, or mPEG-AuNP at a dose of 2.25×10^{12} nanoparticles/25 g

mouse, which corresponds to 0.4mg/kg of antibody per mouse. Treatment was repeated 3 times, for a total of 4 doses over 2 weeks. Mice were followed until tumors reached 1500 mm^3 or for 2 months.

Immunohistochemistry (IHC):

Mice were euthanized by CO_2 asphyxiation 24 hours post 2nd injection. Tumors were embedded in Tissue-Tek optimal cutting temperature compound (Sakura) and were frozen at -80ºC. Tissue blocks were sectioned (14 μm), and were lightly fixed in 10% buffered formalin for 15 minutes. IHC analysis was performed for immune cell detection in tumor sections. CD45 (BD Biosciences), and CD11b (Biolegend) antibodies were used at 1:100 dilutions. Tissues were imaged using a Zeiss LSM 510 META confocal laser scanning microscope (CLSM). Gold nanoparticles were visualized in tissue sections using a silver enhancement kit (Ted Pella) and imaged with an Olympus IX50 light microscope.

Sample	# of Antibodies by Fluorescent labeling	# of Antibodies by OPA assay
Cetuximab-AuNPs	21±7	16±4
Panitumumab-AuNPs	22±4	18±6
Rituximab-AuNPs	17±3	

Table III.S1: Quantification of antibodies on AuNPs surface using two different methods.

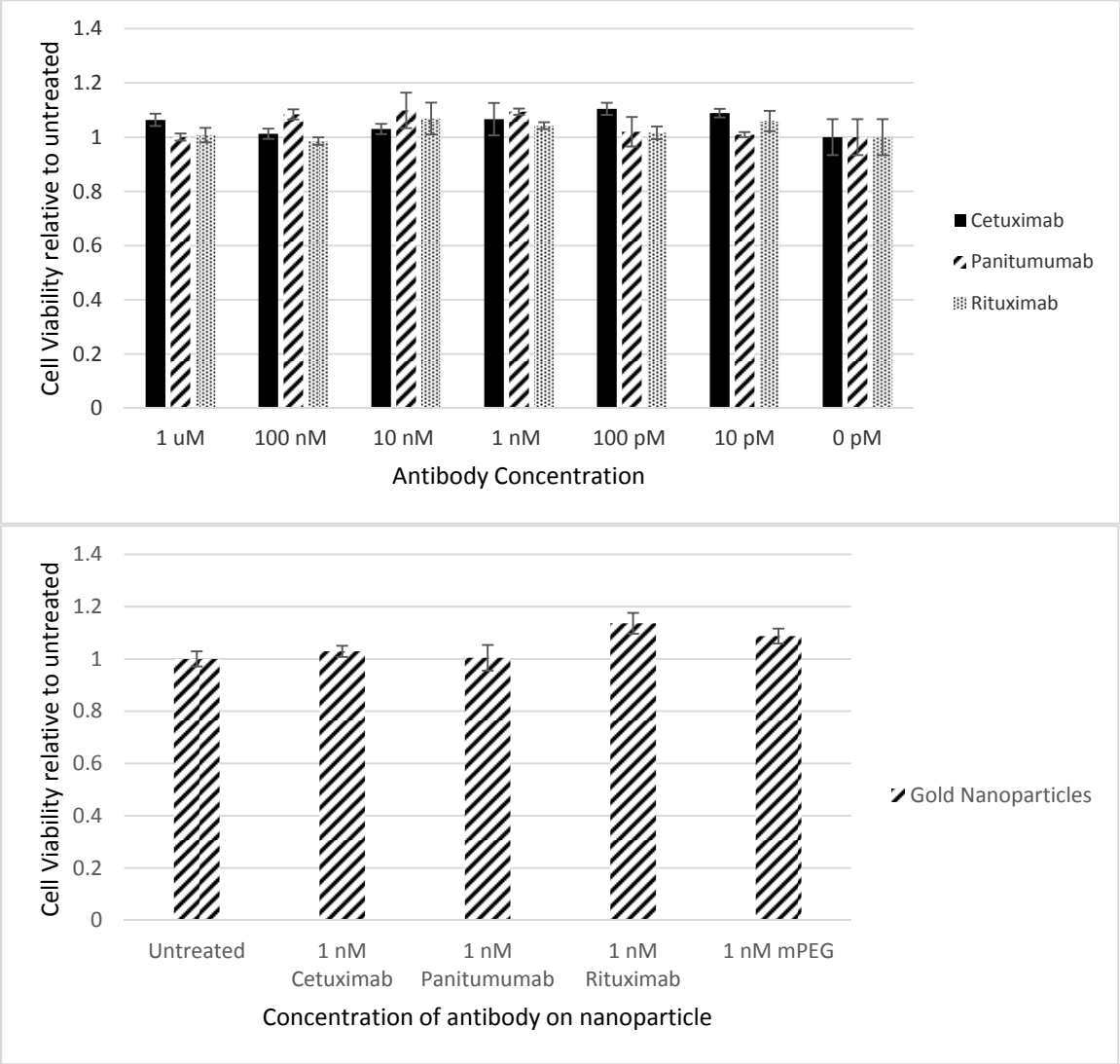

Figure III.S1: Cell viabilities of H1975 cells 72 hours post-incubation with antibodies (top) and antibody-functionalized AuNPs (bottom), as determined by MTS assay. Results reported in terms of average absorbance compared to untreated cells, with error bars denoting the standard error of 5 replicates.

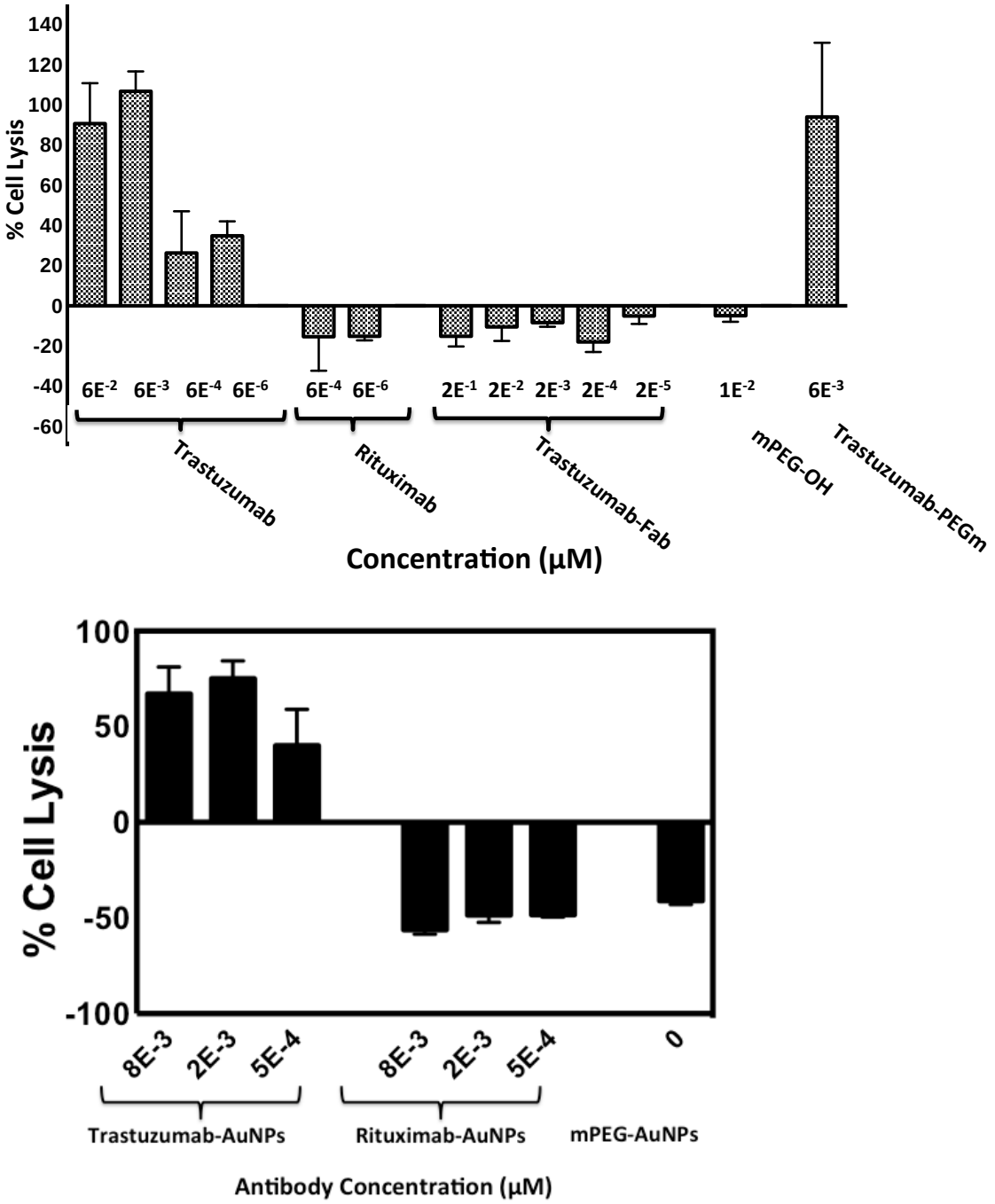

Figure III.S2: ADCC in the BT474M1 cell line occurs with trastuzumab and trastuzumab-PEG but not trastuzumab-Fab or rituximab (top); and with trastuzumab AuNPs but not rituximab- or mPEG-AuNPs (bottom) as determined by the LDH assay.

Tumor

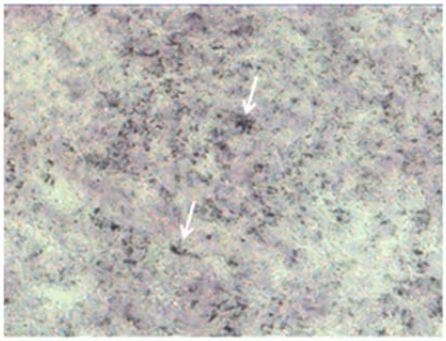

Cetuximab-gold nanoparticle

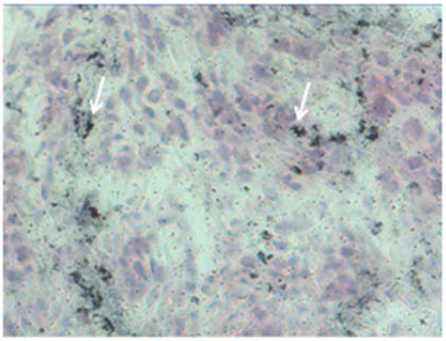

Panitumumab-gold nanoparticle

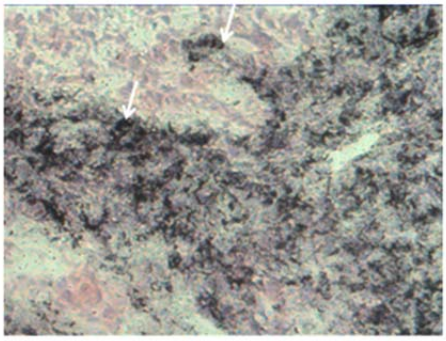

Rituximab-gold nanoparticle

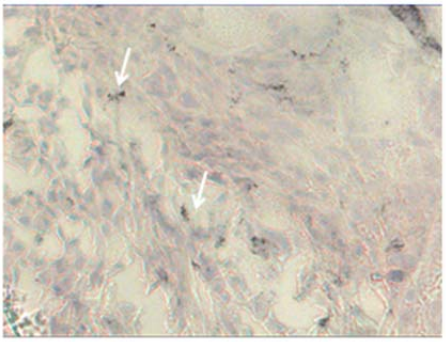

mPEG-gold nanoparticle

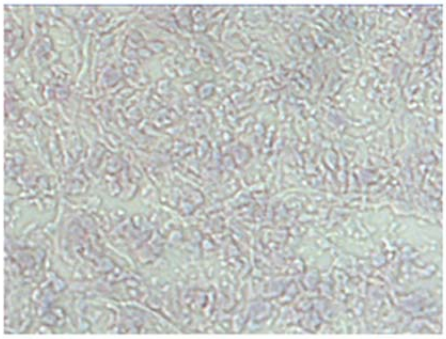

Saline

Liver

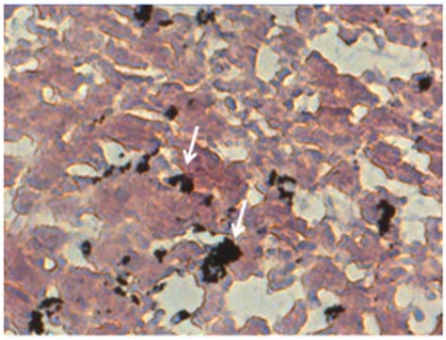

Cetuximab-gold nanoparticle

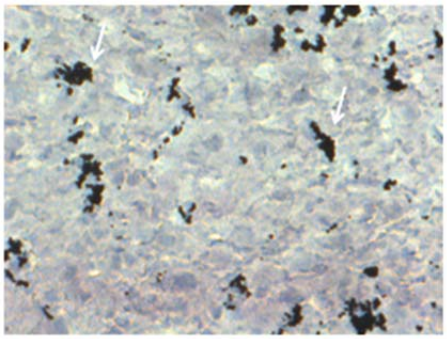

Panitumumab-gold nanoparticle

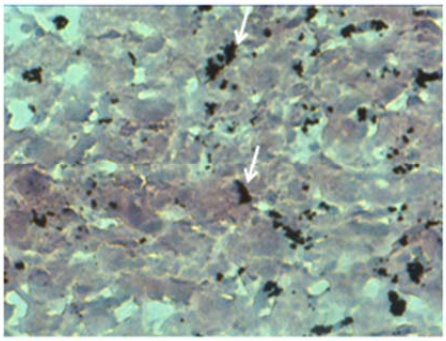

Rituximab-gold nanoparticle

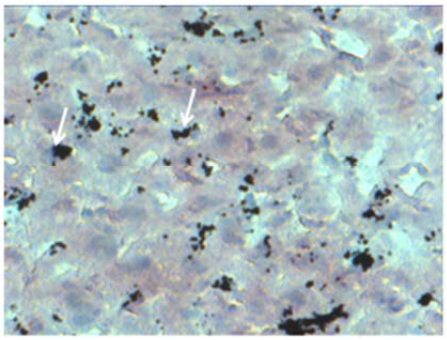

mPEG-gold nanoparticle

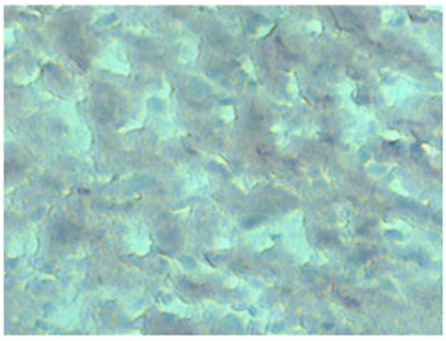

Saline

Spleen

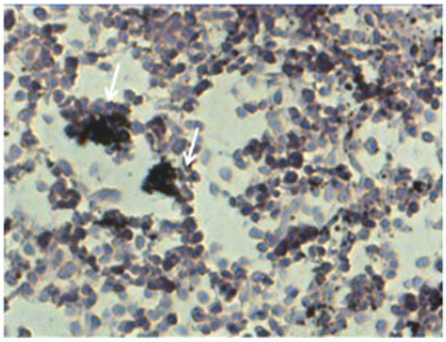

Cetuximab-gold nanoparticle

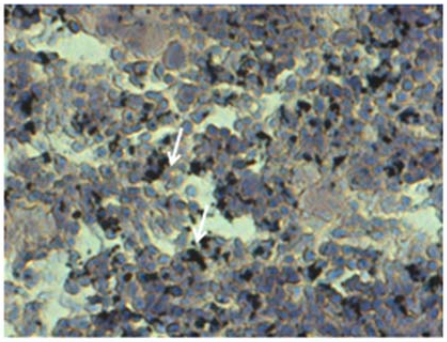

Panitumumab-gold nanoparticle

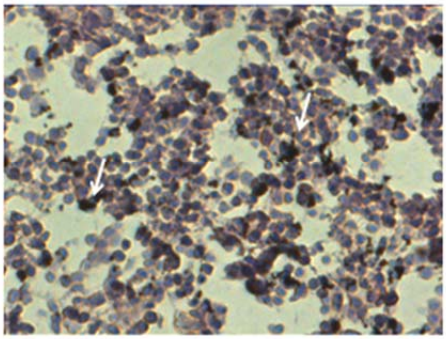

Rituximab-gold nanoparticle

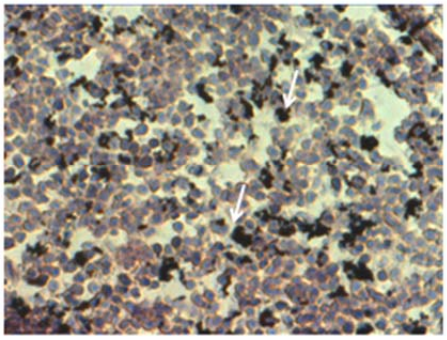

mPEG-gold nanoparticle

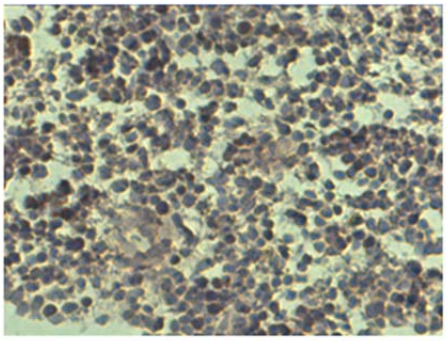

Saline

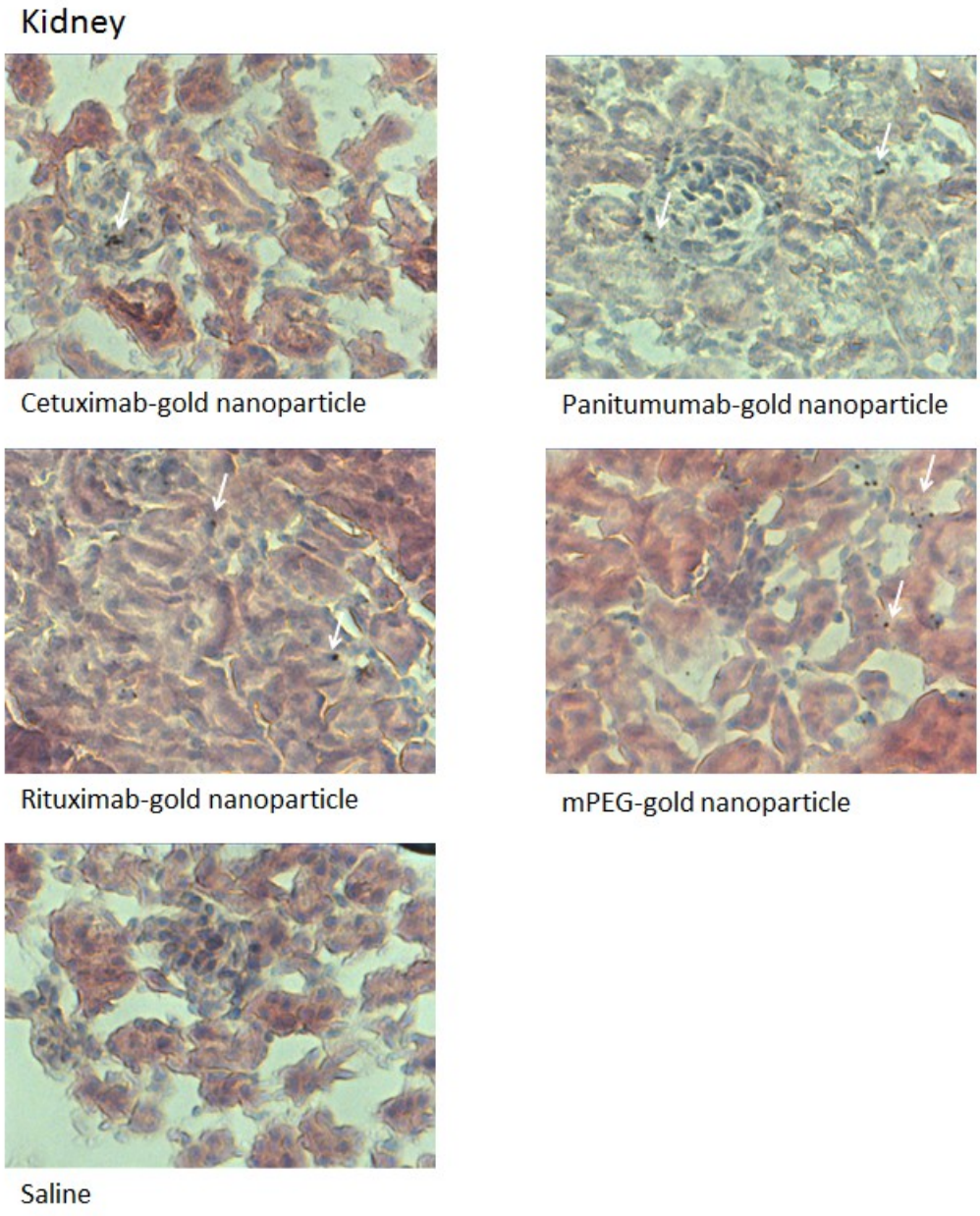

Figure III.S3: Silver enhancement of gold nanoparticles in frozen tissue sections of tumor (pg. 153), liver (pg. 154), spleen (pg. 155), and kidney (pg. 156). The black patches denoted by the white arrows indicate the presence of gold nanoparticles in the tissue sections, which are absent from tissues of saline-treated mice.

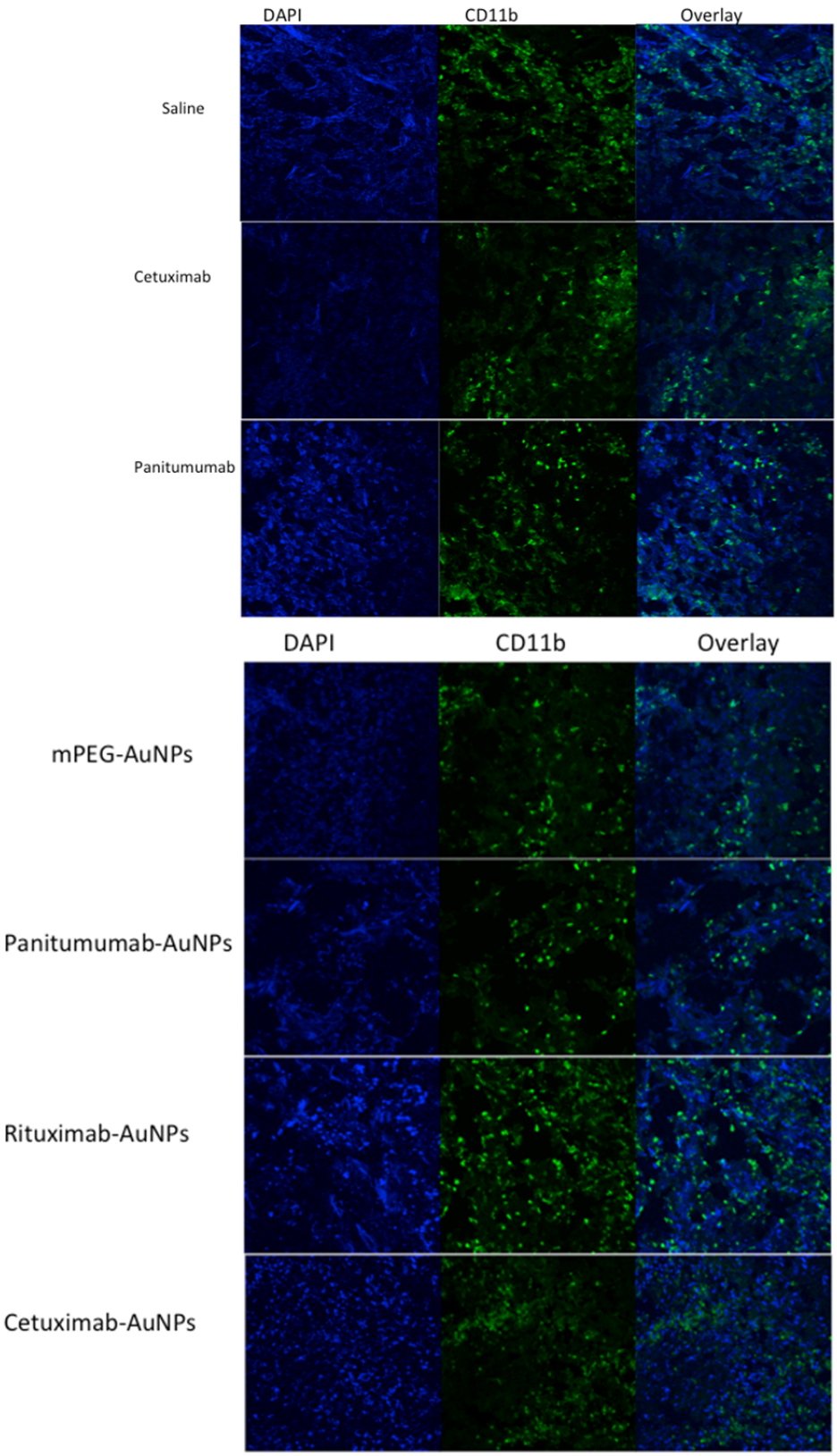

Figure III.S4: CD11b staining of NK cells in tumor tissues. No difference in NK cells present in the tumors can be seen between the various treatment groups.

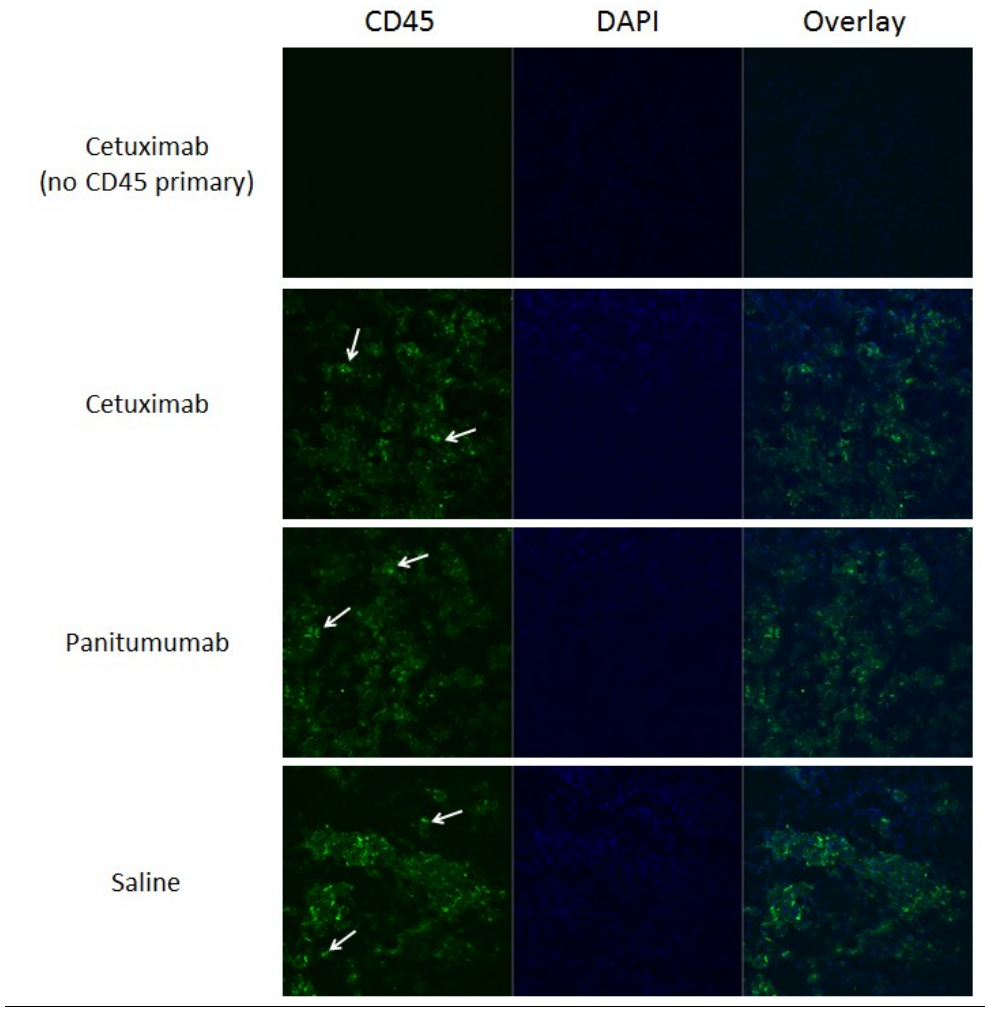
CD45
DAPI
Overlay
Cetuximab
(no CD45 primary)
Cetuximab
Panitumumab
Saline

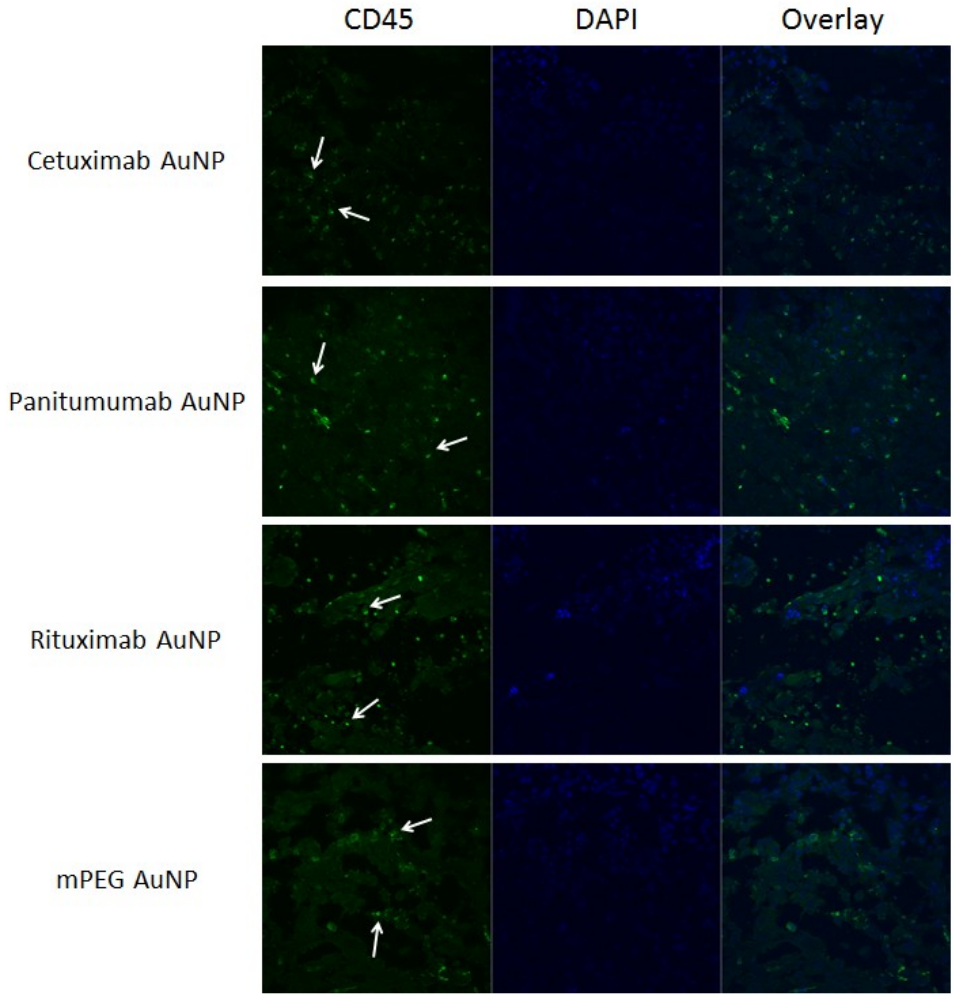

Figure III.S5: CD45 staining of frozen tumor sections as an indication of total immune cell infiltration present in tumors. Antibody (pg. 158) and antibody-functionalized gold nanoparticle (pg. 159) treated mice are shown. No difference can be seen between the various treatment groups.

Acknowledgements:

We thank Kristin Anderson for performing MTS cell viability assays, Mona Shahgholi for MALDI-TOF-MS training, and Andres Collazo (Beckman Imaging Center) for confocal microscopy trainning. This work was supported by the National Cancer Institute Grant CA 151819, and the National Science and Engineering Research Council of Canada (NSERC) (fellowship for MA).

References:

1. Davis, M.E., Chen, Z.G. & Shin, D.M. (2008) Nanoparticle therapeutics: an emerging treatment modality for cancer. *Nat. Rev. Drug Discov.* **7**, 771–782.
2. Bertrand, N. *et al*. (2014) Cancer nanotechnology: The impact of passive and active targeting in the ear of modern cancer biology. *Adv. Drug Del. Rev*. **66**, 2-25.
3. Popov, J., Kapanen, A.I., Turner, C., Ng, R., Tucker, C., *et al.* (2011) Multivalent rituximab lipid nanoparticles as improved lymphoma therapies: indirect mechanisms of action and *in vivo* activity. *Nanomedicine Lond.* 6(9), 1575-1591.
4. Roberti, M.P., Mordoh, J., Levy, E.M. (2012) Biological role of NK cells and immunotherapeutic approaches in breast cancer. *Front Immunol* 3(375): doi: 10.3389/fimmu.2012.00375.
5. Cheng, M., Chen, Y., Xiao, W., Sun, R., Tian, Z. (2013) NK cell-based immunotherapy for malignant diseases. *Cell Mol Immunol* 10(3), 230-252.
6. Clynes, R.A., Towers, T.L., Presta, L.G., Ravetch, J.V. (2000) Inhibitory Fc receptors modulate *in vivo* cytoxicity against tumor targets. *Nat Med* 6(4), 443-446.
7. Seidel, U.J.E., Schlegel, P., and Lang, P. (2013) Natural killer cell mediated antibody-dependent cellular cytotoxicity in tumor immunotherapy with therapeutic antibodies. *Front. Immunol. 4(76),* doi: 10.3389/fimmu.2013.00076.
8. Voigt, M., Braig, F., Gothel, M., Schulte, A., Lamszus, K., *et al.* (2012) Functional Dissection of the epidermal growth factor receptor epitopes targeted by Panitumumab and Cetuximab. *Neoplasia* 14(11), 1023-1031.
9. Patel, D., Guo, X., Ng, S., Melchior, M., Balderes, P., Burtrum, D., Persaud, K., Luna, X., Ludwig, D.L., and Kang, X. (2010) IgG isotype, glycosylation, and EGFR expression determine the induction of antibody-dependent cellular cytotoxicity *in vitro* by cetuximab. *Hum. Antibodies 19,* 89-99.

10. Lopez-Albaitero, A., and Ferris, R.L. (2007) Immune activation by epidermal growth factor receptor-specific monoclonal antibody therapy for Head and Neck Cancer. *Arch Otolaryngol Head Neck Surg* 133(12), 1277-1281
11. Lu, Y., Liang, K., Li, X., and Fan, Z. (2007). Responses of cancer cells with wild-type or tyrosine kinase domain-mutated epidermal growth factor receptor (EGFR) to EGFR-targeted therapy are linked to downregulation of hypoxia-inducible factor-1a. *Mol. Cancer 6,* 63-75.
12. Steiner, P., Joynes, C., Bassi, R., Wang, S., Tonra, J.R., Hadari, Y.R., Hicklin, D.J. (2007) Tumor growth inhibition with cetuximab and chemotherapy in non-small cell lung cancer xenografts expressing wild-type and mutated epidermal growth factor receptor. *Clin Cancer Res* 13(5),1540-1551.
13. Sykes, E.A., Dai, Q., Tsoi, K.M., Hwang, D.M., and Chan, W.C.W. (2012) Nanoparticle exposure in animals can be visualized in the skin and analyzed via skin biopsy. *Nat Commun* 13(5), 3796.
14. Tsai, C.-Y., Lu, S.-L., Hu, C.-W., Yeh, C.-S., Lee, G.-B., & Lei, H-Y. (2012) Size-dependent attenuation of TLR9 signaling by gold nanoparticles in macrophages. *J Immunol* 188(1), 68-76.
15. Dobrovolskaia, M.A. and McNeil, S.E. (2007) Immunological properties of engineered nanomaterials. *Nat Nanotechnol* 2(8), 469-478.
16. Lin, A.Y., Almeida, J.P.M., Bear, A., Liu, N., Luo, L., *et al*. (2013) Gold nanoparticle delivery of modified CpG stimulates macrophages and inhibits tumor growth for enhanced immunotherapy. *PLOS One* 8(5), e63550.
17. Agarwal, P., Bertozzi, C.R. (2015) Site-Specific Antibody-Drug Conjugates: The Nexus of Bioorthogonal Chemistry, Protein Engineering, and Drug Development. *Bioconj. Chem. 26*, 176-192.

Chapter 4

Achieving cell internalization, endosomal escape, and efficacy with the cMAP siRNA nanoparticle system

ABSTRACT

In a previous work, we discussed the creation of a cationic mucic acid polymer (cMAP)-based nanoparticle (NP) siRNA delivery system. An mPEG-cMAP-PEGm triblock polymer showed greatly enhanced circulation time in the bloodstream over a cMAP + 5nPBA-PEG5km NP formulation. We add a targeting agent to effect NP cellular internalization and incorporate histidine in the polymer (TriB-His) to achieve siRNA endosomal escape into the cytosol. This NP formulation was able to achieve knockdown of mRNA expression using (i) 2 mol% cetuximab targeting agent and siEGFR in H1975 NSCLC cells and (ii) 4 mol% transferrin targeting agent and siRRM2 in Neuro-2A neuroblastoma cells. Some effects, though mixed, are seen with (i) the cMAP + 5nPBA-PEG5km NP formulation containing siEGFR and targeted with 0.13 mol% cetuximab-PEG5k-5nPBA in H1975 xenografts and (ii) the TriB-His NP formulation containing siBRAF and targeted with 0.25 mol% transferrin-PEG5k-$(5nPBA)_2$. Further exploration of the appropriate amount of targeting agent to use, or whether the targeting agent should be directly conjugated to cMAP so that it cannot detach from the nanoparticle, is necessary for optimal nanoparticle delivery and internalization into cells for siRNA to function.

INTRODUCTION

Small interfering RNA (siRNA) is a short ca. 21 base pair double stranded siRNA which acts through an RNA interference (RNAi) pathway using the RNA induced silencing

complex (RISC) in the cytosol of cells to cleave the complementary messenger RNA (mRNA). siRNA is a promising candidate as a therapeutic for silencing one or more overexpressed or mutated messenger RNA (mRNA) sequences encoding any type of protein that drives many types of malignant cells.[1] However, siRNA can activate the innate immune system through the complement pathway and is also readily degraded by nucleases in the bloodstream, so a delivery system is need to protect the siRNA from nuclease degradation in the bloodstream as well as to prevent the presence of free siRNA from being injected.[2] Additionally, siRNA is rapidly cleared from the bloodstream through the kidneys, and current siRNA delivery systems that exist only marginally prolong the circulation time.[3-8] We created a biocompatible delivery system for siRNA that has a long circulation time in the bloodstream.[9] These highly stable particles need a targeting agent to be internalized into the cells, where they end up in an endosome. For the siRNA to function, it needs to escape from the endosome to the cytosol of the cell. In order to achieve the latter endosomal escape function, we have incorporated a histidine group between the PEG and cMAP in the mPEG-cMAP-PEGm triblock to form mPEG-His-cMAP-His-PEGm (TriB-His). Histidine contains an imidazole group which acts as a proton sponge to prevent acidification of the endosome, leading it to burst and release siRNA into the cytosol.

RESULTS AND DISCUSSION

We have previously synthesized an mPEG-cMAP-PEGm triblock polymer which encapsulated siRNA and formed stable 30-40 nm particles.[9] These nanoparticles (NPs) had a long circulation time with nearly 10% of the formulation still remaining in the mouse bloodstream 1 h after intravenous (IV) injection. To achieve efficacy with this very stable

nanoparticle, a targeting component is needed so that the nanoparticle can bind to cell surface receptors and be endocytosed. Furthermore, the siRNA contained in the nanoparticle needs to escape from the endosome and reach the cytosol of the cell where the RNA-induced silencing complex (RISC) is located in order to cleave the complementary mRNA.

Nanoparticle Targeting

To target the nanoparticle, we utilized the vicinal diol groups present on the mucic acid entity in cMAP. Boronic acids have the ability to bind to diols. 3-carboxy-5-nitrophenylboronic acid, which has a pKa of 6.8, was used because the electron withdrawing nitro and carboxyl groups allow it to bind to the diol at a physiologic pH of 7.4 and dissociate in an acidic endosomal pH of 5.5, as shown in Scheme IV.1.[10] We linked the 3-carboxy-5-nitrophenylboronic acid to a H_2N-PEG-COOH through an amide bond to synthesize 5-nitrophenylboronic acid-PEG-COOH (5nPBA-PEG-COOH), as shown in scheme IV.2. The carboxylic acid group on the end of PEG can be conjugated to lysine groups on proteins such as transferrin (Scheme IV.3) or antibodies (which are also proteins) such as cetuximab (Scheme IV.4) using EDC/NHS chemistry to form an amide bond. We had discussed in our earlier work around nanoparticle stability the theory that some 5nPBA-PEG5km, used to stabilize NPs formulated with cMAP, sloughs off of NP during circulation in the bloodstream.[9] Therefore, we sought to attach the targeting agent with the same pH-tunable properties but with stronger binding. The presence of the vicinal diols on mucic acid allows 2 boronic acids to bind to the same mucic acid. Therefore, by following scheme IV.5, we synthesized a diboronic acid, di(5-nitrophenylboronic acid), that links two 3-carboxy-5-nitrophenylboronic acid groups onto lysine using an amide bond

between the carboxyl group on the 3-carboxy-5-nitrophenylboronic acid and the amines on lysine (Supporting Information (SI) Figures IV.S1-IV.S4). This diboronic acid has an order of magnitude greater binding affinity using an Alizarin Red S (ARS) assay, 10^7 M^{-1}, than the single boronic acid, 10^6 M^{-1}, to cMAP, though it has the same binding constant of ca. 3 x 10^4 to ARS because ARS only possesses one site for boronic acid binding (Table IV.1).

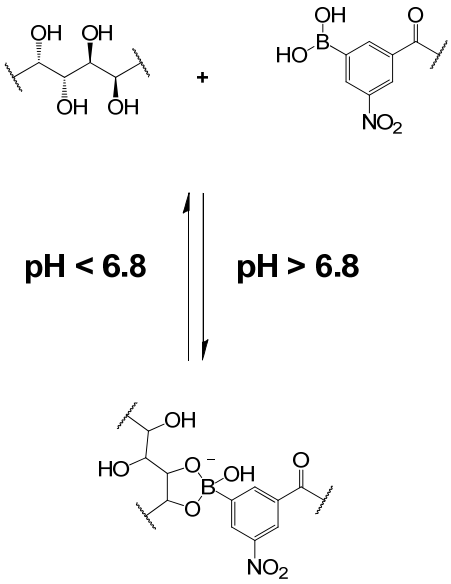

Scheme IV.1: pH dependence of 5-nitrophenyl boronic acid.

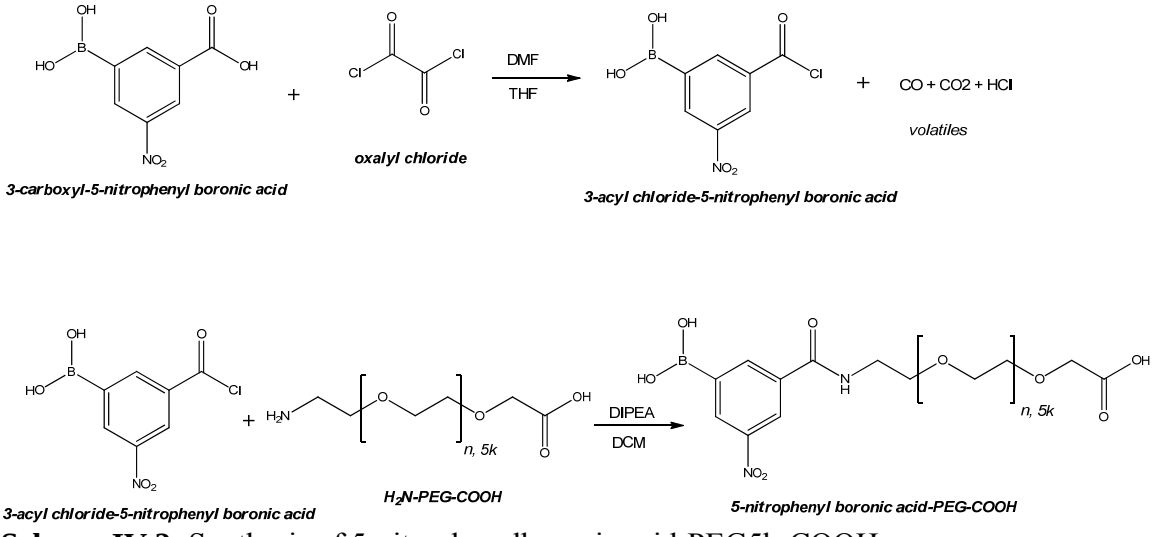

Scheme IV.2: Synthesis of 5-nitrophenylboronic acid-PEG5k-COOH.

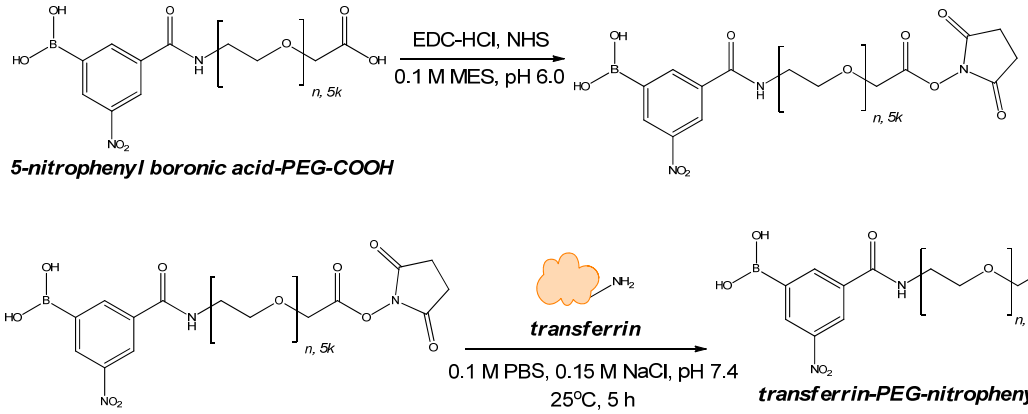

Scheme IV.3: Conjugation of a protein such as transferrin to 5-nitrophenylboronic acid-PEG-COOH.

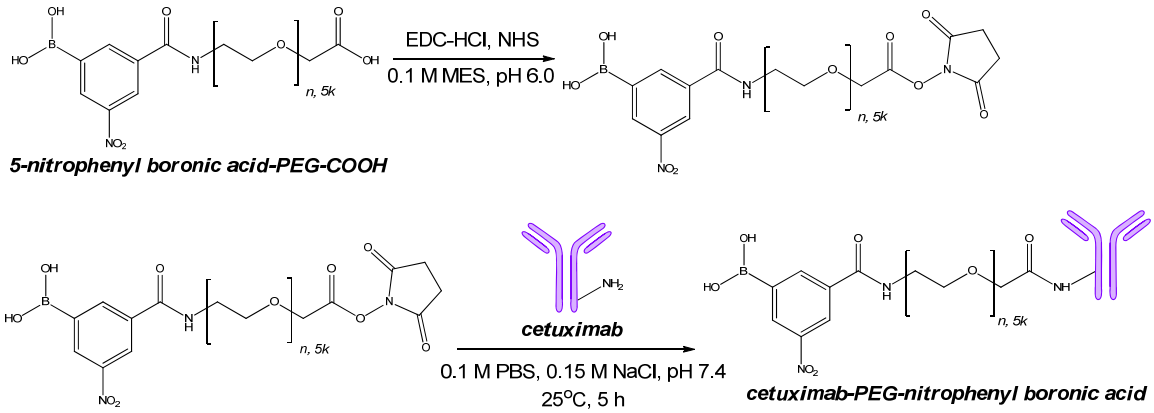

Scheme IV.4: Conjugation of an antibody such as cetuximab to 5-nitrophenylboronic acid-PEG-COOH.

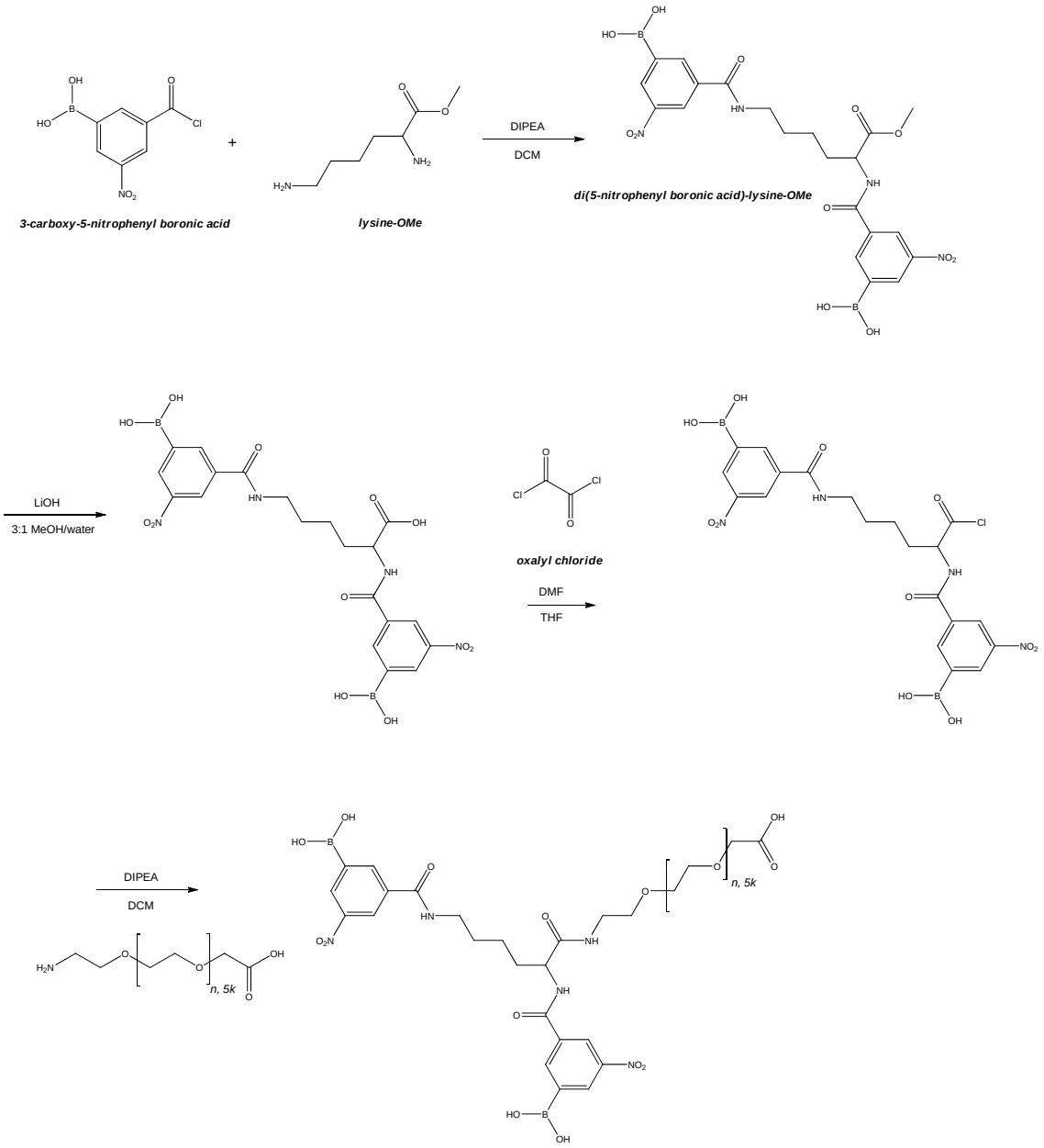

Scheme IV.5: Synthetic scheme for di(5-nitrophenylboronic acid)-PEG-COOH.

Compound	**Binding Constant to Alizarin Red S (M^{-1})**	**Binding Constant to cMAP (M^{-1})**
5-nPBA-PEG-COOH	3.17×10^4	$1.04 \pm 0.29 \times 10^6$
$(5\text{-nPBA})_2$-PEG-COOH	3.01×10^4	$1.01 \pm 0.55 \times 10^7$

Table IV.1: Binding constant of 5nPBA-PEG-COOH and $(5\text{nPBA})_2$-PEG-COOH to Alizarin Red S and to cMAP.

The 5nPBA-PEG-COOH and $(5nPBA)_2$-PEG-COOH components were synthesized in 2 PEG lengths: 5kD (as shown in the above schema) and 10kD, because it was unknown whether a protein attached to a 5kD PEG would be exposed on the surface of the nanoparticle with a dense 5kD brush layer as is present with a NP formed with the triblock polymer. It was hypothesized that a 10kD PEG might allow the protein to be able to come out of the PEG brush layer and bind to cell surface receptors. Both the 5nPBA-PEG-COOH and the $(5nPBA)_2$-PEG-COOH in the 5kD and 10kD PEG lengths were successfully synthesized (SI Figures IV.S5-IV.S13) and conjugated to transferrin (Tf) and cetuximab. The amide formation occurs between an activated carboxylic acid on the PEG and an NH2 group from any lysine on the protein. The direct output of the conjugation reaction is a mixture of un-PEGylated, mono-PEGylated (desired product), di-PEGylated, and small amounts of higher order PEGylated protein as shown by MALDI-TOF mass spectra in the SI Figure IV.S14-IV.S15. A separation was done on a diol-functionalized silica column by binding the boronic acid PEGylated protein to the column at pH 7.4 when un-PEGylated protein elutes. The pH of the buffer is then dropped to 5.7 to dissociate the boronic acid PEGylated protein from the column to isolate mainly the mono-PEGylated fraction (SI Figures IV.S16-IV.S18).

The boronic acid was able to bind to the nanoparticle containing cMAP and form stable 30-50 nm particles with slightly negative -3 to -5 mV surface charge in 10 mM phosphate buffer, pH 7.4, as shown in Table IV.2. These results are similar to those using the triblock polymer alone without targeting agent.

Formulation	**Hydrodynamic Diameter by DLS (nm)**			**Zeta Potential (mV, 10 mM phosphate buffer, pH 7.4)**		
	Mean	Median	S.D.	Mean	Median	S.D.
Triblock	40.6	41.5	3.6	-5.0	-5.2	1.7
Triblock, Tf-PEG_{5k}-5nPBA	47.7	50	7.7	-4.9	-4.9	0.7
Triblock, Tf-PEG_{5k}-$(5nPBA)_2$	49.9	48.8	15.2	-3.7	-3.4	1.5
Triblock, Tf-PEG_{10k}-5nPBA	35.7	30.6	16.5	-4.3	-3.9	1.3
Triblock, Tf-PEG_{10k}-$(5nPBA)_2$	30.5	29.5	5.0	-4.8	-4.1	3.1

Table IV.2: Hydrodynamic diameter and surface charge of targeted nanoparticles formed using the triblock polymer with transferrin as the targeting agent. DLS (dynamic light scattering); S.D. (standard deviation).

There is the possibility that the boronic acid can prematurely dissociate from the nanoparticle in an acidic tumor microenvironment before it is internalized into malignant cells. Therefore, the protein targeting agent was also directly conjugated to the cMAP polymer through a 5kD PEG linkage as shown in scheme IV.6. Because of the high amount of polymer needed for a protein conjugation reaction, both the diblock cMAP-PEG5k-COOH and triblock HOOC-PEG5k-cMAP-PEG5k-COOH were accepted for protein conjugation (SI Figure IV.S19). With the targeting agent directly conjugated to cMAP (SI Figure IV.S20) and with cMAP associated with siRNA in the core of the nanoparticle, the targeting agent attachment will not be subject to dissociating from the nanoparticle regardless of the pH of the environment.

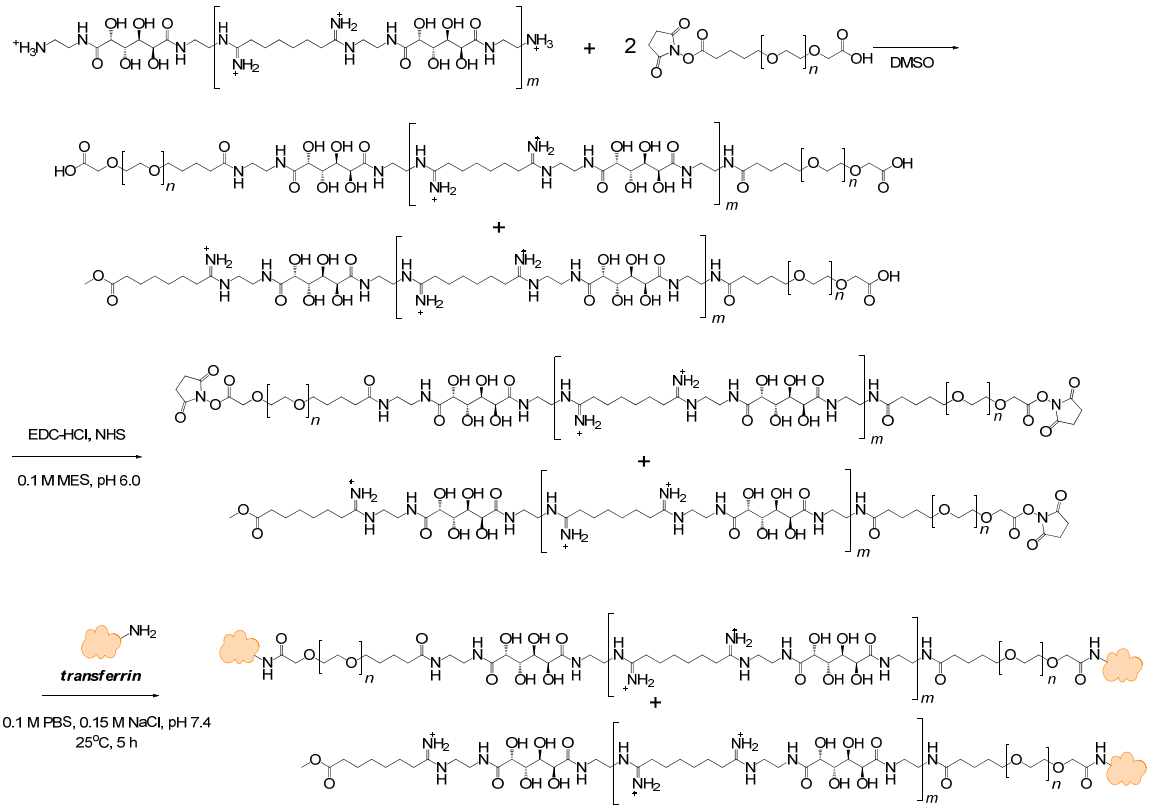

Scheme IV.6: Directly conjugating a protein to cMAP via a PEG linker.

Endosomal Escape

In order to achieve endosomal escape, the mPEG-cMAP-PEGm polymer was modified to include a histidine between the PEG and the cMAP. Histidine contains the requisite imidazole functional group which acts as a proton sponge that prevents the endosome from acidifying and eventually causes the endosome to burst.

As shown in synthetic scheme IV.7, the histidine with an activated carboxylic acid NHS ester and boc-protected amine is able to react with the amines on the ends of cMAP. The Boc-protected amine of the histidine is then hydrolyzed with acid to allow the His-cMAP-His (SI Figure IV.S21) to react with the activated carboxylic acid NHS ester on the mPEG to form the mPEG-His-cMAP-His-PEGm triblock polymer (also called TriB-His

for short) containing histidine (SI Figure IV.S22) after removal of smaller diblock cMAP-His-PEGm, unreacted cMAP, and hydrolyzed mPEG-COOH.

The absolute molecular weight by multi-angle light scattering of cMAP-His and mPEG-His-cMAP-His-PEGm were determined to be approximately 7.3 kD and 26.95 kD, respectively shown in table IV.3. The substitution of imidazole on the triblock polymer was determined by titration with acid and found to be 1.9 ± 0.2 mmol imidazoles per mmol of polymer which means that there is almost complete substitution of histidine on both ends of the cMAP, between the cMAP and PEGm. The titration curve can be seen in SI Figure IV.S23.

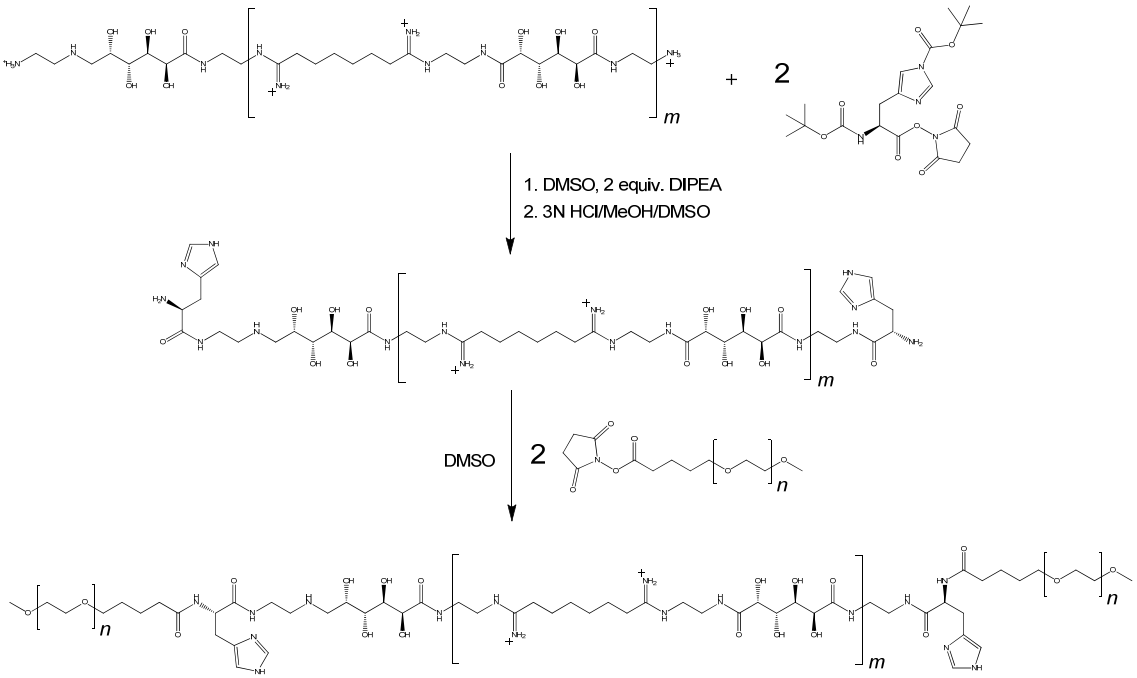

Scheme IV.7: Synthesis of mPEG-His-cMAP-His-PEGm.

Polymer	Mn (kDa)	Mw (kDa)	PDI (Mw/Mn)
cMAP-His	7.266	9.078	1.271
mPEG-His-cMAP-His-PEGm	26.950	27.92	1.036

Table IV.3: Absolute molecular weight of histidine-containing cMAP polymers as determined by multi-angle light scattering.

To demonstrate that adding the histidine to the ends of cMAP results in enhanced mRNA knockdown efficiency, we first tested the cMAP-His polymer without PEG stabilization in cell culture on Neuro-2A cells. Without PEG stabilization, the nanoparticles aggregate and are better able to enter cells immobilized on a tissue culture surface rather than floating around in solution in Brownian motion with fewer cell contacts. The cMAP-His polymer was able to achieve better endosomal escape than cMAP alone with an RRM2 mRNA knockdown study in Neuro2A cells (Figure IV.1), being able to knock down RRM2 mRNA 17% more than with cMAP alone using 50 nM of siRRM2 in both cases.

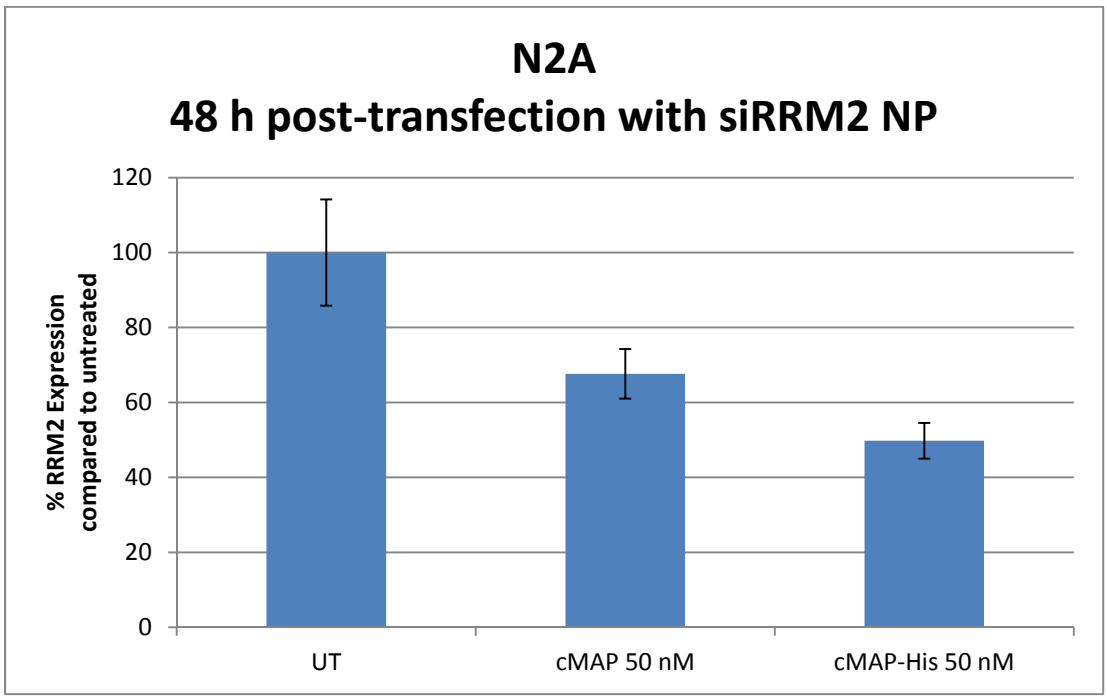

Figure IV.1: mRNA knockdown of RRM2 in Neuro-2A cells using cMAP and cMAP-His siRNA nanoparticles without PEG stabilization.

The mPEG-His-cMAP-His-PEGm polymer, also called TriB-His, is able to form stable nanoparticles similar to those with the triblock polymer not containing histidine, both without and with a Tf-PEG5k-5nPBA targeting agent (Table IV.4).

Formulation	Hydrodynamic Diameter by DLS (nm)			Zeta Potential (mV, 10 mM phosphate buffer, pH 7.4)		
	Mean	Median	S.D.	Mean	Median	S.D.
Triblock-His	22.4	21.9	5.8	-4.0	-3.8	1.7
Triblock-His, Tf-PEG_{5k}-5nPBA	38.9	38.7	13.8	-6.8	-6.8	1.2

Table IV.4: NP size and zeta potential formulated with TriB-His without and with transferrin targeting agent added to the formulation. DLS (dynamic light scattering); S.D. (standard deviation).

In vitro studies

Cell lines and targets

A few cell lines were used to test the efficacy of these nanoparticles. The H1975 non-small cell lung cancer cell line that is a T790M and L858R epidermal growth factor receptor (EGFR) mutant has surface expression of EGFR and it is hypothesized that the mutant EGFR protein drives its growth.[11] The antibody cetuximab was used for targeting the nanoparticle to these cells and a siRNA against EGFR was used to halt its proliferation. The M249hBRAF melanoma cell line is a BRAF V600E mutant with overexpressed transferrin receptor on the cell surface and with the BRAF mutant driving its growth.[12] Tranferrin protein was used for targeting the nanoparticle into these cells and a siRNA against BRAF was delivered in the nanoparticle. The Neuro-2A neuroblastoma cell line was used for testing nanoparticle targeting with the protein transferrin, and a siRNA against ribonucleotide reductase M2 (RRM2) was used for this cell line. The EGFR and BRAF siRNA sequences were validated in their respective cell lines using the Lipofectamine RNAiMAX transfection reagent to confirm mRNA knockdown, as shown in SI Figure IV.S24-IV.S25. The RRM2 siRNA has been used previously in our lab.[13] The control

siRNA sequence, siEGFP, was chosen for its lack of immune stimulation activities *in vivo* as reported in the literature previously.[14]

Targeting agent to receptor binding

Binding of the cetuximab and transferrin targeting agents conjugated to the PEG-boronic acid components to their corresponding receptors were tested in the H1975 and Neuro-2A cells lines expressing EGFR and transferrin receptor, respectively. Cetuximab-PEG with both the 5k and 10k PEG and the single and di-boronic acid retained its binding affinity to EGFR on the surface of H1975 cells (SI Figure IV.S26). However, the transferrin-PEG-boronic acids lost some of their binding affinity to transferrin receptor on the surface of Neuro-2A cells, though some binding still occurred (SI Figure IV.S27). The decrease in transferrin binding to transferrin receptor may be due to functionalization of the protein with PEG, the drops in pH needed to separate unPEGylated Tf from PEGylated Tf, or a change in iron loading of the protein despite iron reloading after purification.

mRNA knockdown

The boronic acid-PEG-targeting agents were loaded onto the surface of nanoparticles formulated using TriB-His at a 1.5 +/- charge ratio of polymer to siRNA to minimize excess free components. The nanoparticles were formulated for a 25 nM concentration of siRNA in the final mixture of cells and nanoparticles in the well. For *in vitro* mRNA knockdown studies, nanoparticles using cMAP-His polymer was used as a comparison for mRNA knockdown because of its strong positive surface charge and ability to aggregate and enter cells which are localized to the bottom of the cell culture wells.[15-16] In comparison, the 30-40 nm particles formed with PEG stabilization move about the entire solution volume by Brownian motion and may make fewer contacts with cells near the

bottom of the well. For that reason, the nanoparticle solution and freshly-detached cells were added to the wells in sequence, and the plate was placed on a shaker in the cell culture incubator to facilitate more contacts between nanoparticles and cells, though the cells do attach to the bottom surface after a few hours.

For the H1975 cell line, the cetuximab (CTX) targeting agent was used at 2 mol% loading of the diol functional groups present of mucic acid in the cMAP component of the triblock-His polymer, which corresponded to 92 nM of cetuximab in the final solution mixture. siRNA against EGFR was loaded into the nanoparticles for treating these cells. Because of the potential for cetuximab to affect EGFR mRNA expression, the same concentration of cetuximab was added to the cMAP-His NP and the TriB-His; under the conditions used in this assay, CTX did not seem to have an effect on EGFR mRNA expression (Figure IV.2). The TriB-His NPs without a targeting agent attached, as expected, were not able to enter cells and decrease EGFR mRNA expression (Figure IV.2). However, the TriB-His NPs with CTX targeting agent on their surface were able to cause a decrease in EGFR mRNA expression similar to that of the cMAP-His NP which aggregates and enters the cells without the need for a targeting agent (Figure IV.2). Furthermore, neither the PEG length of 5k versus 10k, nor having a single versus a di-boronic acid, had an effect on EGFR mRNA expression (Figure IV.2). This suggests that the 5k PEG is sufficient for some of the targeting agent to be exposed on the cell surface or that the 10k PEG might loop out and wrap back into the NP's PEG brush layer so that the targeting agent is equally exposed in both cases. The diboronic acid offers no benefit over the single boronic acid, suggesting that a single boronic acid is sufficient for targeting agent attachment to the nanoparticle. However, the diboronic acid may still be advantageous in

an *in vivo* system with an acidic tumor microenvironment to allow the targeting agent to stay on the nanoparticle long enough for attachment and entry into cells when the pH might cause the boronic acid to detach from the diol groups before the NP has a chance to attach to cells.

Similar results were seen for the Neuro-2A cell line, using transferrin targeting agent at 4 mol% loading of the diol functional groups on the polymer, which corresponds to 218 nM of transferrin in the cell culture medium. siRNA against RRM2 was used for the nanoparticles made to treat these cells. The untargeted TriB-His showed some but not significant decrease in RRM2 mRNA expression compared to untreated cells (Figure IV.3). The NPs with transferrin targeting agents showed similar decreases in RRM2 mRNA expression comparable to that of the cMAP-His NPs. Similar to with the CTX-siEGFR NPs in the H1975 cell line, there was no difference between transferrin targeting agent PEG lengths or whether a single or di-boronic acid was used for attaching the Tf to the NP. This shows that despite the decreased binding affinity of transferrin to transferrin receptor, the avidity effects of multiple transferrins present on the surface of the NP may be enough to compensate to allow the NP to attach to the cell surface and be internalized.

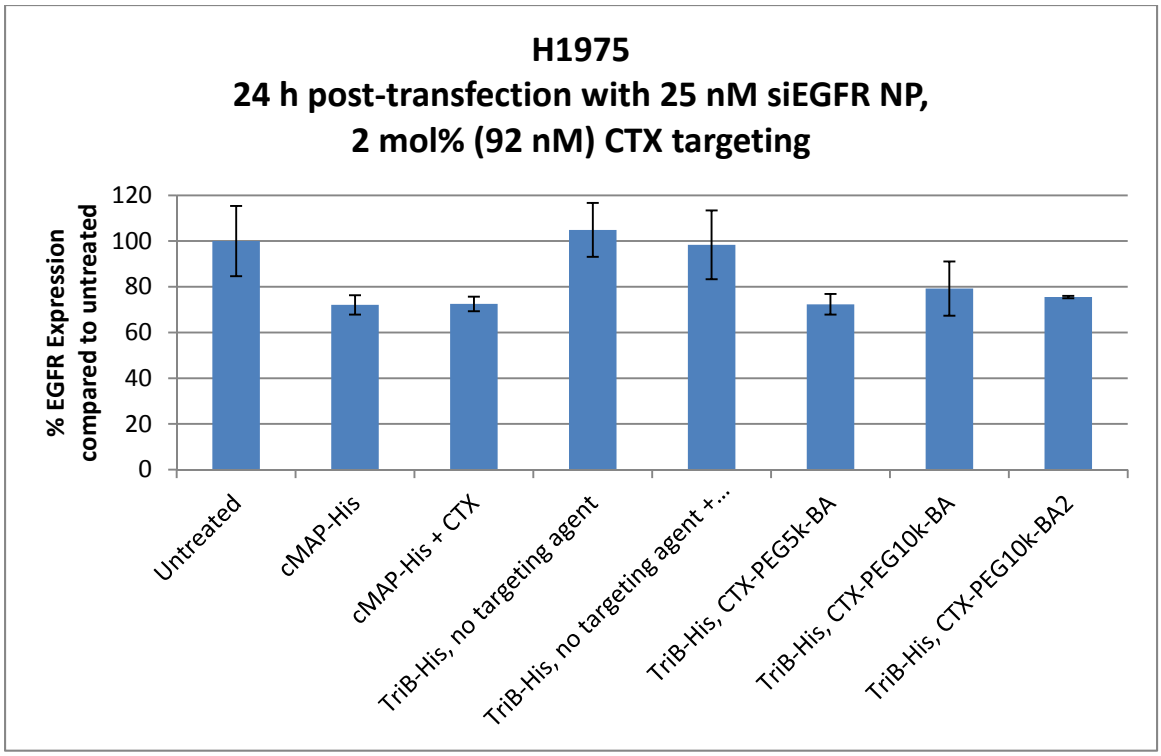

Figure IV.2: EGFR mRNA knockdown with NPs formulated with TriB-His containing siEGFR and targeted with 2 mol% of cetuximab targeting agents.

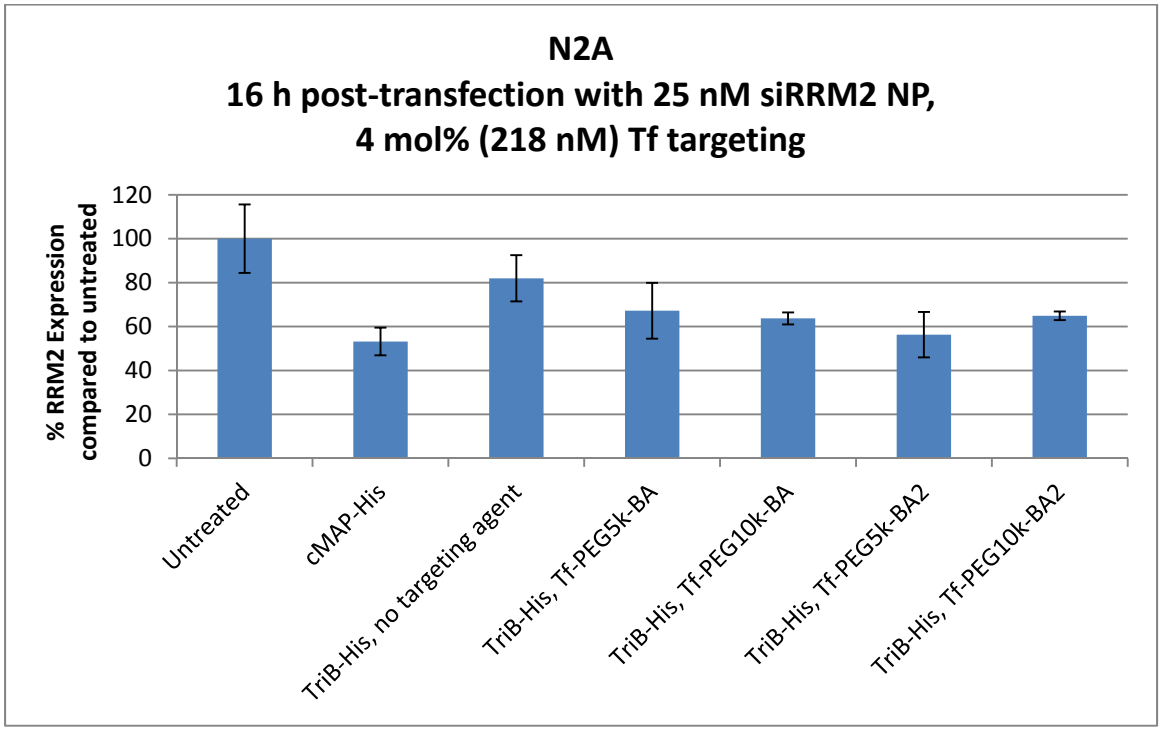

Figure IV.3: RRM2 mRNA knockdown with NPs formulated with TriB-His containing siRRM2 and targeted with 4 mol% of transferrin targeting agents.

In vivo studies

The cMAP + 5nPBA-PEGm and the TriB-His nanoparticle formulations were used for tumor studies. Tumors were also harvested for analysis of mRNA expression and siRNA delivery with the cMAP + 5nPBA-PEGm nanoparticles formulation.

cMAP + 5nPBA-PEGm NP delivering siEGFR to H1975 cells.

H1975 NSCLC xenograft tumors were established in nude mice and used as the model for the cMAP + 5nPBA-PEGm NP formulation. The cMAP polymer was used at a 3+/- charge ratio of polymer to siRNA, so some free components are present in solution. The antibody cetuximab that targets EGFR was used as the targeting agent at 0.13 mol% of the diol groups on mucic acid in cMAP, corresponding to approximately 9 mg/kg of cetuximab in the formulation per dose. A siRNA against EGFR was used as the siRNA in this NP formulation and dosed at a 5 mg/kg per injection. The size and zeta potential of these nanoparticles are shown in Table IV.5. An assay to detect siEGFR, which was validated *in vitro* (SI Figure IV.S28), found the siRNA in these H1975 tumor xenografts with the cMAP + 5-nPBA-PEGm siRNA delivery system after 2 doses 3 days apart (Figure IV.4). This shows that the nanoparticles are reaching the tumor despite no difference in EGFR mRNA expression between the treatment groups. This nanoparticle formulation also did not have an imidazole endosomal escape mechanism, though we hypothesized that the boronic acid on the PEG could provide some acid buffering capacity. However, as mentioned previously, the boronic acid has the potential to prematurely fall off the nanoparticle in an acidic tumor microenvironment, before the nanoparticle is internalized. If this were the case, then the positively charged cMAP could facilitate siRNA entry into tumor cells.[15-16]

Formulation	Hydrodynamic Diameter (nm) by DLS	Zeta Potential (mV) in 10 mM phosphate buffer, pH 7.4	Zeta Potential (mV) in 1 mM KCl, pH 5.5
cMAP (no PEG)	180.3 ± 9.7	14.57 ± 0.56	1.20 ± 0.54
cMAP + 5nPBA-PEG5km	57.3 ± 16.0	-3.14 ± 0.67	0.75 ± 0.37
cMAP + 5nPBA-PEG5km, 0.13 mol% CTX-PEG5k-5nPBA	43.2 ± 12.7	-3.62 ± 0.49	0.95 ± 0.31

Table IV.5: Hydrodynamic diameter and zeta potential of nanoparticle formulation (building up from the cMAP polymer alone) of the CTX-targeted cMAP-siEGFR NPs used for treatment of H1975 tumor xenograft-bearing nude mice.

Some effects of tumor regression are seen with the cMAP + 5nPBA-PEGm system with cetuximab as a targeting agent and siEGFR as the nucleic acid delivered compared to saline-treated mice and cetuximab-treated mice after injecting 4 doses every 3 days (Figure IV.5), but it is not consistent across all mice in a treatment group (SI Figure IV.S29). When regressions do occur, however, they tend to be durable. Perhaps a certain threshold for mRNA knockdown needs to be achieved for cells to stop proliferating and die, or for the immune system to eliminate the tumor.

The cetuximab-treated mice were treated at the same 9 mg/kg dose of cetuximab as was used for targeting the nanoparticle. Cetuximab has the potential for inducing an ADCC response as mentioned in our previous work, and there are free components, including free cetuximab-PEG-5nPBA, in the formulation injected into the nude mice which have intact NK cells despite their deficiency in T cells.[17] Therefore, much of the anti-tumor activity of these nanoparticles can be ascribed to the potent ADCC effect of the cetuximab targeting agent rather than the siEGFR in the NP, though the NP was able to induce more durable responses compared to cetuximab alone (SI Figure IV.S30).

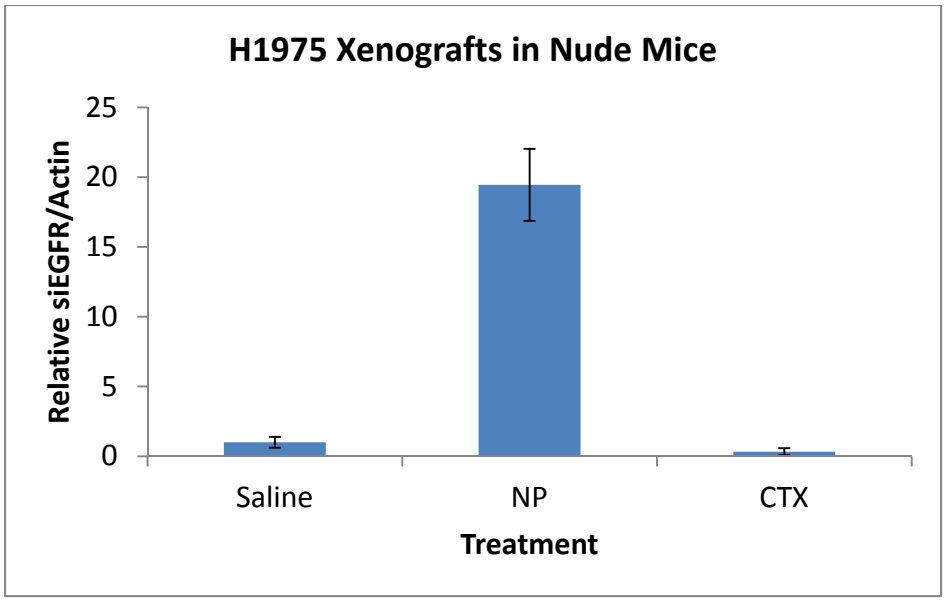

Figure IV.4: Detection of siEGFR as delivered by the cMAP + 5nPBA-PEGm formulation with 0.13 mol% CTX-PEG-5nPBA targeting agent in H1975 xenografts.

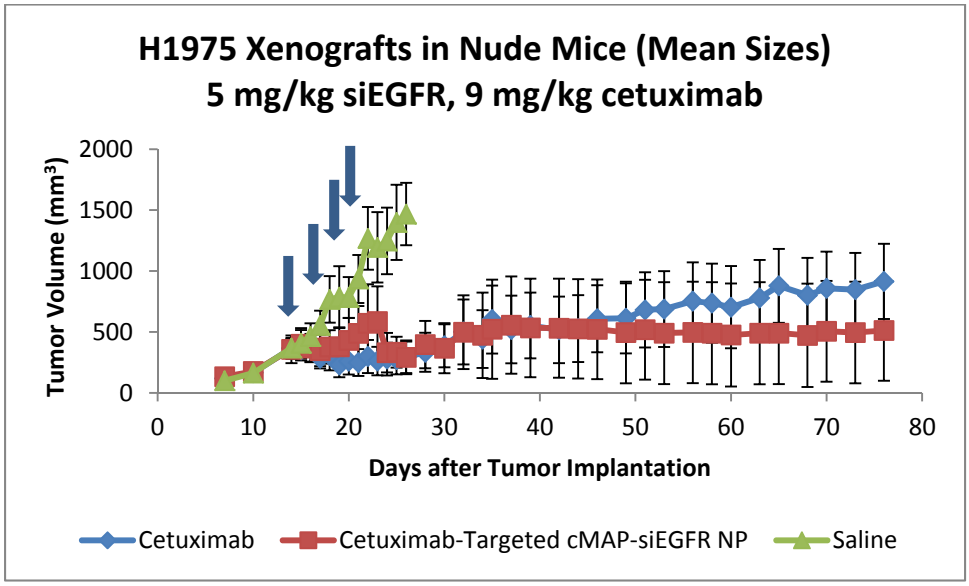

Figure IV.5: H1975 tumor xenograft growth in nude mice treated with siEGFR as delivered by the cMAP + 5nPBA-PEGm formulation with 0.13 mol% CTX-PEG-5nPBA targeting agent, compared to cetuximab alone and saline control.

To distinguish the ADCC effect of the targeting agent from that of the siRNA in the nanoparticle, we explored using a different antibody against EGFR, panitumumab, which is of the IgG2 subtype and does not cause an ADCC response. The panitumumab-PEG5k-

5nPBA was prepared with the same procedures used to produce the cetuximab targeting agent (SI Figure IV.S31). While there was some effect of H1975 tumor growth delay in the mice treated with panitumumab-targeted siEGFR nanoparticles for 6 doses every 3 days compared to saline-treated mice, there was not a significant difference, especially compared to mice treated with nanoparticle loaded with siEGFP, a control siRNA (Figure IV.6). However, the siEGFP does cause a modest knockdown in EGFR mRNA expression (SI Figure IV.S24), which may cause some of an effect on tumor growth. Virtually no difference exists between the groups of mice treated with cetuximab-targeted NPs loaded with the active siEGFR versus the control siEGFP siRNAs, further suggesting that the majority of the NP's effect arises from the ADCC activity of cetuximab, whether it is from the unbound components or targeting agent that has detached from the nanoparticle in an acidic tumor microenvironment. It is possible that knocking down EGFR is not enough to cause death in H1975 cells and additional mutations are driving cell growth, as cell death was not seen *in vitro* in siEGFR-treated cells.

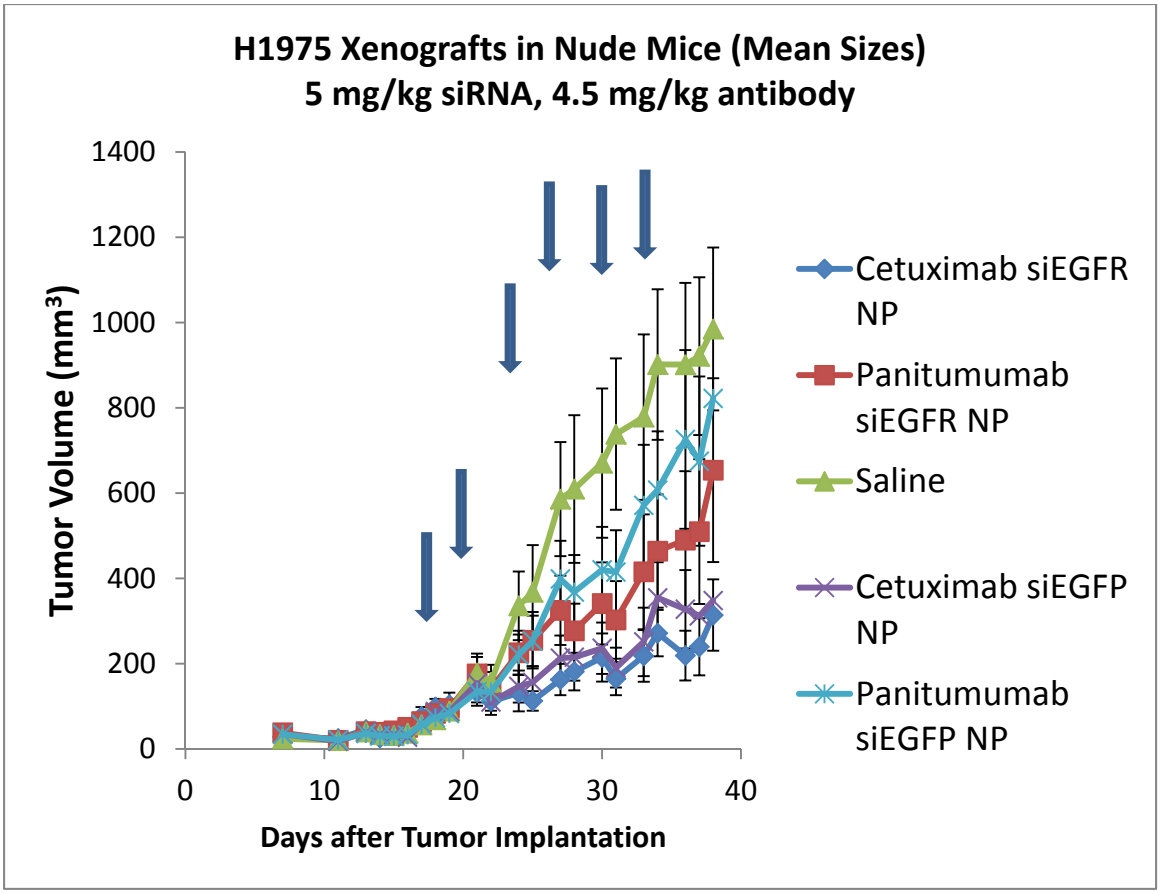

Figure IV.6: H1975 tumor xenograft growth in nude mice treated with siEGFR as delivered by the cMAP + 5nPBA-PEGm formulation with 0.13 mol% CTX-PEG-5nPBA or panitumumab-PEG-5nPBA targeting agent, compared to the NP formulations containing control siEGFP and saline.

TriB-His NP delivering siBRAF to M249shBRAF cells.

We turned to using an M249shBRAF melanoma cell line which contains a BRAF V600E mutation thought to drive the cancer's growth. This cell line was also made to contain a doxycycline inducible shRNA targeting BRAF, and mice with tumor xenografts fed a doxycycline-containing diet show a prolonged duration of tumor regression even after cessation of the doxycycline-containing diet (SI Figure IV.S32). Though a siRNA delivery system would not reach the effect of the inducible shRNA, the durable response seen with the doxycycline diet serves as a target of maximal response that we could hope to see with

a NP which delivers a single siRNA against BRAF. We chose to use the triblock polymer which showed the longest circulation time, and to which we had incorporated a histidine group, TriB-His, for allowing siRNA endosomal escape.[9] We believed that a NP with the longest circulation time would have the highest chance of reaching the tumor by the EPR effect. Adding the imidazole group in histidine to the polymer further increases the chance of siRNA reaching the cytosol of the tumor cells for it to function. Because the M249shBRAF cell line expresses a high level of transferrin receptor on its surface, we chose to use transferrin as the targeting agent. The diboronic acid attachment of the transferrin-PEG5k to the vicinal diols on cMAP in the nanoparticle was chosen due to the order of magnitude greater affinity compared to using a single boronic acid attachment, decreasing the possibility of premature shedding of targeting agent before the NP is internalized.

Transferrin targeting agent was loaded onto the surface of the nanoparticle at 0.25 mol% of the diol groups present in the NP formulation with a 3+/- charge ratio of TriB-His polymer to siRNA. This corresponds to a dose of 9.9 mg/kg of transferrin. The NP was dosed such that 5 mg/kg of siBRAF was dosed per injection. Nude mice bearing established M249shBRAF tumor xenografts on their left front flank were dosed every 3 days, with 4 doses total. Similar to results with the H1975 tumor xenografts, some effect was seen with the active nanoparticle (Figure IV.7), though results were mixed with some mice (n =3) responding very well and with others (n = 2) seeing virtually no effect (SI Figure IV.S33-IV.S34) so that statistical significance was not achieved.

Though a pilot study of delivering siBRAF to tumors with the cyclodextrin polymer system which has a very short circulation time barely longer than that of siRNA showed

some effect (albeit with only n = 2 mice, SI Figure IV.S34), it was puzzling to see that a NP which circulates for much longer had less effect than the CDP siRNA delivery system.[9] There was 0.5 mol% of Tf (9.7 mg/kg) on the surface of the CDP NPs, which is a similar amount to that used for targeting the TriB-His NPs (9.9 mg/kg). Furthermore, the adamantane attachment of the Tf targeting agent to the cyclodextrin cups in CDP is less stable and more prone to shedding (though no pH sensitivity) compared to the boronic acid attachment to diol groups in cMAP. Perhaps the decreased stability of the CDP NPs facilitated the entry of the small amount of NP that was able to enter the tumor by the EPR effect, while even if more of the triB-His NPs arrived at the tumor site with longer circulation the PEG stabilization prevented the NPs from entering cells. Maybe the 4 mol% (compared to 0.25 mol%) loading of transferrin targeting agent onto the surface of nanoparticle (despite the nearly 40 mg/kg dose of transferrin that would be contained), or the Tf-PEG5k-cMAP with transferrin directly conjugated to cMAP so it would not shed from the NP, is necessary to achieve cellular internalization with the stability of these NPs,. It would also be interesting to compare siBRAF delivery with a cMAP-His + 5nPBA-PEGm formulation to see whether just the smaller increase in circulation time but the greater amount of instability without PEG covalently attached to the cationic polymer would be the right balance to achieve optimal siRNA delivery and internalization for tumor regression.

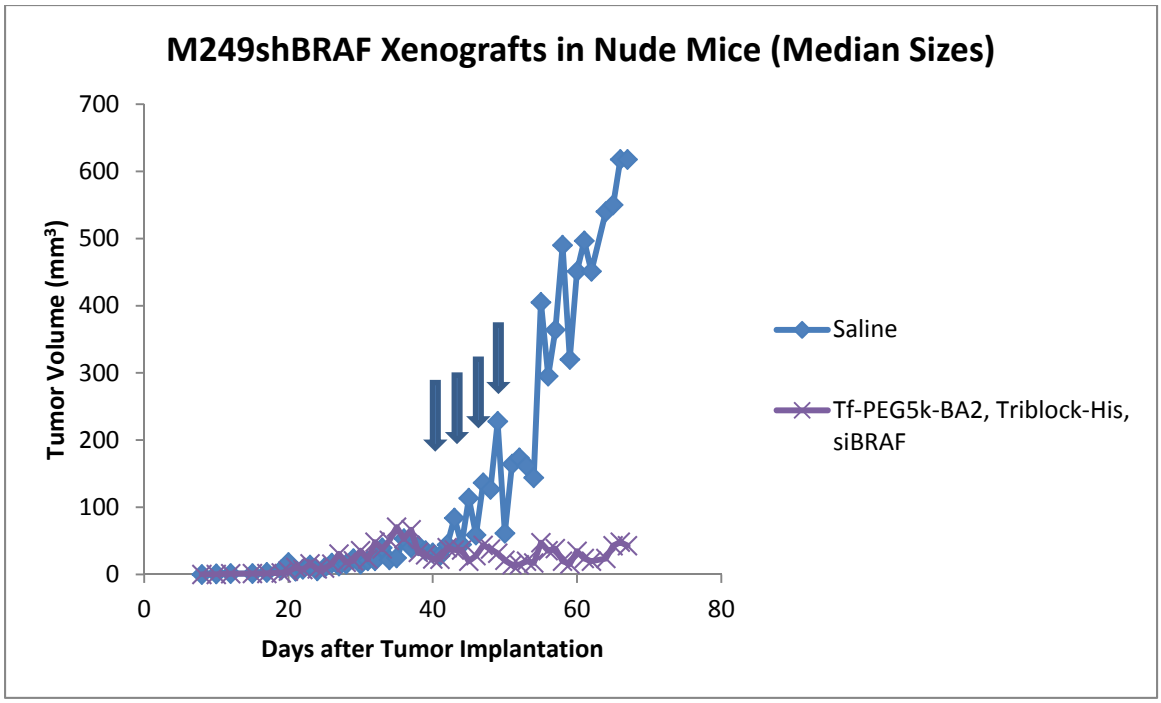

Figure IV.7: M249shBRAF xenograft tumor growth in nude mice using TriB-His NP's containing siBRAF with 0.25 mol% Tf-PEG5k-$(5nPBA)_2$ targeting agent.

Summary

We showed the ability to synthesize a $(5\text{-nPBA})_2$-PEG-COOH with an order of magnitude greater binding affinity than the single boronic acid entity, and to conjugate protein targeting agents to both 5-nPBA-PEG-COOH and the diboronic acid version in 5k and 10k PEG lengths. Furthermore, a histidine group was incorporated into the mPEG-cMAP-PEGm triblock polymer for a siRNA endosomal escape mechanism to achieve enhanced mRNA knockdown. The addition of an imidazole group into the triblock polymer and a targeting agent onto the NP still preserved the desired NP size of 30-40 nm, and the zeta potential remained close to neutral. The NP formulation with the TriB-His polymer and either 2 mol% cetuximab or 4 mole% transferrin targeting agent was able to knock down expression of EGFR or RRM2, respectively, in cell culture with H1975 or Neuro-2A cells,

respectively. Some effect, though mixed, was seen *in vivo* with both the cMAP + 5nPBA-PEG5km formulation delivering 5 mg/kg siEGFR to H1975 NSCLC xenografts using 0.13 mol% cetuximab-PEG5k-5nPBA targeting and with the TriB-His formulation delivering 5 mg/kg siBRAF to M249shBRAF melanoma xenografts using 0.25% transferrin-PEG5k-$(5nPBA)_2$ targeting. Further work is required to determine whether a higher amount of targeting agent, such as 4 mol% transferrin, or direct conjugation of targeting agent to the cationic polymer is required for optimal uptake of NPs into cells for siRNA to reach the cytosol where it can function, or whether a balance that trades the NP's circulation time for more facile entry into cells needs to be achieved. Perhaps using a functional targeting agent that has a therapeutic effect is also beneficial.

EXPERIMENTAL PROCEDURES

Chemistry

Anhydrous solvents, oxalyl chloride, and human holo-transferrin were purchased from Sigma-Aldrich; 3-carboxyl-5-nitrophenyl boronic acid from Alfa-Aesar; and H-Lysine-OMe from Bachem. Polyethylene glycol (PEG) reagents were purchased from either Jenkem Technology USA or Laysan Bio, Inc. Cetuximab and panitumumab were obtained from Dr. Yun Yen at City of Hope Comprehensive Cancer Center in Duarte, CA. Reagents were used without further purification.

Nuclear magnetic resonance (NMR) spectra were acquired on Varian 300 MHz, 400 MHz, 500 MHz, or 600 MHz instruments at 25 degrees Celsius, without spinning at 400 and 600 MHz. For most ^{1}H proton spectra, a delay time of 1-1.5 s was used; for more quantitative integration, a 10 s delay was used. ^{11}B spectra were acquired at 128 MHz.

Matrix-assisted laser desorption/ionization-time of flight (MALDI-TOF) mass spectra for polymers and proteins were acquired on an Applied Biosystems Voyager DE-PRO using a 10 mg/mL alpha-cyano-4-hydroxycinnamic acid matrix for polymers or a 10 mg/mL sinapic acid matrix for proteins.

Gel Permeation Chromatography. An Agilent 1100 HPLC with binary pump and injector was connected to a Tosoh TSKgel G3000PWXL-CP size exclusion column with Wyatt DAWN HELEOS light scattering and Wyatt Optilab Rex refractive index detection. Lyophilized polymer was dissolved at various concentrations in 0.1 M NaNO3, filtered through a 0.2 um PVDF filter, and injected into the refractive index detector directly via a syringe pump for *dn/dc* determination. For absolute molecular weight determination by light scattering, 100 uL of polymer solution was injected onto the column and the detected polymer peak analyzed using ASTRA V software.

Synthesis of cMAP has been previously described. previously.[9]

Synthesis of His-cMAP-His.

cMAP (195 mg, 0.0325 mmol, 1 equiv) and Boc-His(1-Boc)-OSu (147 mg, 0.325 mmol, 10 equiv) were added to an oven-dried 50 mL round bottom flask with a stirbar. The flask was filled with argon. DIPEA dried over molecular sieves (11 uL, 0.065 mmol, 2 equiv), followed by anhydrous DMSO (14 mL), were added to the reaction flask. The reaction was stirred at 25 degrees C for 16 h. 14 mL of 6 N HCl in MeOH was then added to the reaction and stirred for 1 h to remove the Boc protecting groups. The mixture was then diluted to 50 mL with deionized water and dialyzed against deionized water with a 3 kD Amicon Ultra centrifugal spin filter, concentrated to 3 mL, filtered through a 0.2 um PVDF syringe filter, and lyophilized to a white solid (39.2 mg, 18.6% yield), **His-cMAP-**

His, which was stored under argon at -20 degrees C. 1H NMR (600 MHz, D2O): 7.81, 6.99, 4.31, 3.89, 3.57-3.23, 2.43-2.34, 1.52, 1.24. MW (GPC MALS): Mn 7266, Mw 9078, PDI 1.271.

Synthesis of mPEG-His-cMAP-His-PEGm.

His-cMAP-His (39.2 mg, 0.007 mmol, 1 equiv) and mPEG5k-SVA (105 mg, 0.021 mmol, 3 equiv) were added to an oven-dried 25 mL round bottom flask with a stirbar. The flask was filled with argon. Anhydrous DMSO (3 mL) was added to the flask and the reaction was stirred for 48 h. The mixture was then diluted to 25 mL with deionized water and dialyzed against deionized water with a 20 kD Pierce centrifugal spin filter, concentrated to 3 mL, filtered through a 0.2 um PVDF syringe filter, and lyophilized to afford **mPEG-His-cMAP-His-PEGm**, a white solid (38.5 mg, 27.5% yield). 1H NMR (600 MHz, DMSO-d6): 9.58, 9.20, 8.72, 7.90, 7.50, 6.77, 5.40, 4.52, 4.15, 3.82, 3.60-3.36 (PEG), 3.21, 2.39, 1.60, 1.52, 1.33-1.21. MW (GPC MALS): Mn 26950, Mw 27920, PDI 1.036.

Synthesis of COOH-PEG-cMAP-PEG-COOH and cMAP-PEG-COOH mixture.

cMAP (140 mg, 0.025 mmol, 1 equiv) and SC-PEG5k-CM (500 mg, 0.1 mmol, 4 equiv) were added to an oven-dried 25 mL round bottom flask with a stirbar. The flask was filled with argon, and anhydrous DMSO (10 mL) was added to the flask and the reaction was stirred for 48 h. The mixture was then diluted to 25 mL with deionized water and dialyzed against deionized water with a 10 kD Pierce centrifugal spin filter, concentrated to 3 mL, filtered through a 0.2 um PVDF syringe filter, and lyophilized to a **mixture** of **COOH-PEG-cMAP-PEG-COOH** and **cMAP-PEG-COOH**, a white solid (212.6 mg, 33.2% yield).

Synthesis of Tf-PEG-cMAP

cMAP-PEG-COOH (125 mg, 0.0125 mmol, 50 equiv), EDC-HCl (24.0 mg, 0.125 mmol, 500 equiv), and NHS (21.6 mg, 0.188 mmol, 750 equiv) were added to a 1.5 mL Eppendorf tube with a stirbar. 0.1 M MES buffer, pH 6.0 (200 uL) was added and the mixture was stirred for 45 min at room temperature. 20 mg Tf in 800 uL of 0.1 M PBS, 0.15 M NaCL, pH 7.4 was then added and stirred for 6 h at room temperature. The mixture was dialyzed against PBS with a 30 kD Amicon Ultra centrifugal spin filter. Conjugation of Tf to cMAP-PEG-COOH to form **Tf-PEG-cMAP** was confirmed by MALDI-TOF.

Transferrin was iron reloaded by buffer exchange into 0.1 M sodium bicarbonate, pH 8.5, addition of 2.5 mole excess of iron (III) citrate in 0.1 M sodium bicarbonate, pH 8.5, and gentle stirring for 2.5 h. Excess iron was dialyzed away 6 times using 0.1 M sodium bicarbonate, pH 8.5 with a 0.5 mL 30 kD Amicon Ultra centrifugal spin filter. Iron reloading of transferrin was confirmed by measuring the ratio of A_{465}/A_{280} using the UV/Vis function on a Nanodrop 2000. Protein concentration was also determined on the Nanodrop system using an extinction coefficient of 83 and a molecular weight of 79 kD.

Synthesis of 5-nitrophenylboronic acid-PEG5km has been previously described.[9]

Synthesis of 5-nitrophenylboronic acid-PEG5k-COOH.

3-carboxyl-5-nitrophenylboronic acid (200 mg, 0.95 mmol, 1 equiv) was added to an oven-dried 2-necked 10 mL round bottom flask containing a dry stir bar. The flask was vented with argon and sealed with a rubber septum. Anhydrous tetrahydrofuran with BHT inhibitor (5 mL) was added to dissolve the boronic acid, followed by anhydrous DMF (14.7 uL, 0.19 mmol, 0.2 equiv). The flask was cooled to 0^{o}C in an ice-water bath. Oxalyl chloride (195.4 uL, 2.28 mmol, 2.4 equiv) was then added drop wise to the reaction

mixture. The ice-water bath was removed after oxalyl chloride addition was complete, and the reaction continued stirring for 2 hours at room temperature, with an argon vent to allow for the escape of volatiles. Solvent and DMF was removed via rotary evaporator and then under vacuum for 2 days under dark to afford **3-acyl chloride-5-nitrophenyl boronic acid** (217.5 mg, 100% yield) as a yellow solid.

3-acyl chloride-5-nitrophenylboronic acid (68.8 mg, 0.3 mmol, 3 equiv) was added to an oven-dried 25 mL round bottom flask containing a dry stir bar. The flask was sealed with a rubber septum, vented with argon, and cooled to 0^{o}C in an ice-water bath. Anhydrous dichloromethane (5 mL) was added to dissolve the boronic acid. 5 kD H2N-PEG5k-COOH (500 mg, 0.1 mmol, 1 equiv) in an oven-dried 10 mL round bottom flask vented with argon, dissolved in anhydrous dichloromethane (10 mL) and diisopropylethylamine (52.3 uL, 0.3 mmol, 3 equiv) dried with activated molecular sieves, was slowly added to the boronic acid solution. The reaction flask was left in the ice-water bath to slowly warm up to room temperature, and the reaction was stirred overnight under dark. The solvent and DIPEA was removed via rotary evaporator and then under vacuum for 2 days under dark. The solid residue was reconstituted in 0.5 N HCl (15 mL) and stirred for 15 min. The resulting suspension was filtered through a 0.2 um Supor syringe filter, and the resulting clear solution was dialyzed with a 15 mL Amicon Ultra 3 kD spin filter against nanopure water until the pH was constant. The solution of polymer was concentrated to 3-4 mL, filtered through a 0.2 um PVDF syringe filter into a pre-weighed 20 mL glass vial, and lyophilized to dryness to afford **5-nitrophenylboronic acid-PEG5k-COOH** (266.1 mg, 53% yield) as a fluffy white solid. ^{1}H NMR (400 MHz, DMSO-*d*6):

12.54 (s, 1H, COOH), 8.90 (t, 1H), 8.73 (m, 1H), 8.68 (m, 1H), 8.65 (m, 1H), 8.62 (s, 2H), 4.00 (s, 2H), 3.5 (s - PEG, 344H). MALDI: 5496.

Synthesis of 5-nitrophenylboronic acid-PEG10k-COOH was accomplished in a similar fashion, using 10k PEG instead of 5k PEG.

Preparation of 5-nitrophenylboronic acid-PEG5k-cetuximab.

5-nitrophenylboronic acid-PEG5k-COOH (16.94 mg, 0.0033 mmol, 50 equiv) was added to a 1.7 mL Eppendorf tube with a stir bar and dissolved in 0.1 M MES buffer, pH 6.0 (250 uL). EDC-HCl (6.3 mg, 0.033 mmol, 500 equiv) and NHS (5.68 mg, 0.049 mmol, 750 equiv) in 0.1 M MES buffer, pH 6.0 (250 uL) was added to the 5-nPBA-PEG-COOH, and the reaction mixture was stirred for 30 min at room temperature. The reaction mixture was then added to a 0.5 mL Amicon Ultra 3 kD spin filter and spun 3X against 0.1 M MES buffer, pH 6.0 to isolate the activated 5-nPBA-PEG-NHS ester. The activated 5-nPBA-PEG-NHS ester was concentrated to a volume of 100-150 uL and added to a solution of antibody (10 mg, 0.000066 mmol, 1 equiv) in 0.1 M PBS, 0.15 M NaCl, pH 7.4 (1400 uL) in a 1.7 mL Eppendorf tube. The reaction was stirred at 25^{o}C for 5 h. The reaction solution was then spun down and concentrated with a 0.5 mL Amicon Ultra 50 kD spin filter against 0.1 M PBS, 0.15 M NaCl, pH 7.4 to remove excess PEG. The antibody-PEG conjugate was purified via HPLC on 2 TSKgel G3000SWxl columns with an eluent of 0.1 M PBS, 0.15 M NaCl, 0.02% NaN_3, pH 5.7. The mono-PEGylated antibody fraction was concentrated with a 15 mL Amicon Ultra 50 kD spin filter and dialyzed into 0.1 M PBS, 0.15 M NaCl, 0.02% NaN_3, pH 7.2 to afford **5-nitrophenylboronic acid-PEG5k-cetuximab** (1.58 mg, 15% yield) in solution. MALDI: 158,000.

Synthesis of 5-nitrophenylboronic acid-PEG10k-cetuximab was achieved in a similar fashion, substituting 5-nitrophenylboronic acid-PEG10k-COOH for the 5k PEG and preserving the same equivalents of reagents.

Synthesis of 5-nitrophenylboronic acid-PEG5k-panitumumab was accomplished using similar procedures as for the preparation of 5-nitrophenylboronic acid-PEG5k-cetuximab, substituting panitumumab for cetuximab.

Synthesis of boronic acid-PEG-Tf was accomplished using similar procedures as for cetuximab and panitumumab, adjusting for the molecular weight of transferrin and preserving the same equivalents of reagents. Iron was additionally reloaded onto transferrin as described in the synthesis of Tf-PEG5k-cMAP.

Synthesis of diboronic acid.

Synthesis of di(5-nitrophenylboronic acid)-Lysine-OMe.

3-carboxyl-5-nitrophenylboronic acid (4 g, 19 mmol, 1 equiv) was added to an oven-dried 2-necked 100 mL round bottom flask with stirbar. The flask was sealed and vented with argon. Anhydrous THF (40 mL) was added to the flask to dissolve the starting material. DMF (300 uL, 3.8 mmol, 0.2 equiv) was added and the reaction flask was cooled in an ice/water bath. Oxalyl chloride (4 mL, 46 mmol, 2.4 equiv) was added dropwise. Upon completion of oxalyl chloride addition, the reaction flask was removed from the ice bath and reacted for 2 h at room temperature under dark with argon vent to allow the escape of volatiles. Solvent was then removed *in vacuo* to afford **3-acyl chloride-5-nitrophenyl boronic acid**.

To the flask with **3-acyl chloride-5-nitrophenylboronic acid** (3.9 g, 17 mmol, 5 equiv) and a dry stir bar, Lysine-OMe (800 mg, 3.4 mmol, 1 equiv) was added and dried

under vacuum for 1 h before filling the flask with argon and cooling in an ice/water bath. DIPEA dried over molecular sieves (3 mL, 17 mmol, 5 equiv) followed by anhydrous DCM (20 mL) was added to dissolve the reactants. The reaction was left in the ice bath to warm up to room temperature overnight under dark. Solvent was removed on rotovap and *in vacuo*. 20 mL 1 N aqueous HCl was added to the crude product, which was filtered through a fine grain frit and washed with 1 N HCl (3 x 10 mL). The solid retentate was collected by dissolving in MeOH. MeOH was removed *in vacuo* to afford **di(5nitrophenylboronic acid)-Lysine-OMe** (1.8 g, 19% yield), a yellow solid. 1H NMR (600 MHz, CD3OD): 8.75-8.25 (m, 10H), 4.63 (m, 1H), 3.74 (s, 3H), 3.41 (m, 2H), 1.90 (multiplet of doublets, 2H), 1.68 (m, 2H), 1.55 (m, 2H). 11B NMR (128 MHz, CD3OD): 26.56 ppm (s).

Synthesis of di(5-nitrophenylboronic acid)-Lysine.

di(5-nitrophenylboronic acid)-Lysine-OMe (1.8 g, 3.3 mmol, 1 equiv) was added to a 50 mL round bottom flask with a stirbar. LiOH (1.4 g, 33 mmol, 10 equiv) was added, followed by 3:1 MeOH/H2O (16 mL). The flask was sealed and the reaction was run under argon overnight. Solvent was removed *in vacuo* until dry. 6 N aqueous HCl was slowly added with stirring to acidify the solution. The mixture was filtered through a fine grain frit funnel and the solids were collected by dissolution with MeOH and then removing MeOH *in vacuo* to afford **di(5-nitrophenylboronic acid)-Lysine** (550 mg, 31% yield) as a brown solid. 1H NMR (500 MHz, CD3OD): 8.74-8.34 (m, 10H), 4.65 (m, 1H), 3.45 (m, 2H), 2.2 (multiplet of doublets, 2H), 1.74 (m, 2H), 1.61 (m, 2H). 11B NMR (128 MHz, CD3OD): 27.28 ppm (s).

Synthesis of di(5-nitrophenylboronic acid)-PEG5k-COOH.

di(5-nitrophenylboronic acid)-Lysine (550 mg, 1 mmol, 1 equiv) was added to a 100 mL round bottom flask with stirbar. The flask was purged with argon and anhydrous THF (5 mL) was added followed by anhydrous DMF (16 uL, 0.2 mmol, 0.2 equiv). The reaction flask was cooled in an ice/water bath and oxalyl chloride (213 uL, 2.5 mmol, 2.4 equiv) was added dropwise. Upon completion of oxalyl chloride addition, the reaction flask was removed from the ice bath and the contents allowed to react at room temperature for 2 h under dark. Solvent was then removed *in vacuo*.

H_2N-PEG5k-COOH (800 mg, 0.16 mmol, 1 equiv) dissolved in dry DIPEA (140 uL, 0.8 mmol, 5 equiv) and anhydrous DCM (20 mL) was added to BA2-Lysine-acyl chloride (440 mg, 0.8 mmol, 5 equiv) in a 100 mL flask with dry stirbar under argon in an ice bath. The reaction was slowly warmed to room temperature and reacted overnight. The solvent was removed *in vacuo*. The solids were reconstituted in 0.5 N HCl (20 mL) and the solution was filtered through a 0.2 um syringe filter with a Supor membrane. The solution was dialyzed against deionized water using a 3 kD MWCO Amicon Ultra Centrifugal spin filter until the pH of the filtrate remained constant. The retentate was filtered through a 0.2 um PVDF syringe filter and lyophilized to dryness to afford **di(5-nitrophenylboronic acid)-PEG5k-COOH** (379.2 mg, 43% yield) as a white solid. ^{1}H NMR (600 MHz, DMSO-*d*6): 12.49 (s, 1H, COOH), 8.80-8.60 (m, 8H), 4.19 (t, 1H), 3.99 (s, 2H), 3.66 (t, 2H), 3.5 (s - PEG, 704H), 1.77 (m, 4H). MALDI: 5234.

Synthesis of di(5-nitrophenylboronic acid)-PEG10k-COOH was achieved in a similar fashion, except using H_2N-PEG10k-COOH as the PEG reactant.

Synthesis of di(5-nitrophenylboronic acid)-PEG5k-Tf.

di(5-nitrophenylboronic acid)-PEG5k-COOH (63 mg, 0.013 mmol, 50 equiv), EDC-HCl (24 mg, 0.13 mmol, 500 equiv), and NHS (22 mg, 0.19 mmol, 750 equiv) were dissolved in 0.1 M MES, pH 6.0 (250 uL) in a 1.7 mL Eppendorf tube and stirred for 30 min. Transferrin (20 mg, 0.00025 mmol, 1 equiv) dissolved in 0.1 M phosphate buffer, 0.15 M NaCl, pH 7.4 (1 mL) was then added to the reaction mixture and stirred for 5 h. Excess PEG, EDC, and NHS were removed using a 0.5 mL 30 kD MWCO Amicon Ultra centrifugal spin filter.

The retentate containing transferrin with 0-3 PEG attached was filtered through a 0.2 um syringe filter and injected onto an HPLC containing a 1.5 mL injection loop and a Tosoh Bioscience TSKgel G3000SW (21.5 mm ID x 60 cm) column. 50 mM phosphate buffer, 0.15 M NaCl, pH 7.4 buffer was used to remove unbound, unPEGylated transferrin. The eluent was then changed to 50 mM phosphate buffer, 0.15 M NaCl, pH 5.7 to elute mainly mono-PEGylated transferrin. The eluate containing Tf-PEG5k-$(5nPBA)_2$ was concentrated using a 15 mL 30 kD MWCO Amicon Ultra centrifugal spin filter and exchanged into the pH 7.4 buffer. The PEGylated transferrin was exchanged into 0.1 M sodium bicarbonate buffer, pH 8.4 and iron reloaded with Iron (III) citrate (2.5 equiv) based on the nanodrop determined concentration of the transferrin. The mixture was stirred for 2.5 h, and then excess Fe was removed by dialysis against 0.1 M sodium bicarbonate buffer, pH 8.4. The **transferrin-PEG5k-$(5nPBA)_2$** was then exchanged back into pH 7.4 buffer and concentration was determined using a Nanodrop 2000 with extinction coefficient 83 and molecular weight 79 kD to afford pure **transferrin-PEG5k-$(5nPBA)_2$** (3.1 mg, 14.6% yield). MW (MALDI-TOF): 84000.

Synthesis of Tf-PEG10k-(5nPBA)$_2$ was achieved in the same fashion, except with (5nPBA)$_2$-PEG10k-COOH (126 mg, 0.013 mmol, 50 equiv). MW (MALDI-TOF): 89000.

Nanoparticle formulation was accomplished as previously described.[9]

Nanoparticle size and zeta potential. Nanoparticle size was determined using dynamic light scattering (DLS). DLS was performed on a Brookhaven Instruments Corporation (BIC) Zeta-PALS with BIC Particle Sizing Software. The particles were diluted down to a concentration of 0.1 mg/mL siRNA and size was recorded for ten 1-minute measurements.

The nanoparticles' surface charge, or zeta potential, was measured using the same Zeta-PALS used for DLS, with the addition of a Brookhaven aqueous electrode assembly. 10 uL of particle formulation was mixed with 1.5 mL of either 10 mM phosphate buffer pH 7.4 or 1 mM potassium chloride pH 5.5 in a cuvette. The electrode was inserted into the cuvette and zeta potential measured using BIC PALS Zeta Potential Analyzer software with a target residual of 0.012.

Boronic Acid Binding Constant Assay.

The binding constants of the 5nPBA-PEG5k-COOH and (5nPBA)$_2$-PEG5k-COOH to Alizarin Red S and cMAP were measured using an assay previously described.[18]

Transferrin binding assay

The binding of transferrin and transferrin-PEG conjugates to transferrin receptor was determined by displacement of 50 nM transferrin with Alexa-Fluor 488 attached (Tf-AF488 from Jackson ImmunoResearch Laboratories, Inc.). 100,000 Neuro-2A cells in serum-free OptiMEM I were added to each well of a 24-well plate and appropriate amounts of transferrin or transferrin-PEG conjugates were added to the wells. 50 nM of Tf-AF488 was added to each well. The cells were incubated on a shaker at 37^{o}C with 5% CO_2 for 1 h.

The cells were collected into an Eppendorf tube, centrifuged at 200 rpm for 15 min, the media was removed, and the cells were fixed with 100 uL 4% formalin. The cells were then diluted with phosphate buffered saline to 1 mL and run on a BD FacsCalibur to determine the number of cells that were fluorescent by flow cytometry.

Cetuximab binding assay

The binding of cetuximab and cetuximab-PEG conjugates to EGFR was determined by displacement of 50 nM cetuximab with Alexa-Fluor 488 attached (CTX-AF488) made by conjugation with NHS-ester activated AF488 (Life Technologies). All other procedures were similar to those used for the transferrin binding assay.

***In vitro* work.**

Cell lines. The human non-small cell lung cancer adenocarcinoma cell line, NCI-H1975, was obtained from ATCC and maintained in RPMI-1640 medium with 10% fetal bovine serum without the use of antibiotics in a 37^{o}C incubator with 5% CO_2.

The M249shBRAF melanoma cell line with a doxycycline-inducible BRAF shRNA construct (that was made by Jonathan Zuckerman from the M249 cell line obtained from UCLA) was maintained in RPMI-1640 medium with 10% fetal bovine serum and 10 ug/mL puromycin. The shBRAF construct sequence is as follows:

Top:
5'-CCGGAGAATTGGATCTGGATCATTTCTCGAGAAATGATCCAGATCCAATTCTTTTTT-3'
Bottom:
5'-AATTAAAAAAGAATTGGATCTGGATCATTTCTCGAGAAATGATCCAGATCCAATTCT-3'

Neuro-2A cells were obtained from ATCC and maintained in DMEM medium with 10% fetal bovine serum without antibiotics.

Cell culture and siRNA transfection. The night before siRNA transfection, 20,000 cells in 500 uL were plated per well in a 24-well plate. The cells were washed and fresh media was

added the morning of siRNA transfection, which was performed using Lipofectamine RNAiMAX (Life Technologies) according to their protocol. Briefly, equal volumes of various siRNA concentrations and a 1:50 dilution of Lipofectamine, both in Opti-MEM Reduced Serum Medium, were mixed, incubated at room temperature for 15 min, and then 100 uL of the mixture was added to each well of cells for a total volume of 600 uL in each well. Concentrations of siRNA reported are the final concentrations of siRNA in the well. The siRNA sequences are as follows.

siEGFR:
Anti-Sense: 5'-UAA-UUU-CCA-AAU-UCC-CAA-GGA-C-3'
Sense: 5'-CCU-UGG-GAA-UUU-GGA-AAU-UAU-A-3'

siBRAF:
Anti-Sense: 5'AUGAUCCAGAUCCAAUUCUUU 3'
Sense: 5'-AGAAUUGGAUCUGGAUCAUUU-3'

siRRM2:[13]
Sense: 5'-GAUUUAGCCAAGAAGUUCAGA-3'
Anti-Sense: 5'-UGAACUUCUUGGCUAAAUCGC-3'

siEGFP:[14]
Sense: 5'-GGC-UAC-GUC-CAG-GAG-CGC-ACC-3'
Anti-Sense: 5'-UGC-GCU-CCU-GGA-CGU-AGC-CUU-3'

48 h after transfection, the cells were lysed and RNA collected using the Qiagen RNeasy Plus Mini Kit or the Qiagen miRNeasy Mini Kit for an mRNA knockdown or siRNA detection assay, respectively, according to the manufacturer's protocol. RNA concentrations were determined using a NanoDrop 2000. Each condition was performed in triplicate.

Treatment with NP formulations were accomplished in a similar manner except that 100,000 cells in the appropriate cell medium were added to 100 uL of NP formulation in

Opti-MEM in each well of a 24-well plate. Cells were incubated on a shaker in the incubator to allow NPs and cells to better contact each other. The incubation period was shorter, 16-24 h, and RNA was isolated with the same Qiagen RNeasy Plus Mini Kit as described above.

Quantitative real time polymerase chain reaction (qRT-PCR) analysis. For determination of mRNA knockdown, the RNA samples were diluted to 14.4 ng/uL, 9 uL or 130 ng of which was used, for reverse transcription using the Invitrogen High Capacity RNA to cDNA kit, according to the manufacturer's protocol. The reverse transcription reaction was cycled in a Bio-Rad MJ Mini Personal Thermal Cycler, incubating for 60 min at 37^{o}C, 5 min at 95^{o}C to stop the reaction, and then held at 4^{o}C forever. The qRT-PCR reaction used the Life Technologies TaqMan probes with actin beta for normalization as follows:

EGFR (human) - Assay ID: Hs01076078_m1

Actin beta (human) - Assay ID: Hs01060665_g1

BRAF (human): Hs00269944_m1

RRM2 (mouse): Mm00485881_g1

Actin (mouse): Mm02619580_g1

The Life Technologies TaqMan Universal Master Mix II, no UNG, was used for the qPCR reactions, which were performed in duplicate for each triplicate sample in a 96-well PCR plate, set up according to the manufacturer's instructions. The reactions were run using a Bio-Rad iCycler, with polymerase activation at 95^{o}C for 10 min and 40 cycles of PCR (95^{o}C for 15 seconds and 60^{o}C for 1 min). Real time detection was performed with a MyiQ Single Color Real-Time PCR Detection System. The data was imported into Microsoft Excel and the cycle threshold value was used for calculations. The difference in

the cycle threshold was calculated using the equation dCt=2^-([EGFR]Ct-[Actin]Ct). The percent EGFR expression was calculated by comparing the dCt's of siEGFR treated cells with those of untreated or control siRNA treated cells.

For detection of the amount of siRNA in transfected cells, the RNA samples were diluted to 2 ng/uL, 2.5 uL or 5 ng of which was used, for reverse transcription using the Applied Biosystems TaqMan MicroRNA Reverse Transcription Kit, according to the manufacturer's protocol. The reverse transcription primer was a Life Technologies Custom TaqMan Small RNA assay designed for the anti-sense sequence of siEGFR (Assay ID RT: CSPACSP). The reverse transcription reaction was cycled in a Bio-Rad MJ Mini Personal Thermal Cycler, incubating for 30 min at 16^{o}C, 30 min at 42^{o}C, 5 minutes at 85^{o}C to stop the reaction, and then held at 4^{o}C forever. The qRT-PCR reaction used the Life Technologies Custom TaqMan Small RNA assay designed for the anti-sense sequence for siEGFR, as above, for the real time primer (Assay ID TM: CSPACSP) and Actin (Assay ID: Hs01060665_g1) for normalization. The Life Technologies TaqMan Universal Master Mix II, no UNG, was used for the PCR reactions, which were performed in duplicate for each triplicate sample in a 96-well PCR plate, set up according to the manufacturer's instructions. The reactions were run, data collected, and results analyzed as described for the mRNA qRT-PCR, for siEGFR instead of EGFR mRNA.

***In vivo* studies.**

All animal studies were approved by the Institutional Animal Care and Use Committee at Caltech. *In vivo* studies of the nanoparticle formulation included H1975 and M249shBRAF xenograft tumor regression. Nanoparticles were formulated as described

above, and were injected intravenously via the mouse tail vein at a dose of 5 mg siRNA per kg mouse.

Mouse Xenograft Tumor Studies. For the H1975 xenograft tumor regression study, H1975 cells were grown in RPMI1640 containing 10% FBS until there were sufficient numbers of cells to implant 1 x 10^7 cells per mouse. On the day of implantation, media was aspirated and cells were detached using 0.25% trypsin-EDTA. The trypsin was neutralized with media containing FBS, the cells were spun down at 200x*g* for 5 min at room temperature, and the media aspirated. The cells were washed with phosphate buffered saline and then RPMI1640 without FBS in a similar fashion. The cells were re-suspended in fresh RPMI1640 without FBS at a concentration of 5 x 10^7 cells per mL. Sterile 1 mL syringes were filled with 0.2 mL of cells and a 25 gauge needle attached to implant H1975 cells directly into the left hind flank of 8 week old female nude mice under isoflurane anesthesia. M249shBRAF cells were prepared in a similar fashion to the H1975 cells but were implanted into the left front flank of 8 week old female nude mice under isoflurane anesthesia. Tumor size was monitored starting at 7 days after implantation using digital calipers, and tumor volume calculated with the equation $V = l \times w^2/2$. When tumors reached 200 mm^3 at 14 days after implantation, the mice were randomized to treatment groups. Treatment was a total of four to six doses: two doses per week over two to three weeks. Tumor size was monitored every day for the first month after dosing, and at least twice a week up to 80 days after tumor implantation if the mice were still alive.

Tumor analysis

For tumor analysis, tumors were collected from 3 separate mice per group 24 h after the second dose of treatment. For the determination of siEGFR in the tumor, a small 10 mg

piece of tumor tissue was cut and placed in a tube with ceramic beads and QIAzol lysis reagent, homogenized with an MP Bio FastPrep tissue homogenizer. RNA was extracted and qRT-PCR was performed as described for siEGFR determination in cell culture above.

SUPPORTING INFORMATION

Figure IV.S1: 1H NMR of $(5nPBA)_2$-Lysine-OMe.

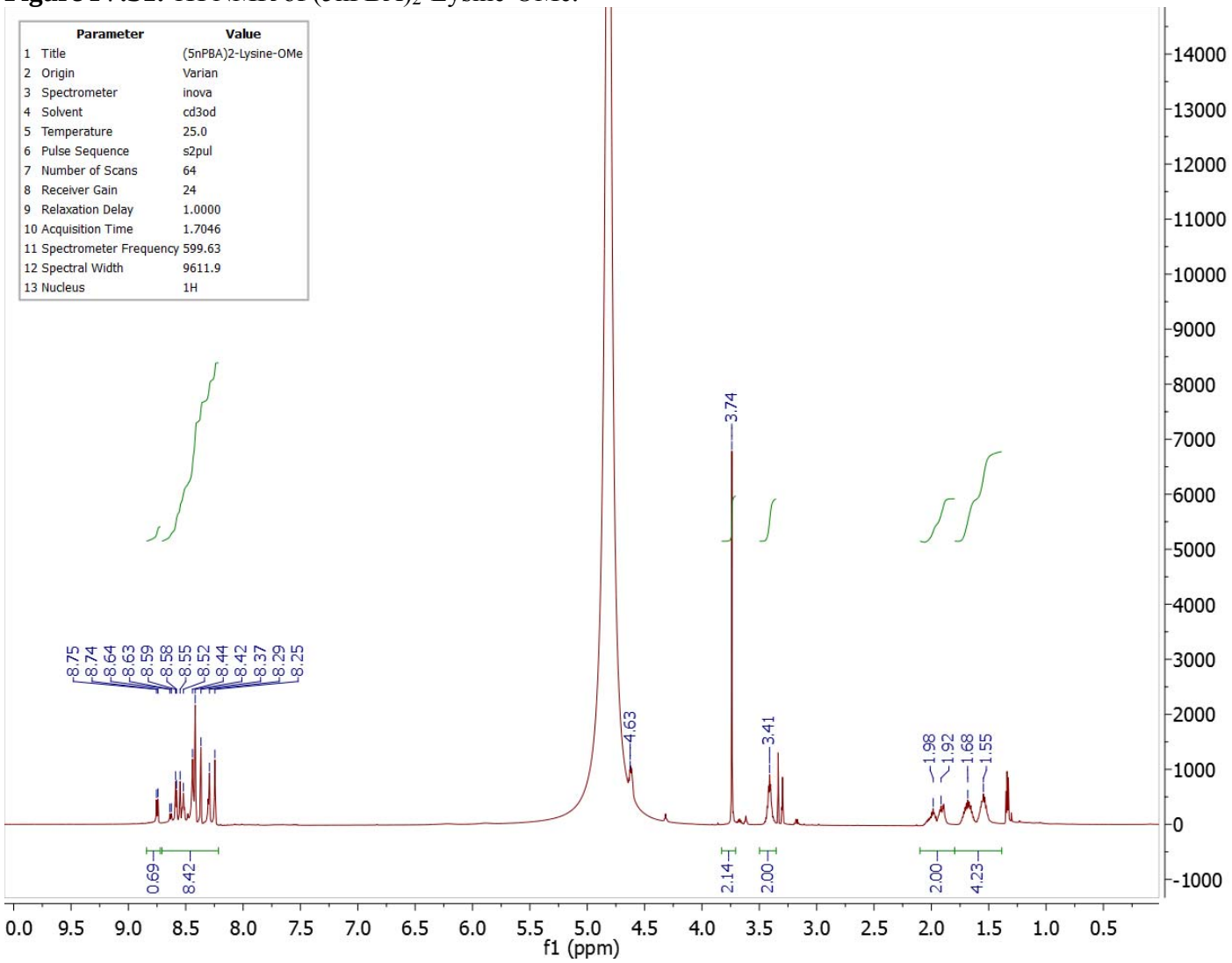

Figure IV.S2: 11B NMR of $(5nPBA)_2$-Lysine-OMe.

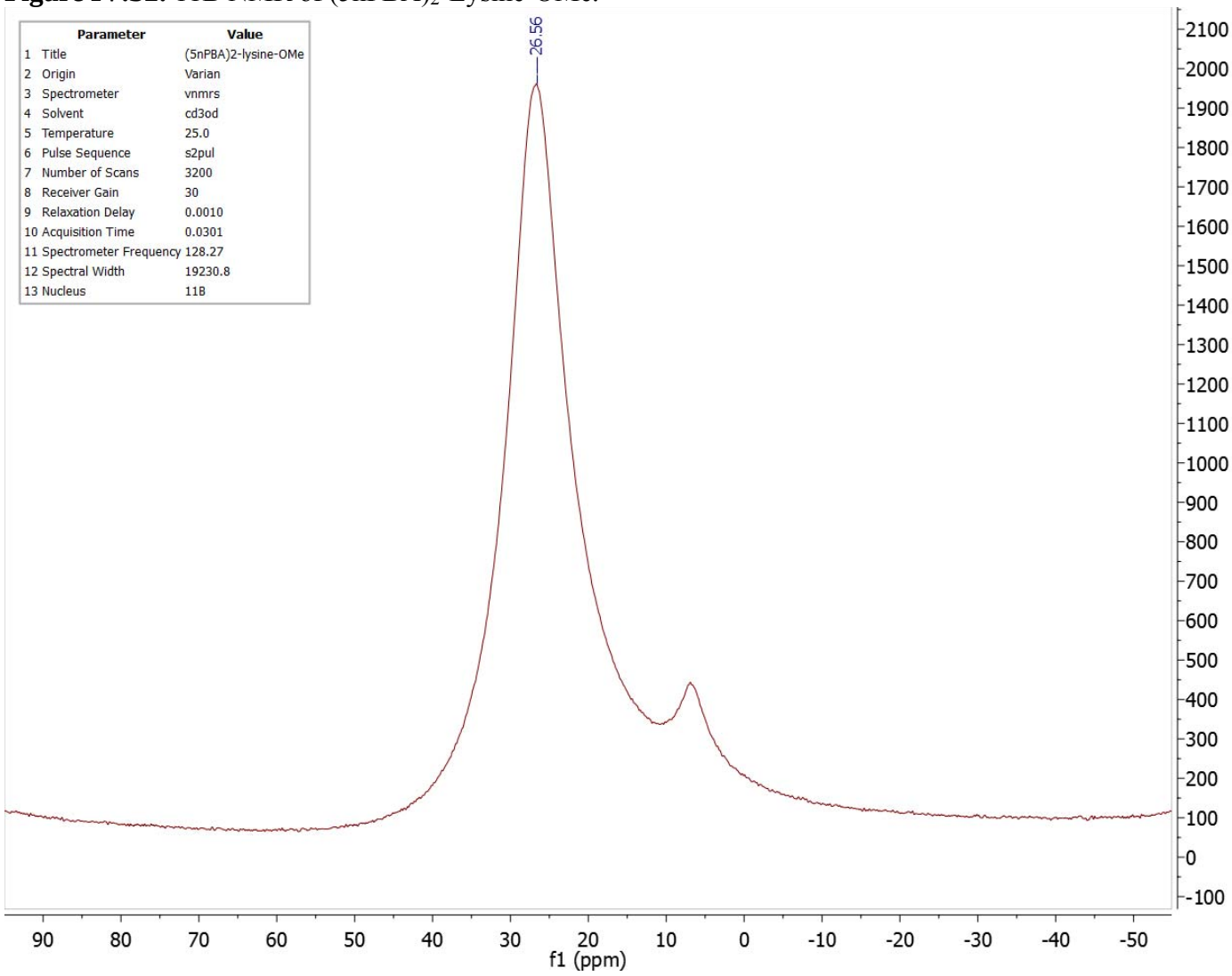

Figure IV.S3: 1H NMR of $(5nPBA)_2$-Lysine.

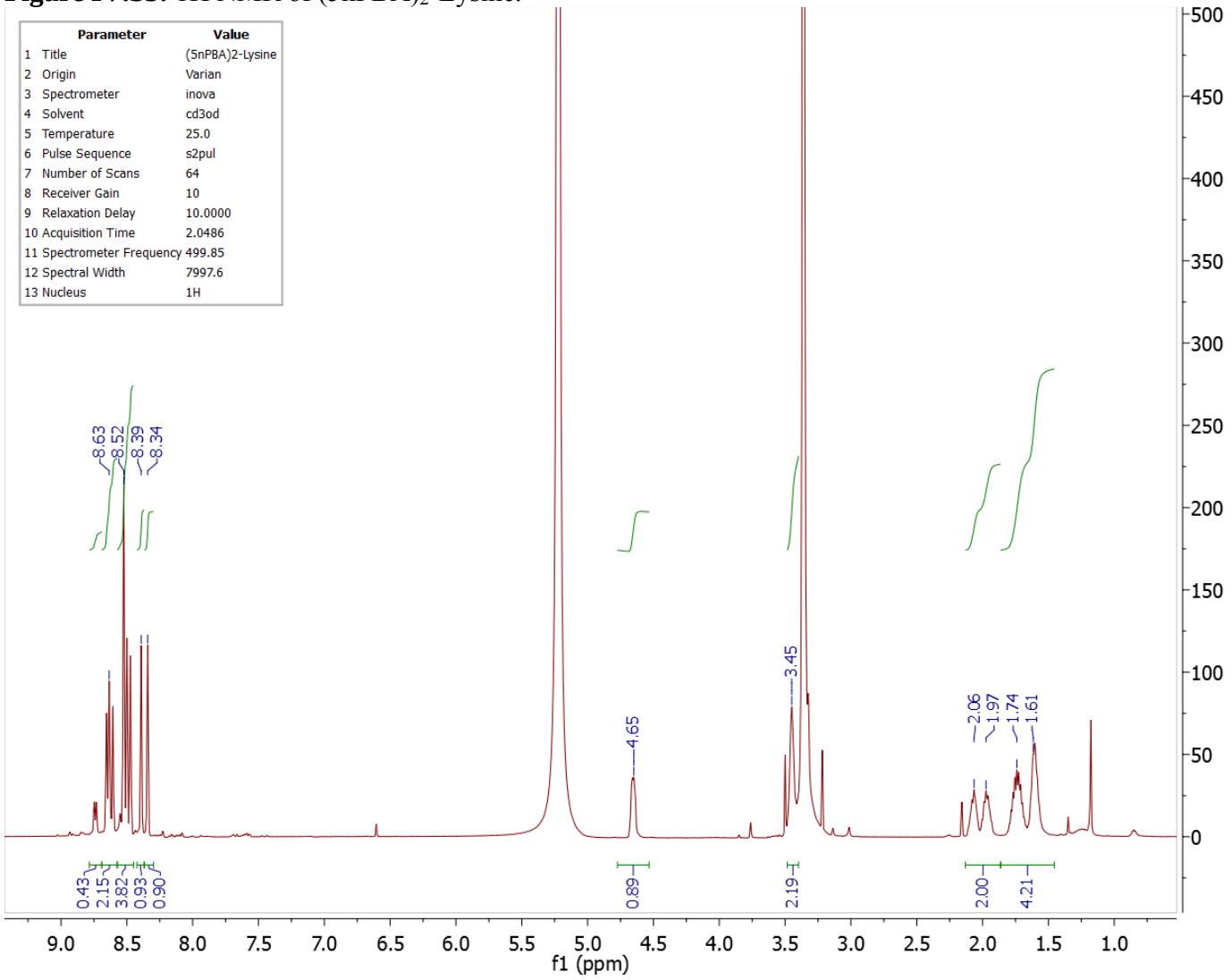

Figure IV.S4: 11B NMR of $(5nPBA)_2$-Lysine.

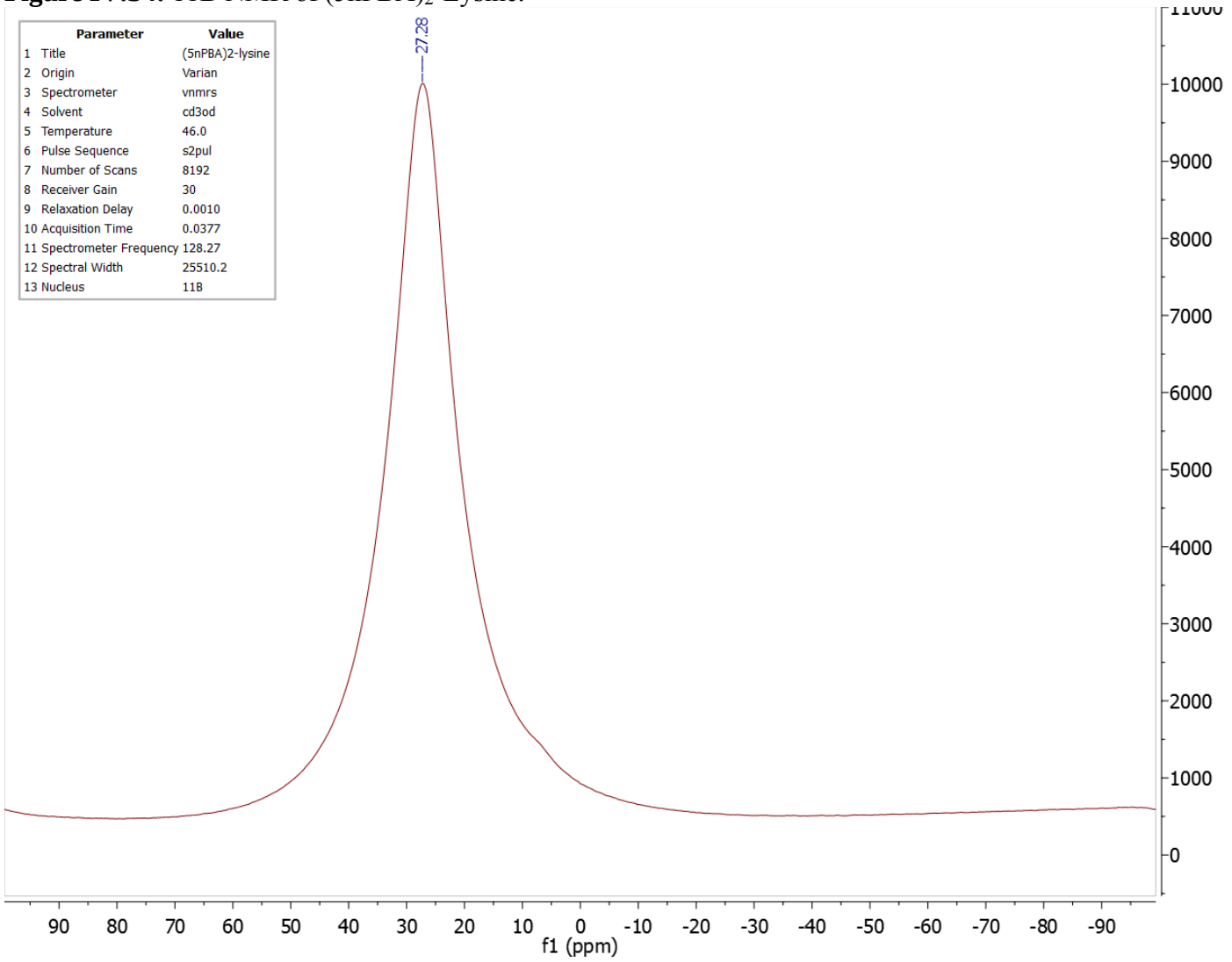

Figure IV.S5: 1H NMR of 5nPBA-PEG5k-COOH.

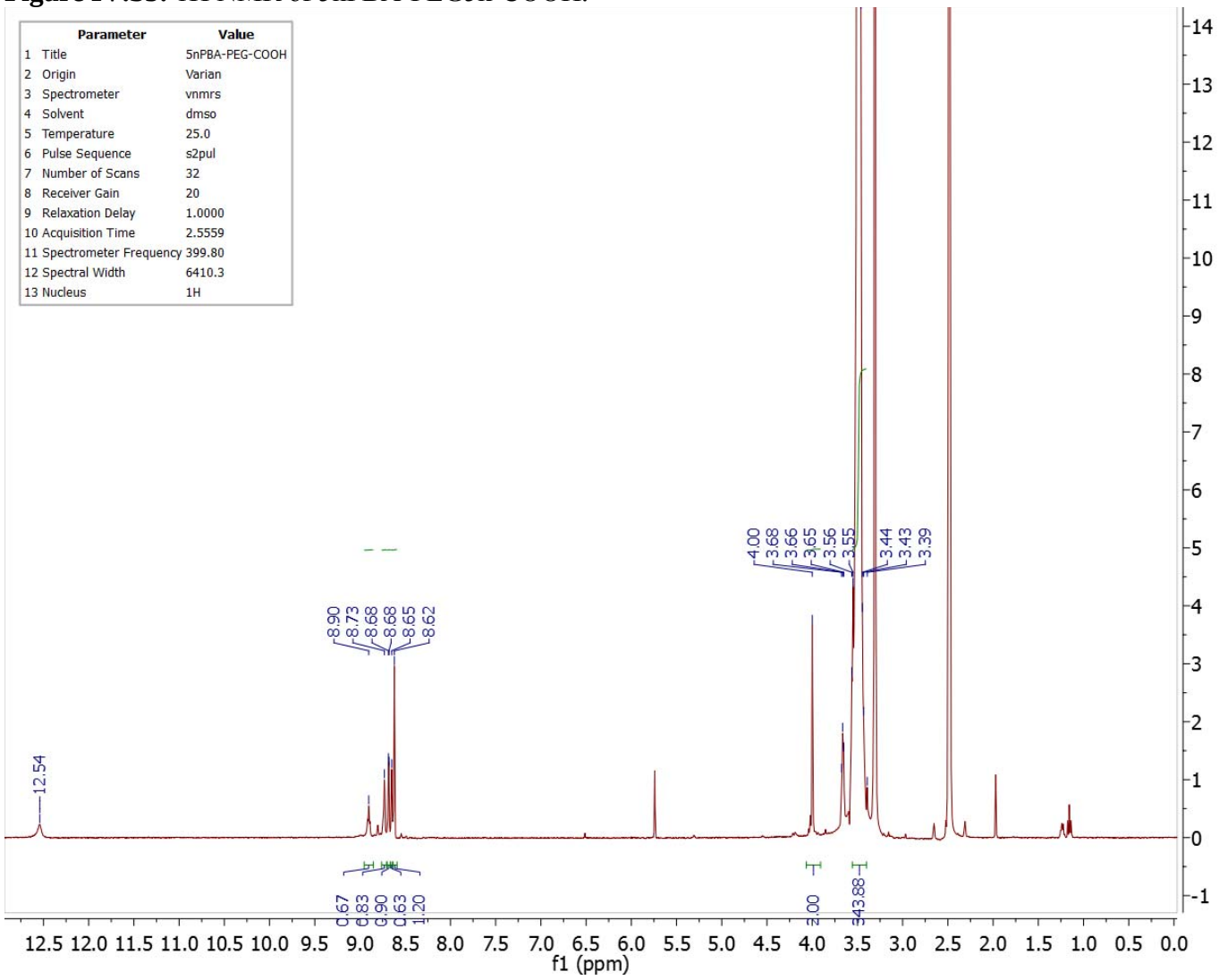

Figure IV.S6: 1H NMR of 5nPBA-PEG5k-COOH with enlarged downfield region.

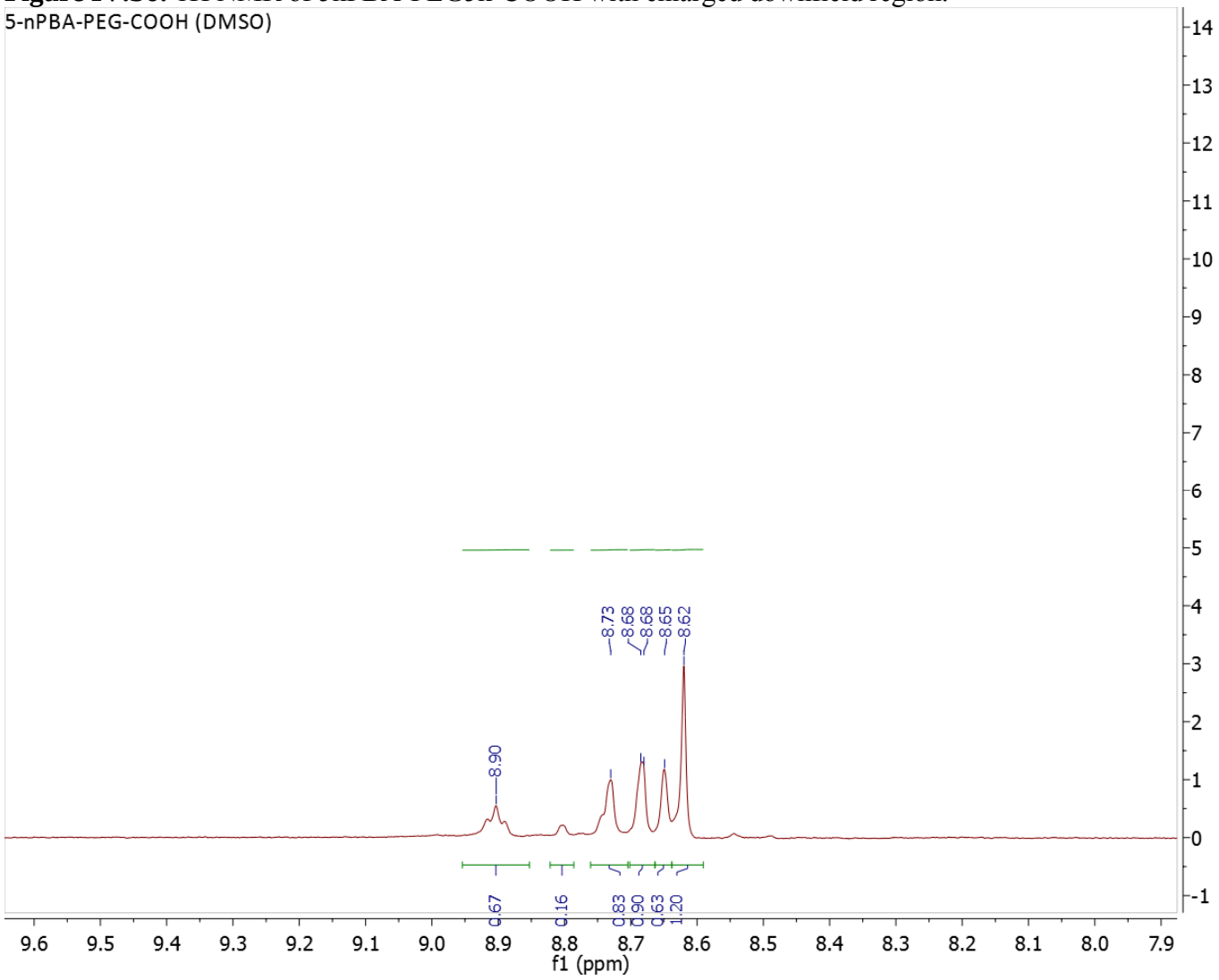

Figure IV.S7: MALDI of 5nPBA-PEG5k-COOH.

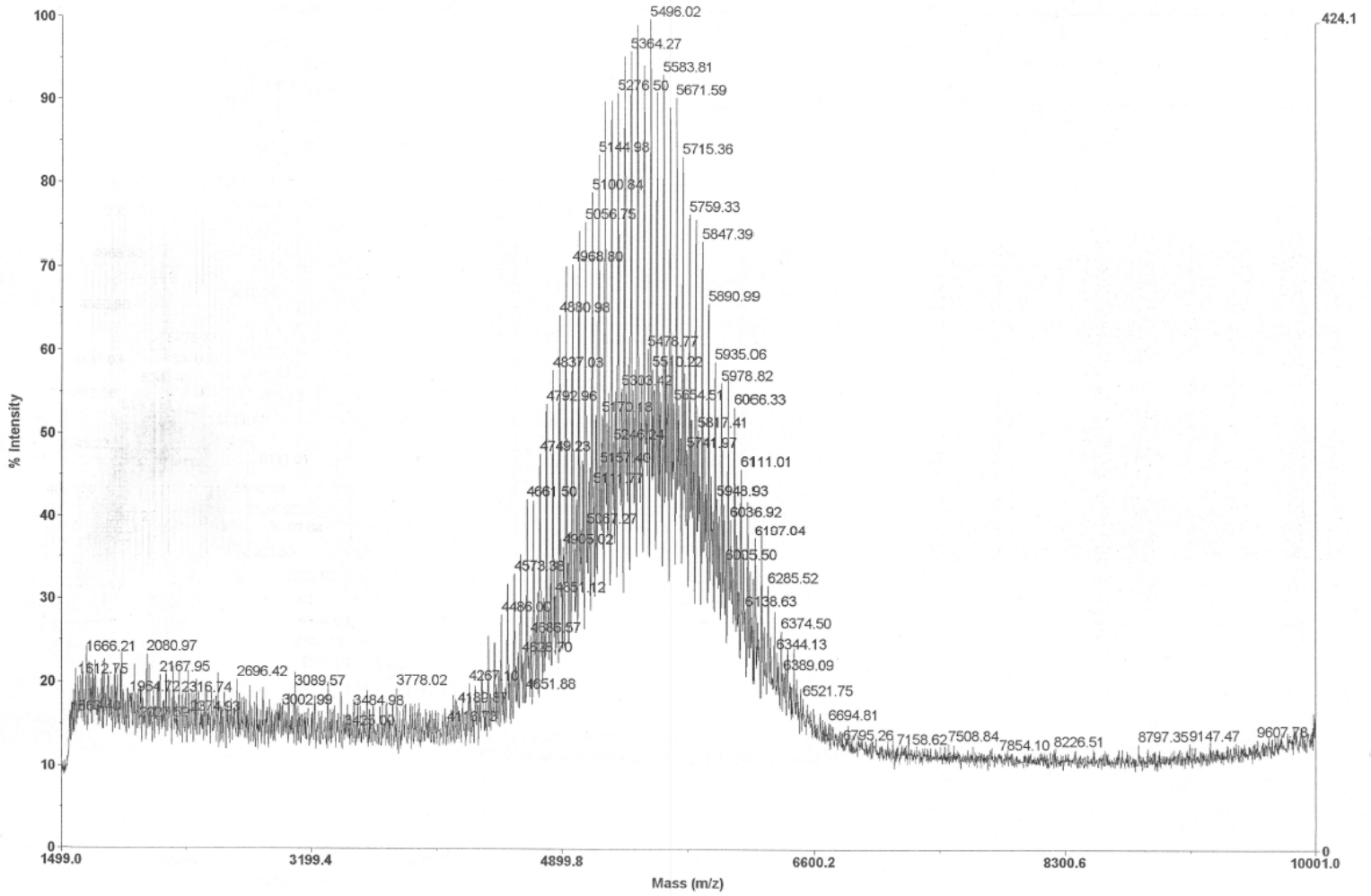

L:\...\20141103_5-nPBA-PEG-COOH_0001.dat
Acquired: 12:25:00, November 03, 2014

Figure IV.S8: 1H NMR of 5nPBA-PEG10k-COOH.

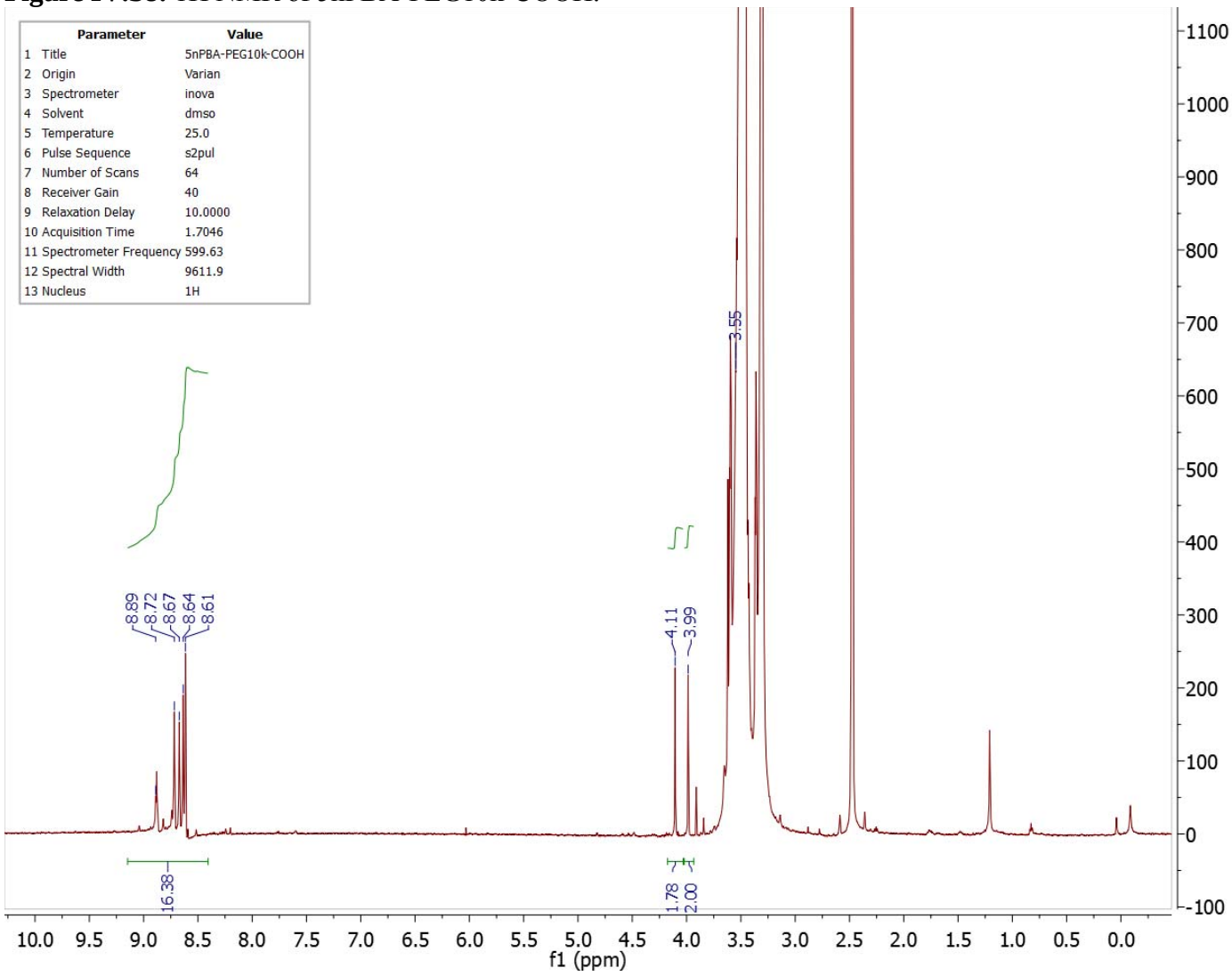

Figure IV.S9: MALDI of 5nPBA-PEG10k-COOH.

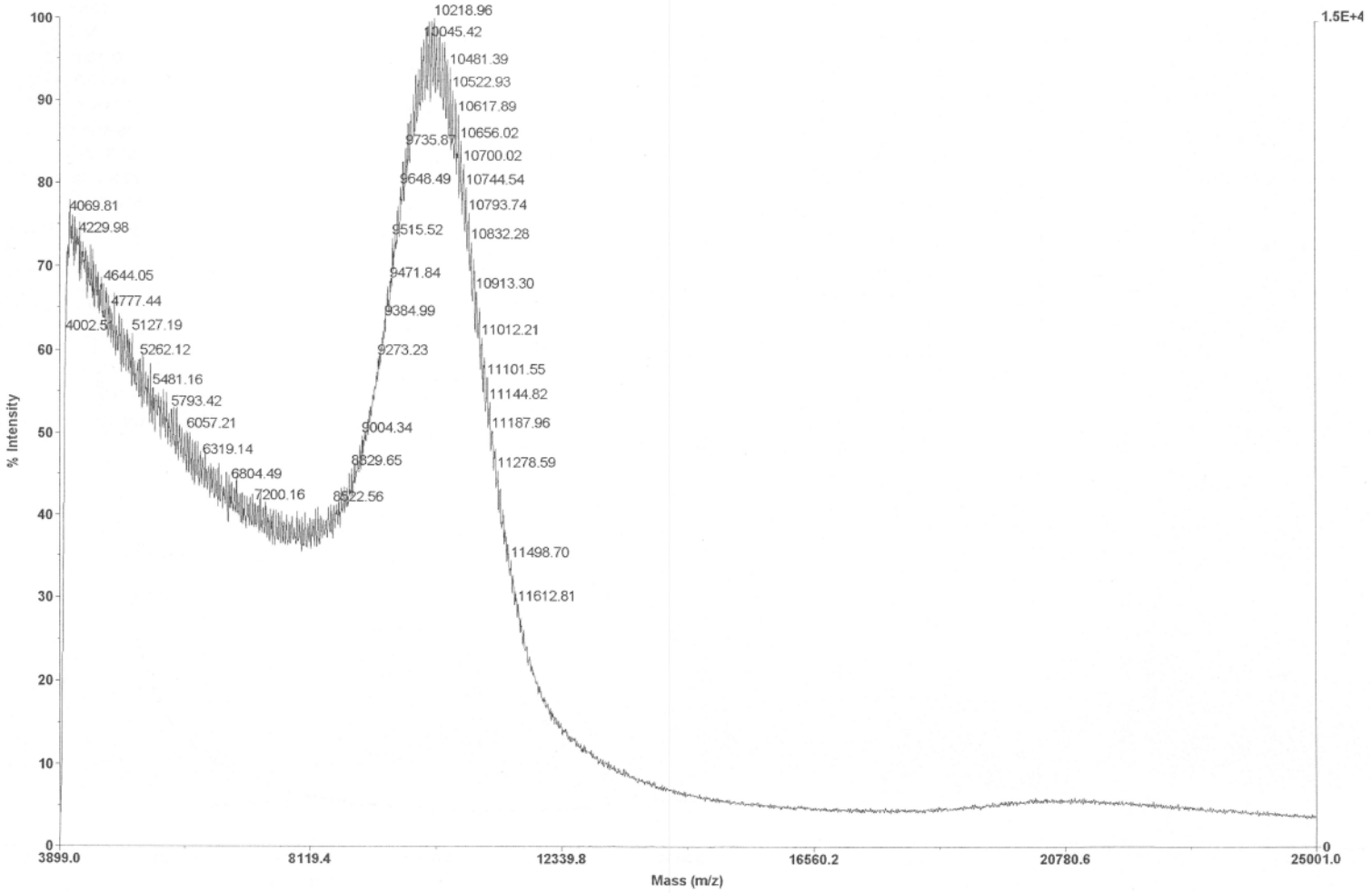

L:\...\20150915_5nPBA-PEG10k-COOH_0002.dat
Acquired: 15:37:00, September 15, 2015

Figure IV.S10: 1H NMR of $(5nPBA)_2$-PEG5k-COOH.

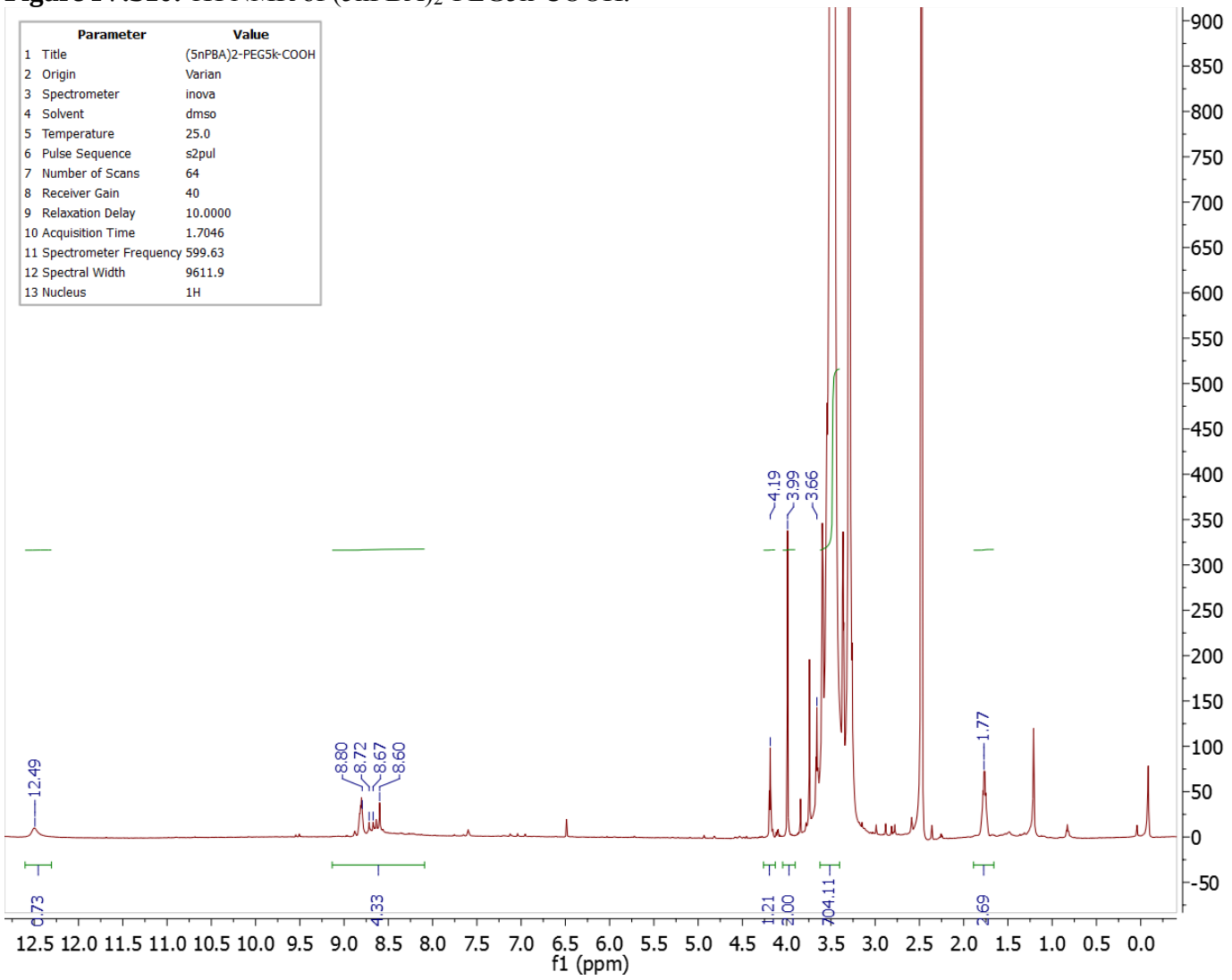

Figure IV.S11: MALDI of $(5nPBA)_2$-PEG5k-COOH.

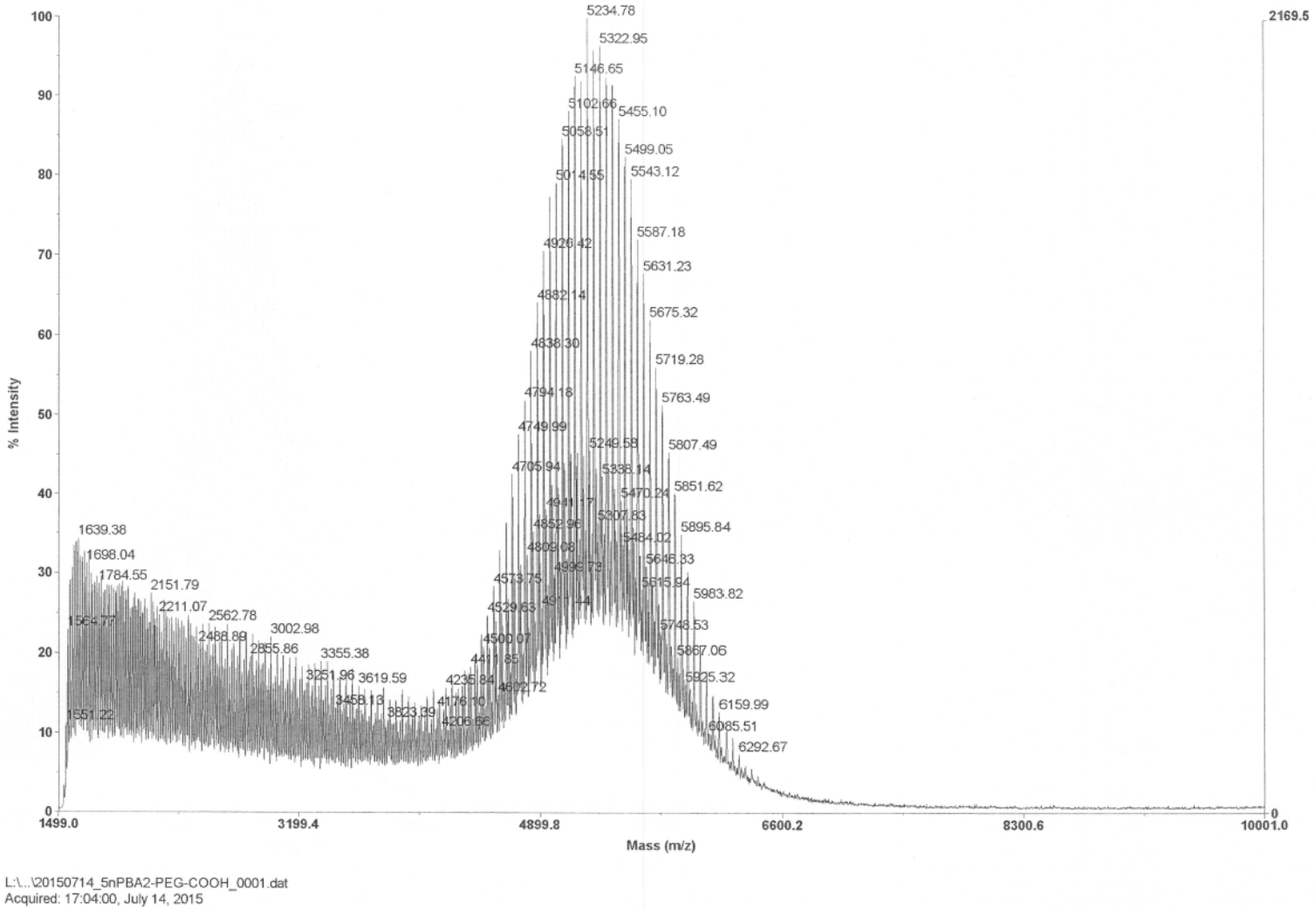

L:\...\20150714_5nPBA2-PEG-COOH_0001.dat
Acquired: 17:04:00, July 14, 2015

Figure IV.S12: 1H NMR of $(5nPBA)_2$-PEG10k-COOH.

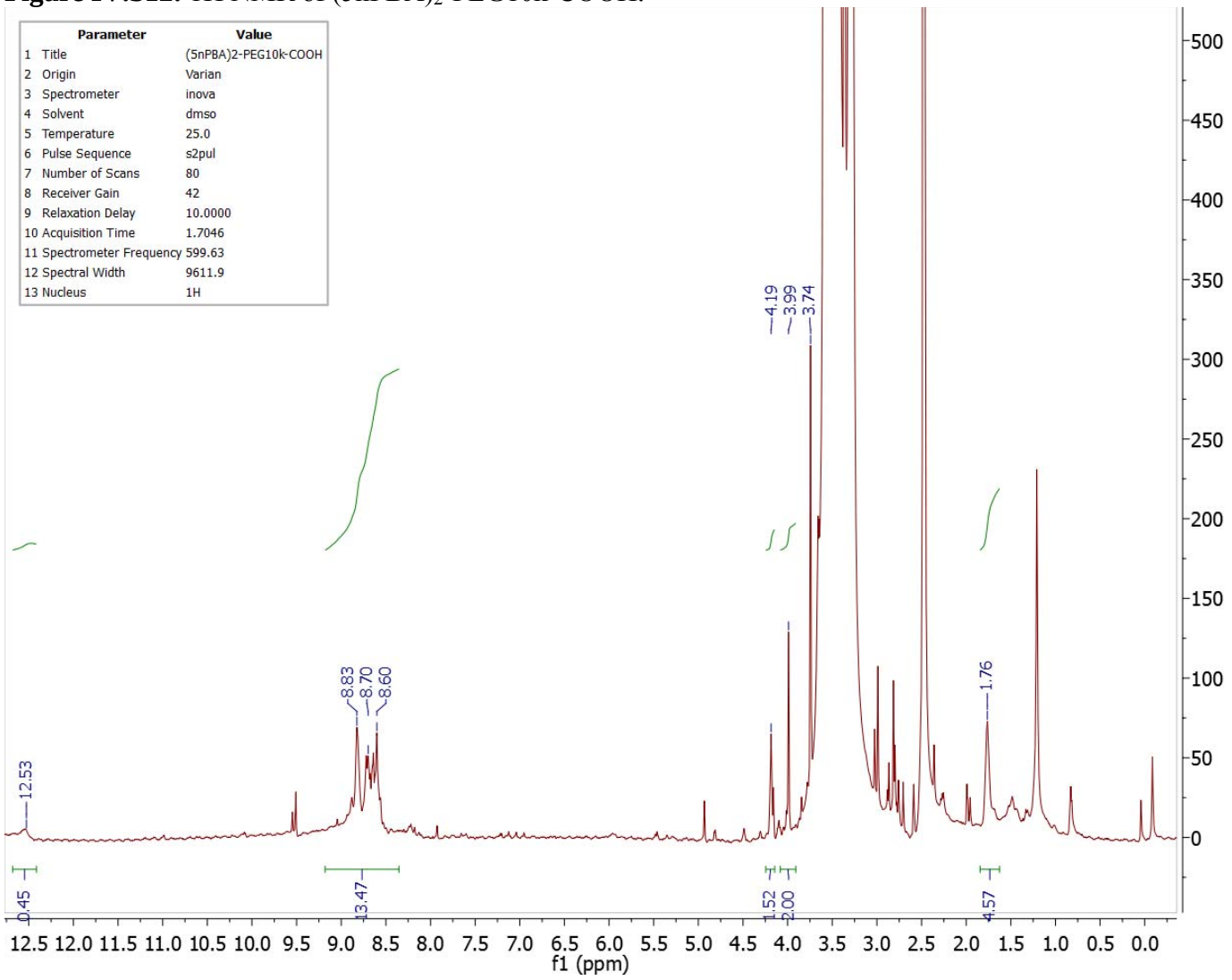

Figure IV.S13: MALDI of $(5nPBA)_2$-PEG10k-COOH.

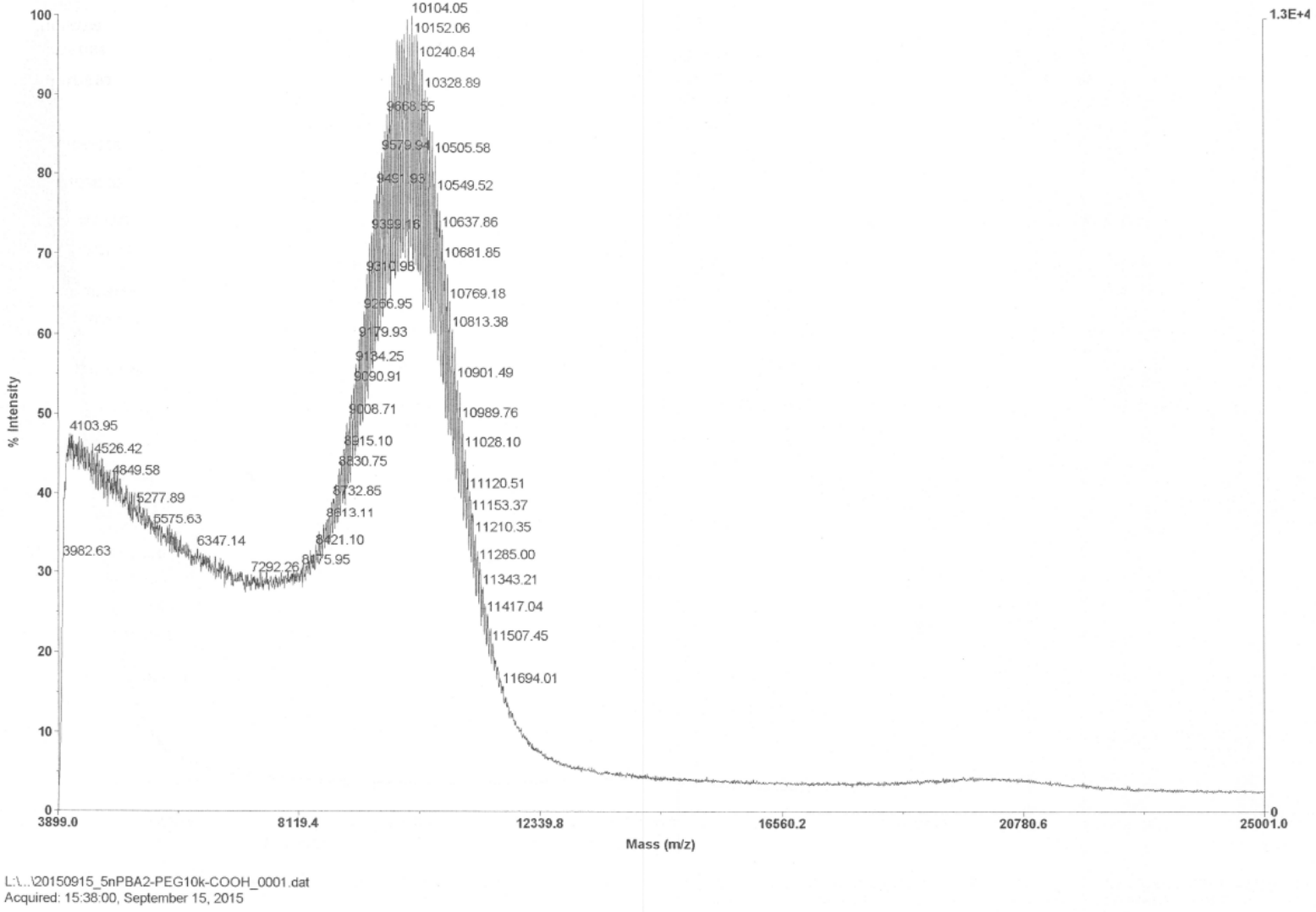

Figure IV.S14: MALDI of crude 5nPBA-PEG5k-Tf showing Tf with 0, 1, 2, and 3+ PEGs conjugated.

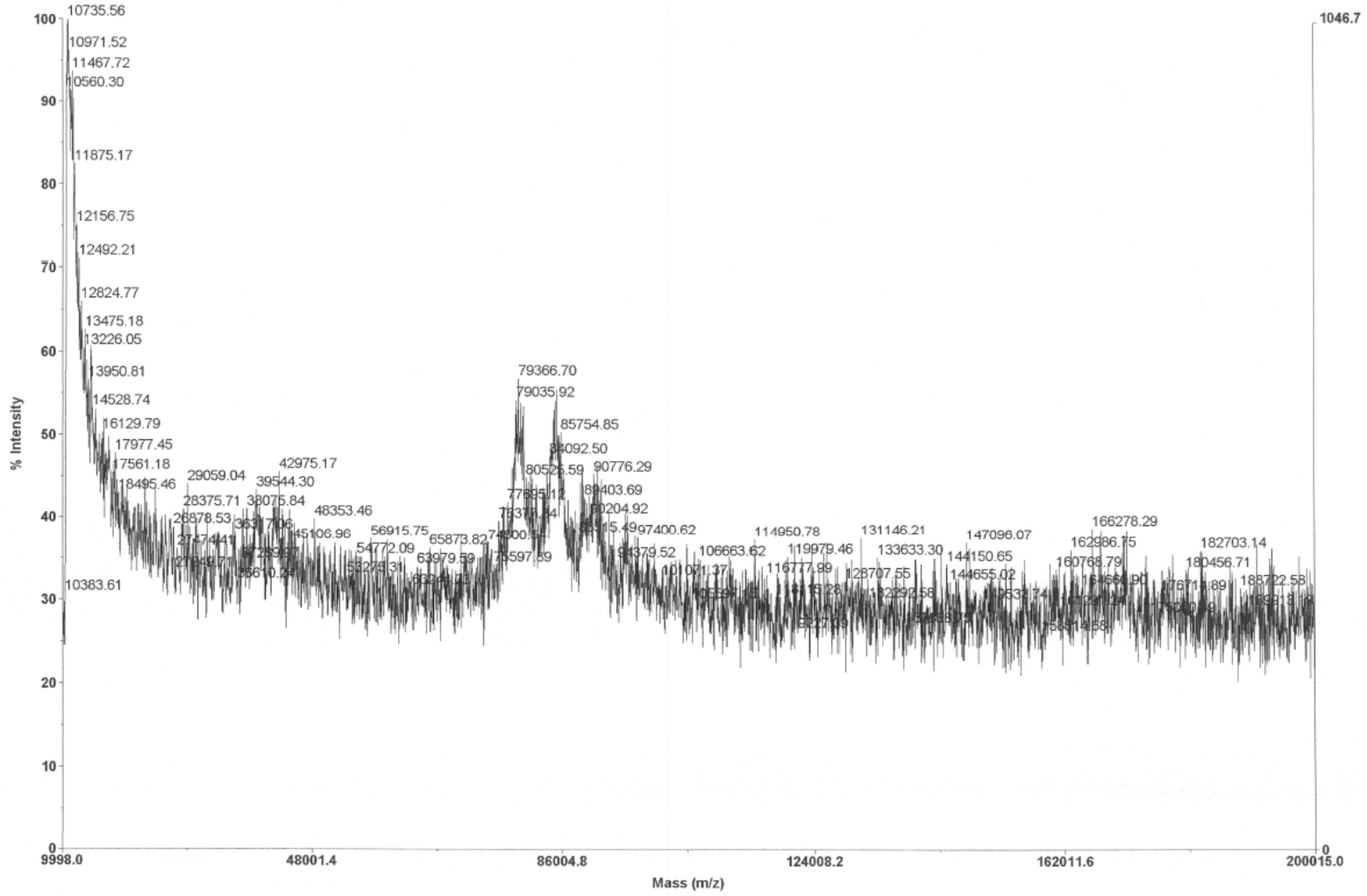

L:\...\20150826_Tf-PEG5k-5nPBA_crude_0001.dat
Acquired: 11:44:00, August 26, 2015

Figure IV.S15: MALDI of crude 5nPBA-PEG5k-CTX showing CTX with 0, 1, 2, and 3+ PEGs conjugated.

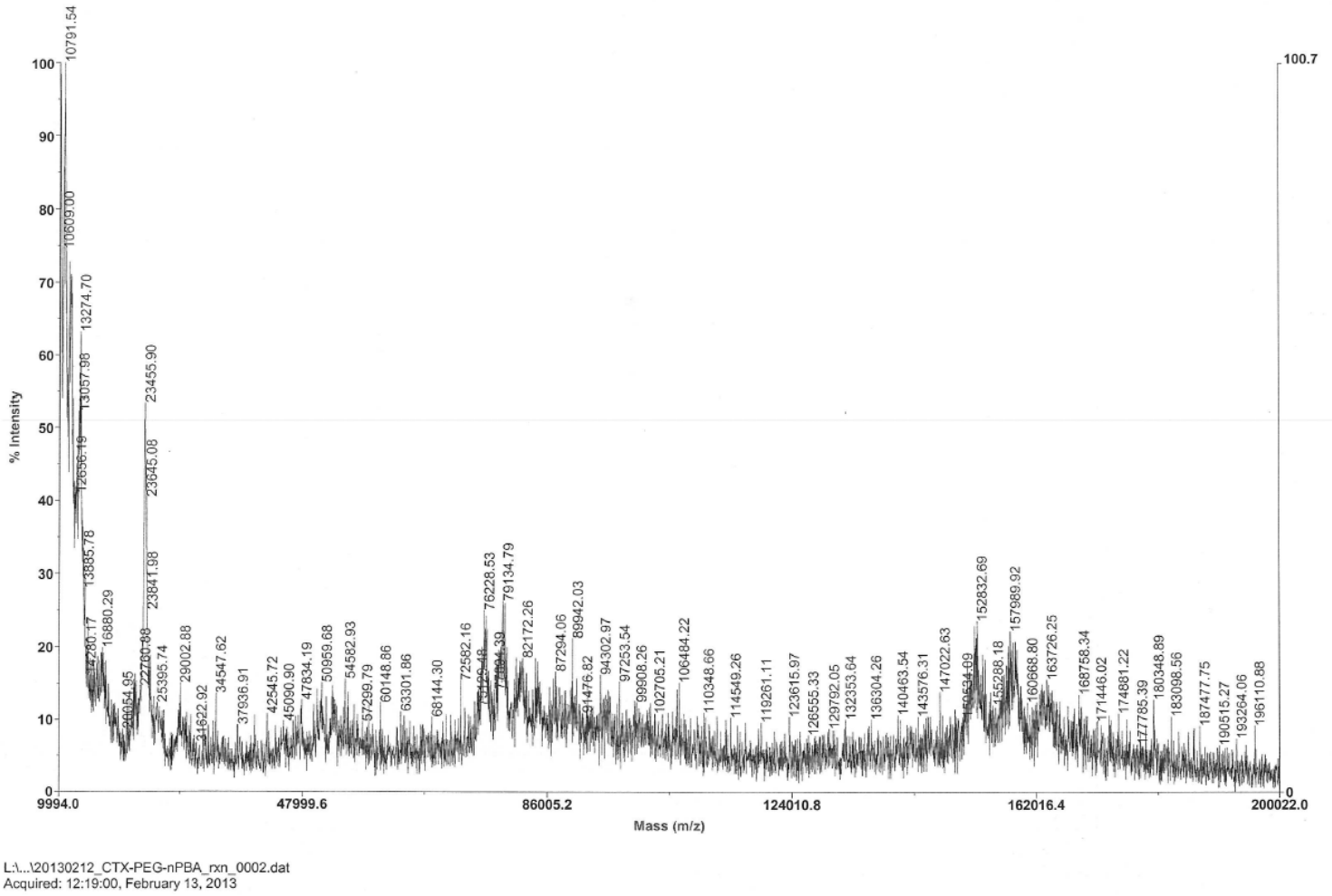

L:\...\20130212_CTX-PEG-nPBA_rxn_0002.dat
Acquired: 12:19:00, February 13, 2013

Figure IV.S16: Purification of crude 5nPBA-PEG5k-CTX by HPLC. Cetuximab is eluted at pH 7.4 and then the pH is dropped to allow 5nPBA-PEGylated cetuximab to elute.

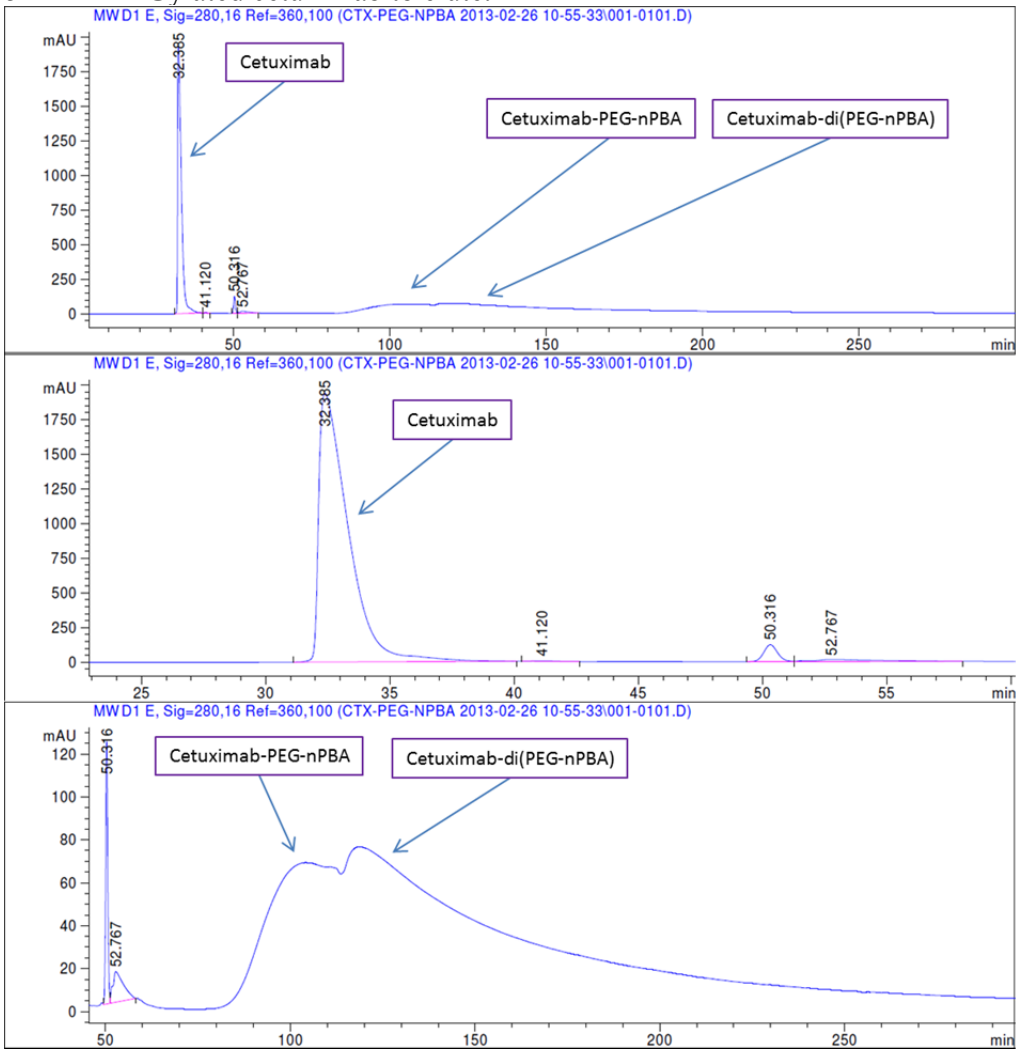

Full HPLC trace
0-300 min

HPLC trace
0-60 min

HPLC trace
50-300 min

Figure IV.S17: MALDI of purified 5nPBA-PEG5k-CTX, 158 kD. Cetuximab is originally 153 kD.

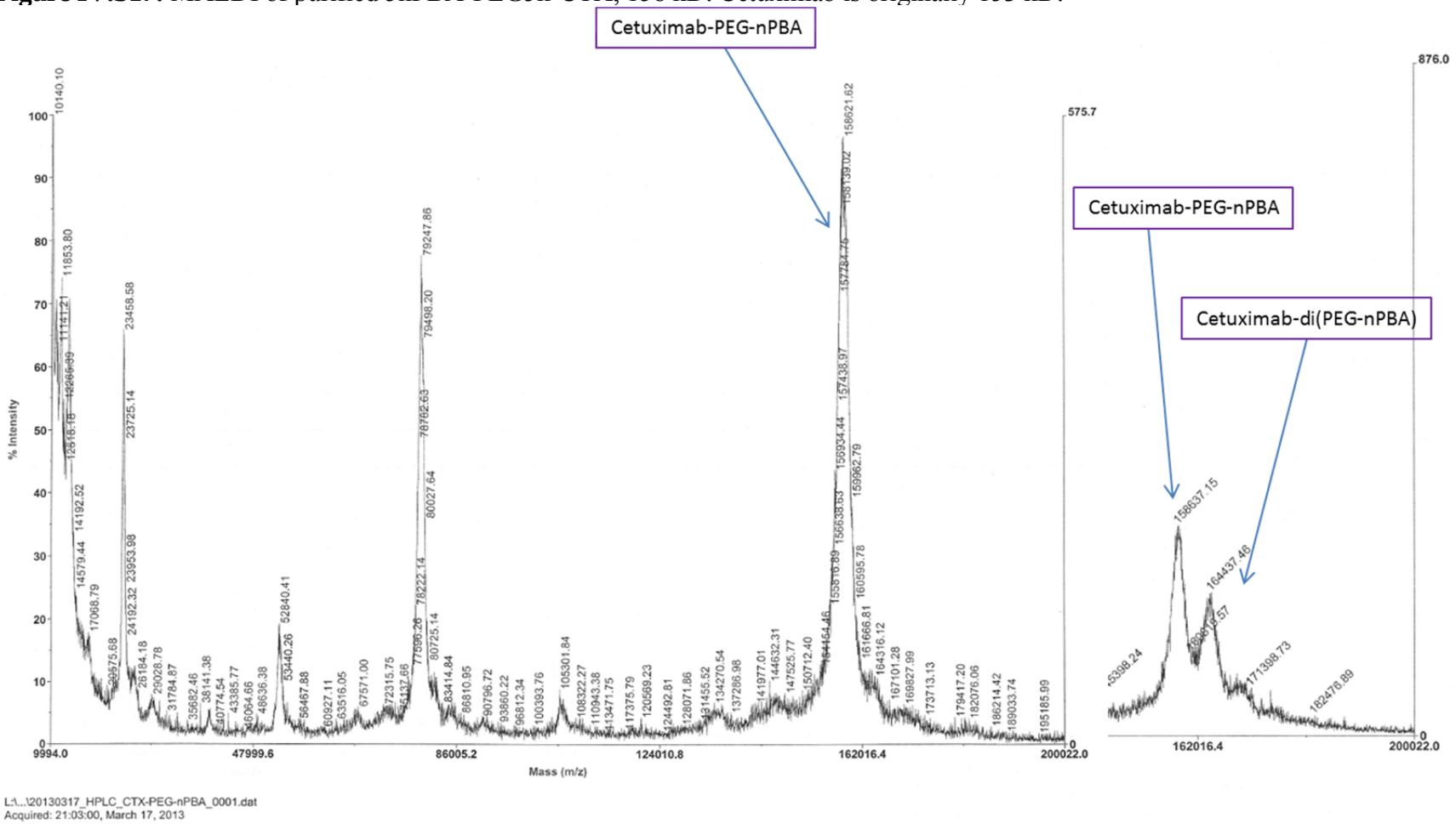

Figure IV.S18: MALDI of purified PEGylated transferrin. Tf is originally 79 kD.
A. Tf-PEG5k-5nPBA, ~85 kD B. Tf-PEG10k-5nPBA, ~90 kD C. Tf-PEG5k-$(5nPBA)_2$, ~85 kD D. Tf-PEG10k-$(5nPBA)_2$, ~90 kD

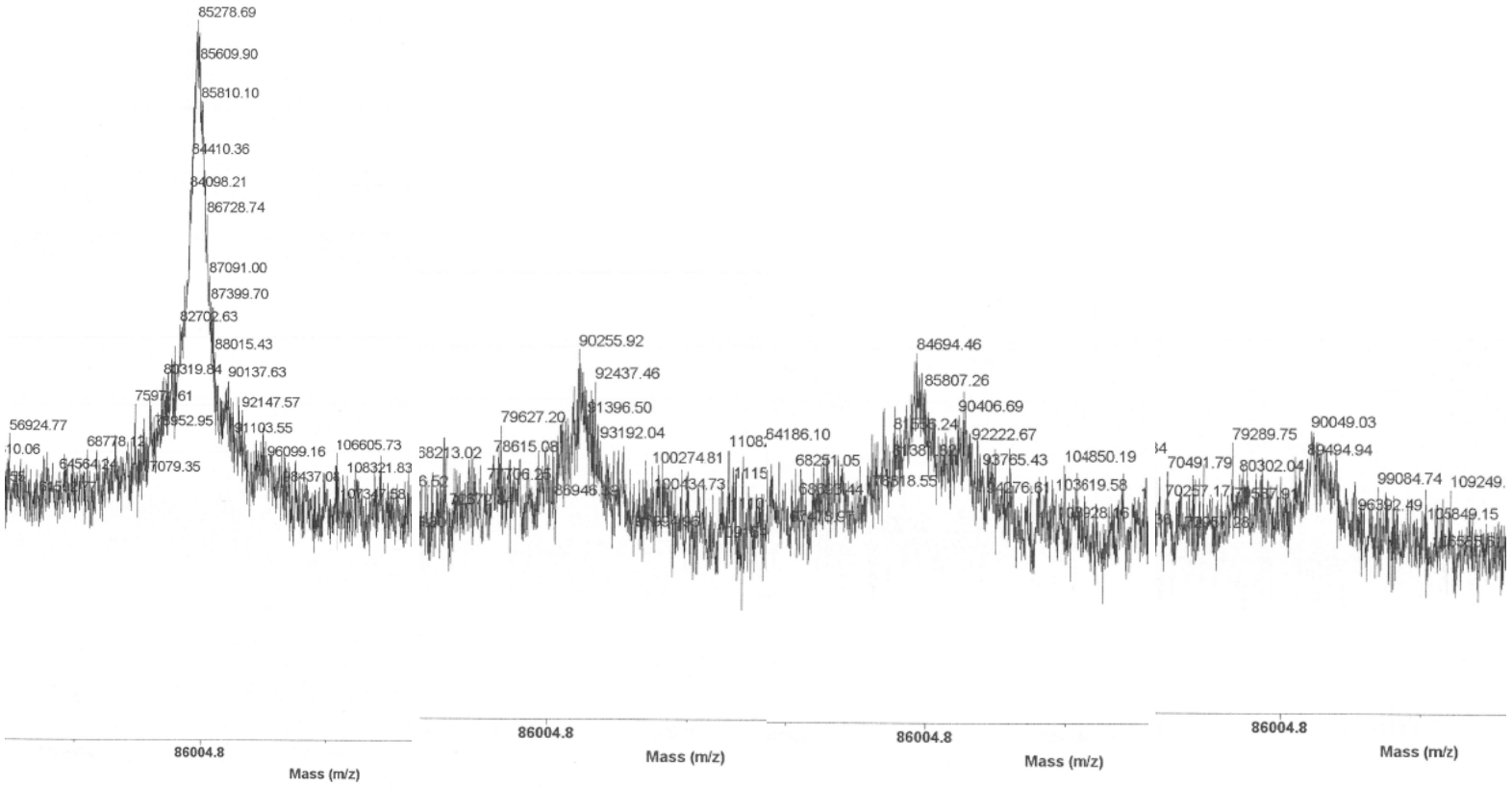

Figure IV.S19: 1H NMR of cMAP-PEG5k-COOH.

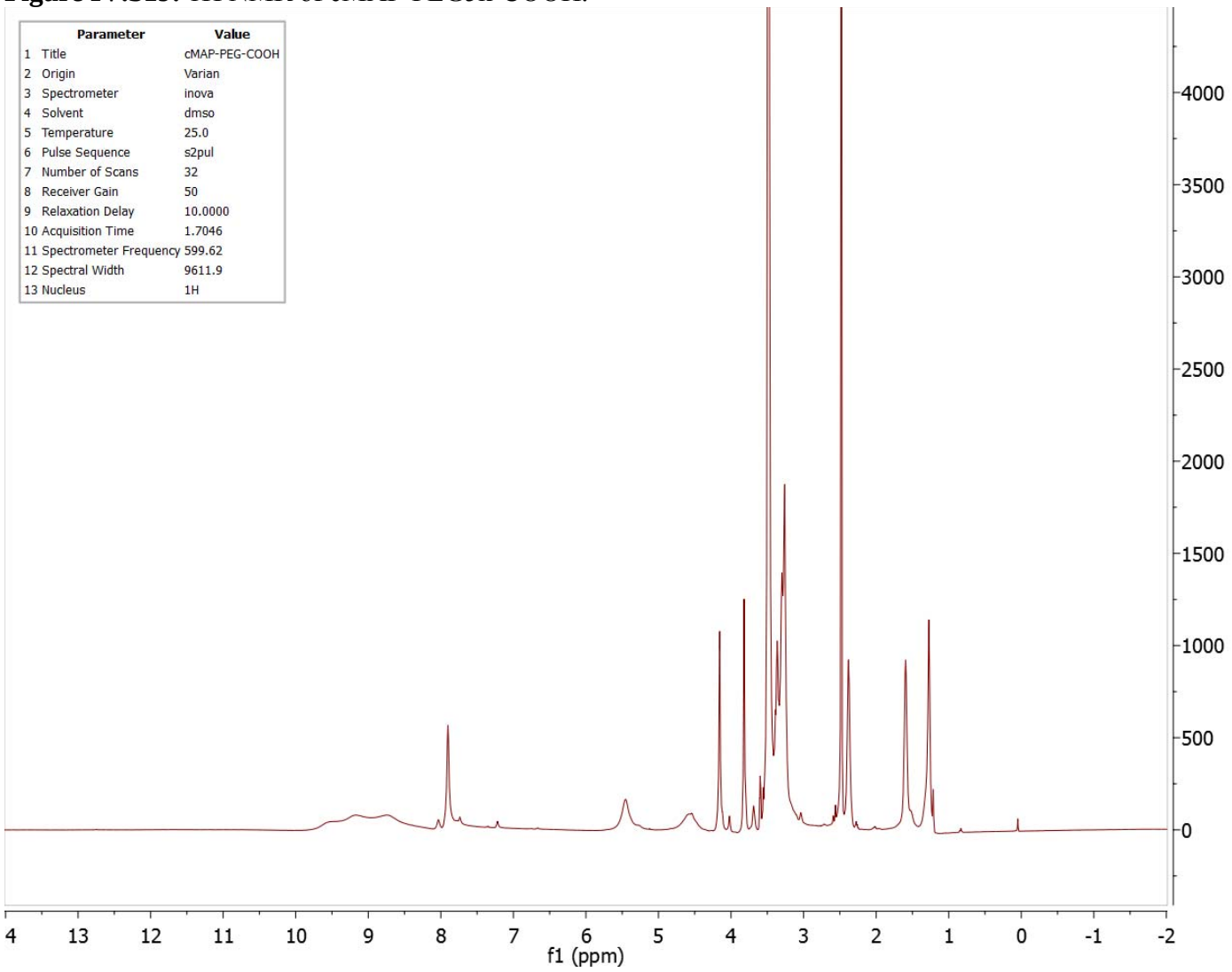

Figure IV.S20: MALDI of cMAP-PEG5k-Tf.

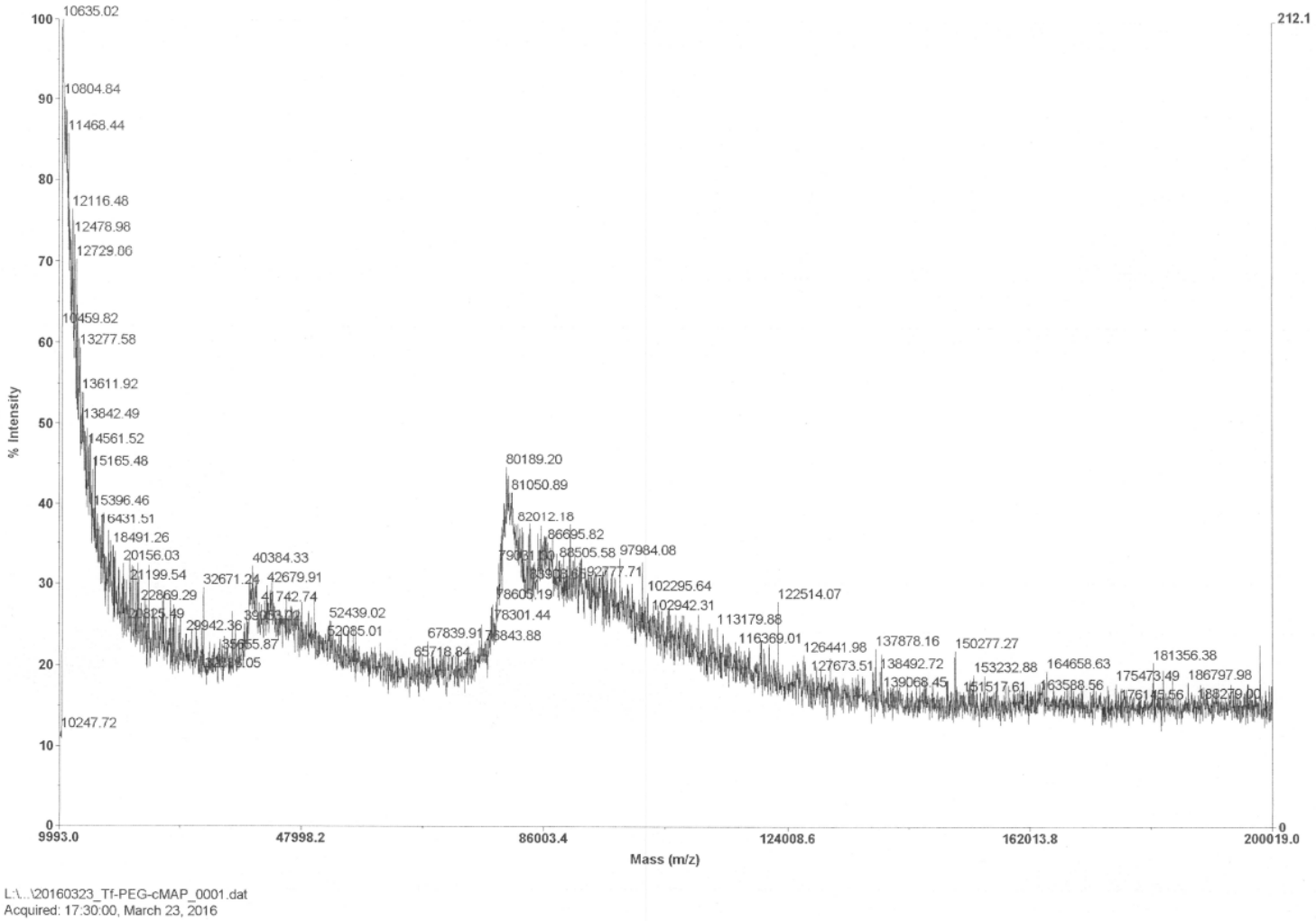

Figure IV.S21: 1H NMR of His-cMAP-His.

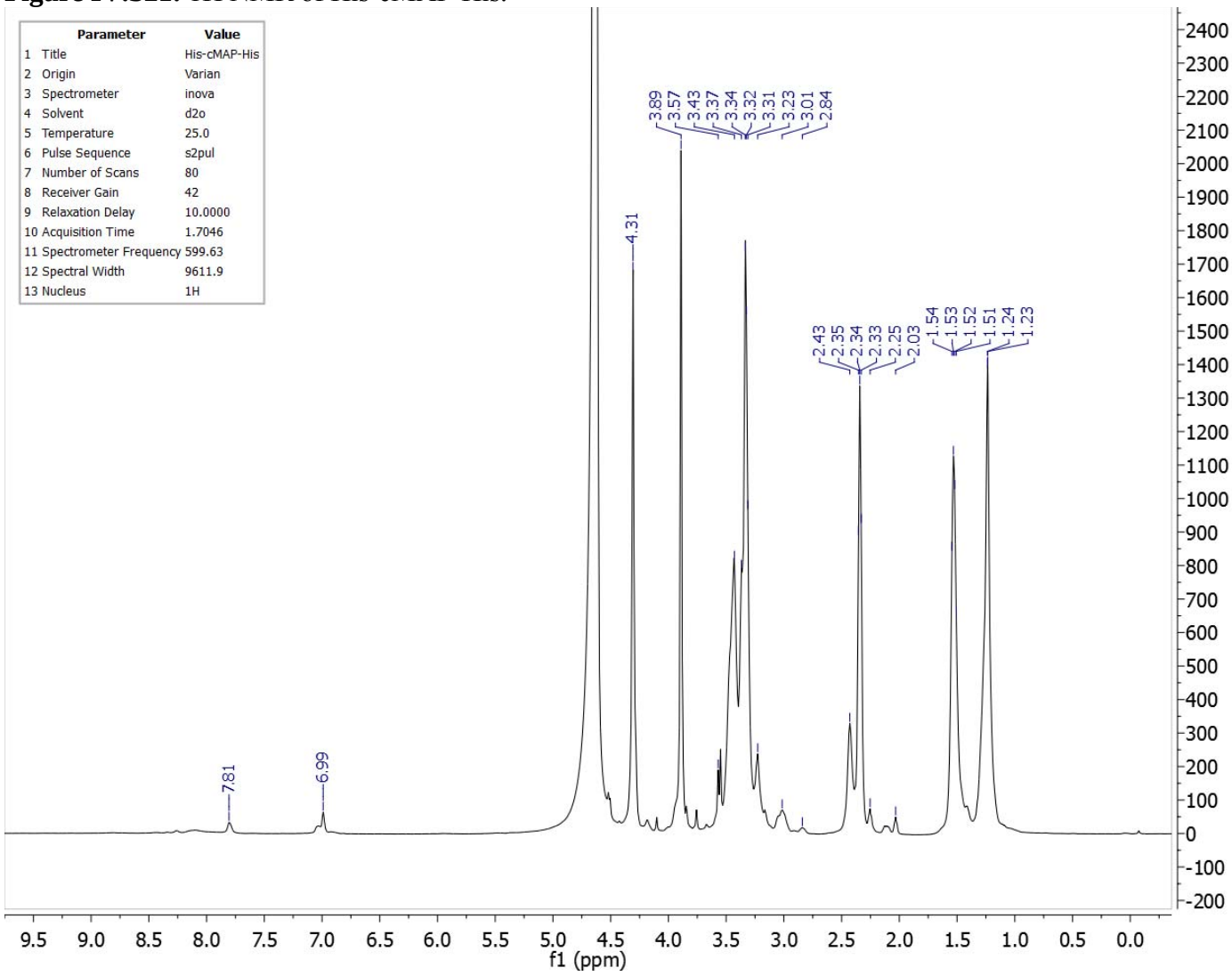

Figure IV.S22: 1H NMR of mPEG-His-cMAP-His-PEGm (TriB-His).

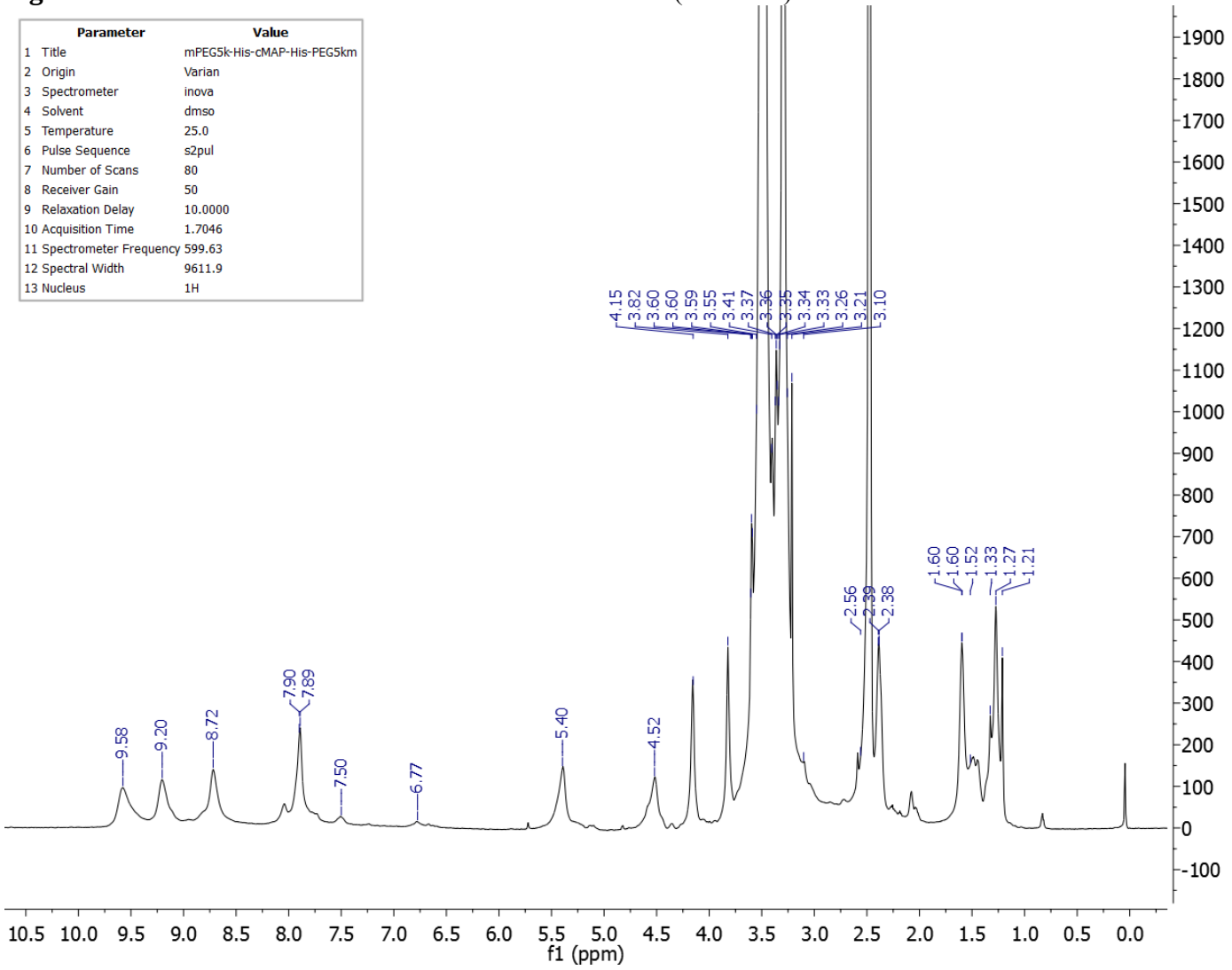

Figure IV.S23: Titration curve of mPEG-His-cMAP-His-PEGm (TriB-His).
To determine how much imidazole is present in the polymer, 3.2 mg of the polymer was dissolved in 5 mL of deionized water and titrated with 1 N HCl. The equivalence point was reached around 40-50 uL of acid added. Calculating the helf-equivalence point results in 1.7-2.1 imidazole groups per mmol of polymer.

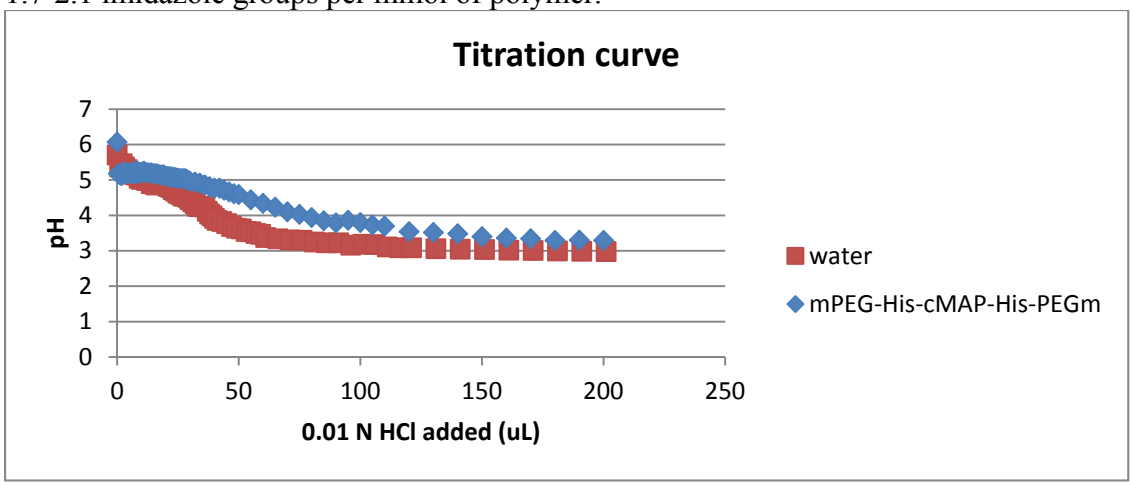

Figure IV.S24: Validation of the siEGFR sequence with Lipofectamine RNAiMAX transfection reagent.

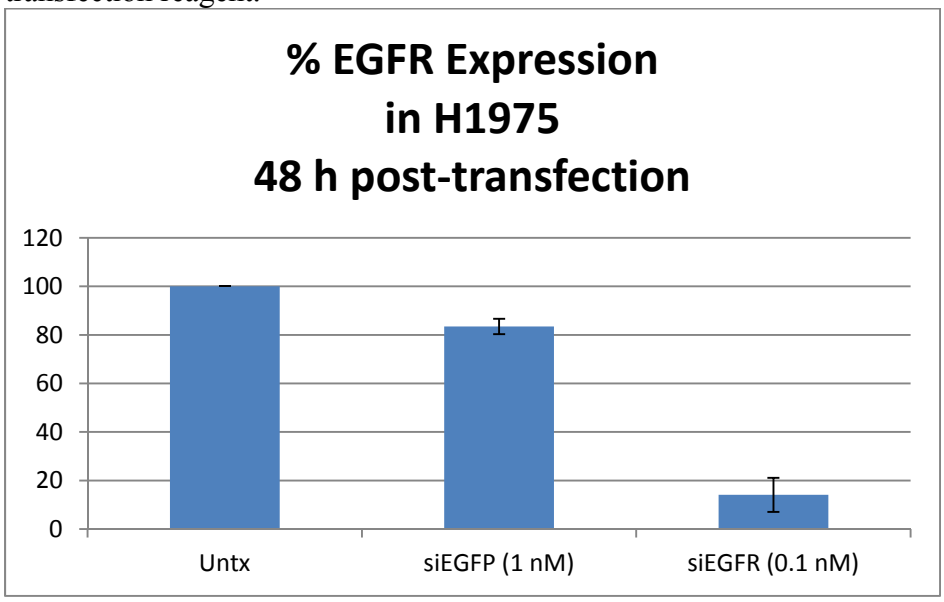

Figure IV.S25: Validation of the siBRAF sequence with Lipofectamine RNAiMAX transfection reagent.

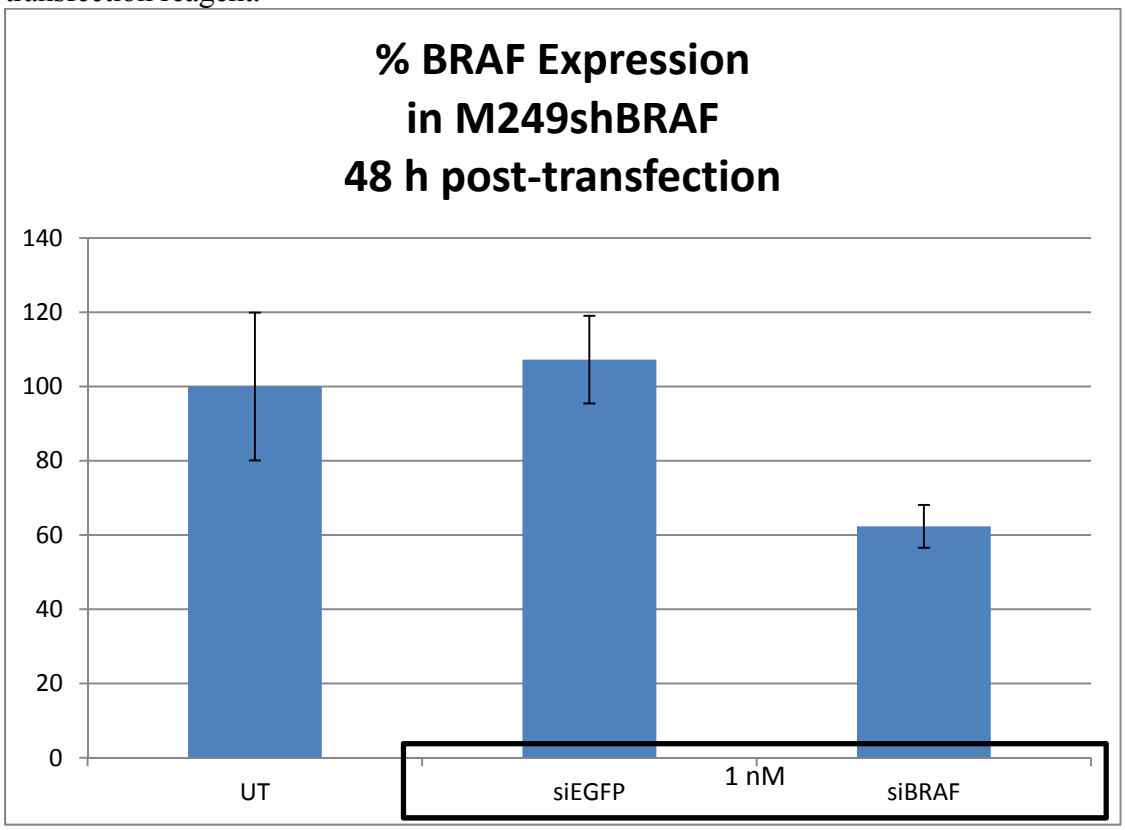

Figure IV.S26: Displacement binding of CTX-AF488 by cetuximab and cetuximab-PEGs to EGFR on H1975 cells.

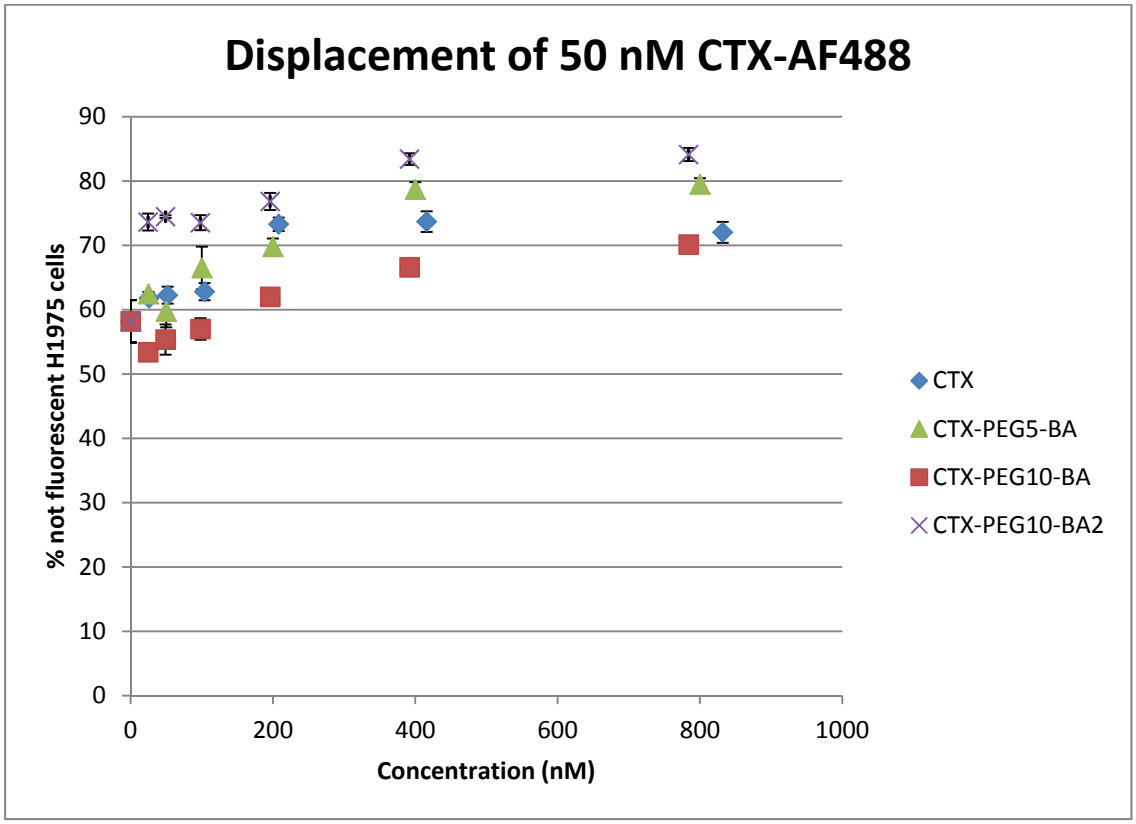

Figure IV.S27: Displacement binding of Tf-AF488 by transferrin and transferrin-PEGs to transferrin receptor on Neuro-2A cells.

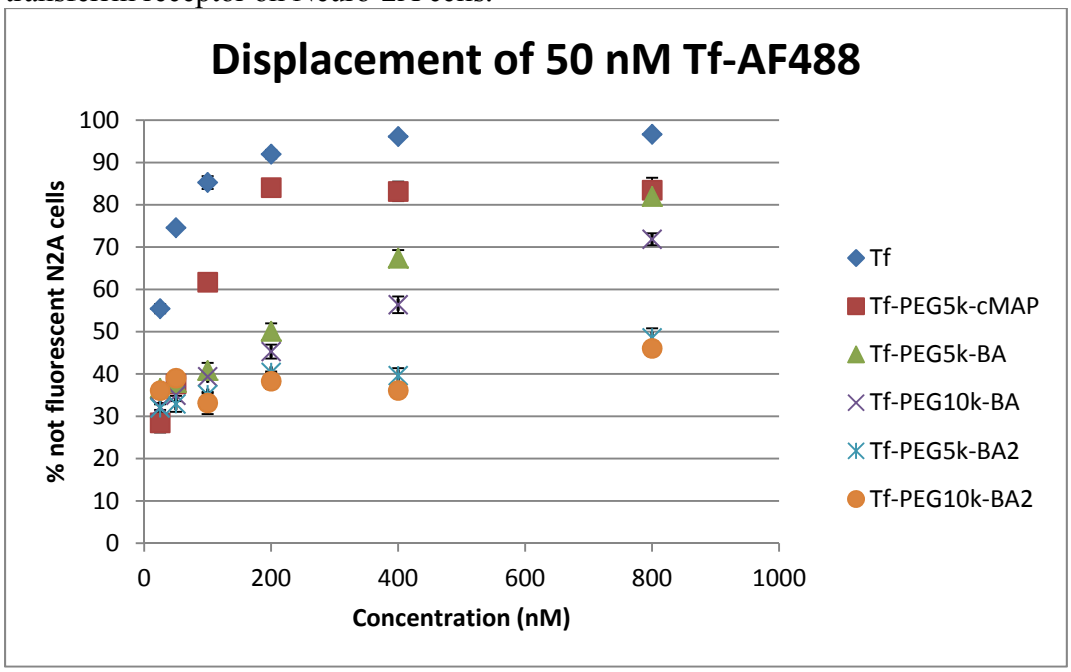

Figure IV.S28: Validation of qRT-PCR assay probe for the siEGFR sequence by transfecting cells with siEGFR using Lipofectamine RNAiMAX transfection reagent.

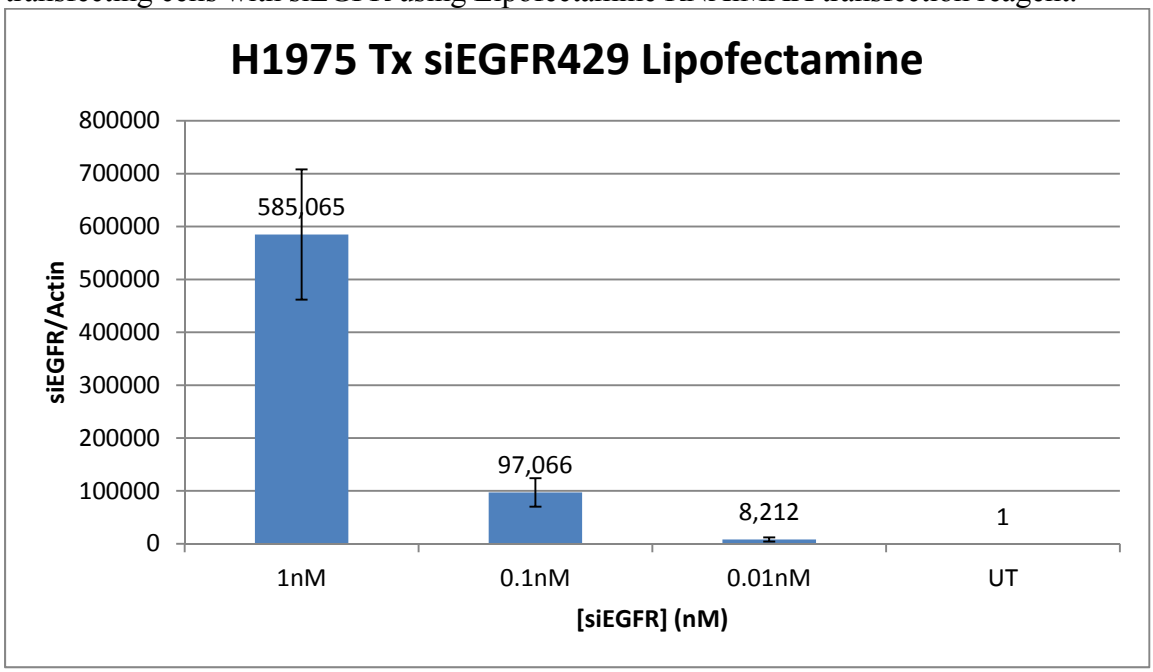

Figure IV.S29: Individual mice for the 0.13 mol% cetuximab-targeted cMAP + 5-nPBA-PEGm NP formulation containing siEGFR group. The average of the saline group is included for comparison. Orange arrows indicate when mice were injected with doses of the NP formulation.

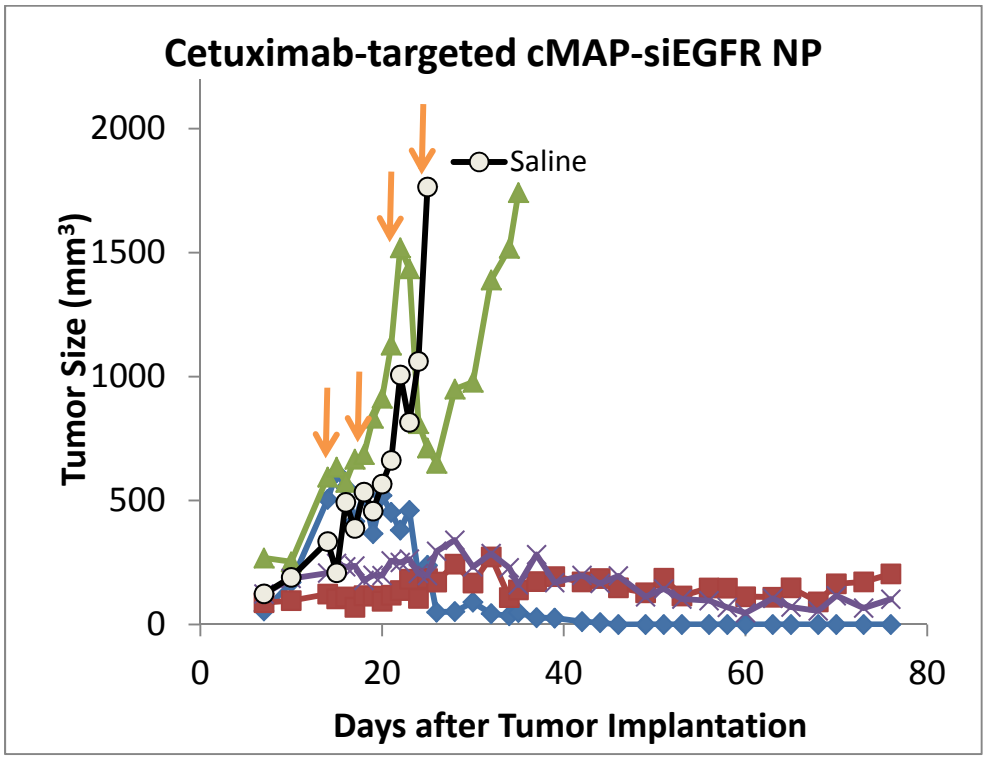

Figure IV.S30: Individual mice for the cetuximab alone group. The average of the saline group is included for comparison. Orange arrows indicate when mice were injected with doses of the NP formulation.

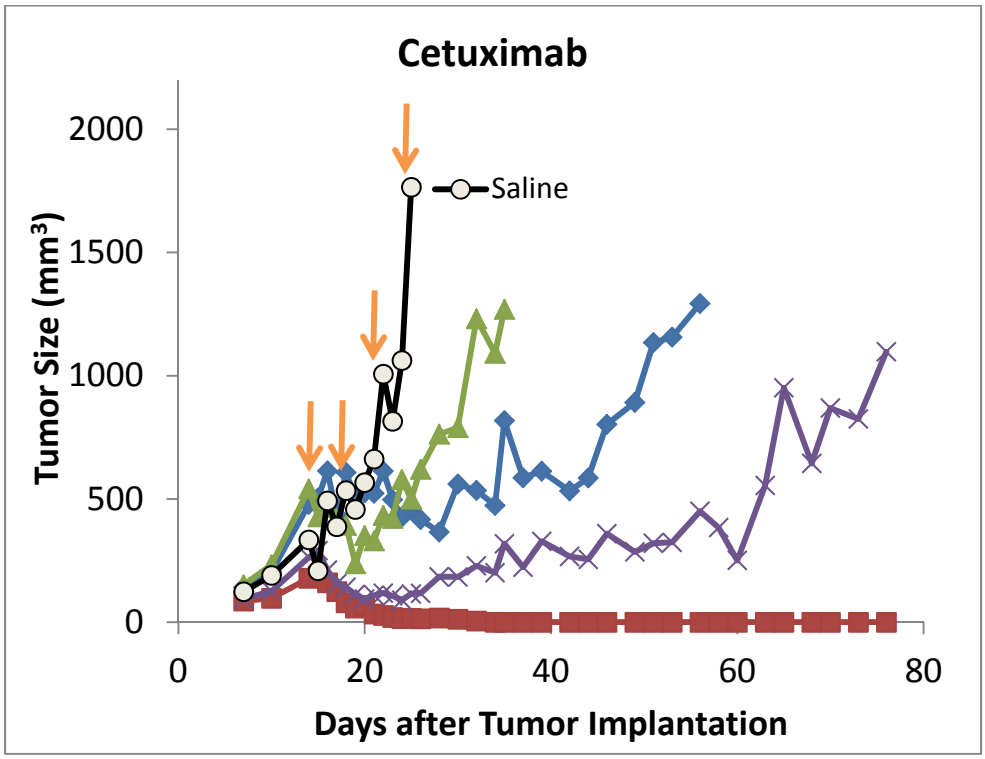

Figure IV.S31: MALDI of panitumumab-PEG5k-5nPBA, 153 kD. Panitumumab (Vectibix) is originally 148 kD.

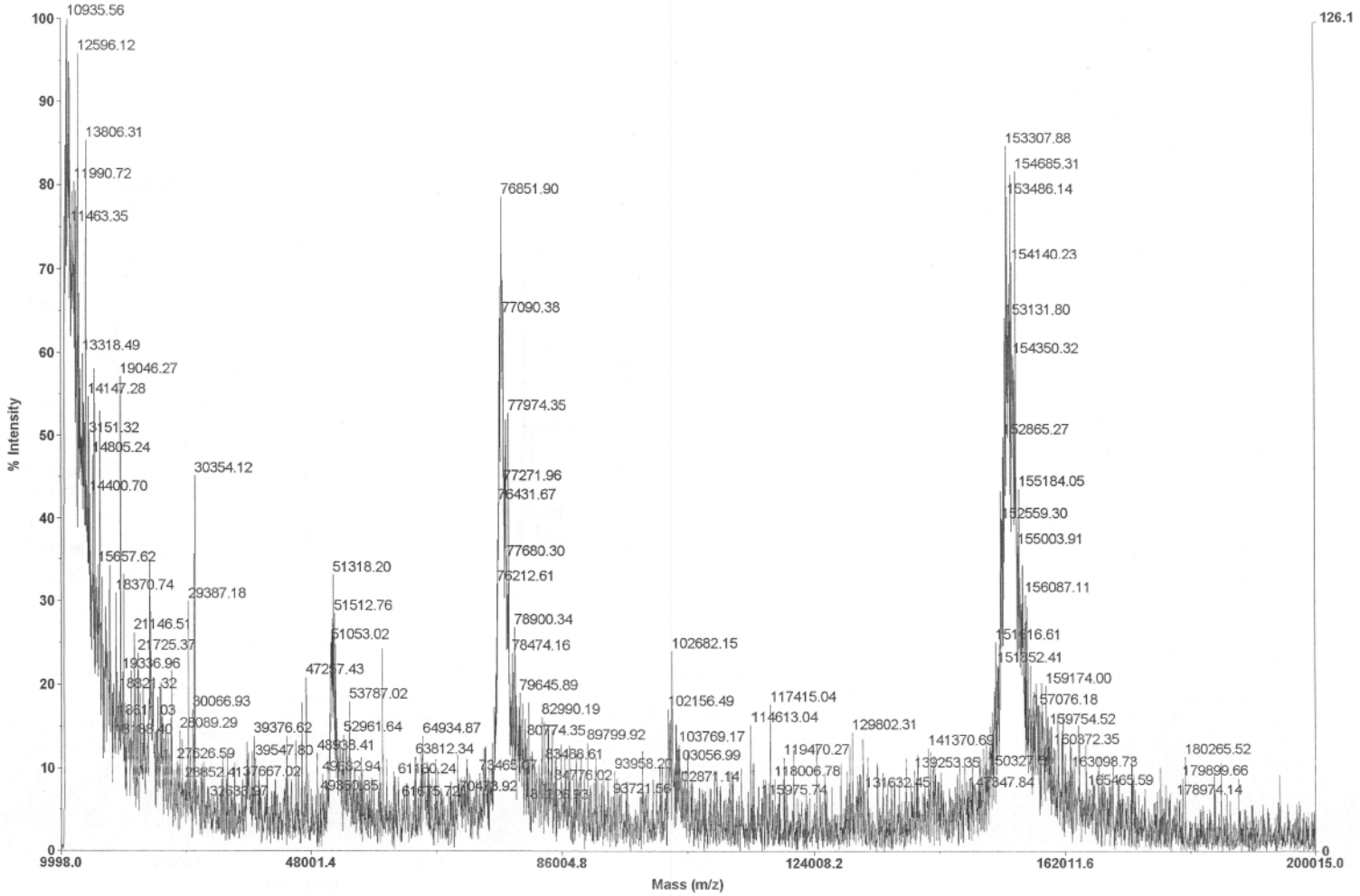

L:\...\20141113_5-nPBA-PEG-Vectibix_88-139_0001.dat
Acquired: 17:58:00, November 13, 2014

Figure IV.S32: Mean sizes of M249shBRAF tumor xenografts in nude mice (n=6) comparing standard diet to doxycycline-containing diet.

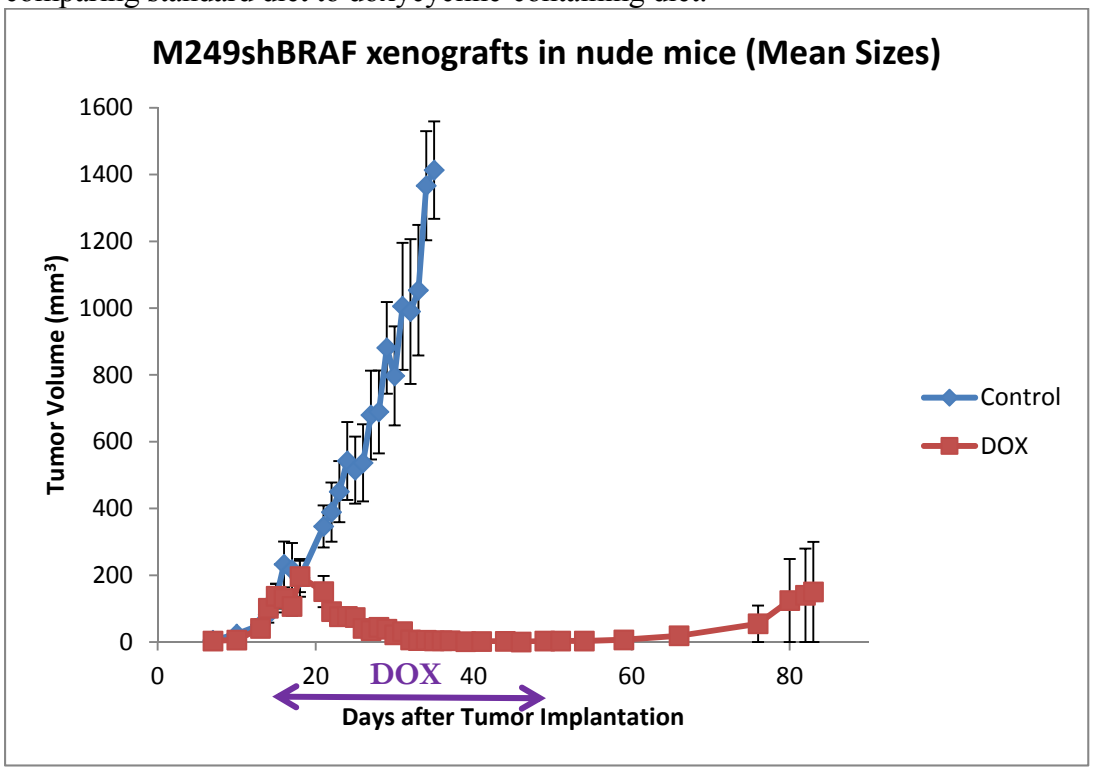

Figure IV.S33: Individual nude mice bearing M249shBRAF tumor xenografts (n = 5) injected with saline control.

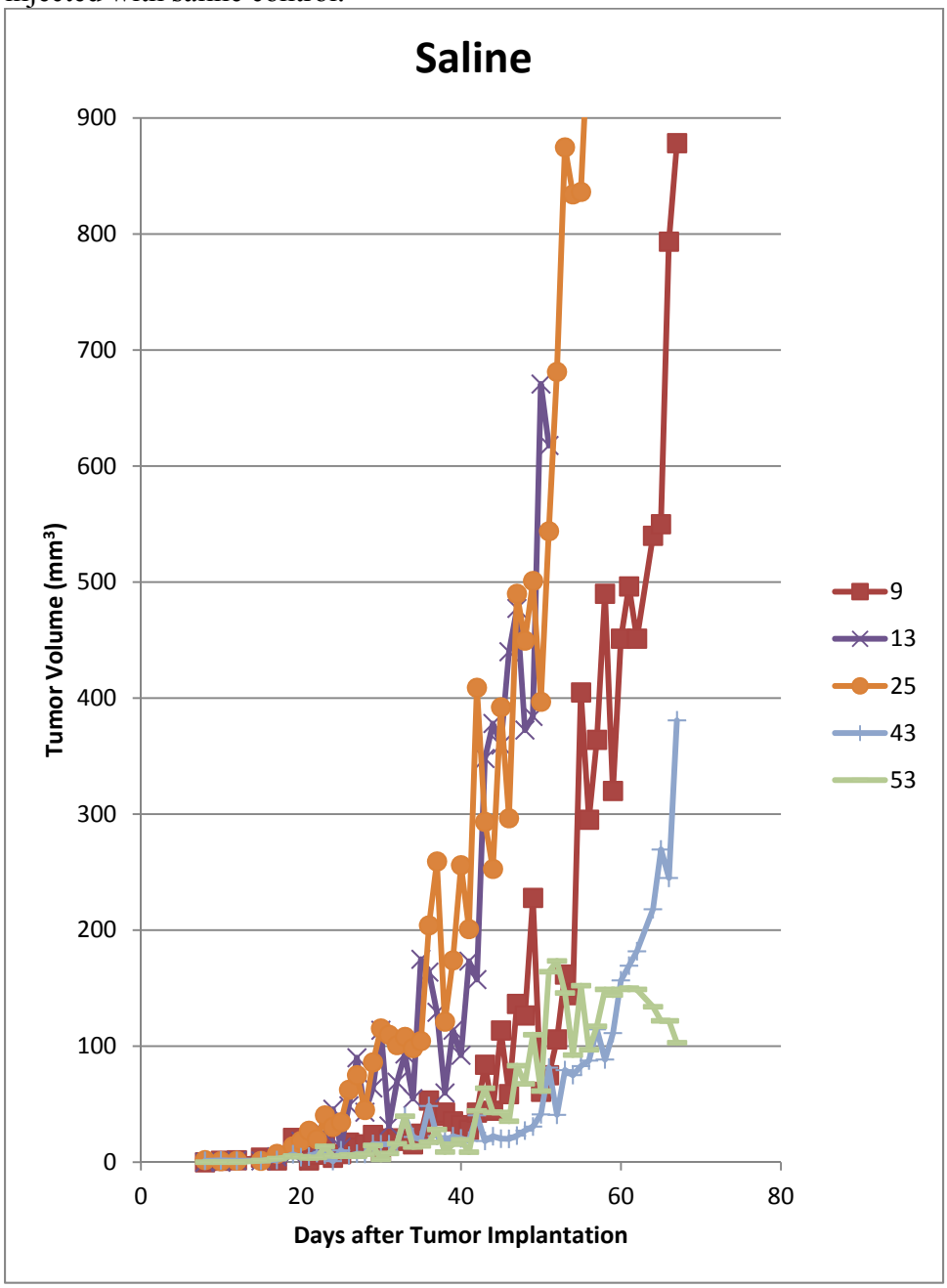

Figure IV.S34: Individual nude mice bearing M249shBRAF tumor xenografts (n = 5) injected with 0.25 mol% Tf-PEG5k-(5nPBA)$_2$ targeted TriB-His NP containing siBRAF at 5 mg/kg per dose.

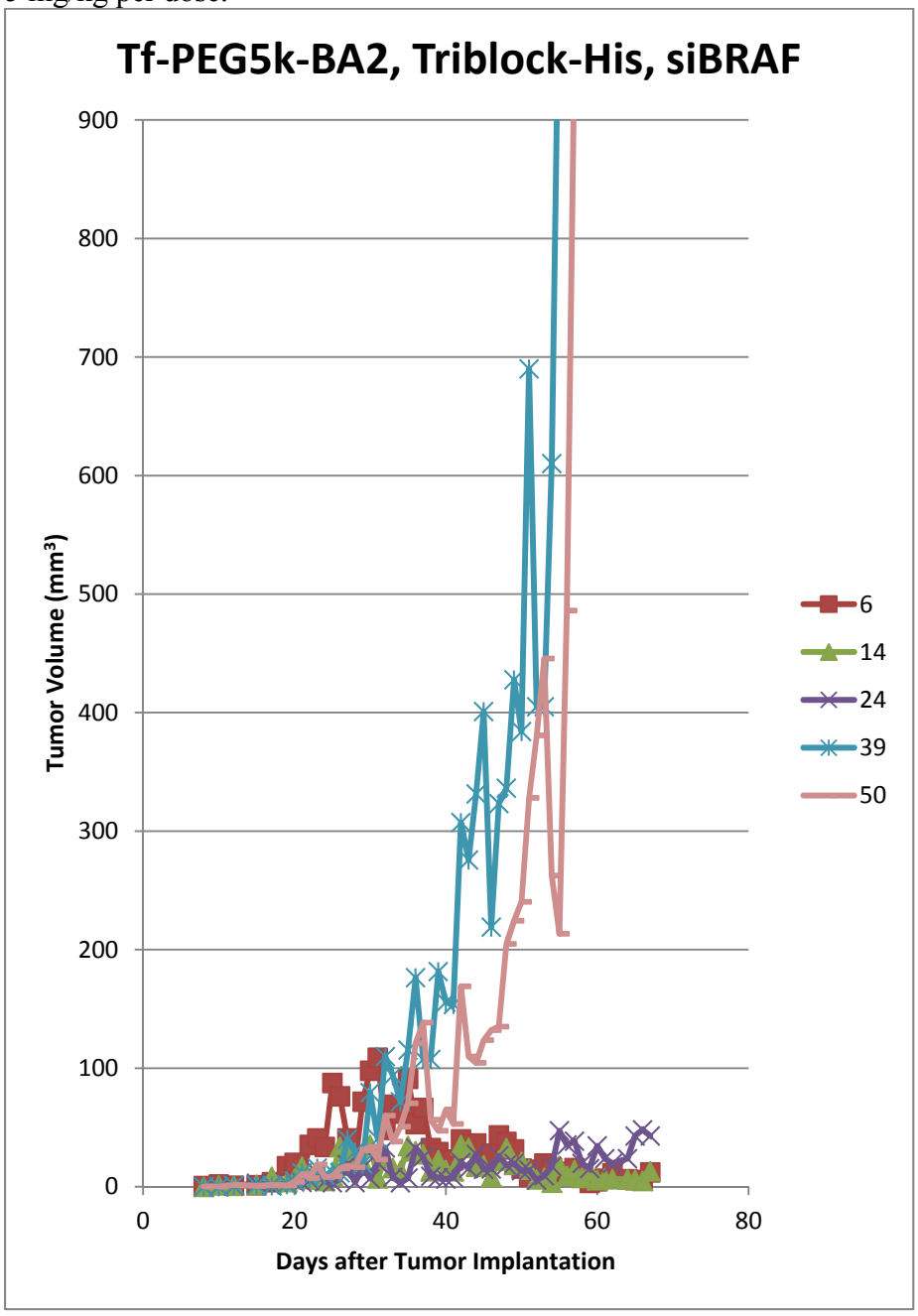

Figure IV.S35: Mean sizes of nude mice (n = 5) bearing M249shBRAF tumor comparing the 0.25 mol% Tf-PEG5k-(5nPBA)$_2$ targeted TriB-His NP containing siBRAF at 5 mg/kg per dose group with that of saline control showing no statistical significance.

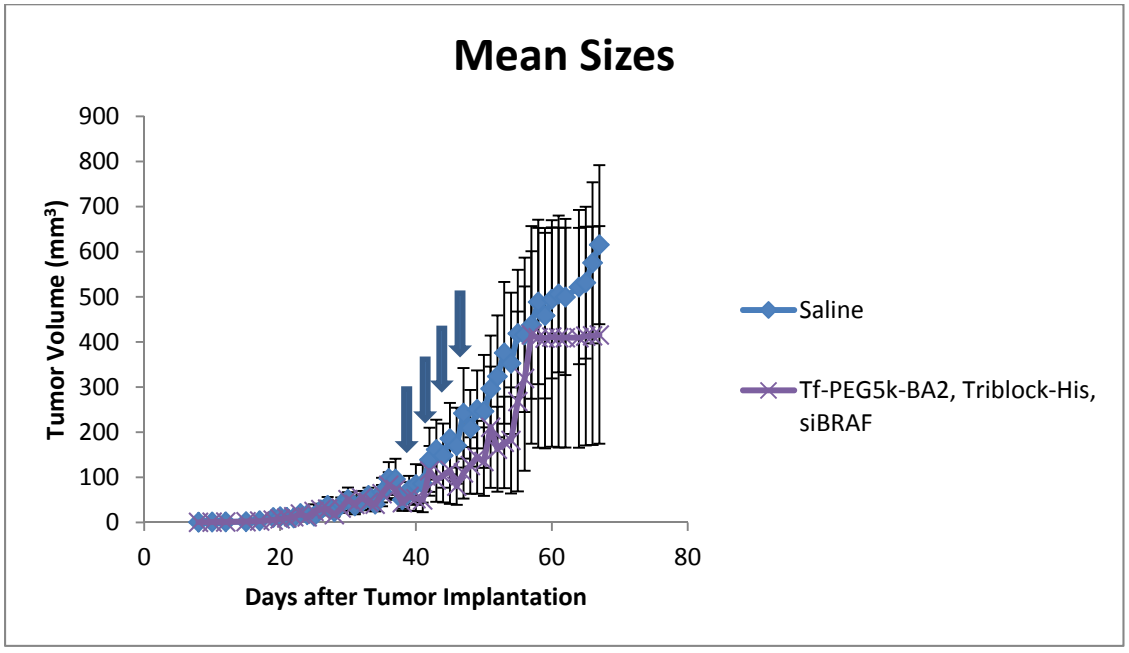

Figure IV.S36: Mean sizes of nude mice (n = 2) bearing M249shBRAF tumor comparing the 0.5 mol% Tf-PEG5k-adamante targeted CDP NP containing siBRAF at 5 mg/kg per dose group with that of saline control showing some difference in effect.

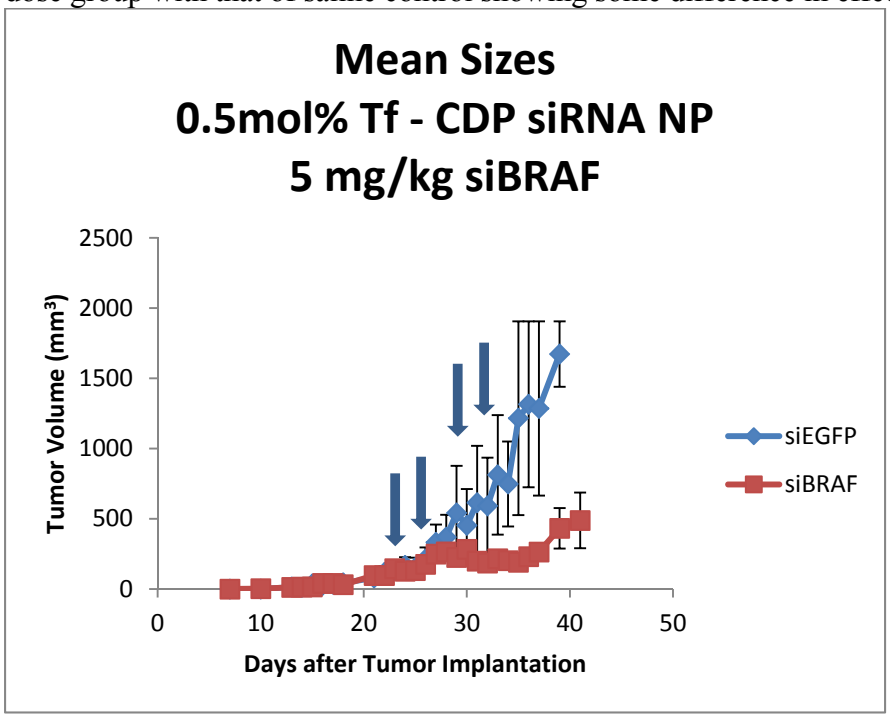

REFERENCES

1. Wu, S. Y., Lopez-Berestein, G., Calin, G. A., and Sood, A. K. (2014) RNAi Therapies: Drugging the Undruggable. *Science Transl. Med. 6*, 240ps7.
2. Ballarin-Gonzalez, B.; Howard, K.A. Polycation-based nanoparticle delivery of RNAi therapeutics: adverse effects and solutions. *Advanced Drug Delivery Reviews* **2012,** *64,* 1717-1729.
3. Zuckerman, J. E., Gritli, I., Tolcher, A., Heidel, J. D., Lim, D., Morgan, R., Chmielowski, B., Ribas, A., Davis, M. E., and Yen, Y. Correlating animal and human phase Ia/Ib clinical data with CALAA-01, a targeted, polymer-based nanoparticle containing siRNA. *Proc. Natl. Acad. Sci. U. S. A.* **2014,** *111*, 11449−11454.
4. Zuckerman, J. E., Choi, C. H. J., Han, H., and Davis, M. E. Polycation-siRNA nanoparticles can disassemble at the kidney glomerular basement membrane. *Proc. Natl. Acad. Sci. U. S. A.* **2012**, *109*, 3137−3142.
5. Naeye, B., Deschout, H., Caveliers, V., Descamps, B., Braeckmans, K., Vanhove, C., Demeester, J., Lahoutte, T., De Smedt, S. C., and Raemdonck, K. *In vivo* disassembly of IV administered siRNA matrix nanoparticles at the renal filtration barrier. *Biomaterials* **2013,** *34*, 2350−2358.
6. Christie, R. J., Matsumoto, Y., Miyata, K., Nomoto, T., Fukushima, S., Osada, K., Halnaut, J., Pittella, F., Kim, H. J., Nishiyama, N., et al. Targeted polymeric micelles for siRNA treatment of experimental cancer by intravenous injection. *ACS Nano* **2012**, *6*, 5174−5189.
7. Nelson, C. E., Kintzing, J. R., Hanna, A., Shannon, J. M., Gupta, M.K., and Duvall, C. L. Balancing cationic and hydrophobic contentof PEGylated siRNA polyplexes enhances endosome escape, stability, blood circulation time, and bioactivity *in vivo*. *ACS Nano* **2013**, *7*, 8870−8880.
8. Barrett, S. E., Burke, R. S., Abrams, M. T., Bason, C., Busuek, M., Carlini, E., Carr, B. A., Crocker, L. S., Fan, H., Garbaccio, R. M., et al. Development of a liver-targeted siRNA delivery platform with a broad therapeutic window utilizing biodegradable polypeptide-based polymer conjugates. *J. Controlled Release* **2014**, *183*, 124−137.
9. Pan, D.W.; Davis, M.E. Cationic mucic acid polymer-based siRNA delivery systems. *Bioconjugate Chemistry* **2015,** *26,* 1791-1803.
10. Han, H., and Davis, M. E. (2013) Targeted nanoparticles assembled via complexation of boronic acid-containing targeting moieties to diol-containing polymers. *Bioconjugate Chem. 24,* 669-677.

11. Van Schaeybroeck, S.; Kyula, J.; Kelly, D.M.; et al. Chemotherapy-induced epidermal growth factor receptor activation determines response to combined gefitinib/chemotherapy treatment in non-small cell lung cancer cells. *Mol. Cancer Ther.* **2006,** *5,* 1154-1165.
12. Parmenter, T.J.; Kleinschmidt, M.; Kinross, K.M.; et al. Response of BRAF mutant melanoma to BRAF inhibition is mediated by a network of transcriptional regulators of glycolysis. *Cancer Discov.* **2014,** *4,* 423-433.
13. Bartlett, D.W.; Davis, M.E. Schedule on tumor growth inhibition after intravenous administration of siRNA-containing nanoparticles. *Biotechnol. Bioeng.* **2008,** *99,* 975-985.
14. Robbins, M.; Judge, A.; Ambegia, E.; et al. Misinterpreting the therapeutic effects of small interfering RNA caused by immune stimulation. *Human Gene Therapy* **2008,** *19,* 991-999.
15. Jewell, C.M.; Lynn, D.M. Surface-mediated delivery of DNA: cationic polymers take charge. *Curr. Opin. Colloid Interface Sci.* **2008,** *13,* 395-402.
16. Frohlich, E. The role of surface charge in cellular uptake and cytotoxicity of medical nanoparticles. *International Journal of Nanomedicine* **2012,** *7,* 5577-5591.
17. Ahmed, M., Pan, D.W., and Davis, M.E. Lack of *in vivo* antibody dependent cellular cytotoxicity with antibody containing gold nanoparticles. *Bioconjugate Chem.* **2015**, *26*, 812-816. doi : 10.1021/acs.bioconjchem.5b00139
18. Springsteen, G.; Wang, B. A detailed examination of boronic acid-diol complexation. *Tetrahedron* **2002,** *58,* 5291-5300.

Chapter 5

Conclusions and Outlook

Small interfering RNA (siRNA) has a lot of promise as a very specific therapy that can silence virtually any gene. As a macromolecular double-stranded RNA, it has a number of hurdles to jump over in order to reach its location of function. It needs be protected from nuclease degradation using a delivery system, which also can serve to slow its quick clearance from circulation. Getting to the location, such as a tumor, can be tricky, and once there it needs to get inside cells. This usually occurs through an endocytic process which will localize the siRNA into the endosome, and so there needs to be a method to break out of the endosomal for the siRNA to reach the cytosol where it can function. Additional challenges include identifying the appropriate targets to stop the growth of a particular type of malignancy, as cancer types even arising from the same site with similar morphology can be genetically very distinct. With the genes in mind, designing siRNA sequences specific to the mRNA with minimal effect on other similar sequences that are very potent to cause durable protein silencing to result in cell death can be challenging.

We addressed some of the siRNA delivery challenges by building a nanoparticle (NP) siRNA delivery system based on cationic-mucic acid polymer (cMAP). cMAP needs 5nPBA-PEGm for creating a stable nanoparticle formulation, while the mPEG-cMAP-PEGm triblock polymer can form stable nanoparticles with siRNA alone. These polymers form 30-45 nm particles with siRNA. The cMAP + 5nPBA-PEGm siRNA NP already circulates in the mouse bloodstream longer than siRNA alone and the CALAA-01 siRNA delivery system previously developed in our lab. The mPEG-cMAP-PEGm siRNA NP

showed the longest circulation time that we have seen, with 10% of the formulation remaining in the bloodstream of mice 1 h after intravenous injection. Targeting the nanoparticle can work by conjugating a protein through a PEG to a boronic acid entity which binds to diols on cMAP, or by covalently conjugating the protein through a PEG directly to cMAP. A histidine added to the cMAP provides for an endosomal escape mechanism for siRNA to reach the cytosol in order to function. The nanoparticles are able to enter cells to decrease mRNA expression of their target and to reach the tumor site. Some tumor regression in non-small cell lung cancer and melanoma tumor xenograft models in nude mice show mixed effects that demonstrate the potential for therapy. Furthermore, it may be advantageous to use a targeting agent which also interferes with cancer growth for maximal therapeutic benefit.

Many of the parameters for siRNA delivery – such as circulation, stability, targeting, and knockdown – continue to be clarified. It may be that there needs to be an appropriate balance between some of these factors that will achieve the optimal delivery system that results in enough mRNA and ultimately protein knockdown to result in cell death. It is feasible that siRNA delivery challenges can be addressed and siRNA sequences can be developed to target many of the drivers of tumor growth. Because of the myriad number of genes and pathways that are dysregulated in malignant cells, and the mosaic of mutated cells present in a tumor, multiple genes may be altered. A siRNA delivery system has the ability to deliver multiple siRNA sequences to target multiple genes which fuel cell proliferation.

With advances in blood detection of circulating tumor cells that reduce the need for invasive biopsies and with cancer genome sequencing, many mutations are identified.

What is complex is to interpret the information and figure out which genes to target as the problematic drivers of cell growth and proliferation. Of course, as with any targeted treatment we have seen that after a good response to therapy, these malignant cells eventually mutate to render the current therapy useless and the tumors return in full force. Therefore, real time detection of the mutations is needed while the tumor is still in regression and before progression can be seen in current imaging techniques used to monitor tumor response. If this type of feedback can be achieved with a well-functioning siRNA delivery system using potent siRNA's which target many of the mutations that can evolve, there eventually will be enough information and therapies to accurately tune treatment "preemptively" under current clinical definitions of the tumor being in remission.